Cavity quantum electrodynamics from semiclassical methods to quantum computing

Dissertation
zur Erlangung des Doktorgrades an der Fakultät für Mathematik, Informatik und Naturwissenschaften
Fachbereich Physik der Universität Hamburg

Vorgelegt von:

Francesco Troisi

Abgabe:
Hamburg, January 2026

Gutachter/innen der Dissertation: Prof. Dr. Angel Rubio
Prof. Dr. Simone Latini

Zusammensetzung der Prüfungskommission: Prof. Dr. Angel Rubio
Prof. Dr. Simone Latini
Prof. Dr. Peter Schmelcher
Prof. Dr. Daniela Pfannkuche
Prof. Dr. Peter Schauss

Vorsitzender der Prüfungskommission: Prof. Dr. Peter Schmelcher

Datum der Disputation: 30.03.2026

Vorsitzender des Fach-Promotionsausschusses Physik: Prof. Dr. Johannes Haller

Leiter des Fachbereichs Physik: Prof. Dr. Markus Drescher

Dekan der Fakultät MIN: Prof. Dr.-Ing. Norbert Ritter

Declaration on oath (Eidesstattliche Erklärung)

I hereby declare and affirm that this doctoral dissertation is my own work and that I have not used any aids and sources other than those indicated.

If electronic resources based on generative artificial intelligence (gAI) were used in the course of writing this dissertation, I confirm that my own work was the main and value-adding contribution and that complete documentation of all resources used is available in accordance with good scientific practice. I am responsible for any erroneous or distorted content, incorrect references, violations of data protection and copyright law or plagiarism that may have been generated by the gAI.

Hamburg, 22/1/2026

Francesco Troisi

Francesco Troisi, doctoral candidate

Contents

Preface

The following work, presented in the form of a cumulative thesis, has been conducted from November 2022 until January 2026 in the theory department of the Max Planck Institute for Structure and Dynamics of Matter (Hamburg, Germany), directed by Prof. Dr. Angel Rubio. It is based on the publications I-IV, presented in the chapters 2, 3 and 4. The work was supervised by Prof. Dr. Angel Rubio. The co-supervisors of this work were Prof. Dr. Simone Latini and Dr. Ivano Tavernelli.

Abstract

Light–matter interactions sit at the heart of modern physics and chemistry, underpinning phenomena and technologies ranging from spectroscopy and ultrafast control to quantum materials and polaritonic chemistry. When the interaction becomes strong, as it can occur for molecules and solids embedded in optical cavities, electronic and photonic degrees of freedom hybridize, giving rise to new mixed light–matter excitations known as polaritons. By tuning this hybridization, one can reshape optical response, energy flow, and even material functionality, opening powerful routes toward cavity-enabled control and design. These capabilities are especially compelling for the control of quantum materials, as cavity coupling can offer new knobs to address hidden or competing phases of matter and to probe electronic correlations in many-body systems. In particular, optical spectroscopies (both perturbative and non-perturbative, including time-resolved approaches) provide a versatile toolbox to access correlation effects and dynamical phenomena that are difficult to reveal otherwise. This cumulative thesis explores these opportunities through three complementary theoretical approaches: semiclassical electromagnetism, fully quantized cavity quantum electrodynamics (QED), and emerging strategies based on quantum computing.

The first part of this thesis presents an *ab initio* semiclassical framework that couples Maxwell's equations to time-dependent density-functional theory (TDDFT) via full minimal coupling in Coulomb gauge. Thanks to the development of a forward-backward interaction scheme, where both the electrons dynamics is influenced by the electromagnetic field and the matter is also a source for the field itself, it is possible to study light-matter coupled systems beyond the dipole approximation. The developed tool, which uses advanced numerical algorithms, was developed in the open-source code Octopus and applied to several applications, specifically for studying the dynamics of Cherenkov radiation from a superluminal electronic wavepacket, the linearly polarized XUV excitation of benzene (revealing phase-retarded atomic dipoles and induced orbital angular momentum) and the Lamb-like radiative frequency shift of a sodium dimer due to the self-induced transverse field.

The second part of this thesis deals with cavity materials engineering, exploring the effect of dark and driven optical cavities on 2D materials with the goal of achieving control of their properties. The discussion is based on the Pauli–Fierz Hamiltonian, formulated in the long wavelength approximation and effective cavity modes, represented on a matter excitation basis and exactly diagonalized to describe the polaritonic states. The key finding is the emergence of cavity-induced long-range interactions, which can be used on the one hand to control topological properties, such the opening of the gap at the Dirac points in Graphene, and on the other hand to induce exciton-exciton interactions and create an all-optical Moiré confinement in TMD heterostructures. These findings are interpreted by employing both exact diagonalization and effective methods, which include virtual excitations of the quantized photonic environment and allow to formulate a photon-free effective Hamiltonian.

The final section of this thesis addresses the computational bottleneck of simulating large electron–photon Hilbert spaces, whose dimensionality increases exponentially with the number of photonic modes, thereby making classical computations intractable. To overcome this, the present work investigates the use of quantum computers as a means to efficiently represent and evolve such composite Hilbert spaces. These devices inherently support compact encoding of bosonic states and can exploit well-established quantum time-evolution algorithms to simulate the dynamics of QED systems. Here, by adapting the structure of the quantum circuit to the specific constraints of the available hardware, accurate recovery of the relevant quantum dynamics is achieved, even when using noisy hardware.

Overall, this work establishes a path toward predictive, scalable control of quantum materials by structured electromagnetic environments.

Zusammenfassung

Licht-Materie-Wechselwirkungen stehen im Zentrum der modernen Physik und Chemie und bilden die Grundlage für Phänomene und Technologien von Spektroskopie und ultraschneller Steuerung bis hin zu Quantenmaterialien und polaritonischer Chemie. Im Regime starker Kopplung, wie sie bei Molekülen und Festkörpern in optischen Hohlräumen auftritt, hybridisieren elektronische und photonische Freiheitsgrade und bilden neue gemischte Licht-Materie-Anregungen, sogenannte Polaritonen. Durch gezielte Beeinflussung dieser Hybridisierung lassen sich optische Antwort, Energiefluss und sogar die Materialfunktionalität kontrollieren. Diese Möglichkeiten sind besonders faszinierend für die Kontrolle von Quantenmaterialien: Die Kopplung an Hohlräume bietet neue Hebel, um verborgene oder konkurrierende Phasen der Materie anzusteuern und elektronische Korrelationen in Vielteilchensystemen zu untersuchen. Insbesondere optische Spektroskopien – sowohl perturbativ als auch nicht-perturbativ, einschließlich zeitaufgelöster Ansätze – stellen eine vielseitige Werkzeugkiste bereit, um Korrelationseffekte und dynamische Prozesse zugänglich zu machen die sonst schwer erfassbar sind. Diese kumulative Dissertation erforscht diese Potenziale durch drei komplementäre theoretische Ansätze: semiklassische Elektrodynamik, vollständig quantisierte Hohlräume-QED sowie neuartige Strategien des Quantencomputings.

Der erste Teil dieser Arbeit präsentiert ein ab initio-semiklassisches Rahmenwerk, das die Maxwell-Gleichungen über vollständige minimale Kopplung in Coulomb-Eichung mit der zeitabhängigen Dichtefunktionaltheorie (TDDFT) verknüpft. Durch die Entwicklung eines Vorwärts-Rückwärts Wechselwirkungsschemas, bei dem die Elektronendynamik vom elektromagnetischen Feld beeinflusst wird und die Materie selbst eine Quelle dieses Feldes darstellt, lassen sich Licht-Materie-gekoppelte Systeme jenseits der Dipolnäherung untersuchen. Das entwickelte Werkzeug, das auf fortgeschrittenen numerischen Algorithmen basiert und im Open-Source-Code Octopus implementiert wurde, wurde auf mehrere Anwendungen angewandt – insbesondere zur Untersuchung der Cherenkov-Strahlungsdynamik eines superluminalen Elektronenwellenpakets, der linear polarisierten XUV-Anregung von Benzol (mit Nachweis phasenverzögerter atomarer Dipole und induziertem Bahndrehimpuls) sowie der Lamb-ähnlichen radiativen Frequenzverschiebung eines Natriumdimers durch das selbstinduzierte transversale Feld.

Der zweite Teil dieser Arbeit widmet sich der Materialgestaltung in Hohlräumen und untersucht den Einfluss dunkler und getriebener optischer Hohlräume auf 2D-Materialien mit dem Ziel, deren Eigenschaften gezielt zu steuern. Die Analyse basiert auf dem Pauli-Fierz-Hamiltonoperator in der langwelligen Näherung mit effektiven Hohlräumemoden, dargestellt auf einer Basis von Materieanregungen und exakt diagonalisiert zur Beschreibung der polaritonischen Zustände. Ein zentrales Ergebnis ist das Auftreten hohlrauminduzierter Langstreckenwechselwirkungen, die einerseits topologische Eigenschaften – wie die Öffnung der Bandlücke an den Dirac-Punkten in Graphen – kontrollieren und andererseits Exziton-Exziton-Wechselwirkungen induzieren sowie eine rein optische Moiré-Einfangung in TMD-Heterostrukturen erzeugen können. Diese Befunde werden durch exakte Diagonalisierung

sowie effektive Methoden interpretiert, die virtuelle Anregungen des quantisierten photonischen Umfelds einbeziehen und die Formulierung eines photonfreien effektiven Hamiltonians ermöglichen.

Der abschließende Teil dieser Arbeit adressiert die rechnerische Engpassproblematik bei der Simulation großer Elektron-Photon-Hilberträume, deren Dimension mit der Anzahl der photonischen Moden exponentiell wächst und klassische Berechnungen unpraktikabel macht. Um dies zu überwinden, untersucht die vorliegende Arbeit den Einsatz von Quantencomputern zur effizienten Darstellung und Zeitentwicklung solcher kompositer Hilberträume. Diese Geräte ermöglichen eine kompakte Kodierung bosonischer Zustände und nutzen etablierte Quanten-Zeitentwicklungsalgorithmen zur Simulation der QED-Dynamik. Durch Anpassung der Quantenschaltung an die spezifischen Einschränkungen der verfügbaren Hardware gelingt die präzise Rekonstruktion der relevanten Quantendynamik, selbst auf verrauschter Hardware.

Insgesamt ebnet diese Arbeit den Weg zu einer prädiktiven, skalierbaren Kontrolle von Quantenmaterialien durch strukturierte elektromagnetische Umgebungen.

List of publications and declaration of contribution

The present cumulative thesis is based on the following publications (I-IV), listed as they appear in this work.

Publication I describes a semi-classical approach for the simulation of light-matter coupled systems, presenting an *ab-initio* tool that combines a framework for beyond-dipole interaction with radiation reaction.

Publications II-III deal with the topic of cavity materials engineering, presenting how one can exploit the enhanced light-matter coupling in an optical cavity to modify the properties of materials, focusing on cavity-mediated interactions. Here we use a fully second-quantized Hamiltonian. Publication II shows that a cavity can produce an all-optical Moiré-like confinement and re-normalize the excitonic bands and effective mass, while Publication III explores how different configurations of the optical modes in the cavity affect the Dirac states in Graphene.

Finally, Publication IV presents and applies a formulation of the light-matter coupled Hamiltonian in optical cavities, optimized for near-term superconducting quantum computers.

- **Publication I (cf. Chapter 2.3):** Franco Bonafé, Esra Ilke Albar, Sebastian Ohlmann, Valeriia Kosheleva, Carlos Bustamante, **Francesco Troisi**, Angel Rubio and Heiko Appel; Full minimal coupling Maxwell-TDDFT: An ab initio framework for light-matter interaction beyond the dipole approximation; *Phys. Rev. B* 111, 085114 (February, 2025)

- **Publication II (cf. Chapter 3.3): Francesco Troisi**, Hannes Hübener, Angel Rubio and Simone Latini; Cavity-QED-controlled two-dimensional Moiré Excitons without twisting; *Nat. Commun.* **17**, 157 (January, 2026)

- **Publication III (cf. Chapter 3.4):** Hang Liu, **Francesco Troisi**, Hannes Hübener, Simone Latini and Angel Rubio; Cavity-Mediated Electron-Electron Interactions: Renormalizing Dirac States in Graphene; *Sci. Adv.* **11**, eadz1855 (October, 2025)

- **Publication IV (cf. Chapter 4.4): Francesco Troisi**, Simone Latini, Heiko Appel, Martin Lüders, Angel Rubio and Ivano Tavernelli; Hardware-efficient formulation of molecular cavity-QED Hamiltonians; *arXiv*, arXiv:2510.17461 [**quant-ph**]

Declaration of contribution

In the following I will state my contribution to all of the presented publications:

- **Publication I:** I developed the code to perform the Helmholtz decomposition, which plays a central role in the simulations as it allows to calculate the vector potential from the electromagnetic field, to be used in the forward coupling. The development also included the creation of two regression tests to ensure the consistency of results. I also wrote the corresponding section in the Supplementary Information (including running the calculations for the creation of the figures). All authors have contributed to the revision of the manuscript.

- **Publication II:** I derived the theory, developed all the code, performed all simulations, analyzed the data, interpreted the results and wrote the manuscript. All authors have contributed to the analysis of the data and the revision of the manuscript.
- **Publication III:** I had developed a code for simulating materials in optical cavities and used it to simulate Graphene, predicting the opening of a optical gap using circularly polarized light. Subsequently, the first author of Publication III developed the QED-HF framework (as well as its code) to explain such findings from the standpoint of the electronic states, as it is not obvious that aside from the optical gap there was also a gap in the electronic states. All authors have contributed to the analysis of the data and the revision of the manuscript.
- **Publication IV:** I derived the theory, developed all the code (except for the `MixedOp` and `MixedMapper` classes, to which I contributed with technical design and code review), performed all simulations, analyzed the data, interpreted the results and wrote the paper. All authors contributed to the revision of the manuscript.

A mio nonno Vaifro,
farò sempre tesoro dei tuoi insegnamenti

To my grandfather Vaifro, I'll always treasure your teachings

1 Introduction

Materiam lucemque cano[1]
- Adapted from *Aeneis, Vergilius (27-19 B.C.)*

How light interacts with matter is a cornerstone theme that runs through the history of physics. Early evidence of such interest dates back to ancient Greeks and Romans, with the works of Euclid, who first stated the principles of geometrical optics (*'Οπτικά*, around 300 BC), and Ptolemy, who first reported tables for the refraction law (*Optics*, around 160 AD). Ancient historians also report of attempts to exploit the interaction between light and matter, in the form of heat (energy) transfer, such as in Archimedes' usage of reflection and focusing to destroy the Roman fleet during the siege of Syracuse (213-212 BC). We mainly know about such sources thanks to the later, more extensive work *Book of Optics*, written by Ibn al-Haytham at the beginning of the XI century, which heavily influenced European science during the renaissance. From these early insights, observations and mathematical tools progressed and two fundamentally different views on the nature of lights emerged. On one hand, Newton's corpuscular theory and on the other Huygens' wave theory. While the former was formalized only in the early days of quantum mechanics (with Plank's blackbody radiation and Einstein's photoelectric effect), the wave theory, which had been more effective in explaining refraction, diffraction (Fresnel) and interference (Young) gained popularity until its formalization in 1865, when Maxwell published his famous equations.

Light, or more generally the radiation field, is indeed fully described, with the exception of quantum-related phenomena, by Maxwell's equations. Using this theory it is possible to make predictions on the electromagnetic field, from its shape and propagation to its microscopic interaction with matter. As an example, by introducing the eikonal approximation one can derive the aforementioned laws of the geometrical optics [1]. On the other hand, classical electromagnetism also allows to semi-quantitatively describe the dynamics of electrons in a metal subject to an electric field [2], which is known as Drude model [3, 4]. While the classical and relativistic description of the electromagnetic field given by the Maxwell's equation is still widely used, when dealing with systems where light and matter interact the latter is mostly treated quantum mechanically. From a theoretical standpoint, methods where quantum matter interacts with classical light are known as semiclassical methods. Examples of applications include systems where the intensity of the field is strong enough to neglect the quantum

---

[1] *I sing the matter and the light.* This citation is adapted from the original preface of Aeneis: *Arma virumque cano*, which means *I sing the man and the weapons.*

effects but weaker than the internal atomic fields, spanning from laser physics and spectroscopy [5], to high harmonic generation [6, 7], as well as to systems whose characteristic dimensions are much bigger than the ones of the field [4]. A further notable application of semiclassical techniques is the modeling of attosecond physics [8, 9], especially known to be the subject of the 2023 Nobel Physics prize. Due to such a variety of applications, semiclassical methods are, to the present day, widely used.

However, semiclassical methods break down in regimes where the quantum nature of light is essential, that is at low photon numbers (few-photon fields) [10, 11], when light–matter entanglement becomes relevant [12], in the strong-coupling regime [13, 14] and, crucially, even in the absence of external illumination, where vacuum fluctuations can still drive measurable effects [15, 16]. Capturing these phenomena requires a fully quantum description of both the electromagnetic field and its interaction with matter. The quantum theory of light begun with the works of Planck (1900) [17] and Einstein (1905) [18], and the experimental works of Millikan (1909) and Compton (1923), until its complete formalization by Dirac (1927) [19]. Einstein [20] and Dirac's works firstly suggested the quantum theory of light-matter interaction, or quantum electrodynamics (QED), explaining the atomic spectrum lines and calculating the spontaneous emission's coefficient. QED, which allows to explain well-known phenomena such as the Lamb shift [21], the spontaneous emission [22] and the Casimir-Polder forces [23], was later formalized by Sin-Itiro Tomonaga, Julian Schwinger and Richard P. Feynman (1965 Nobel Physics prize) [10]. Aside from explaining the aforementioned phenomena, QED is a very powerful theory which allows to make accurate predictions on fundamental properties of matter. Notable examples are the anomalous magnetic dipole moment (or $g-2$) of the electron [24] and of the muon [25], but also estimation of the Rydberg R_∞ and fine structure constant α based on atomic recoil [26] and neutron Compton wavelength. More recently, QED has been involved in a growing number of studies that aim to control and engineer the properties of quantum materials by exploiting the interaction with the quantized electromagnetic field. This area of investigation is called cavity materials engineering [16, 27, 28, 29, 30, 31, 32, 33], and it will be the main focus of this thesis. In order to achieve such a control, light and matter should be strongly coupled (non-perturbative regime), such that the full system cannot be described by light and matter states separately, but rather by their hybridization called polaritonic states (stemming from the polariton, the quasi-particle associated to the light-matter interaction) [34]. However, reaching the strong coupling regime is complicated. In fact, one cannot simply increase the intensity of the electromagnetic field, as doing so for long would likely destroy the sample. An effective way to achieve the coupling required to modify the properties of materials is to use optical cavities. These nanostructures confine the electromagnetic field in the small volume between the mirrors, which enhances the light-matter interaction and allows to reach the strong coupling regime with the embedded matter system while keeping it in equilibrium [35]. Studying light-matter interacting system in the context of optical cavities is referred to as cavity QED. As the fabrication of high-quality cavities is experimentally challenging [13, 36], the developments in theory are more mature than the experimental ones. However, recent advances highlight that this gap is closing [37, 38, 39]. Relevant applications of cavity QED can be found both in the context of polaritonic chemistry, where one can modify molecular polarizabilities [40, 41], inter-molecular properties [42] or reaction rates [43], and in condensed matter, where one can control excitonic states [15, 44], enhance existing properties such as ferroelectricity or electron-phonon coupling [29, 45], induce new properties and phases in the material [16], or spark cavity-mediated non-local interactions [46]. The starting point to model a cavity QED system is the Pauli-Fierz Hamiltonian [10, 35], firstly formulated in 1938 [47]. Such Hamiltonian is the non-relativistic limit of the full QED theory [10], meaning that it is formulated for low-energy systems [48] such is the case for condensed matter or atomic physics within an optical cavity. As the Pauli–Fierz Hamiltonian provides a description of electrons, nuclei, and the quantized electromagnetic field from first principles in the low-energy regime, it is regarded as an *ab initio* theory [49]. When dealing with molecules and materials, one can use the second-quantized formulation of the Pauli-Fierz Hamiltonian, modeling the cavity modes as a set of effective harmonic oscillators (cf. Section 3.1 and Ref. [35]). Upon diagonalizing the Pauli-Fierz Hamiltonian, one obtains the polaritonic states which may be used to predict properties of the material through the computation of observables. An important remark is that QED predicts that light and matter can couple even in the absence of photons thanks to the quantum vacuum fluctuations (dark cavities). The quantum vacuum fluctuations are essential in explaining several phenomena, from the Lamb shift [21], the spontaneous emission [22] and the Casimir-Polder forces [23] to modern works in cavity materials engineering [15, 16, 44, 46, 50, 51]. Despite the modification of matter in dark cavities has attracted great interest among theoreticians, and despite recent advances are close to making it experimentally possible [52, 53], it remains challenging as obtaining a sizable effect only due to vacuum fluctuation requires large light-matter couplings [54]. Alternatively, it is possible to achieve the strong coupling regime by driving the cavities with classical fields [55], which is known in literature as classically driven cavities. Such systems can still be modeled within the framework of the Pauli-Fierz Hamiltonian (cf. Section 3.1.2).

Regardless of whether one wants to study a dark or a driven cavity, handling the Pauli-Fierz Hamiltonian poses numerous theoretical and computational challenges. Firstly, to describe a matter system, both in the context of molecules and condensed matter, one has to deal with the formulation of a many-body problem. Exact solutions are typically unfeasible for realistic systems due to the many degrees of freedom characterizing the many-body Schrödinger equation [56]. To handle such a complexity and solve the matter problem, several approximations are introduced, such as the Born–Oppenheimer one, which treats nuclear positions as parameters of the electronic problem, and the independent particle one, which treats the electron-electron interaction with a mean-field approach. Mean-field approaches such as Hartree–Fock [57, 58] and Kohn–Sham [59, 60] Density Functional Theory (DFT) reformulate the interacting problem by introducing single-particle potentials, and they self-consistently solve coupled single-particle equations in an iterative way [56]. In particular, in Hartree-Fock one typically converges and approximates the many-electron wavefunction with a single Slater determinant, while in DFT the convergence is on the electronic density, constructed as the sum of squares of the non-interacting Kohn-Sham single-particle orbitals (which are obtained by self-consistently solving the Kohn-Sham equations). However, such methods only model the matter part of a QED system.

A promising route to the coupled electron–photon problem is provided by a generalization of density functional theory in which the influence of the quantized electromagnetic field is incorporated through additional functionals. This framework is called quantum electrodynamical density functional theory (QEDFT) [27] and is, in essence, an exact and fully first-principles reformulation of light–matter interaction which establishes a unique, self-consistent mapping from the interacting electron–photon system to an auxiliary *photon-free* (effective) problem that can be treated with DFT-like methods. In this way, QEDFT offers a conceptually unified approach to strongly coupled electron–photon physics and, more broadly, to situations where photons, phonons, and electronic degrees of freedom are intertwined within a single self-consistent formalism. So far, successful demonstrations have been achieved primarily in relatively simple settings, including ground-state [61, 62] and excited-state [63] properties of small molecules. Despite recent progress towards practical photon-free functionals [64, 65], extending QEDFT to quantitatively reliable descriptions of complex condensed-matter systems remains challenging [66], although first applications in solids are now beginning to appear [32, 67]. In particular, the main challenges remain the lack of a universal and accurate exchange-correlation functional [27] as well as the lack, in existing implementations, of a self-consistent solution of the light-matter problem [65, 68]. Besides future QEDFT developments, other techniques to solve coupled light-matter problems are to be pursued.

Despite having previously discussed the necessity of using quantum light to describe a class of phenomena, a first possible solution to QED comes from modified semiclassical methods (cf. Chapter 2). Traditionally, when considering radiation as a classical field, one only considers the effect that light has on matter (forward interaction). However, the electrons in molecules or materials are moving charged particles (whose motion is influenced by the presence of the external field), hence one can define a current associated to their movement. Since it is influenced by a time-dependent vector potential, the current will also be time-dependent, making it a source for the electromagnetic field. Hence the matter should have a backward effect on the external field. By solving for this induced field, one can account for radiative effects and describe, for instance, the spontaneous and stimulated emission [69] or the coupling with illuminated cavities [63]. As using classical fields allows to exploit state-of-the-art numerical algorithms, thus making simulations efficient, many semiclassical methods have been developed in the past years. Examples include multi-trajectory Ehrenfest dynamics [69, 70], Maxwell-TDDFT (Time-Dependent Density Functional Theory) [71] and Casida QEDFT [63]. Such methods typically assume that the field interacting with matter is uniform over the volume of the matter system, which is known as the dipole approximation. Note that in the following paragraphs the long-wavelength approximation will be introduced, which is a more general case compared to the dipole one [35]. However, since for molecular systems the two coincide, and since in Ref. [72] the term dipole is used, all throughout Chapter 2 the term dipole will be used (rather than long wavelength). While such approximation works well for some class of phenomena such as radiative decay [73] and coupling to linearly polarized light [70], beyond-dipole effects become important in applications such as high-energy spectroscopy (X-ray and XUV) [74, 75] and coupling to chiral [76, 77] and nanostructured [78] cavities. The first part of the present thesis (Chapter 2) is dedicated to the exploration of a beyond-dipole semi-classical Maxwell-TDDFT method for studying light-matter interacting systems. This open-source framework, published within the Octopus TDDFT code [79], couples the electrons, described with the use of DFT, to the classical radiation field, represented within the Riemann-Silberstein formalism [71], through the full minimal coupling. The electron's quantum dynamics and the radiation field are propagated simultaneously, considering both the effect of the electromagnetic field on the matter and the matter-induced vector potential (forward-backward interaction). This tool is then employed for both mean-field QED and beyond-dipole spectroscopy applications. In particular, the work showcases the Cherenkov emission from an electronic wavepacket, the presence of magneto-optical effects in XUV spectroscopy and a plasmonic frequency shift of a dimer due to the self-induced coupling of the transverse electromagnetic field [72].

However, it would be desirable to find a solution where the quantum nature of the electromagnetic field is directly encoded in the Hamiltonian, without having to rely on complicated forward-backward interaction schemes. To achieve this, a natural starting point is the second quantized Pauli-Fierz Hamiltonian written in Coulomb gauge [35] and represented in a base which describes the matter transitions between two states mediated by the absorption or the emission of a photon (quantum light). In such a context, the matter is modeled as a collection of Slater determinants, each representing a possible state that the matter system can be in (the ground state and the excited ones), while the electromagnetic field is described as a set of effective harmonic oscillators, each represented with a certain number of Fock states. The advantage of this basis choice is that the uncoupled matter and the uncoupled photons are already diagonal, and all quantum effects from the radiation field, such as the quantum vacuum fluctuation, are naturally described. The complexity of such approach comes from the interaction between the two uncoupled system, which is modeled via the light-matter minimal-coupling prescription [80]. Representing the Pauli-Fierz Hamiltonian onto such a base leads to a matrix (which will be referred to as QED matrix), which can be diagonalized to obtain the polaritonic states and explore the modified properties of materials. However, this method poses complex numerical challenges. Due to the large number of potential excitations (especially when accounting for the full Brillouin zone in condensed matter), and considering the size of joint matter-photons Hilbert space, the QED matrix representing the coupled system can quickly become prohibitively large [81] leading to numerical challenges in its storage and diagonalization. Despite such a complexity, with the use of modern computer clusters and state-of-the-art numerical algorithms, this method can be successfully used for both molecular [81] and condensed matter [15, 16, 30, 33].
The second part of the present thesis (Chapter 3) shows this by presenting two contributions within the context of cavity QED. In the first one, the discussion will focus on a twisted bilayer transition metal dichalcogenides (TMD) heterostucture, typically characterized by the presence of strongly bound Moiré excitons, embedded in an optical cavity. A key finding is that when such quasi-particles interact with the cavity modes of a structured driven cavity it is possible to create an all-optical Moiré-like potential, which promises to enable Moiré physics on monolayers. Conversely, when the interaction is within a dark structured cavity (i.e. only in the presence of vacuum fluctuations), cavity-mediated long-range exciton-exciton interactions emerge. Furthermore, the significance of this contribution also lies in the fact that it goes beyond a common approximation used in cavity QED, which is the long wavelength one (cf. Section 3.1 and Ref. [35, 50]). The second contribution discusses Graphene coupled to both linearly and circularly polarized modes in a dark cavity, for which previous works [81] had shown the opening of an optical gap. In particular, the discussion focuses on how the theoretical treatment of the matter should be modified to correctly account for self-consistent effects on the electronic states as a result of the interaction with light, presenting a new theory called QED Hartree-Fock. Subsequently, that theory is applied to study how different polarizations of light affect the Dirac states. In accordance with the literature [82], in the case of chiral cavities, which break the time-reversal symmetry of Graphene, a gap is opened. The case of linearly polarized light is particularly interesting, as when considering two isotropic modes with perpendicular polarizations, the Fermi velocity changes while no gap is opened, while when only a single mode is considered, a gap is opened, which is fully quantum effect.

Finally, so far the discussion has presented solutions to the QED problem based on algorithm implementation on classical computers. Whether they are based on the semiclassical or on the quantum theory of light-matter interaction, they are typically characterized by a substantial computational cost, which is addressed by either using state-of-the-art classical computers, exploiting parallelization and GPU acceleration, or by introducing approximations. Quantum computers promise to provide a viable route for the simulation of large scale QED systems. In such devices, information is encoded in qubits, which are quantum two-level system such as Josephson junctions, trapped ions or neutral atoms, whose state can be manipulated through the application of quantum gates [83]. Quantum problems are encoded in the form of operations performed on the qubits. Recent developments in quantum hardware have enabled devices with hundreds of qubits and high gate fidelity, allowing them to simulate complex circuits [84]. Quantum computers are particularly promising for the simulation of QED systems for two reasons. First, the application of all the required operations on the qubits that represent the system only takes a few seconds (including latency due to the job submission), compared to the diagonalization time of large matrices on classical hardware which can take several hours. Secondly, quantum computers are naturally efficient in representing bosonic Hilbert spaces [85, 86, 87] which solves the classical bottleneck of storing huge classical matrices. In fact, representing a photonic mode with only the vacuum and the first Fock state only requires adding a single qubit to the matter qubits, compared to the classical case where the size of the QED matrix doubles. The main limitation of modern quantum computers is that quantum state encoded in the qubits is easily deteriorated by quantum noise, for example as a result of decoherence processes in the hardware. This limits the number of operations that can be successfully applied to qubits [83]. To match this constraint one has to design circuits having in mind the hardware characteristics, such as the qubit connectivity (cf. Section 4.2).

The third part of this thesis (Chapter 4) explores how cavity-QED systems can be simulated on quantum computers. The focus is on the efficient representation of photons in problems that require many cavity modes. As a representative case, we study the quantum dynamics of a two-level system initially in its excited state, with all cavity modes in the vacuum. The ensuing time evolution displays Rabi oscillations, reproduced in both ideal simulations and noise-aware simulations of state-of-the-art hardware. These results are enabled by a hardware-efficient formulation of the QED Hamiltonian that maps the problem onto real devices by tailoring the circuit structure and distributing noisy two-qubit gates more effectively. This strategy improves scalability and paves the way toward larger and more realistic quantum simulations of light–matter dynamics.

This thesis is organized into three main chapters. In each chapter, I first introduce the fundamental concepts used in the publication, and then introduce each work. Chapter 2 is dedicated to semiclassical methods for the description of QED systems. First I present the theoretical formalism of the full minimal coupling and describe the Helmoltz decomposition, a key numerical technique. Then I introduce Publication I which presents an *ab initio* framework for light–matter coupled systems based on full minimal coupling Maxwell–TDDFT, combining TDDFT for the electrons with the Riemann–Silberstein formulation of Maxwell's equations and a forward–backward interaction scheme. Chapter 3 is dedicated to cavity materials engineering. First I introduce the Pauli–Fierz Hamiltonian, detailing how to use it various types of cavities (spatially structured and unstructured, dark and driven). Then I discuss the Hamiltonian downfolding technique, which is a powerful tool to understand the complicated action of light-matter interaction. Finally I introduce Publication II and III, which investigate how optical cavities can be used to generate all-optical Moiré-like confinement and cavity-mediated exciton–exciton interactions in TMD heterostructures, and then by formulating a QED Hartree–Fock theory for Graphene to analyze cavity-induced Dirac-band renormalization and gap opening. Chapter 4 explores quantum computing strategies for simulating cavity-QED systems. First I introduce the basic building blocks of quantum computation and review current quantum hardware platforms. Then I describe how to encode the QED Hamiltonian on a quantum computer. Finally, I introduce Publication IV, presenting a hardware-efficient formulation of cavity-QED Hamiltonians tailored to superconducting processors, simulating quantum dynamics on noisy devices. Finally, Chapter 5 gives a summary of this work and provides with insights for future research directions.

2 Enhancing semiclassical methods for light-matter systems: Full minimal coupling Maxwell-TDDFT

> *Quid ergo? non ibo per priorum vestigia? ego vero utar via vetere, sed si propiorem planioremque invenero, hanc muniam. Qui ante nos ista moverunt non domini nostri sed duces sunt. Patet omnibus veritas; nondum est occupata; multum ex illa etiam futuris relictum est.*[1]
> *- Epistulae Morales ad Lucilium, XXXIII, Seneca (about 60-65 A.D.)*

Semiclassical methods describe light-matter coupled system using a quantum mechanical treatment of the electronic problem, and a classical treatment for the electromagnetic field. Despite their popularity for modeling systems where the radiation field cannot described with a few photons, such as in spectroscopy [5] or in high-harmonic generation [6, 7] applications, they are not suitable for studying few photons (or even no photons, i.e. vacuum fluctuations) [10, 11] or strongly coupled [13, 14] electromagnetic fields. Since these latter scenarios have been gaining interest, and since describing light in a classical way is still desirable as it allows for a simpler theoretical description of the fields as well as the possibility of using state-of-the-art algorithms, developing a semiclassical approach that accounts for quantum phenomena is an attractive challenge.

In fact, previous works have already proposed several solutions based on different theoretical models, such as multi-trajectory Ehrenfest dynamics [70, 88] and related semiclassical schemes like Ehrenfest+R [89]. Multi-trajectory Ehrenfest treats the coupled electron–photon dynamics along individual trajectories, where electrons evolve quantum-mechanically under the effect of a classical field. This method can describe effects related to the quantum nature of light by sampling a large number of initial conditions and ensembling over them when calculating the observables. In Ehrenfest+R, additional relaxation and correction terms are introduced on top of mean-field Ehrenfest dynamics. While such methods are suitable to study some quantum effects such as spontaneous emission [70], since they typically operate in the dipole approximation they are ineffective for the description of several

---

[1] *What then? Shall I not follow in the footsteps of my predecessors? I shall indeed use the old road, but if I find one that makes a shorter cut and is smoother to travel, I shall open the new road. Men who have made these discoveries before us are not our masters, but our guides. Truth lies open for all; it has not yet been monopolized. And there is plenty of it left even for posterity to discover.* Here the "old road" is a reference to using the classical description of light, but with the goal of improving it to explore new phenomena.

other applications such as high-energy spectroscopy or coupling to chiral and nanoplasmonic cavities. Note that the dipole approximation used in this chapter is, for molecular systems, equivalent to the long-wavelength approximation [35]. Since in Publication I [72] the term dipole is used, all throughout this chapter the term dipole will be used.

In this chapter, I present a semiclassical *ab initio* tool to simulate light–matter coupled system beyond the dipole approximation. To achieve this, the radiation field is described using the Riemann-Silberstein formulation of the Maxwell's equations and the matter using the TDDFT formalism. The two are coupled using the full minimal coupling, which implies that beside considering the effect that the electromagnetic field has on the motion of the electrons, called forward interaction, the backward interaction is also considered. Thus, the current associated to the motion of the electrons is a source for electromagnetic field. After detailing the implementation in the Octopus TDDFT code, this tool is employed for both QED and beyond-dipole spectroscopy applications. In particular, the work showcases the Cherenkov emission from a super-luminal electronic wavepacket, the presence of magneto-optical effects in XUV spectroscopy and a plasmonic frequency shift of a dimer due to the self-induced coupling of the transverse electromagnetic field. I contributed to this work by implementing the module in the Octopus code that performs the Helmholtz decomposition. This is a core part of the algorithm as it is used to calculated the vector potential used in the forward coupling.

Before presenting the results of the publication, I will now introduce the general formalism of the full minimal coupling. In particular, first I will briefly introduce the time-dependent density functional theory, then the Riemann-Silberstein formulation of the Maxwell's equations and, finally, I will describe how the two system are coupled (forward-backward interaction). Afterwards, I will describe the theory behind the Helmholtz decomposition and lastly introduce the publication.

2.1 Full minimal coupling

To describe the full minimal-coupling formalism for light–matter interactions, we first introduce the models for the two uncoupled subsystems and then their coupling. Electrons are treated within the time-dependent density functional theory (TDDFT), while the classical electromagnetic field is modeled using the Riemann–Silberstein formulation of Maxwell's equations. The interaction between the two is then incorporated through the full minimal-coupling Hamiltonian. In this chapter, all quantities are expressed in SI units (for consistency with respect to Publication I).

2.1.1 Time-dependent density functional theory

Time-dependent density functional theory (TDDFT) [90, 91] extends density functional theory (DFT) to systems evolving under the effect of one or more time-dependent potentials. It is based on the Runge-Gross theorem [92], which establishes a map between the time-dependent potentials under which the electronic system is evolving and the electronic density. TDDFT reformulates the fundamental equations of DFT (which are the Kohn-Sham equations, used to calculate the electronic states) in their time-dependent version, which reads:

$$i\frac{\partial \varphi_j(\boldsymbol{r},\sigma,t)}{\partial t} = \left[\frac{(i\hbar\nabla)^2}{2m} + v_{\mathrm{KS}}[n](\boldsymbol{r},\sigma,t)\right]\varphi_j(\boldsymbol{r},\sigma,t) \tag{2.1}$$

whose electronic density is:

$$n(\boldsymbol{r},t) = \sum_{j=1}^{N_{\text{occ}}} \sum_{\sigma=\pm\frac{1}{2}} \left|\varphi_j(\boldsymbol{r},\sigma,t)\right|^2 \tag{2.2}$$

where $\varphi_j(\boldsymbol{r},\sigma,t)$ are the Kohn-Sham time-dependent electronic wavefunctions of the occupied states N_{occ}, with spin σ. $v_{\text{KS}}[n](\boldsymbol{r},\sigma,t)$ is the time-dependent Kohn-Sham potential defined as

$$v_{\text{KS}}[n](\boldsymbol{r},\sigma,t) = v_{\text{H}}[n](\boldsymbol{r},t) + v_{\text{xc}}[n](\boldsymbol{r},t) + v_n(\boldsymbol{r},t) + v_{\text{ext}}(\boldsymbol{r},\sigma,t) \tag{2.3}$$

where $v_{\text{H}}[n](\boldsymbol{r},t)$ and $v_{\text{xc}}[n](\boldsymbol{r},t)$ are the Hartree and exchange-correlation potentials, respectively, $v_n(\boldsymbol{r},t)$ is the Coulomb potential of the nuclei and $v_{\text{ext}}(\boldsymbol{r},\sigma,t)$ is an external potential acting on the electronic system (such as a laser). While the Hartree potential has the well-know expression [56, 91]

$$v_{\text{H}}[n](\boldsymbol{r},t) = \int \frac{n(\boldsymbol{r'},t)}{|\boldsymbol{r}-\boldsymbol{r'}|} d\boldsymbol{r'} \tag{2.4}$$

the form of the exchange-correlation potential is not known, and one has to choose the functional that better describes the system. Note that in principle, the exchange-correlation functional depends not only on the current time-dependent local electronic density, but on all past densities. This complexity can be simplified by using, for instance, the adiabatic local density approximation (ALDA) [90], which is popular choice when working with weak external perturbations (hence when in the linear regime) and provides reliable excitation energies. ALDA is local in time, which gets rid of the memory effect. While this makes calculations more feasible, it also limits the applications of TDDFT [91]. Improving existing functionals (and developing new ones) is an active field of research [93].

The time-dependent Kohn-Sham equations are solved self-consistently until the electronic density in Eq. 2.2 reaches convergence. The initial Kohn-Sham states are obtained by solving the DFT problem. Subsequently, the electronic states are time propagated, which is a complex numerical challenge [94].

2.1.2 Riemann–Silberstein field

The classical electromagnetic field is described by the Maxwell's equations. Since the end goal is to describe the interaction with matter, here I will use their microscopic formulation in the presence of matter:

$$\nabla \cdot \boldsymbol{E}(\boldsymbol{r},t) = \frac{\rho(\boldsymbol{r},t)}{\epsilon_0}, \tag{2.5a}$$

$$\nabla \cdot \boldsymbol{B}(\boldsymbol{r},t) = 0, \tag{2.5b}$$

$$\nabla \times \boldsymbol{E}(\boldsymbol{r},t) = -\frac{\partial \boldsymbol{B}(\boldsymbol{r},t)}{\partial t}, \tag{2.5c}$$

$$\nabla \times \boldsymbol{B}(\boldsymbol{r},t) = \mu_0 \left(\boldsymbol{j}(\boldsymbol{r},t) + \epsilon_0 \frac{\partial \boldsymbol{E}(\boldsymbol{r},t)}{\partial t}\right) \tag{2.5d}$$

where $\rho(\boldsymbol{r},t) = -|e|n(\boldsymbol{r},t)$ is the electric charge density (related to the electronic density $n(\boldsymbol{r},t)$ in Eq. 2.2) and $\boldsymbol{j}(\boldsymbol{r},t)$ is the displacement current density (which can be expressed terms of the electronic Kohn-Sham states) [95, 96]. Maxwell's equations can be more conveniently reformulated using the

Riemann-Silberstein vectors [95, 97].

$$\boldsymbol{F}^{\pm}(\boldsymbol{r},t)=\sqrt{\frac{\epsilon_0}{2}}\left[\boldsymbol{E}(\boldsymbol{r},t)\pm ic\boldsymbol{B}(\boldsymbol{r},t)\right] \tag{2.6}$$

where c is the speed of light. Throughout this chapter I will use only the positive definition, hence $\boldsymbol{F}(\boldsymbol{r},t)=\boldsymbol{F}^{+}(\boldsymbol{r},t)$. Using this formalism, the four Maxwell's equations can be reformulated as:

$$\nabla\cdot\boldsymbol{F}(\boldsymbol{r},t)=\frac{\rho(\boldsymbol{r},t)}{\sqrt{2\epsilon_0}}, \tag{2.7a}$$

$$\nabla\times\boldsymbol{F}(\boldsymbol{r},t)=\frac{i}{c}\left(\frac{1}{\sqrt{2\epsilon_0}}\boldsymbol{j}(\boldsymbol{r},t)+\frac{\partial\boldsymbol{F}(\boldsymbol{r},t)}{\partial t}\right) \tag{2.7b}$$

where Eq. 2.7a combines the two Gauss laws (Eq. 2.5a and Eq. 2.5b), while Eq. 2.7b unifies the Faraday and Ampère laws (Eq. 2.5c and Eq. 2.5d). This formulation is particularly convenient because in order to study the time evolution of the electromagnetic field it is enough to solve Eq. 2.7b, rather than the coupled Faraday-Ampère laws, which would require ensuring numerical consistency between the two solutions (as in finite difference time domain) [71, 95]. Moreover, it is possible to treat Eq. 2.7b as a time-dependent Schrödinger-like equation [95], which is very convenient for a numerical treatment as one can reuse the same methods employed for solving the electronic dynamics. Finally, since the goal is to describe light-matter interaction, it is important to give an expression for the vector potential $\boldsymbol{A}(\boldsymbol{r},t)$, as it will appear in the full minimal coupling Hamiltonian (cf. Section 2.1.3). Remembering that $\nabla\times\boldsymbol{A}(\boldsymbol{r},t)=\boldsymbol{B}(\boldsymbol{r},t)$, the vector potential is related to the time-propagated Riemann-Silberstein field by:

$$\nabla\times\boldsymbol{A}(\boldsymbol{r},t)=\sqrt{2\mu_0}\,\mathrm{Im}\{\boldsymbol{F}(\boldsymbol{r},t)\} \tag{2.8}$$

Therefore, the vector potential may be obtained by solving three Poisson equations (one for each direction) for Eq. 2.8. This will be explained in more details in Section 2.2.

2.1.3 Coupled Maxwell-TDDFT Hamiltonian

The interaction between the electrons and the electromagnetic field in the framework of full minimal coupling is such that one has to consider both the effect of the electromagnetic field on the electronic Kohn-Sham states (called forward interaction) as well as the radiation emitted by the electrons (backward interaction).

The electrons are described by the time-dependent Kohn–Sham equations (Eq. 2.1). The minimal coupling prescription imposes that the momentum $\hat{\boldsymbol{p}}=-i\hbar\nabla$ of a charged particle moving in an electromagnetic field is modified according to: $-i\hbar\nabla\rightarrow-i\hbar\nabla+\frac{|q|}{c}\boldsymbol{A}(\boldsymbol{r},t)$, where $|q|$ is the charge of the particle (since the focus of this chapter is on electrons, $|q|=|e|$). Hence, the full minimal coupling Hamiltonian written in velocity gauge, which implements the forward coupling, reads:

$$\hat{H}_{\mathrm{FMC}}=\frac{1}{2m}\left[-i\hbar\nabla+\frac{|e|}{c}\boldsymbol{A}(\boldsymbol{r},t)\right]^2+\frac{|e|}{m}\boldsymbol{B}(\boldsymbol{r},t)\cdot\hat{\boldsymbol{s}}+v_{\mathrm{H}}[n](\boldsymbol{r},t)+v_{\mathrm{xc}}[n](\boldsymbol{r},t)+v_{\mathrm{n}}(\boldsymbol{r},t) \tag{2.9}$$

where the term $v_{\mathrm{ext}}(\boldsymbol{r},\sigma,t)=\frac{|e|}{m}\boldsymbol{B}(\boldsymbol{r},t)\cdot\hat{\boldsymbol{s}}$ is the external potential, $\boldsymbol{B}(\boldsymbol{r},t)$ is the magnetic field associated to the vector potential $\boldsymbol{A}(\boldsymbol{r},t)$ and $\hat{\boldsymbol{s}}$ is the spin operator. In the remainder of the chapter I will impose the Coulomb gauge, defined by the condition $\nabla\cdot\boldsymbol{A}(\boldsymbol{r},t)=0$ which ensures that the vector potential remains purely transverse. Furthermore, by setting the initial Riemann-Silberstein vector to zero (hence neglecting any initial charge density) the need for propagating the longitudinal component is eliminated.

Within the full minimal coupling the motion of the electrons is a source for the electromagnetic field. Hence, the total vector potential $\boldsymbol{A}(\boldsymbol{r},t)$ is composed by a matter-induced component $\boldsymbol{A}_{\mathrm{mat}}(\boldsymbol{r},t)$, whose analytical expression is not known and has to be calculated numerically by solving Maxwell's equation, and an external field $\boldsymbol{A}_{\mathrm{ext}}(\boldsymbol{r},t)$. Thus the total vector potential is $\boldsymbol{A}(\boldsymbol{r},t) = \boldsymbol{A}_{\mathrm{mat}}(\boldsymbol{r},t) + \boldsymbol{A}_{\mathrm{ext}}(\boldsymbol{r},t)$. Note that when one calculates the vector potential by solving Eq. 2.8 (for realizing the forward interaction), the *total* vector potential is computed. Hence, the effect of the matter-induced vector potential is already accounted for. The dynamics of the electromagnetic field is described by Eq. 2.7b. The effect of the matter is included in the current density term $\boldsymbol{j}(\boldsymbol{r},t)$, which reads [95, 96]:

$$\begin{aligned}\boldsymbol{j}(\boldsymbol{r},t) = \frac{\hbar}{2im}\sum_{j=1}^{N_{\mathrm{occ}}}\sum_{\sigma=\pm\frac{1}{2}}&\left\{[\nabla\varphi_j^{\dagger}(\boldsymbol{r},\sigma,t)]\varphi_j(\boldsymbol{r},\sigma,t) - \varphi_j^{\dagger}(\boldsymbol{r},\sigma,t)[\nabla\varphi_j(\boldsymbol{r},\sigma,t)]\right\}\\ &+\frac{|e|}{mc}\boldsymbol{A}(\boldsymbol{r},t)n(\boldsymbol{r},t) + \frac{\hbar}{2m}\nabla\times\sum_{j=1}^{N_{\mathrm{occ}}}\sum_{\sigma=\pm\frac{1}{2}}\varphi_j^{\dagger}(\boldsymbol{r},\sigma,t)\hat{\boldsymbol{s}}\varphi_j(\boldsymbol{r},\sigma,t)\end{aligned} \tag{2.10}$$

where φ_j are the time-dependent Kohn-Sham electronic states. Then, the current density is the result of the sum of a paramagnetic (first term), a diamagnetic (second term) and a magnetization current density (third term) contributions. It is possible to compute $\boldsymbol{j}(\boldsymbol{r},t)$ by solving the electronic dynamics.

Finally, the coupled electron-photon problem can be studied by solving the following coupled dynamical equations:

$$i\hbar\frac{\partial}{\partial t}\varphi_j(\boldsymbol{r},\sigma,t) = \hat{H}_{\mathrm{FMC}}\varphi_j(\boldsymbol{r},\sigma,t), \tag{2.11a}$$

$$i\frac{\partial\boldsymbol{F}(\boldsymbol{r},t)}{\partial t} = c\nabla\times\boldsymbol{F}(\boldsymbol{r},t) - \frac{i}{\sqrt{2\epsilon_0}}\boldsymbol{j}(\boldsymbol{r},t) \tag{2.11b}$$

where the Riemann-Silberstein vector is initially zero and the Kohn-Sham states are initially the solution of the DFT problem for the material (without external fields). Looking at such equations, one can note how both equations are first-order differential equations in time, which allows to use the same numerical solver for computing them.

2.2 The Helmholtz decomposition

Section 2.1.3 discussed how the forward interaction in a coupled Maxwell-TDDFT system is realized by calculating the vector potential $\boldsymbol{A}(\boldsymbol{r},t)$ from the time-propagated electromagnetic field. To achieve that, as discussed in Section 2.1.2, one has to solve Eq. 2.8 for the vector potential. The meaning of this operation is that one is extracting the transverse part of vector field $\boldsymbol{F}(\boldsymbol{r},t)$. This is possible thanks to the Helmholtz decomposition theorem [98, 99], for which $\boldsymbol{F}(\boldsymbol{r},t)$ has to fulfill some conditions. For the sake of simplifying the notation, in this section I will omit the time-dependency of all quantities. This is not an approximation as this theorem only deals with spatial differential operators. Moreover, despite the Helmholtz theorem can be formulated in more than three dimensions, I will consider all fields to be defined in the 3D space $\mathbb{R}^3$, which is the case of Publication I.

The Helmholtz decomposition, a fundamental theorem of calculus [98, 99], states that any sufficiently smooth vector field can be expressed as the sum of an irrotational (curl-free or longitudinal) and a solenoidal (divergence-free or transverse) vector field. This means that in general, if one has a generic vector field $\mathbf{G}(\mathbf{r}) \in \mathcal{C}^1(V)$, where $V \subseteq \mathbb{R}^3$ is a bounded domain, then

$$\mathbf{G}(\mathbf{r}) = \mathbf{G}_{long}(\mathbf{r}) + \mathbf{G}_{trans}(\mathbf{r}) = -\nabla\phi(\mathbf{r}) + \nabla \times \mathbf{A}(\mathbf{r}), \tag{2.12a}$$

$$\nabla \times \mathbf{G}_{long}(\mathbf{r}) = 0, \nabla \cdot \mathbf{G}_{trans}(\mathbf{r}) = 0 \tag{2.12b}$$

where $\phi(\mathbf{r})$ is a scalar function (scalar potential) and $\mathbf{A}(\mathbf{r})$ is a vector field (vector potential). The final expression in Eq. 2.12a was obtained by applying the conditions on the transverse and longitudinal fields (Eq. 2.12b) and the vectorial identities $\nabla \times (\nabla\phi) = 0$ and $\nabla \cdot (\nabla \times \boldsymbol{A}) = 0$. Note that this decomposition is not unique, as in general it exists up to an harmonic function $H(\boldsymbol{r})$, such that $\Delta H(\boldsymbol{r}) = 0$. To ensure the uniqueness of the transverse and longitudinal field, here we consider a vector field $\boldsymbol{G}(\boldsymbol{r}, t)$ which decays at infinity [100].

The Helmholtz decomposition is used in various fields of physics, such as fluid dynamics [101], dynamical systems theory [102] and electrodynamics. Since Publication I deals with the latter, I will call $\mathbf{G}_{trans}(\mathbf{r}) = \mathbf{B}(\mathbf{r})$ (magnetic field).

Given the total field $\mathbf{G}(\mathbf{r})$, it is possible to compute its scalar and vector potential as:

$$\phi(\mathbf{r}) = \frac{1}{4\pi}\left(\int \frac{\nabla' \cdot \mathbf{G}(\mathbf{r}')}{|\mathbf{r} - \mathbf{r}'|}\, d\mathbf{r}' - \oint \hat{\mathbf{n}}' \cdot \frac{\mathbf{G}(\mathbf{r}')}{|\mathbf{r} - \mathbf{r}'|}\, dS'\right) \tag{2.13}$$

$$\mathbf{A}(\mathbf{r}) = \frac{1}{4\pi}\left(\int \frac{\nabla' \times \mathbf{G}(\mathbf{r}')}{|\mathbf{r} - \mathbf{r}'|}\, d\mathbf{r}' - \oint \hat{\mathbf{n}}' \times \frac{\mathbf{G}(\mathbf{r}')}{|\mathbf{r} - \mathbf{r}'|}\, dS'\right) \tag{2.14}$$

In both equations two terms appear, a volume integral and a surface integral (where $\hat{\boldsymbol{n}}'$ is the normal vector to the surface S). The former is computed by first applying the appropriate differential operator to $\mathbf{G}(\mathbf{r})$, and then by solving the Poisson equation. Note that in the case of the vector potential $\mathbf{A}(\mathbf{r})$ one has to solve three Poisson equations (one for each direction). Since solving a Poisson equation is a common problem in many fields, there are plenty of efficient numerical methods and implementations. For instance, a common choice is to use Conjugate Gradients methods. However, unless one is dealing with periodic vector field, which is not the case of Publication I, algorithms that exploit periodicity (such as FFT) should be avoided. On the other hand, the surface integral can be neglected if the integration domain V is large enough. However, while this is a common practice to reduce the computational cost, when solving this problem numerically neglecting the surface integral can lead to a potential that diverges greatly from the correct result.

The equations above do not make any assumption on the gauge of the field. Explicitly taking into account the Coulomb gauge allows to simplify the expressions, which may be rewritten as [103]:

$$\mathbf{A}(\mathbf{r}) = \mathbf{A}_t(\mathbf{r}) = \nabla \times \frac{1}{4\pi}\int \frac{\mathbf{B}(\mathbf{r}')}{|\mathbf{r} - \mathbf{r}'|}\, d\mathbf{r}' \tag{2.15}$$

where $\mathbf{A}(\mathbf{r})$ is the transverse part of the vector potential. Due to numerical reasons, this expression is more stable to evaluate than Eq. 2.14. In fact, first the surface integral is zero, regardless of the dimension of the domain V, which reduces the computational cost. Working in Coulomb gauge is also advantageous as it is possible to check the numerical consistency of the numerical solution by checking that the divergence of the vector potential is zero, and if not it possible to correct it [104]. Finally, it should be noted that when working in Coulomb gauge, one should ensure that all the TDDFT Hamiltonian is written in the same gauge (as the electron-electron interactions are assumed to follow the Coulomb gauge).

2.2.1 The Helmholtz decomposition implementation in Octopus

All the implementation required for Publication I were done within the Octopus TDDFT code [79]. Since Octopus is an open-source real-time real-space grid-based code, the Maxwell equations written in Riemann-Silberstein form are discretized in space and derivatives are computed using finite differences. All quantities are then contained in a simulation box. The algorithm for computing derivatives is well-defined in the inner regions of the simulation box, whereas at the boundaries one needs to include extra points (that are not physical). This is because with finite differences, the value of the derivative of a function at a certain point depends on the difference with points in all directions. The artifact is that Octopus assumes any function to be zero in those points outside the simulation box (unless the value is manually set).

Hence, it can happen that during a simulation the value of the total field inside the box is defined and non-zero, while in the extra layer of points required to define the derivatives it is zero. This results in a jump in the value of the fields at the boundaries, thus generating spikes in the derivatives and leading to numerical instabilities both when computing the Poisson equation for $\nabla' \times \mathbf{G}(\mathbf{r}')$ and when using $\mathbf{A}(\mathbf{r})$ in the following time step(s).

Using Eq. 2.15 instead of Eq. 2.14 to compute the vector potential allows to mitigate the problem. In fact, the first operation to be performed is computing the magnetic field $\mathbf{B}(\mathbf{r})$ by solving the three Poisson equations in Eq. 2.15. This does not introduce any spike at the boundaries even if the field is non-zero in those points, therefore one can still assume that the computed magnetic field is numerically correct. Next, before applying the curl one can subtract from the field its mean value at the boundaries. Since this is a constant, it does not affect the curl operation and it makes the value of the field at the boundaries closer to zero. Finally, one can perform the curl on a field which is almost zero at the boundaries, thus generating fewer spikes and improving numerical accuracy.

Finally, as explained in Publication I, the simulation box of the Maxwell system is much bigger than the simulation box of the matter. This implies that even if the value of vector potential at the boundaries is slightly inaccurate, in the area where it interacts with the matter system it is well defined.

2.3 Publication I: Full minimal coupling Maxwell-TDDFT: An ab initio framework for light-matter interaction beyond the dipole approximation

State of the art

Prior to this work, semiclassical descriptions of light–matter interaction like multitrajectory Ehrenfest dynamics [70] or Maxwell–TDDFT [71] were relying on the dipole approximation, and could only retrieve some quantum phenomena by coupling back the dipolar radiation field. Beyond-dipole effects, known to be important in several application such as x-ray/XUV spectroscopy [74, 75], strong-field physics [105], chiral [76, 77] and nanoplasmonic environments [78], and twisted light could only be addressed with methods based on multipolar truncations. While effective, the convergence with the multiple order can be slow [106], and truncations are origin dependent [107]. Non-truncated formulations only existed in specific contexts such as non-dipole strong-field applications [108] and certain x-ray spectra [75]. A general time-domain, self-consistent *ab initio* framework including beyond-dipole radiation reaction was missing.

Main findings

This work introduces an open-source, first-principles framework for simulating coupled Maxwell-TDDFT dynamics in the Coulomb gauge under full minimal coupling, implemented in the Octopus real-time real-space TDDFT code. By coupling the real-time, real-space transverse vector potential to the matter, including both the forward (matter to field) and the backward (field to matter) interactions, and by solving the full set of equations self-consistently, the approach captures beyond-dipole QED effects without relying on any multipolar expansion. After describing the framework and its validation, which includes stringent tests that demonstrate the origin independence of the method, we apply it to study both QED systems and beyond-dipole spectroscopy.

Firstly, we simulate an electronic wave packet traveling faster than the phase velocity of light in a medium and reproduce the formation and time evolution of the associated Cherenkov radiation, including its emission angle. This example highlights the necessity of both backward coupling and beyond-dipole physics.

Then, we compute the beyond-dipole XUV spectroscopy of benzene. For the soft-XUV excitation we resolve phase-retarded atomic dipoles along the propagation direction, identify induced orbital angular momentum that is absent in the dipole approximation, and predict a selective off-diagonal magneto-optical cross response near 290 eV. This demonstrates the qualitative impact of beyond-dipole effects on spectroscopic observables.

Finally, we study the radiative shifts in sodium dimer. For Na_2, the self-consistent transverse field produces a Lamb-like radiative shift of the dipole plasmon mode and a finite phase lag relative to the dipole response. These results expose the limitations of classical point-particle radiation-reaction models and of length-gauge multipolar truncations for describing radiative self-interaction.

Status and Publication details

This paper was published in *Physical Review B* in February 2025 [72]. The supplementary information is available at http://link.aps.org/supplemental/10.1103/PhysRevB.111.085114 (not included in the present thesis).

Contribution

I developed the code to perform the Helmholtz decomposition, which plays a central role in the simulations as it allows to calculate the vector potential from the electromagnetic field, to be used in the forward coupling. The development also included the creation of two regression tests to ensure the consistency of results. I also wrote the corresponding section in the Supplementary Information (including running the calculations for the creation of the figures). All authors have contributed to the revision of the manuscript.

PHYSICAL REVIEW B **111**, 085114 (2025)

Editors' Suggestion

Full minimal coupling Maxwell-TDDFT: An *ab initio* framework for light-matter interaction beyond the dipole approximation

Franco P. Bonafé,[1,*] Esra Ilke Albar,[1] Sebastian T. Ohlmann,[2] Valeriia P. Kosheleva,[1] Carlos M. Bustamante,[1] Francesco Troisi,[1] Angel Rubio,[1,3] and Heiko Appel[1,†]

[1] *Max Planck Institute for the Structure and Dynamics of Matter, Center for Free Electron Laser Science, Luruper Chaussee 149, 22761 Hamburg, Germany*

[2] *Max Planck Computing and Data Facility, Gießenbachstrasse 2, 85748 Garching, Germany*

[3] *Center for Computational Quantum Physics (CCQ), The Flatiron Institute, 162 Fifth Avenue, New York, New York 10010, USA*

(Received 24 September 2024; revised 15 December 2024; accepted 17 January 2025; published 5 February 2025)

We report an *ab initio*, nonrelativistic QED method that couples light and matter self-consistently beyond the electric dipole approximation and without multipolar truncations. This method is based on an extension of the Maxwell-Pauli-Kohn-Sham approach to a full minimal coupling Hamiltonian, where the space- and time-dependent vector potential is coupled to the matter system, and its back reaction to the radiated fields is generated by the full current density. The implementation in the open-source code OCTOPUS is designed for massively parallel multiscale simulations considering different grid spacings for the Maxwell and matter subsystems. Here, we show applications of this framework to simulate renormalized Cherenkov radiation of an electronic wave packet, magneto-optical effects with nonchiral light in nonchiral molecular systems, and renormalized plasmonic modes in a nanoplasmonic dimer. We show that in some cases, the beyond-dipole effects cannot be captured by a multipolar expansion Hamiltonian in the length gauge. Finally, we discuss further opportunities enabled by the framework in the field of twisted light and orbital angular momentum, inelastic light scattering, and strong-field physics.

DOI: 10.1103/PhysRevB.111.085114

I. INTRODUCTION

Quantum electrodynamics (QED) is a fundamental field theory that describes all the phenomena associated with charged particles and photons, including well-known effects such as the Lamb shift [1], spontaneous emission [2,3], and the Casimir-Polder forces between metallic plates [4,5]. QED effects have been particularly important in strong-field physics to describe phenomena such as electron-positron pair creation [6] and vacuum birefringence [7,8]. Just recently, both experimental [9–11] and theoretical [12–14] evidence have suggested that strong coupling between matter and modified vacuum in cavities leads to hybridized light-matter states. This development has paved the way for the emerging field of cavity quantum materials with relevant applications for a variety of quantum systems [15–17]. While the traditional QED approach is currently limited to relatively simple systems, such as few-electron atoms [18–21], including the quantum effects of both light and matter in a fully *ab initio* framework becomes exponentially expensive unless approximated methods are used.

To address these limitations, the theoretical framework of *ab initio* electronic structure theories for understanding light-matter interactions for realistic materials has evolved. Among these methods, time-dependent density functional theory (TDDFT) [22] is particularly successful due to its balance of accuracy and computational efficiency [23]. In most of the cases treated within the TDDFT, an external electromagnetic field (such as a laser pulse) drives the system, which is usually coupled within the electric dipole approximation to the electrons. Quantum electrodynamical density functional theory (QEDFT) [24] has been developed to include the quantized electromagnetic fields as a photon-free QED functional [14]. However, semiclassical treatments that enable the coupling to light in arbitrary electromagnetic environments and recover some relevant QED phenomena are desirable.

In this sense, several semiclassical methods have been developed to account for these radiative effects in quantum systems, all of which demand solving the induced electromagnetic fields at some level, e.g., Maxwell-Bloch, Maxwell-Ehrenfest, and Maxwell-Ehrenfest + R methods [25], multitrajectory Ehrenfest [26,27], coherent electron electric-field dynamics [28], local radiation-reaction potentials [29], Maxwell-Schrödinger [30] and Maxwell-TDDFT

---

[*] Contact author: franco.bonafe@mpsd.mpg.de

[†] Contact author: heiko.appel@mpsd.mpg.de

[31,32], Casida QEDFT [33,34], and its combination with macroscopic QED, among others. Some methods, such as the Ehrenfest + R or multitrajectory Ehrenfest approaches, include effects beyond the classical description, such as spontaneous decay, but implementations in electron *ab initio* calculations are still missing. In most of these methods, only the dipolar radiated field is calculated and its effect is coupled back into the Hamiltonian, which can account for radiative decay [28,29], superradiance [35], and coupling with cavities [26,29].

On the other hand, it has become clear that in several areas of theoretical physics, light-matter interactions must be treated beyond the dipole approximation, with large spectroscopic applications, as this breaks dipole selection rules and creates opportunities for new driven light-matter systems [36]. Beyond-dipole effects have been demonstrated for x-ray and XUV spectroscopy [37–42], strong-field phenomena [43–50], magneto-optical effects [39,51], coupling in chiral cavities [52–54], molecules in nanoplasmonic cavities for enhanced spectroscopy [55–57], and interactions with twisted light [52,58–61], just to name a few. Nonetheless, in these fields, a truncated multipolar expansion is the usual method of choice, which is origin dependent [38] and its convergence with the multipole order can be slow [36]. Methods such as the nondipole strong-field approximation Hamiltonian [48] and nontruncated treatments for x-ray spectra calculations [39,40,42] have gone beyond the multipolar expansion for these specific applications. A single tool that combines a general framework for beyond-dipole interactions in the time domain and can account for radiation reaction has not been achieved so far.

Here, we report an open-source, parallel and efficient implementation of the real-space, real-time Maxwell-TDDFT method in full minimal coupling and showcase applications that highlight its use for QED, beyond-dipole spectroscopy, and both simultaneously. In particular, we show the renormalized Cherenkov emission from an electronic wave packet by coupling back the emitted field into the quantum dynamics. In addition, we show the presence of magneto-optical effects driven by linearly polarized XUV light using benzene as an example, as an atomistic equivalent of dark transitions in nanorings. Finally, we demonstrate that a nanoparticle dimer coupled to the free-space electromagnetic environment has a plasmonic frequency shift as well as non-negligible phase shifts of the density and near field in the Fourier domain, by pure coupling with the transverse field induced by itself. To conclude, we present a few outlooks for the application of this tool to strong-field phenomena, twisted light beams, and periodic systems.

II. THEORY AND NUMERICAL METHODS

The SI system of units is used in the paper, unless specified otherwise. As a starting point, we consider the time-dependent Kohn-Sham equations using the full minimal coupling (FMC) Hamiltonian in velocity gauge, which is based on the nonrelativistic limit of the Dirac equation and correctly describes the coupling to an electromagnetic field to all orders of the charge multipoles. The FMC Hamiltonian reads as follows:

$$\mathcal{H}^{(\mathrm{FMC})} = \frac{1}{2m}\left[-i\hbar\nabla + \frac{|e|}{c}\mathbf{A}(\mathbf{r},t)\right]^2 + \frac{|e|}{m}\mathbf{B}(\mathbf{r},t) \cdot \hat{\mathbf{s}} + V_{\mathrm{H}}[n](\mathbf{r},t) + V_{\mathrm{xc}}[n](\mathbf{r},t) + V_{\mathrm{nuc}}(\mathbf{r},t). \quad (1)$$

Here, $\hbar$ is the reduced Planck constant, m and e are the mass and charge of the electrons, respectively, c is the speed of light in vacuum, $\mathbf{A}(\mathbf{r},t)$ is the transverse vector potential and $\mathbf{B}(\mathbf{r},t)$ is the magnetic field associated with it, $\hat{\mathbf{s}}$ is the spin operator, and $V_{\mathrm{H}}[n](\mathbf{r},t)$ and $V_{\mathrm{xc}}[n](\mathbf{r},t)$ are the Hartree and exchange-correlation potentials, respectively. For all the calculations that consider electron-electron interaction presented in this work, we have used the adiabatic local density approximation (ALDA) for the time-dependent exchange-correlation (xc) potential [62]. For weak external perturbations, such as the ones considered in this work, the ALDA provides relatively good excitation energies, as has been widely used for calculations in the linear regime. The xc functionals used for each calculation, along with other relevant parameters for each system, can be found in the Supplemental Material [63]. $V_{\mathrm{nuc}}(\mathbf{r},t)$ is the Coulomb potential of the nuclei and $n(\mathbf{r},t)$ is the electronic probability density [64],

$$n(\mathbf{r},t) = \sum_{j=1}^{N_{\mathrm{occ}}}\sum_{\sigma=\pm\frac{1}{2}}\left|\varphi_j(\mathbf{r},\sigma,t)\right|^2, \quad (2)$$

where $\varphi_j(\mathbf{r},\sigma,t)$ are the Kohn-Sham wave functions with index j enumerating the N_{occ} occupied orbitals and σ being the spin. The transverse vector potential $\mathbf{A}(\mathbf{r},t)$ can have both external and matter contributions,

$$\mathbf{A}(\mathbf{r},t) = \mathbf{A}_{\mathrm{mat}}(\mathbf{r},t) + \mathbf{A}_{\mathrm{ext}}(\mathbf{r},t). \quad (3)$$

The matter-induced vector potential $\mathbf{A}_{\mathrm{mat}}(\mathbf{r},t)$ is a transverse field that depends on the properties of matter. We note that in most of the cases, $\mathbf{A}_{\mathrm{mat}}(\mathbf{r},t)$ does not have an analytical expression and needs to be calculated numerically by solving Maxwell's equations self-consistently along with the electronic dynamics. Following Ref. [31], we choose the Riemann-Silberstein representation to propagate the electromagnetic fields, where the Riemann-Silberstein vector $\mathbf{F}(\mathbf{r},t)$ is defined as

$$\mathbf{F}^{\pm}(\mathbf{r},t) = \sqrt{\epsilon_0/2}[\mathbf{E}(\mathbf{r},t) \pm ic\mathbf{B}(\mathbf{r},t)], \quad (4)$$

where ϵ_0 is the vacuum permittivity. For the remainder of this work, we use only the positive definition: $\mathbf{F} := \mathbf{F}^{+}$. According to this definition, the Faraday and Ampère laws are unified into a single equation of motion,

$$i\partial_t\mathbf{F}(\mathbf{r},t) = c\nabla \times \mathbf{F}(\mathbf{r},t) - \frac{i}{\sqrt{2\epsilon_0}}\mathbf{J}(\mathbf{r},t), \quad (5)$$

while the two Gauß laws are similarly combined,

$$\nabla \cdot \mathbf{F}(\mathbf{r},t) = \sqrt{\frac{1}{2\epsilon_0}}\rho(\mathbf{r},t). \quad (6)$$

Here, $\rho(\mathbf{r},t)$ is the electronic density that is given by $\rho(\mathbf{r},t) = -|e|n(\mathbf{r},t)$. The source term $\mathbf{J}(\mathbf{r},t)$ in (5) is the total electric current density, related to the probability current density

$\mathbf{j}(\mathbf{r},t)$ by $\mathbf{J}(\mathbf{r},t) = -|e|\mathbf{j}(\mathbf{r},t)$, which is given by [31,65]

$$\begin{aligned}\mathbf{j}(\mathbf{r},t) = {}& \frac{\hbar}{2im}\sum_{j=1}^{N_{\mathrm{occ}}}\sum_{\sigma=\pm\frac{1}{2}}\{[\nabla\varphi_j^\dagger(\mathbf{r},\sigma,t)]\varphi_j(\mathbf{r},\sigma,t) \\ & - \varphi_j^\dagger(\mathbf{r},\sigma,t)[\nabla\varphi_j(\mathbf{r},\sigma,t)]\} + \frac{|e|}{mc}\mathbf{A}(\mathbf{r},t)n(\mathbf{r},t) \\ & + \frac{\hbar}{2m}\nabla\times\sum_{j=1}^{N_{\mathrm{occ}}}\sum_{\sigma=\pm\frac{1}{2}}\varphi_j^\dagger(\mathbf{r},\sigma,t)\hat{\mathbf{s}}\varphi_j(\mathbf{r},\sigma,t),\end{aligned} \tag{7}$$

where the first, second, and third terms are the paramagnetic, diamagnetic, and magnetization current densities, respectively.

The vector potential can now be computed from the time-propagated magnetic field $\mathbf{B}(\mathbf{r},t) = \sqrt{2\mu_0}\,\mathrm{Im}[\mathbf{F}(\mathbf{r},t)]$ by solving the Poisson equation for $\nabla\times\mathbf{A}(\mathbf{r},t) = \mathbf{B}(\mathbf{r},t)$,

$$\begin{aligned}\mathbf{A}(\mathbf{r},t) = {}& \frac{1}{4\pi}\int_V \frac{\nabla'\times\mathbf{B}(\mathbf{r}',t)}{|\mathbf{r}-\mathbf{r}'|}\mathrm{d}^3r' - \frac{1}{4\pi}\oint_S \hat{\mathbf{n}}' \\ & \times \frac{\mathbf{B}(\mathbf{r}',t)}{|\mathbf{r}-\mathbf{r}'|}\mathrm{d}^2r'.\end{aligned} \tag{8}$$

The first term can be efficiently calculated using a Poisson solver, as it corresponds to the solution of the Poisson equation for a simulation box with volume V. The second integral in Eq. (8) is a surface integral, where $\hat{\mathbf{n}}'$ denotes the normal to the surface S of the simulation box. This term becomes necessary if $\mathbf{B}(\mathbf{r}',t)$ does not vanish at the surface of the simulation box. In Coulomb gauge, however, Eq. (8) can be written as a function of the instantaneous magnetic field [66],

$$\mathbf{A}(\mathbf{r},t) = \nabla\times\int\frac{\mathbf{B}(\mathbf{r}',t)}{4\pi|\mathbf{r}-\mathbf{r}'|}\mathrm{d}^3r', \tag{9}$$

which is much more convenient for the numerical implementation [66] [see Eq. (S5) in the Supplemental Material [63]].

As only the transverse component of the electromagnetic fields is coupled back into the matter Hamiltonian, the longitudinal fields do not need to be calculated as a contribution from the Maxwell propagation, as long as the full matter system is interacting via the Coulomb potential. Hence, we do not account for the initial charge density in the Maxwell simulations; instead, we set the initial field to zero and let it evolve in time. In this way, the Gauß law is fulfilled with the charge density *difference* with respect to the ground state,

$$\nabla\cdot\mathbf{E}(\mathbf{r},t') = \frac{1}{\varepsilon_0}[\rho(\mathbf{r},t') - \rho(\mathbf{r},t=0)]. \tag{10}$$

Therefore, the Gauß law is automatically fulfilled and can be used as a side condition to test the method's accuracy (*vide infra*). Another side condition that needs to be fulfilled automatically is the continuity equation $\partial_t\rho(\mathbf{r},t) + \nabla\cdot\mathbf{J}(\mathbf{r},t) = 0$.

The full minimal coupling Hamiltonian (1) gives access to light-matter interactions up to all multipolar orders. However, an approach that allows us to distinguish the effects arising from different orders and types of electromagnetic fields is desired. This can be obtained by a Taylor expansion of the vector potential and magnetic field in Eq. (1) around the center $\mathbf{r}_0$, which leads to the well-known multipolar-expanded (ME) Hamiltonian. We have implemented this Hamiltonian in length gauge up to the second order, which reads as follows [31]:

$$\begin{aligned}\mathcal{H}^{(\mathrm{ME})} = {}& -\frac{\hbar^2}{2m}\nabla^2 + |e|\mathbf{r}\cdot\mathbf{E}_\perp(\mathbf{r}_0,t) + \mathrm{i}\frac{|e|}{2m}\mathbf{B}(\mathbf{r}_0,t) \\ & \cdot(\mathbf{r}\times\nabla) + \frac{1}{2}|e|(\mathbf{r}\cdot\nabla)\mathbf{r}\cdot[\mathbf{E}_\perp(\mathbf{r},t)]\Big|_{\mathbf{r}=\mathbf{r}_0} \\ & + V_{\mathrm{H}}[n](\mathbf{r},t) + V_{\mathrm{xc}}[n](\mathbf{r},t) + V_{\mathrm{nuc}}(\mathbf{r},t),\end{aligned} \tag{11}$$

which, in addition to the commonly used electric dipole term $|e|\mathbf{r}\cdot\mathbf{E}_\perp(\mathbf{r}_0,t)$, also has a magnetic dipole contribution,

$$\mathrm{i}\frac{|e|}{2m}\mathbf{B}(\mathbf{r}_0,t)\cdot(\mathbf{r}\times\nabla) = -\frac{|e|}{2m}\mathbf{B}(\mathbf{r}_0,t)\cdot\hat{\mathbf{L}}, \tag{12}$$

and the electric quadrupole term,

$$\frac{1}{2}|e|(\mathbf{r}\cdot\nabla)\mathbf{r}\cdot[\mathbf{E}_\perp(\mathbf{r},t)]\Big|_{\mathbf{r}=\mathbf{r}_0} = \frac{1}{2}|e|\sum_{ij}r_i\mathbb{Q}_{ij}r_j. \tag{13}$$

Here, $\mathbf{L}$ is the orbital angular momentum operator and $\mathbb{Q}_{ij} = \partial_i\mathbf{E}_{\perp,j}(\mathbf{r},t)|_{\mathbf{r}=\mathbf{r}_0}$ is the electric field gradient tensor.

As we solve the time propagation by integrating partial differential equations, the initial conditions can be freely chosen depending on the application. For the calculations of this paper (and in most cases in general), the ground state is chosen as the initial condition. In summary, the initial conditions for the Kohn-Sham orbitals φ^0 and Riemann-Silberstein vectors $\mathbf{F}^0$ are given by

$$\begin{aligned}&\left\{-\frac{\hbar^2}{2m}\nabla^2 + V_{\mathrm{H}}[n](\mathbf{r}) + V_{\mathrm{xc}}[n](\mathbf{r}) + V_{\mathrm{nuc}}(\mathbf{r})\right\}\varphi_j^0(\mathbf{r},\sigma) \\ &\quad = E_j\varphi_j^0(\mathbf{r},\sigma),\end{aligned} \tag{14}$$

$$\mathbf{F}^0(\mathbf{r}) = 0, \tag{15}$$

and their coupled dynamics are defined by the following equations (summarized in Fig. 1):

$$i\hbar\partial_t\varphi_j(\mathbf{r},\sigma,t) = \mathcal{H}^{(\mathrm{FMC})}\varphi_j(\mathbf{r},\sigma,t), \tag{16}$$

$$i\partial_t\mathbf{F}(\mathbf{r},t) = c\nabla\times\mathbf{F}(\mathbf{r},t) - \frac{i}{\sqrt{2\epsilon_0}}\mathbf{J}(\mathbf{r},t). \tag{17}$$

A. Numerical methods

We solve the coupled Kohn-Sham-Maxwell equations as given by the full minimal coupling Hamiltonian within TDDFT as implemented in the open-source code OCTOPUS [67]. The Kohn-Sham equations are solved in real space and real time. The Maxwell equations in Riemann-Silberstein form are discretized in space using the same finite differences as for the Kohn-Sham equations and in time using an exponential propagation scheme [31]. Both the Kohn-Sham equations and the Maxwell equations have been implemented as different systems coupled via the new multisystem framework in OCTOPUS [67]. The use of the new framework has not only enabled the interaction among more than two systems, giving more freedom for the types of simulation, but also has opened the way to couple several electronic and Maxwell systems and to extend this to other levels of theory, such

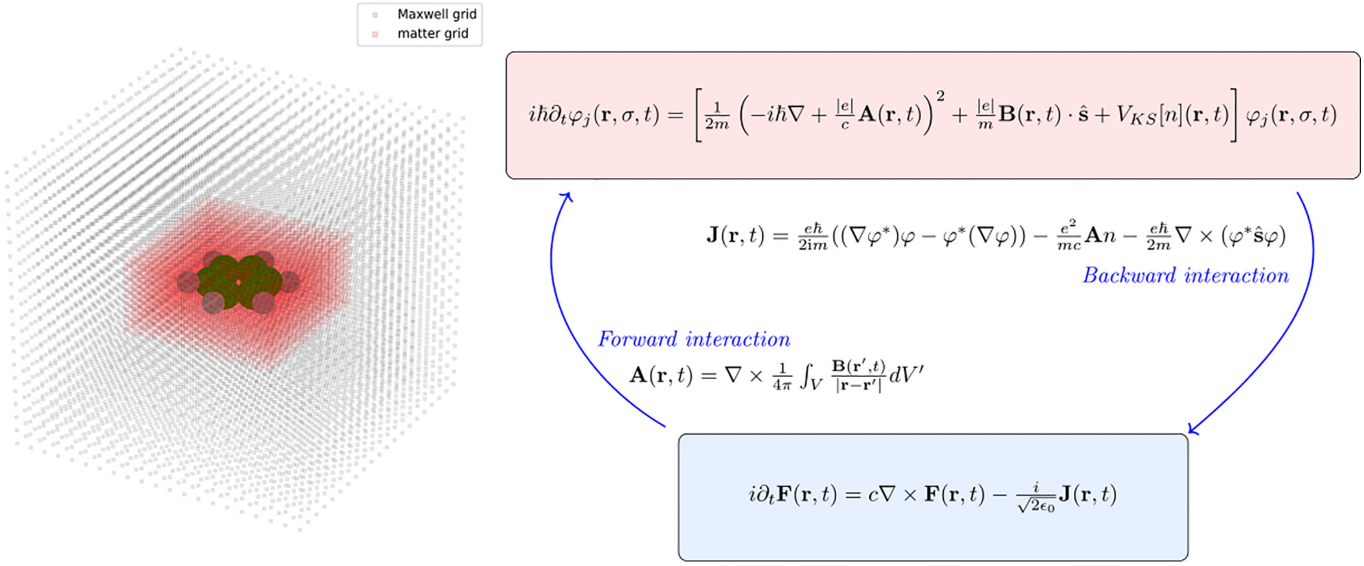

FIG. 1. Sketches of the Maxwell and matter simulation boxes (left) and the forward-backward self-consistent coupling scheme (right). For this sketch, each grid point that is plotted represents a cube of 8×8×8 grid points in the real calculation.

as continuum electromagnetic models, and density functional tight-binding calculations, having potential for truly multiscale simulations.

The current implementation allows the inclusion of different boundary conditions for solving Maxwell's equations: zero fields, constant fields, and absorbing boundary conditions using a perfectly matched layer (PML). Moreover, plane waves can be introduced into the simulation box by using Dirichlet boundary conditions. For this paper, we have used PML absorbing boundaries for the Maxwell simulations, to simulate emission of the scattered fields in free space. This, however, demands the use of a much larger Maxwell box than the matter box, so that the PML and the matter system do not overlap in space.

The coupling between systems supports different grids with arbitrary shapes and spacings (see Fig. 1). The transfer of quantities (called regridding) from one grid to the other is a central operation in our framework, as it is implemented using both linear and nearest-neighbor interpolations on the overlapping parts of the grids. It also supports grids with different parallel distributions. With this approach, we can adapt the grid spacing and shape for the different systems, thus saving computational effort.

Finally, the coupling of systems supports various time steps through the multisystem framework, where the mapped quantities are interpolated in time to ensure that the order of the time propagation methods is retained. Mostly, a fourth-order Taylor expansion of the exponential operator (and thus also a fourth-order time interpolation) is used. This feature allows us to efficiently capture different temporal scales of the different systems (as the Maxwell equations have a naturally faster timescale and demand a smaller time step than the electron dynamics).

B. Validation of the Maxwell solver

In this section, we illustrate the validation of our Maxwell solver. We first consider in Sec. II B 1 the radiation of an electron in the presence of a harmonic potential. We show that the numerical simulation is in perfect agreement with analytical results. As a next step, we verify in Sec. II B 2 the numerical solution of the Poisson equation (8) and check the accuracy of the Helmholtz decomposition. In Sec. II B 3, we investigate the effects of origin dependence on the dipole moment of benzene driven by a laser field. And finally, in Sec. II B 4, we discuss how the observables calculated with the usage of the nonlocal potential (widely used pseudopotentials) deviate from the case of local (all-electron) potentials.

1. TDDFT to Maxwell (backward interaction): Radiation from the harmonic oscillator

As a test of the implementation, we have studied the electromagnetic fields induced by an electron wave packet oscillating in a harmonic potential in three dimensions. As this simulation considers a single electron, the potential in the Hamiltonian of Eqs. (1) and (14) has no electron-electron interaction terms, and the initial wave function is just the solution of the Schrödinger equation in the displaced quadratic potential $V = \frac{1}{2}[(x-10)^2 + y^2 + z^2]$. To trigger the dynamics, we displace the potential from the origin such that the electron moves in the (static) potential $V = \frac{1}{2}(x^2 + y^2 + z^2)$. The wave packet is then propagated for 40 a.u. of time (0.97 fs), while the spatially resolved radiation from the wave packet is obtained by solving Maxwell's equations with absorbing boundary conditions (see the details of the grids used in the Supplemental Material [63]). The results of the simulation are depicted in Fig. 2.

Far from the source wave packet, where the effect of the Gaussian charge distribution is smaller, the generated electromagnetic fields have to match the Liénard–Wiechert (LW) fields of a point-charged particle. The electric and magnetic fields described by the LW formulas are given

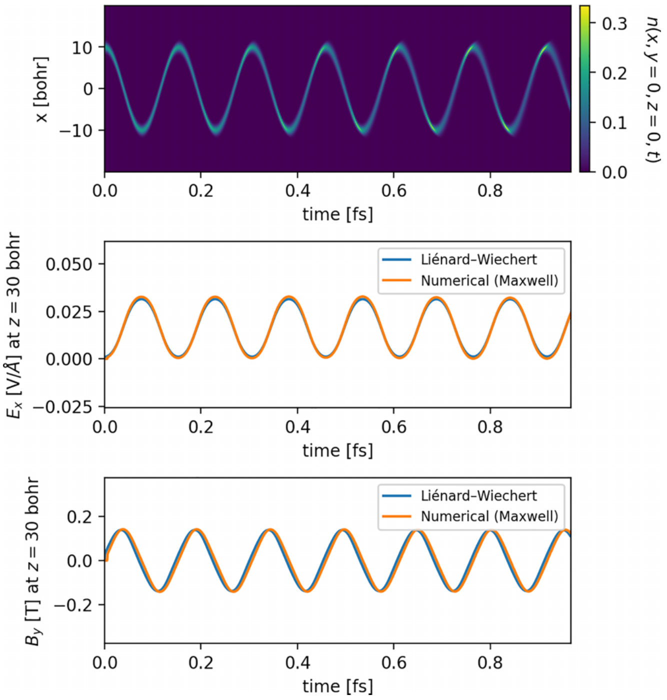

FIG. 2. Dynamics of a wave packet in a harmonic oscillator (top) and its generated electromagnetic fields as a function of time (bottom). The top panel depicts a one-dimensional (1D) slice of the density in the x axis ($y = 0, z = 0$) as a function of time. From the full volumetric density, the dipole moment is calculated and is fed into the Liénard-Wiechert equations for the analytical fields, fulfilling the role of the particle position $\mathbf{r}_p$. The middle panel shows the x component of the time-propagated electric field and its analytical counterpart at the (0,0,30 bohr) point as a function of time, while the magnetic field y component is compared for both cases in the bottom panel.

by [68]

$$\mathbf{E}(\mathbf{r},t) = \frac{q}{4\pi\epsilon_0}\frac{\tilde{r}}{(\tilde{\mathbf{r}}\cdot\mathbf{u})^3}[(c^2 - v^2)\mathbf{u} + \tilde{\mathbf{r}}\times(\mathbf{u}\times\mathbf{a})],$$

$$\mathbf{B}(\mathbf{r},t) = \frac{1}{c}\frac{\tilde{\mathbf{r}}}{\tilde{r}}\times\mathbf{E}(\mathbf{r},t). \tag{18}$$

Here, $\mathbf{r}$ represents the position of the field, $\tilde{\mathbf{r}} = \mathbf{r} - \mathbf{r}_p$, where $\mathbf{r}_p$ is the source position, considered in our calculations as the mean value position of the wave packet. The vector $\mathbf{u} = c\tilde{\mathbf{r}}/\tilde{r} - \mathbf{v}$, where $\mathbf{v}$ is the velocity vector of the source and $\mathbf{a}$ is its acceleration vector.

In the bottom panels of Fig. 2, the simulated and the LW fields are compared at one spatial point relatively far from the source, showing almost perfect agreement, with the small deviation arising from the finite width of the wave packet. As the results have not been rescaled by any factor, this test shows that the Maxwell time propagation with an electronic system as the source is correct and consistent with the employed unit system in our code.

2. Maxwell to TDDFT (forward interaction):
Magnetic vector potential and Helmholtz decomposition

To verify that the vector potential from a Maxwell system is properly coupled to the electronic system, we have propagated a plane-wave pulse in a Maxwell box, imposing the initial values at the boundaries (Dirichlet conditions), and calculated its vector potential using Eq. (8), which implies solving a Poisson equation for the magnetic field. The comparison of the calculated $\mathbf{A}(\mathbf{r},t)$ and the analytical expression from the plane wave ($\mathbf{A} = -\partial_t\mathbf{E}$) proves that the calculation is valid in most of the box (see Fig. S1 in the Supplemental Material [63]), especially for points which are far from the boundaries, where the error is larger due to the approximate description of the derivatives at the boundaries (see the description of the methods for the Helmholtz decomposition in the Supplemental Material [63]).

We also verified that transverse and longitudinal electric field components are correct. These components were calculated using the Helmholtz decomposition for an oscillating point dipole, described as a space-dependent spatial current, where the emitted fields are absorbed by the PML absorbing boundaries. The accuracy of the decomposition for different box sizes and PML widths can be evaluated by comparing the total field with the sum of the transverse and longitudinal fields (see Figs. S2–S7 in the Supplemental Material [63]). This comparison is useful to establish the minimum box size and maximum wavelength that can be simulated within a certain tolerance, for a charge distribution of a given spatial extent.

3. Origin independence in full minimal coupling

It is well known that truncating the light-matter interaction at a given multipole order beyond dipole leads to origin-dependent observables [38]. As the multipolar expansion is a common choice in electronic structure calculations, it is important to test its accuracy. Here we compare different coupling levels for the time propagation of a benzene molecule located at two different positions in the box, driven by an XUV pulse of frequency 270 eV which propagates along the y axis and is depicted in Fig. 3. The two locations for the center of mass $\mathbf{r}_0$ [see Eq. (11)] are, namely, the origin (0, 0, 0) (referred to as *centered*) and at (8, 8, 0) bohr (*displaced*). First of all, we observe non-negligible differences between the full minimal coupling and the dipolar level, shown in the top panel, which will be analyzed in detail later.

Here we focus on the comparison between full minimal coupling and a multipolar expansion that considers electric dipole, magnetic dipole, and electric quadrupole couplings. In all these cases, we consider only forward coupling of the plane wave with the electronic system, ignoring the back reaction. In the bottom panel of Fig. 3, the dipole moments of the centered and displaced molecules are compared. As the plane wave propagates along the y direction, one molecule experiences the effect of the external field earlier than the other. To correct for this delay and to have comparable time traces, the dipole moment of the displaced system has been translated in the time axis by an offset of $t_{\text{off}} = (8\ \text{bohr})/c = 0.058$ a.u. It is visible that the results in full minimal coupling match perfectly, while the simulations with truncated multipolar treatment show deviations. Considering that the beyond-dipole effects induced by a plane wave of this frequency are still within a few percent, the expected effects when the multipolar truncation is done on much more inhomogeneous fields (such as a

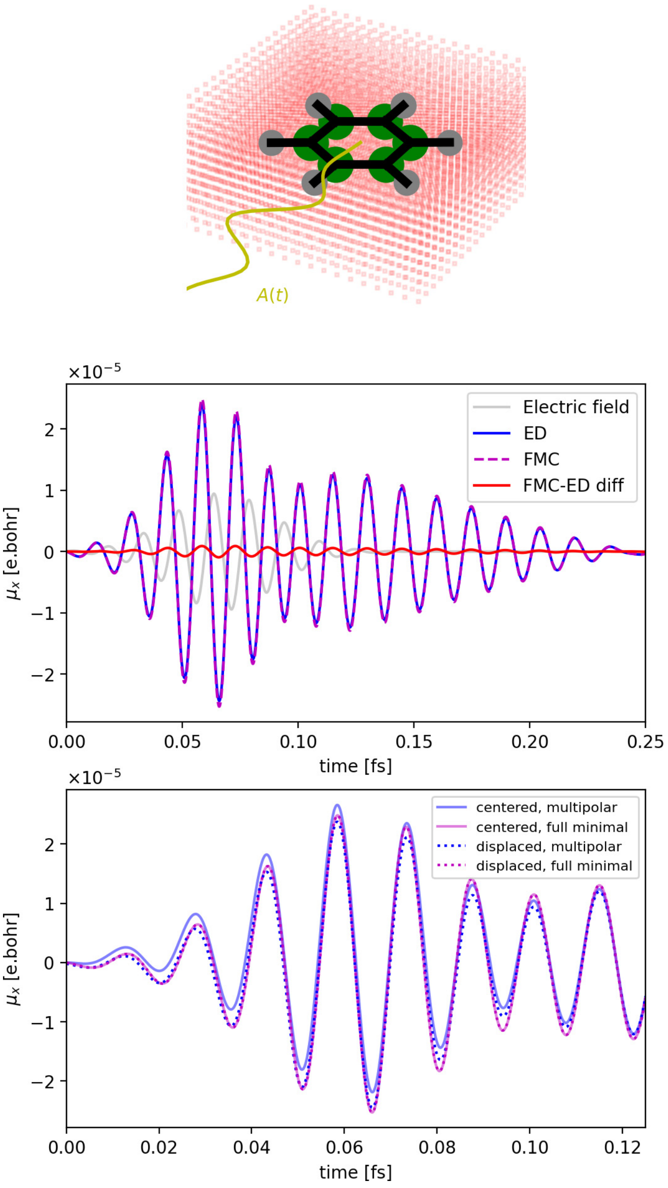

FIG. 3. Laser-driven benzene molecule by a pulse with central frequency $\omega = 270$ eV, comparing full minimal coupling with the truncated multipolar coupling at the magnetic dipole/electric quadrupole level. Top panel: Sketch of the simulation box and incoming field. Middle panel: Comparison of the time-dependent dipole moment, x component, in electric dipole, full minimal coupling and its difference, for the benzene molecule centered at the (0,0,0) point (the external field time trace is included for reference). Bottom panel: Comparison of the dipole moment dynamics in full minimal coupling and with the multipolar expansion including electric dipole, magnetic dipole, and electric quadrupole terms, with the molecule placed at two different locations: in one case (centered) with the center of mass at $r_0 = (0,0,0)$ and in the other (displaced) with $r_0 = (8,8,0)$ bohr.

plasmonic near field) are expected to be much more important, potentially leading to incorrect conclusions.

4. Pseudopotentials vs all-electron calculations

The path ambiguity in the gauge transformation of the nonlocal part of the atomic pseudopotentials is well known and possible solutions have been proposed, although with limited applicability in realistic scenarios [69,70]. In specific cases, e.g., when a kick is applied and therefore a vector potential is not present in the simulation, the problem can be overcome by transforming the momentum operator [71]. However, in general, there is not an efficient method to overcome this limitation and, in this work, we focus on calculations that do not involve a nonlocal potential by using an all-electron description.

To understand the error produced by the use of pseudopotentials, we compare simulations using both descriptions for a benzene molecule illuminated with a 7 eV external pulse, while the electrodynamics is propagated from the current density of the benzene molecule (without self-consistent forward coupling of the scattered field). In Fig. 4, we compare two quantities that can be computed from the electronic and the Maxwell systems, and analyze their consistency under the two electronic descriptions. Namely, we compare the electronic density calculated in two ways: as defined in Eq. (2), as well as by solving Eq. (10) (left panels); and the longitudinal electric field, which can be computed from the Helmholtz decomposition of the total electric field, as well as from the gradient of the time-dependent Hartree potential in DFT: $\mathbf{E}^{\parallel} = -\nabla(V^H - V^H_{GS})$. We see that while the all-electron quantities agree when calculated from the different physical systems (albeit small deviations close to the atomic nuclei arising due to the grid discretization), the same quantities differ inside the pseudopotential sphere for the calculations using pseudopotentials. Due to the computational cost of all-electron calculations, in future works it would be desirable to find a solution for the gauge invariance when pseudopotentials are used. For that purpose, the visual representation of the differences presented here could be a hint to find an adequate approach to overcome the path ambiguity.

III. CHERENKOV RADIATION FROM AN ELECTRONIC WAVE PACKET

The Vavilov-Cherenkov radiation is the emitted radiation from a particle that is traveling faster than the speed of light in a medium [72,73]. As the radiated Cherenkov field is highly inhomogeneous and is emitted in the vicinity of the particle, backward coupling of the induced radiation in the dynamics of the particle itself could, in principle, have considerable effects. As probing the Cherenkov angle is crucial to extract information from the superluminal travel of particles in a wide range of applications [74], beyond-dipole self-consistent corrections to the spatial distribution of the wave packet as well as its dynamics would have practical applications.

To test this hypothesis, we perform simulations of an electronic wave packet traveling at a higher velocity than the phase velocity of light in a medium. From these simulations, we analyze the emitted radiation with and without back reaction of such radiation on the wave-packet dynamics. As in the harmonic oscillator case, here we have a single-electron wave packet, and hence the Kohn-Sham Hartree exchange-correlation potential is zero. The initial condition of the Gaussian electronic wave packet is chosen as follows:

$$\varphi(x, y, z, t = 0) = C_0 e^{-ip(x-x_0)} e^{-\frac{1}{4}\left(\frac{x^2}{(\Delta x)^2}+\frac{y^2}{(\Delta y)^2}+\frac{z^2}{(\Delta z)^2}\right)}, \quad (19)$$

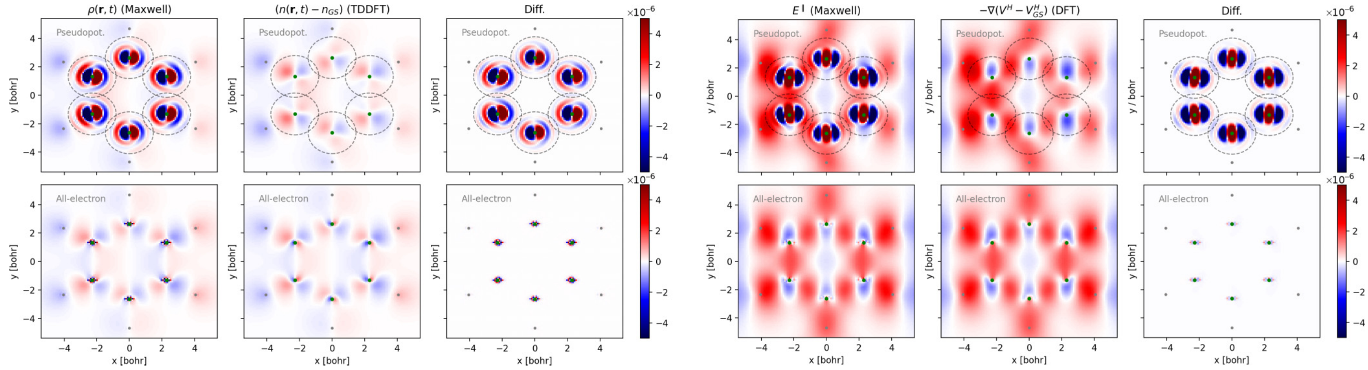

FIG. 4. Comparison of slices in the xy plane of the electron density (left panels) and longitudinal electric field (right panels) as calculated from the DFT subsystem and from the electromagnetic fields in the Maxwell solver, when using pseudopotentials and for an all-electron calculation. The circles in dashed lines indicate the pseudopotential sphere. In all cases, the simulation consisted of a benzene molecule centered at (0,0,0) driven in electric-dipole approximation by an external pulse of frequency $\omega = 7.2$ eV, tuned to the lowest-energy transition. The snapshots are taken at time $t = 0.3$ fs.

where C_0 denotes the amplitude, while Δx, Δy, and Δz indicate the width of the wave packet in three directions. The term $e^{-ip(x-x_0)}$ shows that the wave packet has momentum p along the x direction, initially centered at x_0. In our simulations, $p = 2.5$ a.u., while the medium has a refractive index of 100 and, consequently, the phase velocity of light is $v_l = 1.37$ a.u.

To observe the Cherenkov effect, the wave packet should not disperse too quickly during the dynamics. This implies keeping the momentum spread δp low enough without making the position spread δx too large for the simulation box that is used. The momentum itself sets a constraint in the spacing that is used due to the spatial modulations of the wave function. After carefully choosing the parameters, we employed a simulation box of size $60 \times 18 \times 18$ bohr^3 and a uniform spacing of 0.3 bohr. The wave-packet width in the three directions is set to $\Delta x = 5.5$ bohr and $\Delta y = \Delta z = 2.5$ bohr. The wave packet moves in the positive x direction. We offset the starting point of the particle by -30 nm in the x direction.

As can be seen in Fig. 5, as time evolves, the wave packet disperses, while the electric field (x component, in this case) starts to develop the well-known Cherenkov cone. The nondispersive Cherenkov angle is given by $\beta_{\text{nondisp}} = \arctan(v_l/p) = 56.8^\circ$. Here we study the birth of the Cherenkov radiation and the time evolution of the angle, which is first close to 90° (initial field aligned with the axis of propagation), as it develops, and tends to ≈54°. The slight difference with the nondispersive value can be attributed to the dispersion of the wave packet and the numerical resolution of the grid.

Then, we included the back-action corrections, which are also shown in Fig. 5 both for dipolar and full minimal couplings. As can be seen, the corrections to the density and the emitted field are around 0.1% with dipolar back action (spatial average of the radiated field), but over 3% with full minimal coupling back action. The dipolar correction shows the expected dipolar pattern in the direction of propagation of the wave packet, namely, a slight shift in space of the density (which can be interpreted as a slightly larger velocity with respect to the uncoupled case). However, the correction with full minimal coupling shows a rich spatial distribution, creating a slight accumulation on the front and lateral sides, and a strong depletion on the back of the wave packet, thereby changing its shape. The emitted field also shows an increase of the wavefront width and a decrease (in absolute values) of the field at the tip of the cone. In the literature, the corrections to Cherenkov dynamics have been addressed in a nonperturbative QED approach [75]. The present methodology has the potential to simulate the corrected nonperturbative dynamics of arbitrary particles described at the first-principles level and to study the angular distribution of radiation for relevant scenarios.

IV. MAGNETO-OPTICAL RESPONSE OF NONCHIRAL MOLECULES WITH NONCHIRAL SOFT X RAYS

It is known that nondipole corrections in x-ray spectroscopy, particularly in x-ray absorption spectroscopy (XAS), are around 5–10% for dipole-allowed transitions in the soft x-ray region [40]. Numerous works have proposed methods to calculate the nondipole response function from first principles without truncation of the multipolar expansion (e.g., in full minimal coupling) [39,40,42]. Here, we analyze the beyond-dipole effects in real space and real time, by simulating the soft x-ray excitation of a single benzene molecule considering different angles of incidence, as defined by the wave vector. In this section, we omit the back reaction as it is very small (only a frequency shift of around 0.05% is observed); therefore, the electromagnetic field that is used is only of external origin.

The setup is the same as discussed in Sec. II B 3. By considering an incident beam with both propagation and polarization vectors in the plane of the molecule ($\mathbf{k} = k\mathbf{e}_y$, $\mathbf{A} = A(r,t)\mathbf{e}_x$), the atomic dipole oscillations are dephased along the propagation direction, which is not visible in the dipolar approximation. This phenomenon is not observed at normal incidence, i.e., when the propagation of the beam is along the direction perpendicular to the molecule ($\mathbf{k} = k\mathbf{e}_z$).

This effect can be understood as the atomic-scale version of the phase retardation effects on the optical spectra of nanorings [76]. As in the case of the nanorings, the in-plane beam excites higher-order modes which would otherwise be "dark" or dipole forbidden. As the first order beyond the electric

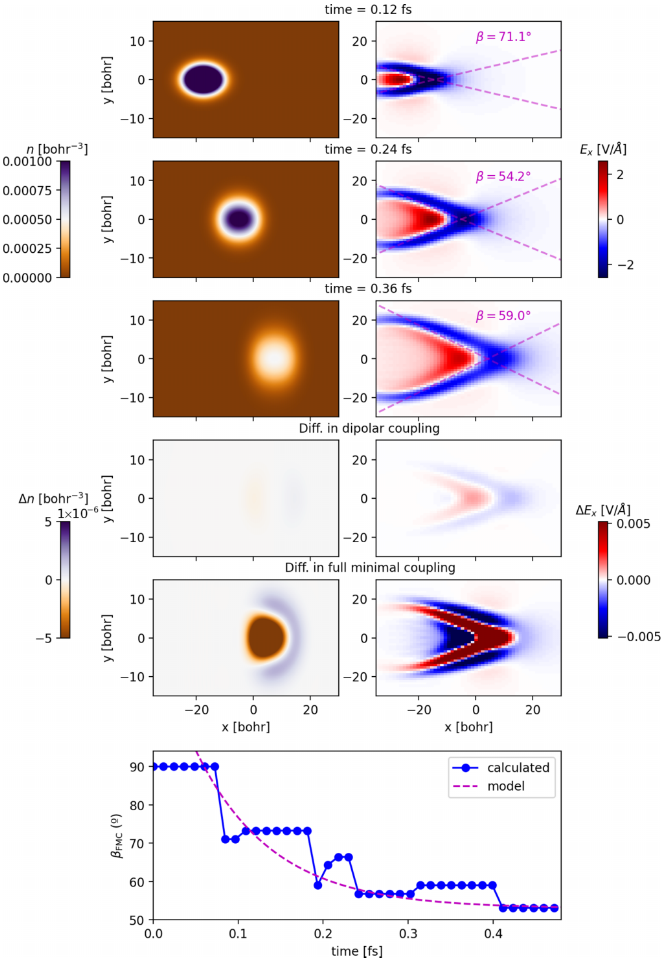

FIG. 5. Cherenkov radiation: Electron density and transverse electric field for different time steps (top); corrections that arise in dipolar and full minimal coupling (middle); and dynamics of the Cherenkov angle formation (bottom). For the three time snapshots chosen in the top panels, the wave packet is propagating freely without any external drive and without back reaction. It can be seen how the wave packet disperses while the radiation forms the well-known cone. The corrections are plotted with the same color scale, which shows a minor effect from the dipolar coupling as well as variations along the axis of propagation of the wave packet, while a rich angular dependence arises in our full minimal coupling approach. The angle dynamics (bottom) show the time evolution of the angle measured from the simulations (calculated), together with an exponential fit (model) with a characteristic time of 0.09 fs.

dipole is the electric quadrupole and the magnetic dipole, we examine the dynamics of the induced orbital angular momentum as follows.

The angular momentum expectation value is calculated as $\mathbf{L}(t)=\sum_{j=1}^{N_{occ}}\int d\mathbf{r}\psi_j^{\dagger}\hat{\mathbf{L}}\psi_j$. As shown in Fig. 6, angular momentum in the z direction is driven when the full minimal coupling approach is used, but not in the dipolar coupling case. The induced magnetic moment $\mathbf{m}=\mathbf{L}$ (for a spin-unpolarized case) ignoring higher-order terms can be written as [71]

$$\mathbf{L}(\omega)=\boldsymbol{\chi}(\omega)\mathbf{B}(\omega)+\frac{i\omega}{c}\boldsymbol{\beta}(\omega)\mathbf{E}(\omega), \tag{20}$$

where χ is the magnetic susceptibility tensor and β is the crossed response tensor.

As the linear magnetic contribution is a trivial source of induced angular momentum, we subtract the magnetic dipole effect by running a simulation where the external field couples only through the magnetic dipole term [see Eq. (11)]. The difference between the full coupling and the magnetic dipolar coupling is the magneto-optical response (see Fig. 6), which can be related to the time-domain magnetization as

$$\mathbf{L}(t)-\mathbf{L}^{\mathrm{MD}}(t)=\frac{i}{c}\int_{-\infty}^{\infty}\omega\boldsymbol{\beta}(\omega)\mathbf{E}(\omega)e^{i\omega t}d\omega, \tag{21}$$

where $\mathbf{L}(t)$ and $\mathbf{L}^{\mathrm{MD}}(t)$ are z components of the angular momenta calculated in full minimal coupling and at the magnetic dipole level, respectively.

For the calculation of circular dichroic spectra, only the diagonal elements of the crossed $\boldsymbol{\beta}$ tensor are considered to be relevant, since they are linked to the rotatory strength $R(\omega)=\frac{3\omega}{\pi c}\mathrm{Im}(\bar{\beta}(\omega))$. However, the off-diagonal components which vanish upon spherical averaging could play a role in novel beyond-dipole spectroscopies. In particular, here we compute the off-diagonal cross response as

$$\beta_{xz}(\omega)=\frac{1}{2\omega E_x(\omega)}\int_0^{\infty}\left[L_z(t)-L_z^{\mathrm{MD}}(t)\right]e^{i\omega t}dt. \tag{22}$$

The magneto-optical resonances due to the cross response can be visualized in the magneto-optical spectrum, which is compared with the dipolar (absorption) spectra (calculated as $\omega\mathrm{Im}[\langle x\rangle(\omega)/E_x(\omega)]$) and with the angular spectra (defined as $\omega\mathrm{Im}[L_z(\omega)/E_x(\omega)]$) in the bottom-right panel of Fig. 6. While the dipole spectrum shows very similar peaks both in dipolar and FMC levels, with two major peaks around 278 and 290 eV, the magneto-optical spectrum shows only a clear resonance around 290 eV and other minor peaks. It is possible to see that the angular momentum spectrum directly calculated from the total L_z does not show this selectivity for the 290 nm excitation, allowing us to discriminate between magnetic dipole and higher-order (e.g., electric-quadrupole) excitations. The reason for the selectivity of the magneto-optical spectrum on the second excited state still needs to be explored in depth and is beyond the scope of this publication. In summary, the effects that arise from the higher-order coupling when using nonchiral light could be important to describe the origin of chirality in nonchiral oriented samples, especially in conditions where the dipole approximation is not valid (e.g., small wavelengths).

V. REAL-TIME RADIATION REACTION OF PLASMONIC DIMERS

Plasmonic nanostructures and nanocavities have proven to be useful platforms for driving nonequilibrium phenomena, including strong coupling [10], ultrafast transport [77], and nonlinear [78] and quadrupolar effects [36,79]. The highly localized plasmonic fields at the apex of atomically sharp tips are being used to achieve more and more resolved spectromicroscopy techniques, including TERS images [56,80]. Precise knowledge of the spatial shape [81,82] and waveform [83] of the plasmonic near fields is important to understand

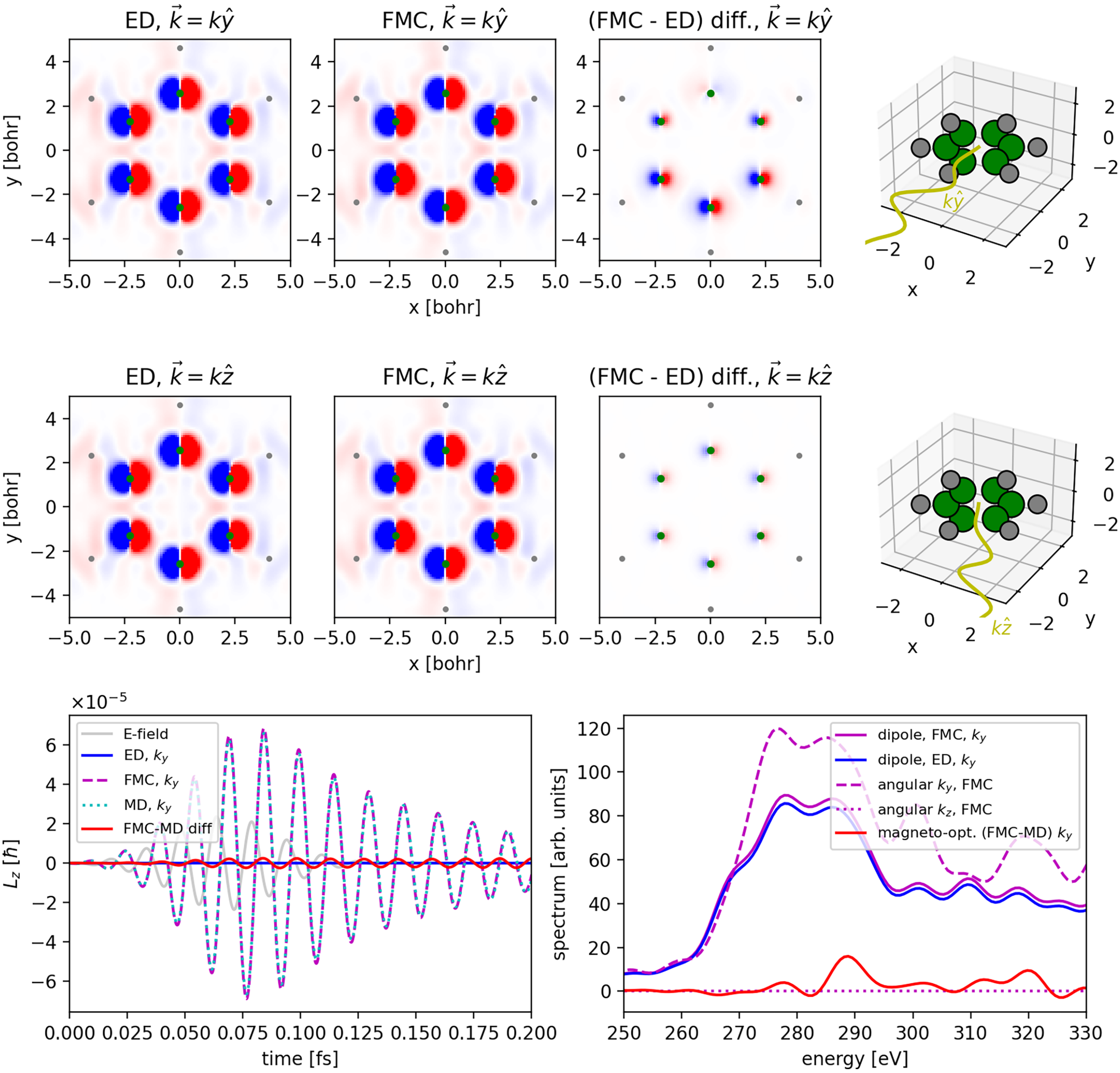

FIG. 6. Laser-driven benzene at 270 eV in full minimal coupling (FMC) vs electric-dipole (ED) and magnetic dipole (MD): magneto-optical effects dependent on the incidence angle. The top panel shows snapshots of the electronic density in the xy plane for the case of the XUV pulse propagating along the y direction. From the difference of the densities (FMC-ED), it can be seen that the atomic dipoles show a delay along the direction of propagation, which is a radiation pressure feature. This effect is not present when the angle of incidence is perpendicular to the molecule. A consequence of the retarded response along the propagation direction is a generation of angular momentum (bottom left). Subtracting the angular momentum induced by the magnetic dipole, the L_z difference (red line) can be attributed to the magneto-optical effects. The spectrum of this cross response is plotted in the bottom-right panel, along with the (dipole) absorption spectra in FMC and ED, together with the angular spectra at different incidence angles, for comparison. It can be seen that the cross response tensor is mostly sensitive to one of the excitation peaks.

the mechanisms and push the envelope in the atomic-scale resolution techniques [84].

In this sense, radiation dynamics and radiative decay are often ignored aspects, which can lead to considerable frequency shifts when treated [85,86] and could be used to tailor the modal structure of the radiative rate with respect to the excitation rates [87]. The mentioned frequency shift can be attributed to a nanoplasmonic analog of the atomic Lamb shift [85]. Such a shift has also been demonstrated to arise in *ab initio* simulations with radiation reaction included at the mean-field level [54]. However, radiation damping and the associated Lamb-like shifts are expected to arise for large cluster sizes [88].

Here we demonstrate that even in free space, there is a potentially measurable renormalization of the dimer plasmonic mode in clusters of ≈1 nm diameter. We have modeled a

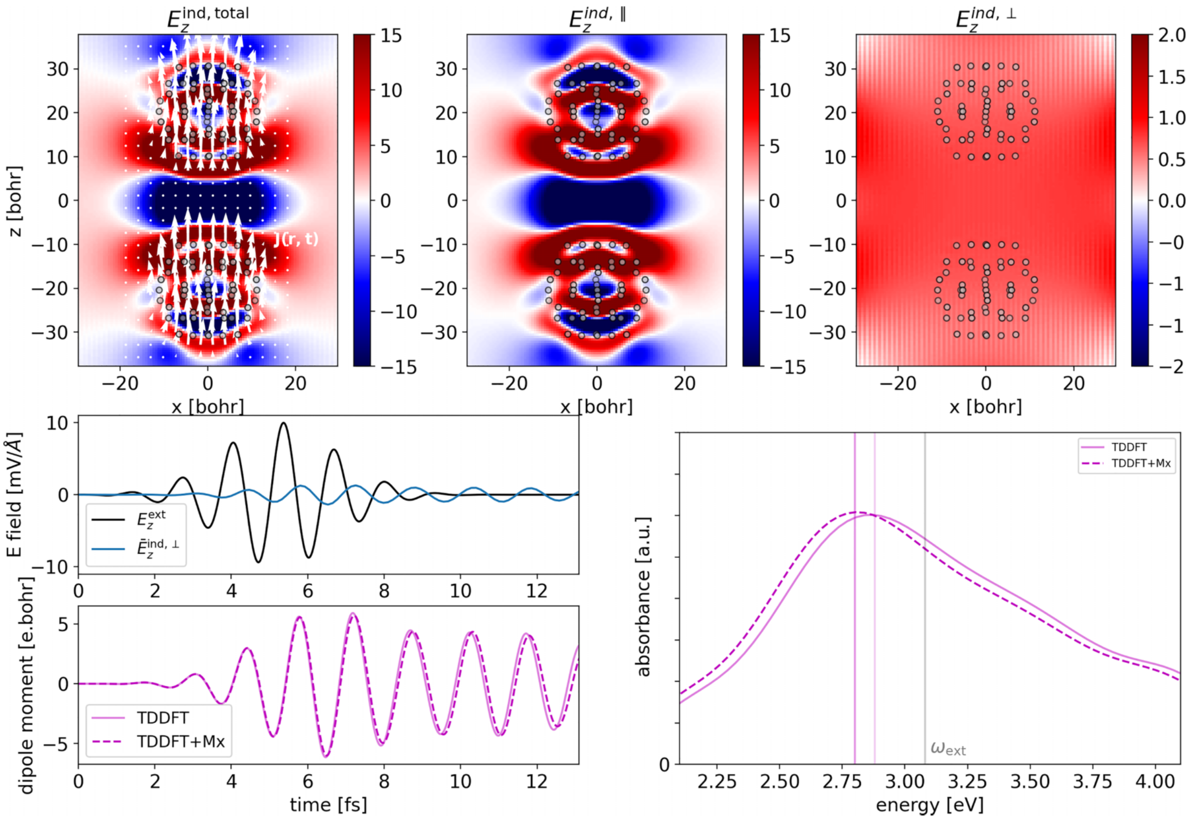

FIG. 7. Transverse-field effects on the plasmon-driven dynamics of a dimer of sodium clusters: total, longitudinal, and transverse electric field spatial distribution at $t = 7.5$ fs (top), transverse-field (external and induced) dynamics and dipole moment (bottom left), and spectra which evidence the renormalized plasmon frequency (bottom right).

plasmonic dimer using two icosahedral sodium clusters of 55 atoms each, oriented in a face-to-face configuration and with an interparticle distance of 0.7 nm. We use a simulation box of $38 \times 38 \times 83$ bohr^3 with a spacing of 0.28 bohr for the matter system, while for the Maxwell system, the box is of size $113 \times 113 \times 159$ bohr^3 and the spacing is 0.56 bohr (see Fig. 7, top-left panel). The Maxwell box includes a PML boundary region of width 28 bohr in all directions. We propagate the dynamics for 13 fs using the exponential midpoint method, using time steps of 0.5 as and 0.02 as for the matter and Maxwell systems, respectively, under an external laser coupled in electric-dipole approximation, tuned to the plasmonic resonance of the 55-atom cluster (3.08 eV).

Figure 7 shows a snapshot of the induced currents of the dimer at $t = 7.5$ fs, along with the total induced electric field and its decomposition in longitudinal and transverse components. As expected, the transverse component is smaller than the longitudinal one (which shows near-field enhancement with respect to the external field), but its amplitude reaches approximately 10% of the external field. The transverse component is coupled back to obtain the renormalized radiative dynamics. The time-dependent dipole moment and the absorption spectra for the two simulations (with and without radiation-reaction effects) are compared, where a frequency shift of the dipole plasmon mode of ≈ -70 meV is evident when the back coupling is included, together with a broad absorption enhancement for energies below the absorption maximum.

In addition to the Lamb-like shift, the spatial and temporal electrodynamics is obtained by the Maxwell propagation. As expected by Gauß law, the time-resolved longitudinal electric field and charge density dynamics evolve in phase, which can be seen in Fig. 8 (top panel) by comparing the phase of the longitudinal field, $E_\parallel$, at a point with the dipole moment μ_z. However, the transverse electric field shows a small phase shift with the dipole moment (better visualized in the plot inset) due to the retarded evolution present in the Faraday and Ampère laws. In contrast to standard radiation damping theory, which predicts the reaction field to be proportional to $\dddot{\mu}$ [89], we show that its time dependence is far from the classical point-particle radiation limit and needs to be evaluated with a self-consistent framework.

The spatial distribution at the time step of maximum polarization of the system was also calculated. A 2D rectangular box located at 10 bohr away from the farthest atom in each direction was used as a detector box (see Fig. 8, bottom-left panel). The scattered electric field components were collected on each point of this box and the angular distribution was evaluated (Fig. 8, bottom-right panel). As this box is located mostly in the near-field region, the longitudinal electric field shows the typical pattern of the near field for a dimer of metallic particles. The transverse field, however, has a rather constant angular distribution at this distance, confirming that the dipole-approximation in-coupling of the scattered field in the self-consistent scheme is valid for this setup. It is important to emphasize that in a standard TDDFT propagation, there

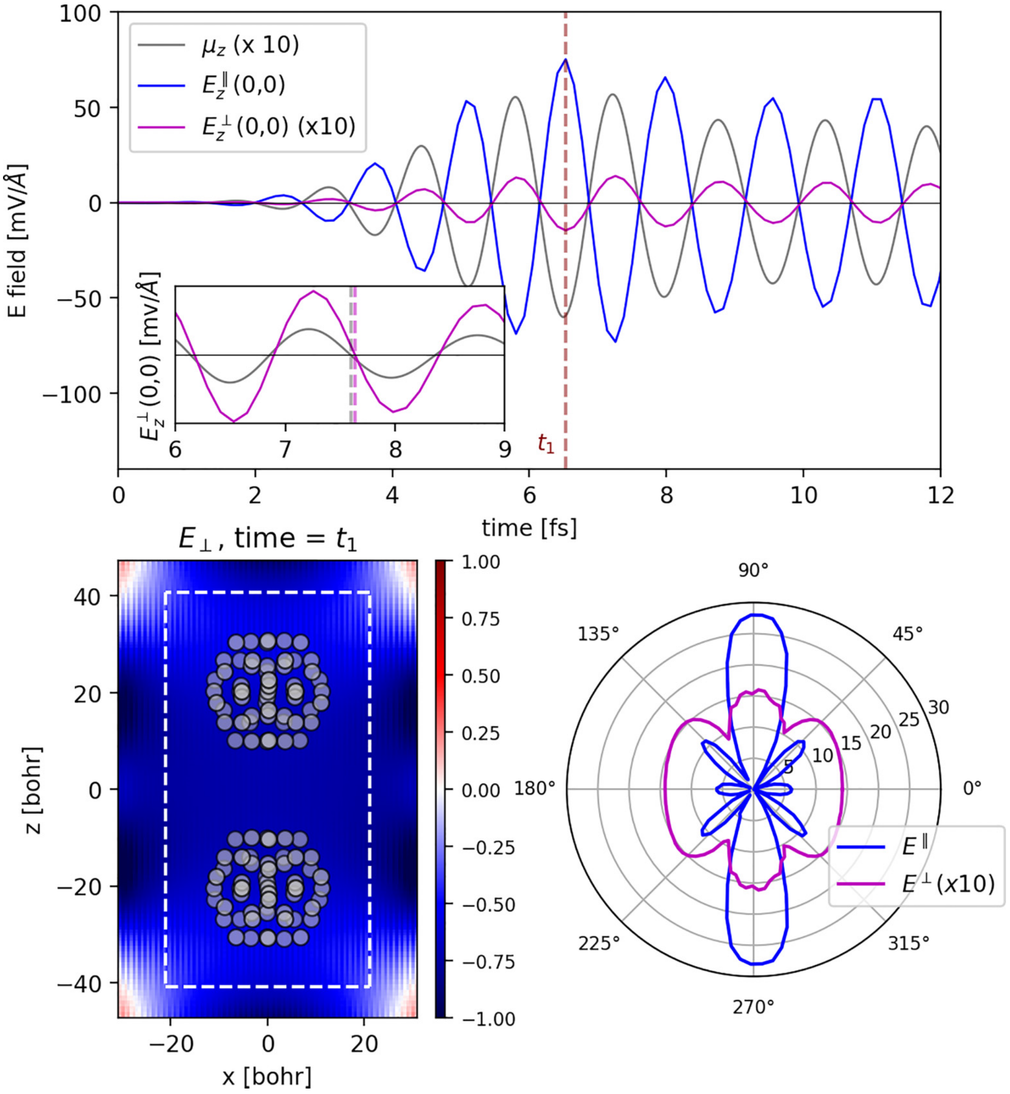

FIG. 8. Spatiotemporal features of the transverse electric field. Top panel: Time-dependent z component of dipole moment μ_z, longitudinal electric field $E_\parallel$ at the origin, and transverse electric field $E_\perp$ at the origin. Inset: The time propagation of the dipole moment and transverse field, which allows one to more clearly visualize the phase difference between them. Bottom panels: Definition of the detector box (left) and angle dependence of the longitudinal and transverse field at the time of maximum polarization t_1 (right).

is no information about the transverse degrees of freedom and it is not possible to draw any conclusion on the radiation-reaction characteristics.

Finally, the renormalization of the matter properties under these conditions has been analyzed. Both the phase of the electronic density (Fig. S8 of the Supplemental Material [63]) and the near field (Fig. S9 of the Supplemental Material [63]) are affected when the self-consistent Maxwell coupling is applied. While the phase shifts are small for this particular setup given by the few-nm size of the system, they are expected to be relevant for situations where spill-out effects appear in the gap region, as is the case for ultrafast electron transport in plasmonic gaps [77]. Moreover, since the near-field phase is affected by the plasmonic gap geometry and dielectric properties of the nanostructures, this phenomenon suggests that radiative dynamics could play a role in experiments that probe on the quantum dynamics of plasmonic nanojunctions, e.g., in light-driven scanning tunneling microscopy (STM) [83] or TERS [80].

VI. CONCLUDING REMARKS

In summary, in this work, we have proven that there are significant effects beyond dipole that play a role in the dynamics of quantum systems in electromagnetic environments. We have done so by implementing a self-consistent Maxwell-TDDFT method in full minimal coupling with the total (external and induced) spatiotemporal electromagnetic fields. Generally speaking, the beyond-dipole response in mean-field QED will be relevant whenever (a) the transverse-induced field is large compared to the external field and (b) either the external or the induced vector potential has spatial inhomogeneities in the length scale of the system, which causes magnetic or higher-order electric effects. Relevant examples of such conditions, which have not been covered in this article but will be studied in future works, are the excitation of quantum systems with orbital angular momentum beams (also called “twisted light”), strong-field phenomena such as photoionization or high harmonic generation, x-ray absorption spectra using structured light, and plasmon-enhanced scattering spectra such as TERS. Overall, this new framework constitutes a powerful tool to assess the beyond-dipole effects as new knobs to control nonequilibrium phenomena by tailoring light-matter interactions in optical cavities.

ACKNOWLEDGMENTS

The authors would like to thank the OCTOPUS developers team, especially Nicolas Tancogne-Dejean, Micael Oliveira, Martin Lüders, and Alex Buccheri, for contributing to code development and optimization, and Hans Fangohr, Fabian Gropp, Victor Horvath, and Andrea Petrocchi for their support on the use of the POSTOPUS tool and their work on reproducibility. We also would like to thank Michael Ruggenthaler and Christian Schäfer for discussions. This work was supported by the European Research Council (Grant No. ERC-2015-AdG694097), the Cluster of Excellence "Advanced Imaging of Matter" (AIM), Grupos Consolidados (Grant No. IT1453-22), and the Deutsche Forschungsgemeinschaft (DFG)–SFB-925–Project No. 170620586. The Flatiron Institute is a division of the Simons Foundation. We acknowledge support from the Max Planck-New York City Center for Non-Equilibrium Quantum Phenomena. F.P.B. acknowledges financial support from the European Union's Horizon 2020 research and innovation program under the Marie Sklodowska-Curie Grant Agreement No. 895747 (NanoLightQD). E.I.A. acknowledges support from the International Max Planck Research School. The authors also would like to acknowledge the computational support provided by the Max Planck Computing and Data Facility.

---

[1] W. E. Lamb and R. C. Retherford, Fine structure of the hydrogen atom by a microwave method, Phys. Rev. **72**, 241 (1947).

[2] P. W. Milonni and W. A. Smith, Radiation reaction and vacuum fluctuations in spontaneous emission, Phys. Rev. A **11**, 814 (1975).

[3] P. W. Milonni, Why spontaneous emission? Am. J. Phys. **52**, 340 (1984).

[4] H. B. G. Casimir and D. Polder, The influence of retardation on the London–van der Waals forces, Phys. Rev. **73**, 360 (1948).

[5] S. Y. Buhmann, *Dispersion Forces I: Macroscopic Quantum Electrodynamics and Ground-state Casimir, Casimir–Polder and van der Waals forces* (Springer, New York, 2013), Vol. 247.

[6] J. Schwinger, On gauge invariance and vacuum polarization, Phys. Rev. **82**, 664 (1951).

[7] Z. Bialynicka-Birula and I. Bialynicki-Birula, Nonlinear effects in quantum electrodynamics. photon propagation and photon splitting in an external field, Phys. Rev. D **2**, 2341 (1970).

[8] F. Karbstein, C. Sundqvist, K. S. Schulze, I. Uschmann, H. Gies, and G. G. Paulus, Vacuum birefringence at x-ray free-electron lasers, New J. Phys. **23**, 095001 (2021).

[9] A. Thomas, J. George, A. Shalabney, M. Dryzhakov, S. J. Varma, J. Moran, T. Chervy, X. Zhong, E. Devaux, C. Genet, J. A. Hutchison, and T. W. Ebbesen, Ground-state chemical reactivity under vibrational coupling to the vacuum electromagnetic field, Angew. Chem. Intl. Ed. **55**, 11462 (2016).

[10] R. Chikkaraddy, B. De Nijs, F. Benz, S. J. Barrow, O. A. Scherman, E. Rosta, A. Demetriadou, P. Fox, O. Hess, and J. J. Baumberg, Single-molecule strong coupling at room temperature in plasmonic nanocavities, Nature (London) **535**, 127 (2016).

[11] E. Orgiu, J. George, J. A. Hutchison, E. Devaux, J. F. Dayen, B. Doudin, F. Stellacci, C. Genet, J. Schachenmayer, C. Genes, G. Pupillo, P. Samorì, and T. W. Ebbesen, Conductivity in organic semiconductors hybridized with the vacuum field, Nat. Mater. **14**, 1123 (2015).

[12] J. Fregoni, G. Granucci, E. Coccia, M. Persico, and S. Corni, Manipulating azobenzene photoisomerization through strong light–molecule coupling, Nat. Commun. **9**, 4688 (2018).

[13] C. Schäfer, M. Ruggenthaler, H. Appel, and A. Rubio, Modification of excitation and charge transfer in cavity quantum-electrodynamical chemistry, Proc. Natl. Acad. Sci. USA **116**, 4883 (2019).

[14] C. Schäfer, F. Buchholz, M. Penz, M. Ruggenthaler, and A. Rubio, Making *ab initio* QED functional(s): Nonperturbative and photon-free effective frameworks for strong light–matter coupling, Proc. Natl. Acad. Sci. USA **118**, e2110464118 (2021).

[15] A. Frisk Kockum, A. Miranowicz, S. De Liberato, S. Savasta, and F. Nori, Ultrastrong coupling between light and matter, Nat. Rev. Phys. **1**, 19 (2019).

[16] F. Schlawin, D. M. Kennes, and M. A. Sentef, Cavity quantum materials, Appl. Phys. Rev. **9**, 011312 (2022).

[17] J. Bloch, A. Cavalleri, V. Galitski, M. Hafezi, and A. Rubio, Strongly correlated electron–photon systems, Nature (London) **606**, 41 (2022).

[18] D. A. Glazov, A. V. Volotka, O. V. Andreev, V. P. Kosheleva, S. Fritzsche, V. M. Shabaev, G. Plunien, and T. Stöhlker, Ground-state hyperfine splitting of B-like ions in the high-z region, Phys. Rev. A **99**, 062503 (2019).

[19] V. P. Kosheleva, A. V. Volotka, D. A. Glazov, D. V. Zinenko, and S. Fritzsche, g factor of lithiumlike silicon and calcium: Resolving the disagreement between theory and experiment, Phys. Rev. Lett. **128**, 103001 (2022).

[20] D. V. Zinenko, D. A. Glazov, V. P. Kosheleva, A. V. Volotka, and S. Fritzsche, Electron correlation effects on the g factor of lithiumlike ions, Phys. Rev. A **107**, 032815 (2023).

[21] V. P. Kosheleva, A. V. Volotka, D. A. Glazov, and S. Fritzsche, Many-electron effects in the hyperfine splitting of lithiumlike ions, Phys. Rev. Res. **2**, 013364 (2020).

[22] E. Runge and E. K. U. Gross, Density-functional theory for time-dependent systems, Phys. Rev. Lett. **52**, 997 (1984).

[23] *Time-Dependent Density Functional Theory*, edited by M. A. L. Marques, C. A. Ullrich, F. Nogueira, A. Rubio, K. Burke, and E. K. U. Gross (Springer, Berlin, 2006).

[24] M. Ruggenthaler, J. Flick, C. Pellegrini, H. Appel, I. V. Tokatly, and A. Rubio, Quantum-electrodynamical density-functional theory: Bridging quantum optics and electronic-structure theory, Phys. Rev. A **90**, 012508 (2014).

[25] T. E. Li, H. T. Chen, A. Nitzan, and J. E. Subotnik, Understanding the nature of mean-field semiclassical light-matter dynamics: An investigation of energy transfer, electron-electron

correlations, external driving, and long-time detailed balance, Phys. Rev. A **100**, 062509 (2019).

[26] N. M. Hoffmann, C. Schäfer, N. Säkkinen, A. Rubio, H. Appel, and A. Kelly, Benchmarking semiclassical and perturbative methods for real-time simulations of cavity-bound emission and interference, J. Chem. Phys. **151**, 244113 (2019).

[27] N. M. Hoffmann, C. Schäfer, A. Rubio, A. Kelly, and H. Appel, Capturing vacuum fluctuations and photon correlations in cavity quantum electrodynamics with multitrajectory Ehrenfest dynamics, Phys. Rev. A **99**, 063819 (2019).

[28] C. M. Bustamante, E. D. Gadea, A. Horsfield, T. N. Todorov, M. C. González Lebrero, and D. A. Scherlis, Dissipative equation of motion for electromagnetic radiation in quantum dynamics, Phys. Rev. Lett. **126**, 087401 (2021).

[29] C. Schäfer and G. Johansson, Shortcut to self-consistent light-matter interaction and realistic spectra from first principles, Phys. Rev. Lett. **128**, 156402 (2022).

[30] M. Sukharev, Efficient parallel strategy for molecular plasmonics–A numerical tool for integrating Maxwell-Schrödinger equations in three dimensions, J. Comput. Phys. **477**, 111920 (2023).

[31] R. Jestädt, M. Ruggenthaler, M. J. Oliveira, A. Rubio, and H. Appel, Light-matter interactions within the Ehrenfest–Maxwell–Pauli–Kohn–Sham framework: Fundamentals, implementation, and nano-optical applications, Adv. Phys. **68**, 225 (2019).

[32] A. Yamada and K. Yabana, Multiscale time-dependent density functional theory for a unified description of ultrafast dynamics: Pulsed light, electron, and lattice motions in crystalline solids, Phys. Rev. B **99**, 245103 (2019).

[33] J. Flick, D. M. Welakuh, M. Ruggenthaler, H. Appel, and A. Rubio, Light-matter response in nonrelativistic quantum electrodynamics, ACS Photon. **6**, 2757 (2019).

[34] L. Konecny, V. P. Kosheleva, H. Appel, M. Ruggenthaler, and A. Rubio, Relativistic linear response in quantum-electrodynamical density functional theory, arXiv:2407.02441.

[35] C. M. Bustamante, E. D. Gadea, T. N. Todorov, and D. A. Scherlis, Tailoring cooperative emission in molecules: Superradiance and subradiance from first-principles simulations, J. Phys. Chem. Lett. **13**, 11601 (2022).

[36] N. Rivera, I. Kaminer, B. Zhen, J. D. Joannopoulos, and M. Soljačić, Shrinking light to allow forbidden transitions on the atomic scale, Science **353**, 263 (2016).

[37] S. Bernadotte, A. J. Atkins, and C. R. Jacob, Origin-independent calculation of quadrupole intensities in x-ray spectroscopy, J. Chem. Phys. **137**, 204106 (2012).

[38] P. J. Lestrange, F. Egidi, and X. Li, The consequences of improperly describing oscillator strengths beyond the electric dipole approximation, J. Chem. Phys. **143**, 234103 (2015).

[39] N. O. Foglia, D. Maganas, and F. Neese, Going beyond the electric-dipole approximation in the calculation of absorption and (magnetic) circular dichroism spectra including scalar relativistic and spin-orbit coupling effects, J. Chem. Phys. **157**, 084120 (2022).

[40] N. H. List, J. Kauczor, T. Saue, H. J. A. Jensen, and P. Norman, Beyond the electric-dipole approximation: A formulation and implementation of molecular response theory for the description of absorption of electromagnetic field radiation, J. Chem. Phys. **142**, 244111 (2015).

[41] A. Sakko, A. Rubio, M. Hakala, and K. Hämäläinen, Time-dependent density functional approach for the calculation of inelastic x-ray scattering spectra of molecules, J. Chem. Phys. **133**, 174111 (2010).

[42] E. Aurbakken, B. S. Ofstad, H. E. Kristiansen, Ø. S. Schøyen, S. Kvaal, L. K. Sørensen, R. Lindh, and T. B. Pedersen, Transient spectroscopy from time-dependent electronic-structure theory without multipole expansions, Phys. Rev. A **109**, 013109 (2024).

[43] D. W. Lindle and O. Hemmers, Breakdown of the dipole approximation in soft-x-ray photoemission, J. Electron/Spectros. Relat. Phenom. **100**, 297 (1999).

[44] M. Førre and A. S. Simonsen, Generalized velocity-gauge form of the light-matter interaction Hamiltonian beyond the dipole approximation, Phys. Rev. A **93**, 013423 (2016).

[45] T. Iwasa and K. Nobusada, Nonuniform light-matter interaction theory for near-field-induced electron dynamics, Phys. Rev. A **80**, 043409 (2009).

[46] M. Førre, J. P. Hansen, L. Kocbach, S. Selstø, and L. B. Madsen, Nondipole ionization dynamics of atoms in superintense high-frequency attosecond pulses, Phys. Rev. Lett. **97**, 043601 (2006).

[47] M. Førre, S. Selstø, J. P. Hansen, and L. B. Madsen, Exact nondipole Kramers-Henneberger form of the light-atom Hamiltonian: An application to atomic stabilization and photoelectron energy spectra, Phys. Rev. Lett. **95**, 043601 (2005).

[48] S. V. B. Jensen, M. M. Lund, and L. B. Madsen, Nondipole strong-field-approximation Hamiltonian, Phys. Rev. A **101**, 043408 (2020).

[49] R. KahvedŽić and S. Gräfe, Shift of the photoelectron momentum against the radiation pressure force in linearly polarized intense midinfrared laser fields, Phys. Rev. A **106**, 043122 (2022).

[50] K. Lin, S. Eckart, A. Hartung, D. Trabert, K. Fehre, J. Rist, L. P. H. Schmidt, M. S. Schöffler, T. Jahnke, M. Kunitski, and R. Dörner, Photoelectron energy peaks shift against the radiation pressure in strong-field ionization, Sci. Adv. **8**, eabn7386 (2022).

[51] S. Sun, R. A. Beck, D. Williams-Young, and X. Li, Simulating magnetic circular dichroism spectra with real-time time-dependent density functional theory in gauge including atomic orbitals, J. Chem. Theory Comput. **15**, 6824 (2019).

[52] S. Sun, B. Gu, and S. Mukamel, Polariton ring currents and circular dichroism of Mg-porphyrin in a chiral cavity, Chem. Sci. **13**, 1037 (2022).

[53] R. R. Riso, L. Grazioli, E. Ronca, T. Giovannini, and H. Koch, Strong coupling in chiral cavities: Nonperturbative framework for enantiomer discrimination, Phys. Rev. X **13**, 031002 (2023).

[54] C. Schäfer and D. G. Baranov, Chiral polaritonics: Analytical solutions, intuition, and use, J. Phys. Chem. Lett. **14**, 3777 (2023).

[55] X. Chen, P. Liu, Z. Hu, and L. Jensen, High-resolution tip-enhanced Raman scattering probes submolecular density changes, Nat. Commun. **10**, 2567 (2019).

[56] P. Liu, X. Chen, H. Ye, and L. Jensen, Resolving molecular structures with high-resolution tip-enhanced Raman scattering images, ACS Nano **13**, 9342 (2019).

[57] Y. Litman, F. P. Bonafé, A. Akkoush, H. Appel, and M. Rossi, First-principles simulations of tip enhanced Raman scatter-

ing reveal active role of substrate on high-resolution images, J. Phys. Chem. Lett. **14**, 6850 (2023).

[58] A. Picón, J. Mompart, J. R. Vázquez de Aldana, L. Plaja, G. F. Calvo, and L. Roso, Photoionization with orbital angular momentum beams, Opt. Express **18**, 3660 (2010).

[59] G. F. Quinteiro, F. Schmidt-Kaler, and C. T. Schmiegelow, Twisted-light-ion interaction: The role of longitudinal fields, Phys. Rev. Lett. **119**, 253203 (2017).

[60] K. A. Forbes, Raman optical activity using twisted photons, Phys. Rev. Lett. **122**, 103201 (2019).

[61] V. P. Kosheleva, V. A. Zaytsev, R. A. Müller, A. Surzhykov, and S. Fritzsche, Resonant two-photon ionization of atoms by twisted and plane-wave light, Phys. Rev. A **102**, 063115 (2020).

[62] M. Marques and E. Gross, Time-dependent density functional theory, Annu. Rev. Phys. Chem. **55**, 427 (2004).

[63] See Supplemental Material at http://link.aps.org/supplemental/10.1103/PhysRevB.111.085114 for details on the harmonic oscillator parameters, validation of the implementation for the vector potential and the Helmholtz decomposition calculation, and analysis of the renormalization due to radiation reaction of density and near-field dynamics in plasmonic dimers.

[64] C. A. Ullrich, *Time-dependent Density-functional Theory: Concepts and Applications* (Oxford University Press, Oxford, 2011).

[65] V. Berestetskii, E. Lifshitz, and P. Pitaevskii, *Relativistic Quantum Theory, Part 1* (Pergamon, Oxford, 1971).

[66] A. M. Stewart, Vector potential of the Coulomb gauge, Eur. J. Phys. **24**, 519 (2003).

[67] N. Tancogne-Dejean, M. J. T. Oliveira, X. Andrade, H. Appel, C. H. Borca, G. Le Breton, F. Buchholz, A. Castro, S. Corni, A. A. Correa, U. De Giovannini, A. Delgado, F. G. Eich, J. Flick, G. Gil, A. Gomez, N. Helbig, H. Hübener, R. Jestädt, J. Jornet-Somoza *et al.*, Octopus, a computational framework for exploring light-driven phenomena and quantum dynamics in extended and finite systems, J. Chem. Phys. **152**, 124119 (2020).

[68] D. J. Griffiths, *Introduction to Electrodynamics* (Cambridge University Press, Cambridge, 2023).

[69] S. Ismail-Beigi, E. K. Chang, and S. G. Louie, Coupling of nonlocal potentials to electromagnetic fields, Phys. Rev. Lett. **87**, 087402 (2001).

[70] C. J. Pickard and F. Mauri, Nonlocal pseudopotentials and magnetic fields, Phys. Rev. Lett. **91**, 196401 (2003).

[71] D. Varsano, L. A. Espinosa-Leal, X. Andrade, M. A. L. Marques, R. di Felice, and A. Rubio, Towards a gauge invariant method for molecular chiroptical properties in TDDFT, Phys. Chem. Chem. Phys. **11**, 4481 (2009).

[72] P. A. Čerenkov, Visible radiation produced by electrons moving in a medium with velocities exceeding that of light, Phys. Rev. **52**, 378 (1937).

[73] I. Frank and Ig. Tamm, Coherent visible radiation of fast electrons passing through matter, in *Selected Papers*, edited by B. M. Bolotovskii, V. Ya. Frenkel, and R. Peierls (Springer, Berlin, Heidelberg, 1991), pp. 29–35.

[74] B. M. Bolotovskii, Vavilov–Cherenkov radiation: Its discovery and application, Phys. Usp. **52**, 1099 (2009).

[75] C. Roques-Carmes, N. Rivera, J. D. Joannopoulos, M. Soljačić, and I. Kaminer, Nonperturbative quantum electrodynamics in the cherenkov effect, Phys. Rev. X **8**, 041013 (2018).

[76] F. Hao, E. M. Larsson, T. A. Ali, D. S. Sutherland, and P. Nordlander, Shedding light on dark plasmons in gold nanorings, Chem. Phys. Lett. **458**, 262 (2008).

[77] M. Ludwig, G. Aguirregabiria, F. Ritzkowsky, T. Rybka, D. C. Marinica, J. Aizpurua, A. G. Borisov, A. Leitenstorfer, and D. Brida, Subfemtosecond electron transport in a nanoscale gap, Nat. Phys. **16**, 341 (2020).

[78] T. P. Rasmussen, A. Rodríguez Echarri, F. J. García de Abajo, and J. D. Cox, Nonlocal and cascaded effects in nonlinear graphene nanoplasmonics, Nanoscale **15**, 3150 (2023).

[79] S. Sanders, A. May, A. Alabastri, and A. Manjavacas, Extraordinary enhancement of quadrupolar transitions using nanostructured graphene, ACS Photon. **5**, 3282 (2018).

[80] S. Liu, F. P. Bonafe, H. Appel, A. Rubio, M. Wolf, and T. Kumagai, Inelastic light scattering in the vicinity of a single-atom quantum point contact in a plasmonic picocavity, ACS Nano **17**, 10172 (2023).

[81] M. Barbry, P. Koval, F. Marchesin, R. Esteban, A. G. Borisov, J. Aizpurua, and D. Sánchez-Portal, Atomistic near-field nanoplasmonics: Reaching atomic-scale resolution in nano-optics, Nano Lett. **15**, 3410 (2015).

[82] E. I. Albar, F. P. Bonafé, V. P. Kosheleva, S. T. Ohlmann, H. Appel, and A. Rubio, Time-resolved plasmon-assisted generation of optical-vortex pulses, Sci. Rep. **13**, 14748 (2023).

[83] D. Peller, C. Roelcke, L. Z. Kastner, T. Buchner, A. Neef, J. Hayes, F. Bonafé, D. Sidler, M. Ruggenthaler, A. Rubio, R. Huber, and J. Repp, Quantitative sampling of atomic-scale electromagnetic waveforms, Nat. Photon. **15**, 143 (2021).

[84] T. Siday, J. Hayes, F. Schiegl, F. Sandner, P. Menden, V. Bergbauer, M. Zizlsperger, S. Nerreter, S. Lingl, J. Repp, J. Wilhelm, M. A. Huber, Y. A. Gerasimenko, and R. Huber, All-optical subcycle microscopy on atomic length scales, Nature (London) **629**, 329 (2024).

[85] C. A. Downing, E. Mariani, and G. Weick, Radiative frequency shifts in nanoplasmonic dimers, Phys. Rev. B **96**, 155421 (2017).

[86] C. A. Downing, E. Mariani, and G. Weick, Retardation effects on the dispersion and propagation of plasmons in metallic nanoparticle chains, J. Phys.: Condens. Matter **30**, 025301 (2018).

[87] K. Bedingfield and A. Demetriadou, On the excitation and radiative decay rates of plasmonic nanoantennas, Nanophotonics **11**, 2271 (2022).

[88] U. Kreibig and M. Vollmer, *Optical Properties of Metal Clusters* (Springer Science & Business Media, New York, 2013), Vol. 25.

[89] L. D. Landau and E. M. Lifshitz, *The Classical Theory of Fields*, Course of Theoretical Physics, Vol. 2 (Pergamon Press, Oxford, 1975).

3 Cavity materials engineering: shaping materials with quantum vacuum fluctuations (QED)

Nel mezzo del cammin di nostra vita
mi ritrovai per una selva oscura[1]
- Inferno I, Divina Commedia, D. Alighieri (1321)

When light interacts with matter, it is possible to study and predict a large variety of effects based on the physical setup of the system and on how strong the interaction is. For instance, in weakly-coupled systems, where the light-matter coupling strength is much smaller than the decay rates of matter and cavity, one primarily probes existing transitions and symmetries. Light is treated as a perturbation, and the response of the matter system is typically well described by linear theories [68, 109, 110], such as the Fermi Golden rule, or non-linear ones in the cases where the intensity of electromagnetic field is large [109].

Beyond the weak-coupling limit, perturbative descriptions break down, and fundamentally new physical behavior emerges from the hybridization of the electronic states in the material and the electromagnetic field. To accurately capture the properties of these strongly coupled systems, it becomes necessary to diagonalize the full light-matter Hamiltonian [15, 68], or to use other non-perturbative methods such as QEDFT [27]. The new states arising from the joint system are called polaritonic states, from the polariton, the quasi-particle associated with the light-matter interaction [34]. Polaritons are characterized by distinctive spectral signatures such as Rabi splittings and avoided band crossings, and provide a pathway for several application both in chemistry and in condensed matter. For instance in the former one can modify molecular polarizabilities [40, 41], inter-molecular properties [42] or reaction rates [43], while in the latter, one can control excitonic states [15, 44], enhance existing properties such as ferroelectricity or electron-phonon coupling [29, 45], induce new properties and phases in the material [16], or spark cavity-mediated non-local interactions [46].

As the natural strength of light–matter coupling is set by the fine-structure constant α and therefore cannot be tuned at will, achieving the strong-coupling regime requires enhancing the effective interaction. In practice, this is accomplished by engineering structured electromagnetic environments,

---

[1] *When half way through the journey of our life I found that I was in a gloomy wood.* Here the "gloomy wood", or in a more literal translation from Italian "dark wood", is a reference to the dark cavities described in this chapter. Eventually, Dante's gloomy wood will help him improve his life, like using dark cavities improves our understanding of QED systems.

such as cavities, resonators, or nanophotonic architectures, and by exploiting collective effects from the interaction with the same mode, both of which can significantly amplify the coupling strength. In particular, optical cavities provide a versatile platform to reach and control these regimes under well-defined and stable conditions. By confining the electromagnetic field between mirrors, first a cavity discretizes the spectrum into effective modes, defined by a polarization and spatial profile, and secondly it increases the field amplitude, which is inversely related to the effective mode volume. This results in a strong coupling even with a dim field, or with no field of at all (vacuum fluctuations). Controlling the mixing of matter states and the electromagnetic field is the subject of the emerging field of cavity materials engineering [33], which indeed exploits the light-matter interaction to control the properties of materials. Since quantum fluctuations become relevant, one should describe the radiation within the framework of quantum electrodynamics (QED). A central prediction in QED is that light and matter are coupled even in the absence of photons, due to the vacuum fluctuations. It is important to note that it is possible to engineer materials properties using both classical light (classically driven cavities) and quantum light (dark cavities), as it will be shown both in Publication II and III. Within quantum electrodynamics, an *ab initio*, nonrelativistic description of the light-matter interaction is given by the Pauli-Fierz Hamiltonian [10], written in Coulomb gauge. A detailed discussion on the Pauli-Fierz Hamiltonian is provided in Section 3.1.

Within this framework, it is possible to achieve cavity control of quantum materials by engineering the properties of the confined electromagnetic field. The structure of the cavity itself is an important tool for shaping such properties [35, 46]. In particular, an important distinction is whether the cavity is spatially unstructured or structured. The former is characterized by plain mirrors (e.g. a Fabry-Perot cavity) and the confined field can be modeled with a single effective mode which does not carry any momentum (also referred to as long-wavelength approximation). Structured cavities, on the other hand, present a modulation in the mirrors which selects only optical modes whose momentum is compatible with the spatial modulation. A more extensive discussion will be provided in Section 3.1.1. Both alternatives allow to achieve cavity control, as shown by Publication II, where a structured cavity allows to create an all-optical Moiré potential and to induce long-range exciton-exciton interactions, and by Publication III, where a chiral cavity is used to open a topological gap in Graphene. Conversely, unstructured cavities are used in Publication II to control excitonic localization. Furthermore, within the same type of cavity, one can control how the properties of the material are modified by either classically driving the optical cavity or operating in the dark-cavity regime (i.e., coupling to vacuum fluctuations). This is exemplified in Publication II, where driven cavities are used to create an all-optical Moiré potential while dark one to induce long-range exciton-exciton interactions. Finally, one also may exploit the polarization of the cavity modes [30]. This is shown in Publication III, where circularly polarized modes (chiral cavities) open an isotropic gap in Graphene, while linearly polarized modes may open a gap or not depending on whether one uses a single linearly polarized photon mode or two isotropic linearly polarized modes.

Building on these ideas, the present chapter develops cavity QED as a tool for materials engineering. Section 3.1 introduces the Pauli–Fierz Hamiltonian, laying the theoretical foundation. Furthermore, it discusses the differences between spatially structured and unstructured cavities. Section 3.2 presents the photon-free downfolding, a technique used both in Publication II and III to reveal the nature of cavity-mediated interactions. Section 3.3 presents Publication II, which shows that spatially structured cavities can produce an all-optical Moiré-like confinement of excitons without twisting and that, in dark cavities, vacuum fluctuations mediate long-range exciton–exciton interactions that renormalize masses and curvature. Section 3.4 presents Publication III, which presents a photon-free, self-consistent QED Hartree–Fock theory for Graphene and demonstrate substantial cavity-mediated renormalizations of Dirac states contingent on mode polarization.

All throughout this chapter, SI-based atomic units will be used.

3.1 The electromagnetic field in cavities and the semi-relativistic Pauli-Fierz Hamiltonian

The *ab initio* framework used in this chapter to describe light–matter interaction is the semi-relativistic limit of QED, using the Pauli–Fierz Hamiltonian [10, 35, 47]. Despite this equation can be formulated to accurately describe nuclei [49, 71] and systems with a relativistic energy [111], here the discussion will focus on electronic systems within the low-energy (non-relativistic) limit of quantum electrodynamics.

Before exploring the coupling between light and matter, it is important to properly describe the quantized electromagnetic field. The following discussion will assume the Coulomb gauge, hence all of the expressions for the vector potential refer to its transversal part. The longitudinal part of the vector potential does not couple to the matter, but leads to the matter-matter Coulomb interaction [112]. The transverse vector potential in free space can be formulated as [12, 35]:

$$\hat{\mathbf{A}}_{\text{free}}(\mathbf{r}) = \sqrt{\frac{2\pi}{V}} \sum_{\mathbf{q}\lambda} \frac{\boldsymbol{\epsilon}_{\mathbf{q}\lambda}}{\sqrt{\omega_{\mathbf{q}}}} e^{i\mathbf{q}\cdot\mathbf{r}} \left(\hat{a}_{\mathbf{q}\lambda} + \hat{a}^{\dagger}_{-\mathbf{q}\lambda} \right) \tag{3.1}$$

where V is the quantization volume, $\omega_{\boldsymbol{q}}$ is the energy of the mode with momentum $\boldsymbol{q}$, and $\boldsymbol{\epsilon}_{\boldsymbol{q},\lambda}$ is the polarization function. $\lambda = s, p$ indicates the polarization. The energy of the electromagnetic field is given by $\hat{H}_{EM} = \sum_{\boldsymbol{q},\lambda} \omega_{\boldsymbol{q}} \left(\hat{a}^{\dagger}_{\boldsymbol{q},\lambda} \hat{a}_{\boldsymbol{q},\lambda} + \frac{1}{2} \right)$, which corresponds to a set of harmonic oscillators, each associated to a mode function and a polarization [10]. Conversely, to describe the electromagnetic field confined by an ideal planar optical cavity (such as the Fabry-Perot one), only modes whose momentum in the confinement direction satisfies the standing-wave condition $q_z = n\frac{\pi}{L_c}, n \in \mathbb{N}$ are supported, where L_c is the length of the cavity in the direction of confinement (assumed to be the z direction). For realistic cavities instead, where the mirrors do not have a perfect reflectivity, the full mode function must be considered, which in general extends beyond the mirrors [35]. The vector potential in a Fabry-Perot cavity can then be formulated as [35]:

$$\hat{\mathbf{A}}(\mathbf{r}) = \frac{1}{\sqrt{V}} \sum_{\mathbf{q}_{\parallel},\lambda} \sum_{q_z,\alpha} A_{0\mathbf{q}} e^{i\mathbf{q}_{\parallel}\cdot\mathbf{r}} \left(\mathbf{M}_{\mathbf{q}_{\parallel}\lambda,q_z\alpha}(z) \hat{a}_{\mathbf{q}_{\parallel}\lambda,q_z\alpha} + \mathbf{M}^{*}_{-\mathbf{q}_{\parallel}\lambda,q_z\alpha}(z) \hat{a}^{\dagger}_{-\mathbf{q}_{\parallel}\lambda,q_z\alpha} \right) \tag{3.2}$$

where $\boldsymbol{q}_{\parallel}$ is the in-plane momentum of the mode, α is a top-bottom propagation index and $\boldsymbol{M}_{\mathbf{q}_{\parallel}\lambda,q_z\alpha}(z)$ is the mode function encoding the effect of the Fabry-Perot cavity.

The Pauli-Fierz Hamiltonian couples light and matter by the minimal coupling prescription, performed through the canonical momentum substitution $\hat{\boldsymbol{p}} \rightarrow \hat{\boldsymbol{p}} + \hat{\boldsymbol{A}}$. This type of coupling ensures the charge continuity by satisfying the local $\mathcal{U}(1)$ invariance and implies that the charge current in the Dirac equation [19] is the source of the quantized electromagnetic field and, at the same time, the radiation field modifies the momentum of the Dirac fields [10]. This is the quantum equivalent of the full minimal coupling prescription described in Section 2.1. The formulation of the second-quantized Pauli-Fierz Hamiltonian for a condensed matter system embedded in an optical cavity reads [35]:

$$
\begin{aligned}
&\hat{H}_{\mathrm{PF}} = \hat{H}_{\mathrm{EM}} + \hat{H}_{\mathrm{el}} + \frac{1}{\sqrt{V}} \sum_{ij\sigma\boldsymbol{k}_{\parallel}} \sum_{\boldsymbol{q}_{\parallel},\lambda} \sum_{q_z,\alpha} \int_{\Omega_z} dz\, \hat{c}^{\dagger}_{i\boldsymbol{k}_{\parallel}+\boldsymbol{q}_{\parallel},\sigma} \hat{c}_{j\boldsymbol{k}_{\parallel},\sigma} A_{0\boldsymbol{q}_{\parallel}q_z} \boldsymbol{p}_{ij\sigma\boldsymbol{k}_{\parallel}\boldsymbol{q}_{\parallel}q_z}(z) \cdot \\
&\left[\boldsymbol{M}_{\boldsymbol{q}_{\parallel}\lambda,q_z\alpha}(z)\hat{a}_{\boldsymbol{q}_{\parallel}\lambda,q_z\alpha} + \boldsymbol{M}^{*}_{-\boldsymbol{q}_{\parallel}\lambda,q_z\alpha}(z)\hat{a}^{\dagger}_{-\boldsymbol{q}_{\parallel}\lambda,q_z\alpha}\right] + \\
&\frac{1}{2V} \sum_{ij\sigma\boldsymbol{k}_{\parallel}} \sum_{\boldsymbol{q}_{\parallel},\boldsymbol{q}'_{\parallel},\lambda\lambda'} \sum_{q_z q'_z,\alpha\alpha'} \int_{\Omega_z} dz\, \hat{c}^{\dagger}_{i\boldsymbol{k}_{\parallel}+\boldsymbol{q}_{\parallel}+\boldsymbol{q}'_{\parallel},\sigma} \hat{c}_{j\boldsymbol{k}_{\parallel},\sigma} A_{0\boldsymbol{q}_{\parallel}q_z} A_{0\boldsymbol{q}'_{\parallel}q'_z} s_{ij\sigma\boldsymbol{k}_{\parallel}\boldsymbol{q}_{\parallel}\boldsymbol{q}'_{\parallel}}(z) \cdot \\
&\left[\boldsymbol{M}_{\boldsymbol{q}_{\parallel}\lambda,q_z\alpha}(z)\hat{a}_{\boldsymbol{q}_{\parallel}\lambda,q_z\alpha} + \boldsymbol{M}^{*}_{-\boldsymbol{q}_{\parallel}\lambda,q_z\alpha}(z)\hat{a}^{\dagger}_{-\boldsymbol{q}_{\parallel}\lambda,q_z\alpha}\right] \cdot \left[\boldsymbol{M}_{\boldsymbol{q}'_{\parallel}\lambda',q'_z\alpha'}(z)\hat{a}_{\boldsymbol{q}'_{\parallel}\lambda',q'_z\alpha'} + \boldsymbol{M}^{*}_{-\boldsymbol{q}'_{\parallel}\lambda',q'_z\alpha'}(z)\hat{a}^{\dagger}_{-\boldsymbol{q}'_{\parallel}\lambda',q'_z\alpha'}\right]
\end{aligned}
\tag{3.3}
$$

where $\hat{c}^{\dagger}$ ($\hat{c}$) are electronic creation (annihilation) operators, Ω_z is the matter unit cell in the z direction, $\boldsymbol{p}_{ij\sigma\boldsymbol{k}_{\parallel}\boldsymbol{q}_{\parallel}q_z}(z)$ is the momentum matrix element and $s_{ij\sigma\boldsymbol{k}_{\parallel}\boldsymbol{q}_{\parallel}\boldsymbol{q}'_{\parallel}}(z)$ is the overlap matrix element (cf. Ref. [35] for the definitions). In this equation, the first two terms represent the uncoupled light and matter Hamiltonian. Next, one finds the bilinear coupling (paramagnetic term), which is proportional to $\boldsymbol{p} \cdot \boldsymbol{A}$ and couples the transverse field to the electronic current. It allows the electromagnetic field to create or annihilate matter excitations by coupling the ground state to excited states and it scatters existing excitations across momentum space by exchanging cavity photons. Finally, the last term is the diamagnetic term, proportional to $\boldsymbol{A}^2$. It couples to the electronic density and dresses the photon sector by renormalizing mode frequencies and amplitudes. It guarantees that the Hamiltonian is bounded from below, ensuring the existence of a ground state. Diagonalizing the Hamiltonian 3.3, which in the context of the strong-coupling regime (typical of optical cavities) is typically done through exact diagonalization, gives access to the polaritonic states. However, despite the quantization condition imposed by the cavity mirrors, Eq. 3.3 contains an infinite sum of cavity modes, mutually coupled by the diamagnetic term, making the numerical treatment challenging.

To overcome this, one can operate in the long-wavelength approximation (LWA), as well as using an effective mode formalism. An in-depth description of the two can be found in Ref. [35]. Within the LWA, the sums over the indexes $\boldsymbol{q}_{\parallel}$ and q_z reduce to only a few modes whose momentum is smaller than a cutoff which depends on the matter system [35]. Furthermore, small momenta in the z direction imply that the field appears uniform across the thickness of the material embedded in the cavity, while small in-plane momenta imply that the field is almost uniform across an extended number of unit cells in the plane. Hence it is possible to remove the integrals. Considering only modes with $\boldsymbol{q}_{\parallel} \to \boldsymbol{0}$ also implies that there is no momentum transfer between the electromagnetic field and the matter, meaning that only transitions which are vertical in the k-space are allowed. The LWA is used both in Publication II and III. While the latter uses only a single effective mode at $\boldsymbol{q}_{\parallel} = 0$ (which still carries the weight of a continuum of modes), publication II uses a structured optical cavity, which does not support a mode at $\boldsymbol{q}_{\parallel} = 0$, but rather two effective modes such that $\boldsymbol{q}_{\parallel,1} = -\boldsymbol{q}_{\parallel,2}$ allowing a momentum transfer between light and matter (cf. Section 3.1.1). Subsequently, the effective mode formalism indicates a grouping of cavity modes, such that the resulting effective one represents a summation over a continuum of modes centered around a certain in-plane momentum $\boldsymbol{q}_{\parallel}$. One of the results that follows from it, is that it allows to drop the summation over q_z completely, further simplifying the solution of the Pauli-Fierz Hamiltonian. Working with effective modes is necessary to guarantee a finite light-matter coupling strength in the bulk limit of extended cavity-matter systems when working with a finite number of modes for the description of the electromagnetic field.

3.1.1 Spatially structured and unstructured optical cavities

Accounting for the shape of the optical cavity is essential to correctly formulate the Pauli-Fierz Hamiltonian for the setup that one is interested in studying. A key distinction is the usage of structured or unstructured cavities, as it is extensively exemplified by Publication II. In this work a spatially unstructured cavity is characterized by plain mirrors which confine the electromagnetic field and embed the matter system, while a spatially structured cavity presents a modulation in the mirrors.

A typical example of spatially unstructured cavity is the Fabry-Perot one. Within the LWA, when describing this system one considers only a single effective mode characterized by $\boldsymbol{q}_{\parallel} = \mathbf{0}$ and energy $\omega = cq_z$, where c is the speed of light and $q_z = \frac{\pi}{L_z}$. Note that in principle the number of modes entering the description of the effective mode depends on the cavity finesse [35]. While this is an important aspect to link theoretical and experimental results, one often takes the limit where the mirrors have perfect reflectivity, hence $\mathcal{F} \to \infty$, as it allows to properly quantify the mode strength [35].

Spatially structured cavities, on the other hand, are fabricated in such a way that they sustain cavity modes with finite momentum. This can be realized in different ways, such as by implementing a modulation of the mirrors (cf. Fig. 1d of Publication II) or by introducing a dielectric grating [113]. The effect is that an optical lattice is created, which selects only the effective modes whose in-plane momentum is compatible with the periodicity of the lattice. This is especially interesting when dealing with condensed matter systems, as it allows to transfer momentum between the cavity modes and the matter, hence allowing non-vertical transition in the k-space. Publication II exploits this and shows that using a structured cavity it is possible to create all-optical Moiré-like phenomena and induce long-range exciton-exciton interactions. However, structured cavities are more complicated to simulate, and to fabricate (due to the spatial modulation required). For instance, a cavity with a 1D grating (such as in Publication II) will generate an optical lattice supporting both a mode with momentum $\boldsymbol{q}_{\parallel}$ and, for symmetry, a mode with $-\boldsymbol{q}_{\parallel}$. Thus, one should consider at least two modes (although more complicated lattices may required the inclusion of more modes).

Aside from the momentum one can also structure a cavity to control the polarization of the effective modes. As in the case of structured and unstructured cavities, the mirrors control the type of polarization [30]. For instance, by attaching a Faraday rotator to the mirror it is possible to create a chiral cavity, which is an effective way of breaking time-reversal symmetry. As shown by Publication III, controlling the polarization allows to control topological properties of the material, such as the opening of an optical gap in Graphene. Even more strikingly, Publication III shows linearly polarized modes in anisotropic (single-mode) cavities open a gap at the Dirac points in Graphene.

3.1.2 Optically driven cavities

In the literature of theoretical cavity materials engineering, one typically couples materials to dark cavities, meaning that no photons are confined and the coupling happens through the quantum vacuum fluctuations [15, 16, 29, 33, 45, 46, 114]. However, dark cavities remain experimentally challenging as obtaining a sizable effect only due to vacuum fluctuation requires large light-matter couplings [54]. In order to achieve higher coupling regime, experiments can drive the cavities with classical fields [55], known as classically driven cavity. Within the framework of the Pauli-Fierz Hamiltonian, it is possible to utilize coherent states of light, which are known to be a good quantum representation of classical light [12].

First, to describe the driven system, the far field driving has to couple to the modes sustained by the cavity ($\boldsymbol{q}_{\parallel} = \boldsymbol{0}$ for unstructured cavities and finite momentum $\pm\boldsymbol{q}_{\parallel}$ via the grating for structured ones). Here I will discuss the case of a structured cavity with a 1D grating, able to sustain two cavity modes as in Publication II, but the discussion can trivially be extended to a single-mode cavity at $\boldsymbol{q}_{\parallel} = \boldsymbol{0}$ (cf. Publication III). To model classical radiation, the photonic creation and annihilation operators shall be replaced by their mean-field value. A possible choice is to model this excitation for single-polarization ($\lambda = s$) modes as a time-dependent coherent state $|\tilde{\lambda}_{\boldsymbol{q}_{\parallel}}\tilde{\lambda}_{-\boldsymbol{q}_{\parallel}}(t)\rangle = |\tilde{\lambda}_{\boldsymbol{q}_{\parallel}}(t)\rangle \otimes |\tilde{\lambda}_{-\boldsymbol{q}_{\parallel}}(t)\rangle$, where $|\tilde{\lambda}_{\boldsymbol{q}_{\parallel}}(t)\rangle = e^{-\frac{i\omega_{\boldsymbol{q}_{\parallel}}t}{2}}|e^{-i\omega_{\boldsymbol{q}_{\parallel}}t}\tilde{\lambda}_{\boldsymbol{q}_{\parallel}}\rangle$ and the last ket goes by the usual definition $|\alpha\rangle = e^{-\frac{|\alpha|^2}{2}}\sum_{s=0}^{\infty}\frac{\tilde{\alpha}^s}{\sqrt{s!}}|s\rangle$ of coherent states. Then, writing thew coherent state explicitly leads to:

$$|\tilde{\lambda}_{\boldsymbol{q}_{\parallel}}\tilde{\lambda}_{-\boldsymbol{q}_{\parallel}}(t)\rangle = e^{-\frac{i\left(\omega_{\boldsymbol{q}_{\parallel}}+\omega_{-\boldsymbol{q}_{\parallel}}\right)t}{2}}|e^{-i\omega_{\boldsymbol{q}_{\parallel}}t}\tilde{\lambda}_{\boldsymbol{q}_{\parallel}}, e^{-i\omega_{-\boldsymbol{q}_{\parallel}}t}\tilde{\lambda}_{-\boldsymbol{q}_{\parallel}}\rangle \tag{3.4}$$

And the action of an annihilation operators reads:

$$\hat{a}_{\boldsymbol{q}_{\parallel}}\left|\tilde{\lambda}_{\boldsymbol{q}_{\parallel}}\tilde{\lambda}_{-\boldsymbol{q}_{\parallel}}(t)\right\rangle = \tilde{\lambda}_{\boldsymbol{q}_{\parallel}}e^{-\frac{i\left(3\omega_{\boldsymbol{q}_{\parallel}}+\omega_{-\boldsymbol{q}_{\parallel}}\right)t}{2}}\left|\tilde{\lambda}_{\boldsymbol{q}_{\parallel}}, e^{-i\omega_{-\boldsymbol{q}_{\parallel}}t}\tilde{\lambda}_{-\boldsymbol{q}_{\parallel}}\right\rangle$$

Next, one should project the Pauli-Fierz Hamiltonian onto the coherent state basis by computing:

$$\hat{H}^{\mathrm{cl}}_{\mathrm{PF}} = \langle\tilde{\lambda}_{\boldsymbol{q}_{\parallel}}\tilde{\lambda}_{-\boldsymbol{q}_{\parallel}}(t)|\hat{H}_{\mathrm{PF}}|\tilde{\lambda}_{\boldsymbol{q}_{\parallel}}\tilde{\lambda}_{-\boldsymbol{q}_{\parallel}}(t)\rangle \sim H^{(n=0)} + H^{(n=1)}e^{i\omega_{\boldsymbol{q}_{\parallel}}t} + H^{(n=-1)}e^{-i\omega_{\boldsymbol{q}_{\parallel}}t} \tag{3.5}$$

where $H^{(n=0)}$ is the projection of the uncoupled Hamiltonian and $H^{(n=\pm1)}$ is the time-*independent* projection of the interaction Hamiltonian onto the coherent state, with n the Floquet frequency index. $\hat{H}^{\mathrm{cl}}_{\mathrm{PF}}$ does not contain any photonic creation or annihilation operator, hence now the Hamiltonian is purely defined on a matter excitation basis. However, $\hat{H}^{\mathrm{cl}}_{\mathrm{PF}}$ is time-dependent, which means that it cannot be directly diagonalized. Note that for our structured optical cavity one can assume that $\omega_{\boldsymbol{q}_{\parallel}} = \omega_{-\boldsymbol{q}_{\parallel}}$.

Since the obtained Hamiltonian is time periodic, one can use the Floquet theory to solve $\hat{H}^{\mathrm{cl}}_{\mathrm{PF}}$ [30, 115]. The advantage of this approach is that the Floquet Hamiltonian is time independent, which makes it computationally cheaper while still being able to capture the polaritonic effects from the light-matter coupling. In fact, previous works show that using the Floquet can correctly capture the opening of optical gaps in Graphene or Weyl semimetals [82, 116]. Note that in the high-frequency limit the contribution from $H^{(n=\pm1)}$ vanishes for $\omega \to \infty$, as it can be shown by taking the Van Vleck expansion [115]:

$$H_{\mathrm{eff}} = H^{(n=0)} + \frac{\left[H^{(n=-1)}, H^{(n=1)}\right]}{\omega} + \mathcal{O}\left(\frac{1}{\omega^2}\right) \tag{3.6}$$

This can be understood by imagining that the Floquet theory builds many replicas of the uncoupled problem, shifted in energy by $\pm\omega_{\boldsymbol{q}_{\parallel}}$. Hence, if $\omega_{\boldsymbol{q}_{\parallel}}$ is small (in the range of few tens of meV) these replicas will be close in energy and they will mix more [30, 82].

In Publication II, this technique is used to highlight that light with finite momentum $\pm\boldsymbol{q}_{\parallel}$ enters the coupled Hamiltonian as the potential created by a Moiré super-lattice, by generating interacting Floquet replicas.

3.2 Photon-free formulation through Hamiltonian downfolding

The Pauli–Fierz Hamiltonian provides a fully quantized description of coupled light–matter systems, and its diagonalization gives access to the polaritonic eigenstates. However, there are cases when it is convenient not to perform a direct exact diagonalization. A first motivation come from cases where the matrix representation of the Pauli-Fierz Hamiltonian is too large. In fact, a common choice for representing such Hamiltonian is to project it to a base which is the tensor product of a basis where the matter problem is diagonal and a basis where the photonic problem is diagonal. As electrons in condensed matter can be described by Slater determinants, a suitable basis is to consider a Slater determinant representing the ground state and one singly-excited Slater determinant for each possible excitation. Thus one has $\{|\Psi_{GS}\rangle, |\Psi_{ex,1}\rangle, \cdots |\Psi_{ex,n}\rangle\}$. As for the photon, as each cavity mode is an effective harmonic oscillator a natural choice is a set of Fock number states: $\{|0\rangle, |1\rangle, \cdots\}$. Thus the full basis is given by:

$$\{|\Psi_{GS}\rangle, |\Psi_{ex,1}\rangle, \cdots |\Psi_{ex,n}\rangle\} \otimes_{\boldsymbol{q}_{\|}} \{|0\rangle, |1\rangle, \cdots\}_{\boldsymbol{q}_{\|}} \tag{3.7}$$

The matrix resulting from the representation of the Hamiltonian in this basis can become large, especially for condensed matter system where large k-points grids must be used to describe particular feature. A notable example is Graphene, which requires a dense grid around the Dirac point to capture the linear dispersion. Section 4.3 of Ref [81] describes this problem in more details. Handling such large matrices is computationally expensive, and it makes the investigation process slow. A second motivation for not directly diagonalizing a QED matrix is that due to the complexity in the mixing between the matter and the photonic state, it can be difficult to gain a physical intuition of the the processes that are happening just by looking at the resulting polaritonic states.

An effective solution for this problem comes from the Hamiltonian downfolding method in the dressed photon space [14, 16]. This approach allows to define an effective Hamiltonian, composed only of the zero photon sector, that contains the action of the full QED Hamiltonian [16]. The first-order expansion of such an approximation for a system with N modes can be written as:

$$\begin{aligned}\hat{H}_{\text{eff}} = {} & \langle 0_1, \cdots, 0_N | \hat{H} | 0_1, \cdots, 0_N \rangle - \\ & \sum_{\alpha}^{N} \frac{1}{\omega_\alpha} \Big[\langle 0_1, \cdots, 0_N | \hat{H} | 0_1, \cdots, 1_\alpha, \cdots, 0_N \rangle \cdot \langle 0_1, \cdots, 1_\alpha, \cdots, 0_N | \hat{H} | 0_1, \cdots, 0_N \rangle \Big] + \mathcal{O}\left(\frac{1}{\omega^2}\right)\end{aligned} \tag{3.8}$$

where $\hat{H}$ is the Hamiltonian one wants to approximate. In practice, this method integrates out the photonic modes, leaving an effective Hamiltonian which is defined only on the basis of the matter transitions ($\{|\Psi_{GS}\rangle, |\Psi_{ex,1}\rangle, \cdots |\Psi_{ex,n}\rangle\}$). For this reason it is also called *photon-free* formulation. Although the first-order expansion is perturbative, and no feedback on the light is included, this methods allows to retrieve non-perturbative features of the light-matter interaction. Note that for this expansion to be valid, the dressed mode energy ω_α should be large enough compared to the relevant matter transitions. Under these conditions, virtual photon exchange dominates and real photons are not populated in the ground state. Conversely, in the low-frequency regime one should proceed with the full diagonalization of the Pauli-Fierz Hamiltonian. Moreover, the lower the frequency the more important it becomes to include higher Fock states. In fact, considering a single effective mode Pauli-Fierz Hamiltonian and by computing the the energy dispersions associated to the Fock states one has:

$$E_n = \langle n| \hat{H}_{PF} |n\rangle = \omega_{\boldsymbol{q}_\parallel} \left(n_{\boldsymbol{q}_\parallel} + \frac{1}{2} \right) + \frac{A^2_{0,\boldsymbol{q}_\parallel}}{2V_{\text{eff},\boldsymbol{q}_\parallel}} \left(n_{\boldsymbol{q}_\parallel} + \frac{1}{2} \right) \tag{3.9}$$

Thus,

$$E_1 = \frac{3}{2}\omega_{\boldsymbol{q}_\parallel} + \frac{3A^2_{0,\boldsymbol{q}_\parallel}}{2V_{\text{eff},\boldsymbol{q}_\parallel}}, \quad E_2 = \frac{5}{2}\omega_{\boldsymbol{q}_\parallel} + \frac{5A^2_{0,\boldsymbol{q}_\parallel}}{2V_{\text{eff},\boldsymbol{q}_\parallel}}$$

from which one can see that if $\omega_{\boldsymbol{q}_\parallel}$ is small, E_1 and E_2 are close, hence an appropriate description of the electromagnetic field should include the Fock state $|2\rangle$ as well.

The Hamiltonian downfolding technique was used in both Publication II and Publication III to reveal cavity-mediated interactions in two-dimensional materials. Publication II used downfolding in the excitonic sector to expose how structured dark cavities mediate exciton–exciton interactions. Starting from a low-energy excitonic representation obtained by solving the Mott–Wannier equation in momentum space, the bilinear light–matter contains a term that creates excitons from the ground state, and a term that scatters existing excitons between different momenta by exchanging cavity photons. Downfolding the Hamiltonian produced an effective four-operator term in the excitonic Hamiltonian, coupling pairs of excitons at momenta separated by the cavity-mode momentum and leading to long-range interactions. Conversely, under classical driving the same bilinear scattering mechanism acts as an optical Moiré potential, folding the excitonic bands and opening miniband gaps without twisting the heterostructure. Publication III applied downfolding to the electronic sector of Graphene to construct a photon-free QED–HF theory. After dressing the mode by the diamagnetic term and projecting onto the zero-photon manifold, the effective Hamiltonian contains the local velocity-renormalizing term and the nonlocal electron–electron term discussed above. Solving this Hamiltonian self-consistently in a Hartree–Fock approximation yields cavity-renormalized Dirac bands that depend sensitively on mode polarization.

3.3 Publication II: Cavity-QED-controlled two-dimensional Moiré Excitons without twisting

State of the art

Two-dimensional van der Waals materials, especially transition metal dichalcogenides (TMDs), are characterized by strongly bound excitons. Traditionally twist engineering [117, 118], a technique in which atomically thin TMD layers are stacked with a predefined twist angle, has been used to achieve spatial control of excitons and consequent modification of their optical activity [119]. Changing the twist angle modifies the Moiré potential, which allows to control the excitons. However, in reality twist engineering allows to select only a specific angle, which is determined when the heterostructure is fabricated. As excitons in van der Waals heterostructures can be strongly coupled to confined light in optical cavities (forming hybrid exciton–polaritons) [15], exploiting the light-matter interaction to achieve excitonic control similar to twist engineering is an interesting challenge. Most cavity studies in the context of cavity QED have focused on planar Fabry–Perot geometries operating in the long-wavelength approximation [15, 35], where the cavity mode carries negligible in-plane momentum and couples vertically in k-space. However, to emulate the effect of the Moiré potential, one has to allow a momentum transfer between the electromagnetic field and the excitons, meaning that one has to relax the long-wavelength approximation. Moreover it is necessary to utilize two effective modes, which poses numerical challenges.

Main findings

This work proposes spatially structured optical cavities as an all-optical route to Moiré-like exciton confinement in bilayer transition-metal dichalcogenide (TMD) heterostructures (e.g., $MoSe_2/WSe_2$) without mechanical twisting. The cavity structuring provides controlled momentum transfer between photons and excitons, creating an optical lattice that effectively mimics a Moiré potential and reshapes the excitonic Brillouin zone. In classically driven structured cavities, this engineered lattice produces exciton confinement analogous to that in twisted systems. Strikingly, even in dark structured cavities, quantum vacuum fluctuations alone generate nonlocal exciton–exciton interactions and renormalize the exciton effective mass. Together, these results establish structured cavities as a versatile platform for engineering excitonic confinement, topology, and optical response in 2D materials.

Status and Publication details

This paper was published in *Nature Communications* in December 2025 [50]. The supplementary information is available at https://static-content.springer.com/esm/art%3A10.1038%2Fs41467-025-67570-2/MediaObjects/41467_2025_67570_MOESM1_ESM.pdf (not included in the present thesis).

Contribution

I derived the theory, developed all the code, performed all simulations, analyzed the data, interpreted the results and wrote the paper. All authors contributed to the revision of the manuscript. A detailed list of each author's contribution can be found at the end of the publication.

nature communications

Article

https://doi.org/10.1038/s41467-025-67570-2

Cavity-QED-controlled two-dimensional Moiré excitons without twisting

Received: 5 August 2025

Accepted: 3 December 2025

Francesco Troisi [1], **Hannes Hübener** [1], **Angel Rubio** [1,2] & **Simone Latini** [1,3]

We propose an all-optical Moiré-like exciton confinement by means of spatially periodic optical cavities. Such periodic photonic structures can control the material properties by coupling the matter excitations to the confined photons and their quantum fluctuations. We develop a low energy non-perturbative quantum electro-dynamical description of strongly coupled excitons and photons at finite momentum transfer. We find that in the classical limit of a laser driven cavity the induced optical confinement directly emulates Moiré physics. In a dark cavity instead, the sole presence of quantum fluctuations of light generates a sizable renormalization of the excitonic bands and effective mass. We attribute these effects to long-range cavity-mediated exciton-exciton interactions which can only be captured in a non-perturbative treatment. With these findings we propose spatially structured cavities as a promising avenue for cavity material engineering.

Two-dimensional van der Waals materials have emerged as a versatile platform for opto-electronic devices thanks to their highly tunable properties, such as optical and electronic band gaps and dielectric response[1–5]. Among this class of materials, transition metal dichalcogenides (TMDs) have attracted particular interest due to their strongly bound excitons and related optical activity in the visible range[6–8]. Excitons do indeed dominate the dynamics of several phenomena of TMDs, such as valley polarization and non-linear optical response[9,10]. Hence, controlling the behavior of excitons offers a direct route to program optical functionalities in this class of materials. Twist engineering[11–13], a technique in which atomically thin TMD layers are stacked with a predefined twist angle, allows for spatial control of excitons and consequent modification of their optical activity[14]. This is possible because twisting two-dimensional (2D) crystals with respect to each other leads to the formation of Moiré patterns, which generate spatially periodic electrostatic potentials strong enough to influence the motion and confinement of the otherwise free excitons, c.f. Fig. 1a. Aside from excitonic control, twist engineering, also dubbed twistronics, allows for generating novel quantum phases[5,15], including correlated insulator states[16], unconventional superconductivity[12], and fractional Chern insulators[17].

In this work, we propose an alternative strategy for spatial confinement of excitons that utilizes optical cavities instead of twist engineering. Optical cavities confine the electromagnetic field in a small volume, strengthening its intensity and making it possible to strongly couple to excitons of embedded TMDs. Such interaction can in turn lead to the formation of exciton-polaritons[18–22]. Previous works show that due to the strong light-matter interaction, planar optical cavities allow the control of the creation and mixing of polaritons made of composite excitons[18], as well as excitons, phonon and photon quasi-particles, the so-called phonoriton[23]. Cavity confinement not only alters the excitonic spectrum[24,25] but can also give rise to new equilibrium quantum phases due to the coupling of the host material with the vacuum fluctuations of light[26–33]. Here, we propose using spatially structured optical cavities, such as those sketched in Fig. 1, to produce an all-optical Moiré-like exciton confinement without twisting. This is a different paradigm compared to previous works that deal with exciton-polaritons in grated systems as they aim to reshape the properties of emitted light[20,34]. With our approach, instead, we demonstrate that we can control the matter properties by specifically structuring the excitonic quasi-particle, using both quantum fluctuations and classical fields.

---

[1]Max Planck Institute for the Structure and Dynamics of Matter and Center for Free-Electron Laser Science, Hamburg, Germany. [2]Initiative for Computational Catalysis (ICC), The Flatiron Institute, New York, NY, USA. [3]Department of Physics, Technical University of Denmark, Kgs. Lyngby, Denmark. e-mail: francesco.troisi@mpsd.mpg.de; hannes.huebener@mpsd.mpg.de; angel.rubio@mpsd.mpg.de; simola@dtu.dk

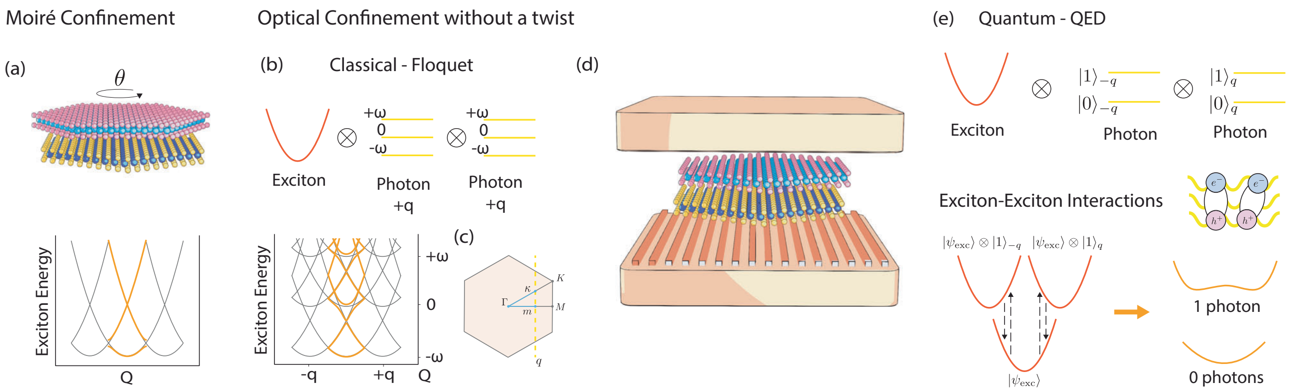

Fig. 1 | Schematics of the Moiré band formation and cavity-mediated interaction in a TMD bilayer heterostructure. a A structural twisted bilayer TMD heterostructure forms a Moiré super-lattice, leading to spatial modulation of the excitonic states. **b** Untwisted heterostructure embedded into a classically driven spatially structured cavity, the light-matter interaction generates an all-optical Moiré potential. **c** Representation of the *k*-points path used in the spectral function. We use the standard $M-\Gamma-K$ path, which we shorten to $m-\Gamma-\kappa$, where m, κ are taken at the value of the photon momentum along the aforementioned path. **d** Representation of an untwisted TMD heterostructure embedded in a spatially structured optical cavity. **e** When the heterostructure is untwisted (no standard Moiré potential) and embedded into a dark spatially structured cavity (where the vacuum fluctuation plays a role), light-matter coupling mediates exciton-exciton interactions and renormalizes the excitonic mass.

We analyze the role of cavity-mediated interactions in a prototypical type-II MoSe$_2$/WSe$_2$ heterostructure embedded in a planar cavity setup. We consider both an unstructured planar cavity and a structured (grated) cavity. The former can be described as a single effective mode of the electromagnetic field, where light carries no momentum, while the latter requires a multi-mode description and allows for momentum transfer between light and matter. Our theoretical framework builds, on the one hand, on the methodology for the first-principles treatment of excitons in Moiré potentials established in ref. 14 and on the other hand, on a low-energy quantum electrodynamical (QED) Hamiltonian approach for the coupling of excitons to the cavity[18,35]. More specifically, we solve the Mott–Wannier equation in momentum space to obtain the low-energy excitonic states. Subsequently, we derive a low-energy QED Hamiltonian that can describe both the electrostatic Moiré potential arising from twisting the bilayer and the coupling to the photonic modes by using an excitonic representation of the many-body QED problem. Finally, we perform the full diagonalization of the QED Hamiltonian to obtain the hybrid exciton-polariton states, from which we predict the excitonic dispersion, via the excitonic spectral function, and the optical properties of the cavity-matter system by computing the interacting optical linear absorption spectra.

We find that spatially unstructured cavities, where the electromagnetic field carries no momentum, can alter the twist-induced excitonic confinement from the Moiré potential when the cavity mode is resonant with the excitonic transition. This result is in agreement with previous works[36], where they applied a Hopfield diagonalization to a tight-binding model to study how bare photonic and excitonic states contribute to exciton-polariton states in unstructured Fabry–Perot cavities at different twist angles. We show that the same result can be obtained using a more general theory, starting with a first-principles QED Hamiltonian, and focusing on controlling the localization of exciton-polaritons. Conversely, spatially structured cavities, where momentum can be exchanged between light and matter, can induce optical confinement and emulate the Moiré potential when driven with a classical electromagnetic field (i.e., a laser), even in the *absence* of twist in the embedded bilayer. For dark spatially structured cavities, instead, where the light-matter coupling arises from the quantum fluctuations of the electromagnetic field inside the cavity, we find the emergence of cavity-induced exciton-exciton interactions in untwisted bilayers. This leads to both excitonic confinement and mass renormalization and consequently to a modification of the optical properties of the material in equilibrium, going beyond what is possible to achieve with twisting.

Results

Theory

To study the behavior of Moiré excitons in an optical cavity, we first model the two uncoupled systems (excitons and photons) and subsequently describe their interaction. Then, we formulate and discuss the QED Hamiltonian for Moiré excitons, which constitutes one of the main results of the paper. All throughout this work, we use atomic units.

The uncoupled matter Hamiltonian $\hat{H}_M$ of a twisted bilayer heterostructure can be formulated in an excitonic representation following ref. 14 as

$$\begin{aligned}\hat{H}_M = &\sum_{ll',\nu}\sum_{i\in C,j\in V}\sum_{\boldsymbol{Q}}\mathcal{E}^{\nu}_{ll',ij,\boldsymbol{Q}}\hat{X}^{\nu\dagger}_{ll',ij,\boldsymbol{Q}}\hat{X}^{\nu}_{ll',ij,\boldsymbol{Q}}\\ &+\sum_{ll',\nu}\sum_{i\in C,j\in V}\sum_{\boldsymbol{Q},\boldsymbol{q}}\mathcal{M}^{\nu}_{ll',ij,\boldsymbol{q}}\hat{X}^{\nu\dagger}_{ll',ij,\boldsymbol{Q}+\boldsymbol{q}}\hat{X}^{\nu}_{ll',ij,\boldsymbol{Q}}\end{aligned} \tag{1}$$

where i, j are band indexes which span over conduction (C) or valence (V) band states, and l, l' are layer indexes. The operators $\hat{X}^{\dagger}, \hat{X}$ create (annihilate) an exciton between any pair of bands of either the same layer (when $l = l'$, in which case one has intralayer excitons) or different layers (interlayer excitons), $\boldsymbol{Q}$ is the momentum associated with the center of mass of the exciton, and $\boldsymbol{q}$ is the momentum transferred by the Moiré potential. The index ν refers to the bound state (i.e., 1*s*, 2*s*...). $\mathcal{E}^{\nu}_{ll',ij,\boldsymbol{Q}} = \frac{\boldsymbol{Q}^2}{2m_{ll',ij}} + E_{g,ll'} + E^{\nu}_{b,ll'}$ encodes the dispersion relation of a free exciton, which we assume parabolic, where $m_{ll',ij}$ is the excitonic effective mass, $E_{g,ll'}$ is the energy gap and $E^{\nu}_{b,ll'}$ is the binding energy, which we obtain by solving the Mott–Wannier equation (c.f. Supplementary Information Section V.A). $\mathcal{M}$ is the matrix element of the Moiré potential in the excitonic basis, describing the Moiré scattering of excitons with different momenta. Note that $\mathcal{M}$ carries the information on the Mott–Wannier states (c.f. Supplementary Information Eq. A25). Refer to the Supplementary Information Section I for a detailed derivation.

We describe the uncoupled light system with a Hamiltonian consisting of a set of effective harmonic oscillators (the photon modes of the cavity):

$$\hat{H}_{ph} = \sum_{\bar{\boldsymbol{q}},\lambda} \omega_{\bar{\boldsymbol{q}}} \left(\hat{a}^{\dagger}_{\bar{\boldsymbol{q}},\lambda} \hat{a}_{\bar{\boldsymbol{q}},\lambda} + \frac{1}{2} \right) \tag{2}$$

where $\omega_{\bar{\boldsymbol{q}}}$ represents the energy of the photon mode $\bar{\boldsymbol{q}}$ and λ is the polarization. $\bar{\boldsymbol{q}}$ is the momentum of the photon in the *xy* plane of the 2D material. In a planar setup, electromagnetic waves propagate in the in-plane direction, while they are standing waves in the *z*-direction (which is orthogonal to the cavity mirrors). We assume that the matter couples with the in-plane component of the electric field and therefore only consider modes for which it is finite. The momentum of the photon in the *z*-direction is set by the standing wave condition for the fundamental cavity mode. Additionally, when a periodic grating is present, the *xy* plane momentum is finite and determined by the periodicity of the grating. When studying optical properties of materials in the far field, one usually makes the approximation that the light does not carry any momentum, the long-wavelength approximation (LWA). We recently showed that, also within a QED framework, the LWA is applicable[35] and reduces the description of the electromagnetic Hamiltonian to one with a single effective mode at $\bar{\mathbf{q}} = 0$. In practice, the LWA implies that an electron cannot scatter to another *k*-point following the absorption of a photon (vertical transition in $k-$ space). In contrast, if the cavity is spatially structured with a grating, the photon modes can acquire a finite momentum $\bar{\boldsymbol{q}}$ and couple matter excitations with different momenta. As shown later, this can give rise to a non-local interaction of excitons in *k*-space. Note that even though the construction of effective cavity modes is provided in ref. 35 is within the LWA, we here apply a similar procedure to construct the few effective collective modes in Eq. (2) for which the in-plane momenta are not averaged around $\bar{\mathbf{q}} = 0$, but around the finite momenta $\bar{\boldsymbol{q}}$ set by the cavity. We stress here that the term "effective", when referring to the cavity modes, indicates that such modes represent a summation over a continuum of modes centered around a certain momentum $\bar{\boldsymbol{q}}$. Working with effective modes is necessary to guarantee a finite light-matter coupling strength in the bulk limit of extended cavity-matter systems when working with a finite number of modes for the description of the electromagnetic field.

To describe the light-matter coupling, we start by performing the canonical momentum substitution $\hat{\boldsymbol{p}} \to \hat{\boldsymbol{p}} + \hat{A}$ to the uncoupled matter Hamiltonian, obtaining the second-quantized Pauli-Fierz Hamiltonian[35]. The Hamiltonian in the excitonic representation reads (c.f. the Supplementary Information Section I for the complete derivation):

$$\begin{aligned}\hat{H} = {} & \sum_{\bar{\boldsymbol{q}},\lambda} \omega_{\bar{\boldsymbol{q}}} \left(\hat{a}^{\dagger}_{\bar{\boldsymbol{q}},\lambda} \hat{a}_{\bar{\boldsymbol{q}},\lambda} + \frac{1}{2} \right) + \sum_{ll',\nu} \sum_{i\in C, j\in V} \sum_{\boldsymbol{Q}} \left(\mathcal{E}^{\nu}_{ll',ij,\boldsymbol{Q}} \hat{X}^{\nu\dagger}_{ll',ij,\boldsymbol{Q}} \hat{X}^{\nu}_{ll',ij,\boldsymbol{Q}} \right. \\ & \left. + \sum_{\boldsymbol{q}} \mathcal{M}^{\nu}_{ll',ij,\boldsymbol{Q}\boldsymbol{q}} \hat{X}^{\nu\dagger}_{ll',ij,\boldsymbol{Q}+\boldsymbol{q}} \hat{X}^{\nu}_{ll',ij,\boldsymbol{Q}} \right) + \sum_{\bar{\boldsymbol{q}},\lambda} \tilde{A}_{0,\bar{\boldsymbol{q}}} \sum_{ll',\nu} \sum_{i\in C, j\in V} \sum_{\boldsymbol{Q}} \\ & \left[\mathcal{B}^{\nu\lambda}_{ll',ij,\boldsymbol{Q}\bar{\boldsymbol{q}}} \hat{X}^{\nu\dagger}_{ll',ij,\boldsymbol{Q}+\bar{\boldsymbol{q}}} \hat{X}^{\nu}_{ll',ij,\boldsymbol{Q}} \left(\hat{a}^{\dagger}_{\bar{\boldsymbol{q}},\lambda} + \hat{a}_{-\bar{\boldsymbol{q}},\lambda} \right) \right. \\ & \left. + \mathcal{I}^{\nu,\lambda}_{ll',ij,\boldsymbol{Q}\bar{\boldsymbol{q}}} \hat{X}^{\nu\dagger}_{ll',ij,\bar{\boldsymbol{q}}} \left(\hat{a}^{\dagger}_{\bar{\boldsymbol{q}},\lambda} + \hat{a}_{-\bar{\boldsymbol{q}},\lambda} \right) + h.c. \right]\end{aligned} \tag{3}$$

where $\tilde{A}_{0,\bar{\boldsymbol{q}}} = \frac{A_{0,\bar{\boldsymbol{q}}}}{\sqrt{V_{\mathrm{eff},\bar{\boldsymbol{q}}}}}$, $A_{0,\bar{\boldsymbol{q}}}$ is the coupling strength of the mode $\bar{\boldsymbol{q}}$ and $V_{\mathrm{eff},\bar{\boldsymbol{q}}}$ is the effective mode volume. The first line of the Hamiltonian contains the uncoupled photon and the uncoupled matter, while the second represents the paramagnetic bilinear coupling between photon modes and excitons. Note that we absorbed the diamagnetic term into the uncoupled photon Hamiltonian by performing a Bogoliubov transformation[37,38]. $\mathcal{B}$ and $\mathcal{I}$ are the matrix elements describing the coupling to the matter momenta[35] in momentum-conserving exciton-photon interactions and are defined in Supplementary Information Section I.C. The former allows an exciton to scatter to another *k*-point after absorbing or emitting a photon, the implications of which will be discussed in depth in the next sections. Importantly, $\mathcal{B} = 0$ when $\bar{\boldsymbol{q}} = \mathbf{0}$ (see Supplementary Information Section V.C). The matrix elements $\mathcal{I}$ couple the material ground state to the light by creating an exciton. Hence, while the term $\mathcal{B}$ explicitly conserves the number of excitons, $\mathcal{I}$ deals with the creation or destruction of such particles. In order to access the polaritonic states via full diagonalization, the Hamiltonian in Eq. (3) is projected onto a combined light-matter product state, with excitonic states and the many-body ground state for the matter[18], which are written in a Slater determinant representation, and number states for each photonic mode. This basis keeps the N-particles electronic states explicit, so that even if the number of excitons is not conserved, the total number of particles is fixed.

In Eq. (3), we observe that the standard Moiré potential $\mathcal{M}$ and the first term of the bilinear coupling $\mathcal{B}$ share the same excitonic operators $\hat{X}^{\dagger}, \hat{X}$, in case $\bar{\boldsymbol{q}} = \boldsymbol{q}$. For the Moiré potential, $\boldsymbol{q}$ refers to the super-lattice Moiré periodicity. The bilinear coupling $\bar{\boldsymbol{q}}$ refers to the periodicity of the electromagnetic field inside the cavity. Despite having different physical meanings, both indices determine a lattice periodicity, which modifies the symmetry experienced by the excitons. To highlight this equivalence, we let $\bar{\boldsymbol{q}} = \boldsymbol{q}$ and rewrite the interaction terms of the Hamiltonian in Eq. (3) (which also includes the non-conserving bilinear coupling $\mathcal{I}$) as:

$$\begin{aligned}\hat{H}_{\mathrm{int}} = {} & \textstyle\sum_{ll',\nu} \sum_{i\in C, j\in V} \sum_{\boldsymbol{Q},\boldsymbol{q}} \left[\hat{X}^{\nu\dagger}_{ll',ij,\boldsymbol{Q}+\boldsymbol{q}} \hat{X}^{\nu}_{ll',ij,\boldsymbol{Q}} \right. \\ & \left(\mathcal{M}^{\nu}_{ll',ij,\boldsymbol{Q},\boldsymbol{q}} + \tilde{A}_{0,\boldsymbol{q}} \textstyle\sum_{\lambda} \mathcal{B}^{\nu\lambda}_{ll',ij,\boldsymbol{Q}\boldsymbol{q}} \left(\hat{a}^{\dagger}_{\boldsymbol{q},\lambda} + \hat{a}_{-\boldsymbol{q},\lambda} \right) \right) + \\ & \left. \tilde{A}_{0,\boldsymbol{q}} \textstyle\sum_{\lambda} \mathcal{I}^{\nu,\lambda}_{ll',ij,\boldsymbol{Q}\boldsymbol{q}} \hat{X}^{\nu\dagger}_{ll',ij,\boldsymbol{q}} \left(\hat{a}^{\dagger}_{\boldsymbol{q},\lambda} + \hat{a}_{-\boldsymbol{q},\lambda} \right) + h.c. \right]\end{aligned} \tag{4}$$

This similarity, and indeed mutual mathematical interchangeability, of the exciton-exciton interaction provided by the Moiré potential and the structured optical modes is the central theoretical result of this work. In the following section, we investigate the effect of $\hat{H}_{\mathrm{int}}$ on the excitonic system when the radiation field is treated both in a classical and quantum manner.

In our simulations, we consider only the 1*s* $\mathrm{MoSe_2}$ intralayer exciton in the hetero-bilayer and reduce the photon space to the Fock number states $\{|0\rangle, |1\rangle\}$. This choice is motivated by computational feasibility, but we expect the predicted phenomena to hold for interlayer excitons at even larger grating periodicities. Throughout this work, the cavity periodicity is always one-dimensional (see Fig. 1d). Finally, we note that for the following comparison, we either simulate the Moiré term $\mathcal{M}$ or the cavity periodicity $\mathcal{B}$, but we never consider both of them in the same simulation.

Classically driven cavity

We consider the effect of a driven structured cavity on the excitonic states of the untwisted bilayer material and show that it gives confinement signatures similar to a twist-induced Moiré potential, which include the formation of a Moiré Brillouin-Zone, and the opening of miniband gaps. Examining Eq. (4), we note that the bilinear coupling $\mathcal{B}$ shares the same excitonic operators of the Moiré potential $\mathcal{M}$, but it is additionally paired with photonic operators. In the case of classical radiation, these operators are replaced by their mean-field value. To describe the driven system, we assume that the far field driving can couple to finite momentum cavity modes ($\pm\bar{\boldsymbol{q}}$) via the grating of the cavity. We model this excitation for single-polarization ($\lambda = s$) modes as a time-dependent coherent state $|\tilde{\lambda}_{\bar{\boldsymbol{q}}} \tilde{\lambda}_{-\bar{\boldsymbol{q}}}(t)\rangle = |\tilde{\lambda}_{\bar{\boldsymbol{q}}}(t)\rangle \otimes |\tilde{\lambda}_{-\bar{\boldsymbol{q}}}(t)\rangle$. Here we define the time-dependent coherent states as $|\tilde{\lambda}_{\bar{\boldsymbol{q}}}(t)\rangle = e^{-\frac{i\omega_{\bar{\boldsymbol{q}}} t}{2}} |e^{-i\omega_{\bar{\boldsymbol{q}}} t} \tilde{\lambda}_{\bar{\boldsymbol{q}}}\rangle$ where the last ket goes by the usual definition $|\alpha\rangle = e^{-\frac{|\alpha|^2}{2}} \sum_{s=0}^{\infty} \frac{\tilde{\alpha}^s}{\sqrt{s!}} |s\rangle$ of coherent states. Using that $\omega_{\bar{\boldsymbol{q}}} = \omega_{-\bar{\boldsymbol{q}}}$ and $\tilde{A}_{0,\bar{\boldsymbol{q}}} = \tilde{A}_{0,-\bar{\boldsymbol{q}}}$, and projecting the interaction Hamiltonian in Eq. (4) onto these states introduces a

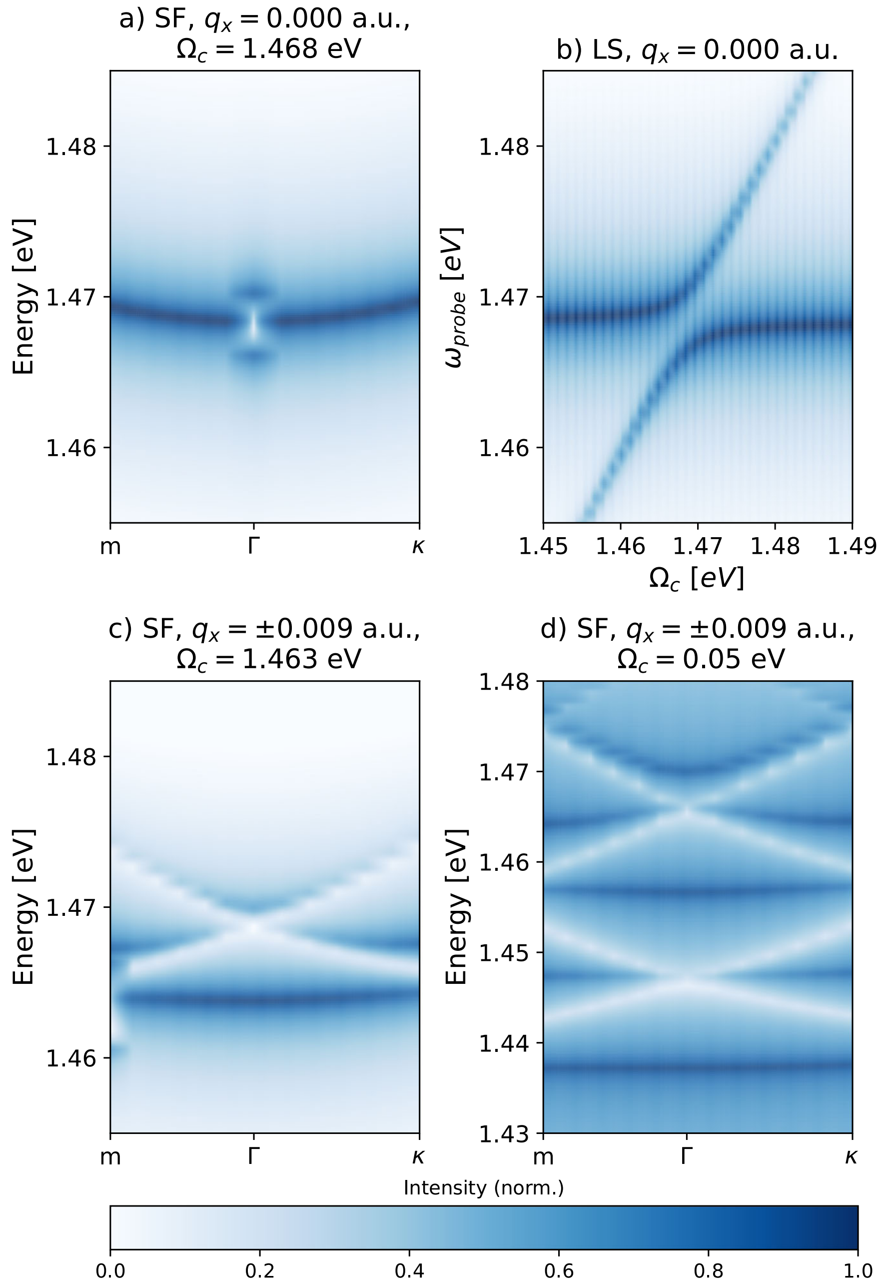

Fig. 2 | Spectral function and imaginary part of the linear susceptibility for the untwisted heterostructure in a driven optical cavity (both structured and unstructured). Spectral function (SF, c.f. Sec., **a**, **c**, **d**) and imaginary part of the linear susceptibility (LS, c.f. Sec., **b**) for the 1s intralayer exciton in the $MoSe_2$ layer when light can be treated classically and in the absence of twist-induced Moiré potential (in Eq. (4)). We use Floquet theory to solve the light-matter problem. We used $\tilde{A}_0 = 0.04$ a.u. for (**a**–**c**) and $\tilde{A}_0 = 0.02$ a.u. for (**d**). All panels use a normalized log scale for the intensity. For the spectral function, we use the standard $M - \Gamma - K$ path (which we shorten to $m - \Gamma - \kappa$, as shown in Fig. 1c and Supplementary Information Section II.B). **a**, **b** The light does not carry any momentum, so no terms in the Hamiltonian connect two k-points. Hence, we observe a parabolic dispersion in the spectral function. In the linear response, we observe avoided crossing of the UP and LP formed from the excitonic state. **c**, **d** We used two photon modes carrying momentum $q_x = \pm 0.009$ a.u. In this case, the bilinear coupling generates a confining potential, and we observe the folding of the bands. (**c**) is at excitonic resonance (we can observe the Rabi splitting). The value slightly differs from (**a**) due to the bilinear coupling $\mathcal{B}$. On the contrary, (**d**) is at off-resonance, but the spectrum is rich due to the mixing of the Floquet replicas. The value of $\Omega_c = 0.05$ eV ensures the mixing of Floquet replicas.

time dependence of the form:

$$\left\langle \tilde{\lambda}_{\bar{\boldsymbol{q}}}\tilde{\lambda}_{-\bar{\boldsymbol{q}}}(t)|\hat{H}_{\text{int}}|\tilde{\lambda}_{\bar{\boldsymbol{q}}}\tilde{\lambda}_{-\bar{\boldsymbol{q}}}(t)\right\rangle \sim H^{(n=1)}e^{i\omega_{\boldsymbol{q}}t} + H^{(n=-1)}e^{-i\omega_{\boldsymbol{q}}t}$$

where $H^{(n=\pm1)}$ is the time-*independent* projection of the interaction Hamiltonian onto the coherent state, with n the Floquet frequency index. See Supplementary Information Section III for the complete expression.

Since the obtained Hamiltonian is time periodic, we use Floquet theory to solve it[39,40]. The advantage of this approach is that the Floquet Hamiltonian is time independent, which makes it computationally cheaper while still being able to capture the polaritonic effects from the light-matter coupling. With this semi-classical treatment, light with finite momentum $\bar{\boldsymbol{q}}$ enters the coupled Hamiltonian in Eq. (4) exactly as the potential created by a Moiré super-lattice, by generating interacting Floquet replicas, as sketched in Fig. 1b. This means that we can use classically driven cavities to induce an all-optical Moiré potential.

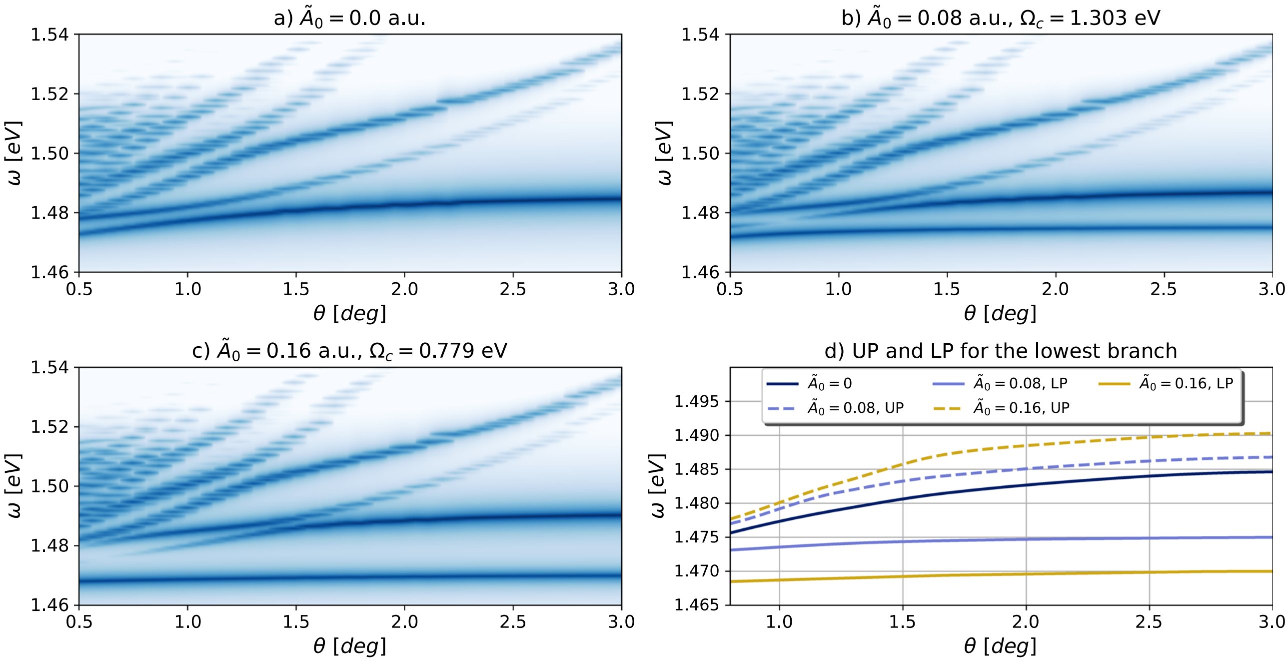

Fig. 3 | Imaginary part of the linear susceptibility for the 1*s* intralayer exciton in the MoSe$_2$ layer, as a function of the twist angle. The spacing used for the grid allows for a resolution of at most $\Delta\theta = 0.05$ deg, which explains the coarse nature of the lines (especially at small angles). (**a**–**c**) use a normalized log scale for the intensity (see Fig. 2). **a** Twisted heterostructure without the cavity (see ref. 14 Fig. 5a and ref. 36 Fig. 4a). **b**, **c** Twisted heterostructure embedded in a spatially unstructured cavity ($\bar{\boldsymbol{q}} = \mathbf{0}$) for different light-matter coupling strengths. After fixing the energy of the mode to a constant value for all twist angles (in resonance with the lowest branch), we scanned over θ. While all other states are mostly unaffected by the cavity, the lowest branch is split into the Upper (UP) and Lower (LP) Polariton, and the separation increases with the light-matter coupling $\tilde{A}_0$. Note that for these two panels, Ω_c is significantly smaller than the excitonic resonance due to the diamagnetic shift. These results are qualitatively in agreement with ref. 36 Fig. 4b. **d** Trace of the UP and LP formed from the lowest branch of the bare excitonic system (taken from the previous panels). The separation between UP and LP increases with the light-matter coupling. Furthermore, the LP is almost flat for all twist angles, meaning it is mainly unperturbed by the Moiré potential in the presence of a cavity, whereas the UP is affected by the Moiré potential only at low angles.

Figure 2 shows the results for a classically driven unstructured cavity as well as for a spatially structured cavity (with a one-dimensional spatial periodicity), both coupled to the 1*s* intralayer exciton in the MoSe$_2$ layer within the untwisted heterostructure (i.e., $\mathcal{M} = 0$). For the unstructured cavity (Fig. 2a, b), where we study the system at the resonance between the cavity mode and the exciton, the dispersion relation of the exciton remains parabolic, as seen in the spectral function (SF, c.f. "Methods" section for its definition) in Fig. 2a. On top of the unperturbed dispersion, we observe a signature of the formation of an exciton-polariton by the appearance of a splitting at Γ, corroborated by the expected avoided crossing of upper and lower polariton branches in the imaginary part of the linear susceptibility (LS, c.f. "Methods" section for its definition) as a function of cavity energies, our proxy for an absorption experiment (c.f. Fig. 2b). We then shift focus to a structured cavity both at and out of resonance with the excitons (Fig. 2c, d). Here, the excitons experience a confining potential generated by the bilinear coupling, which modifies the excitonic bands. Specifically, at resonance (Fig. 2c), we observe a simple band folding stemming from the periodicity of the grating together with the mixing with the finite momentum replica of the many-body ground state. The polariton splitting is now shifted to finite momentum (the *m*-point), as compared to Fig. 2a. Off-resonance, at small frequencies (Fig. 2d), the positive and negative excitonic replicas mix, generating a rich spectrum. We find that to achieve this mixing the cavity energy should be such that the excitonic replicas can intersect within the BZ. Finally, we find that at large off-resonant driving frequencies (not shown), the external driving does not induce any modification to the parabolic dispersion. This is because within the first-order high-frequency expansion of the Floquet Hamiltonian[39], $H^{\omega\to\infty}_{\text{Floquet}} = H^{(n=0)} + \frac{[H^{(n=-1)}, H^{(n=1)}]}{\Omega} + \mathcal{O}(\frac{1}{\Omega^2})$, the commutator in the numerator vanishes, i.e., $[H^{(n=-1)}, H^{(n=1)}] = 0$. In the Supplementary Information Section III.A, we show the explicit calculation of the commutator as well as the spectral function for various values of the cavity frequency.

Dark cavity

We now analyze the cavity-exciton system for a dark cavity, i.e., in the absence of external fields, where the effect of the photons on the matter is via their quantum fluctuations. We begin by focusing on the quantum effects on the heterostructure embedded in a spatially unstructured cavity ($\mathcal{B} = 0$), including in this case the periodic confining potential from the Moiré pattern caused by twisting. In the absence of momentum exchange, light and matter are coupled only through the bilinear coupling associated with $\mathcal{I}$ in Eq. (4). Here, we examine how the unstructured planar cavity influences the twist-angle dependence of the excitonic response. For reference, in Fig. 3a–c, we show the imaginary part of the linear susceptibility (c.f. "Methods" section for its definition) as a function of the twist angle θ and the optical probe energy ω outside the cavity. As the twist angle decreases, the Moiré Brillouin-zone contracts, the excitonic bands fold closer to the Γ point, and more folded states enter the investigated energy window. Therefore, the resulting linear response displays a richer spectrum at small twist angles, in line with earlier findings[14,36].

In the presence of cavity-matter coupling, when the cavity resonates with the MoSe$_2$ excitonic transition, we expect the Rabi splitting to dominate the behavior of the exciton-polariton response. We observe that compared to the case of uncoupled light and matter (Fig. 3a), the coupling splits the lowest branch into two, the upper (UP) and lower polariton (LP) (Fig. 3b, c). The magnitude of this splitting increases linearly with the light-matter coupling $\tilde{A}_0$. Interestingly, the

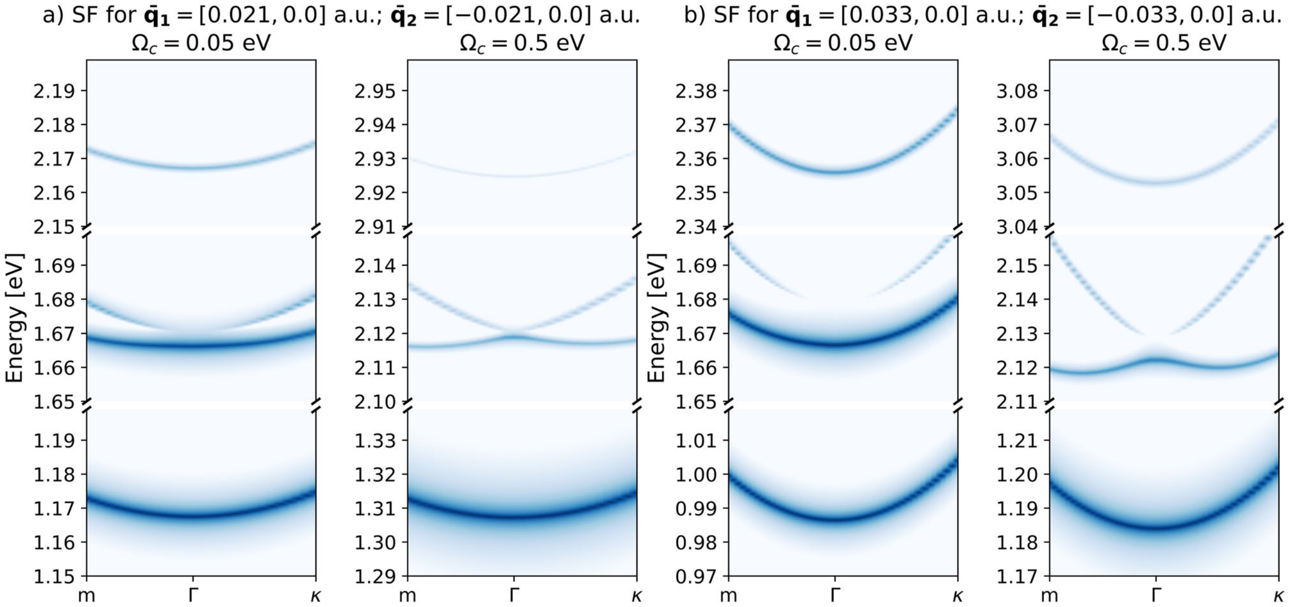

Fig. 4 | Spectral function for the untwisted heterostructure ($\mathcal{M} = 0$ in Eq. (4)) in a dark spatially structured optical cavity with two photonic modes. On the *x*-axis, we report the *k*-point. *m* and *κ* are the borders of the BZ with periodicity induced by the momentum carried by light (see Supplementary Information Section II.B). We used $\tilde{A}_{0,\bar{\boldsymbol{q}}} = 0.08$ a.u. for all panels. All panels use a normalized log scale for the intensity (see Fig. 2). Note that the separation between the three bands depends both on the cavity energy Ω_c, on the diamagnetic term $\tilde{A}^2_{0,\bar{\boldsymbol{q}}}$, and on the interaction energy $\tilde{A}_{0,\bar{\boldsymbol{q}}}\mathcal{B}^{\nu,\lambda}_{ll',ij,\boldsymbol{Q}\bar{\boldsymbol{q}}}$. Finally, the position of the bottommost band is shifted towards lower energies due to the interaction energy contribution. **a** Spectral function for $\bar{\boldsymbol{q}}_{1,2} = [\pm 0.021, 0.0]$ a.u., for both low and high frequency. In both cases, the curvature of the dispersion relation in the uppermost and lowermost bands is small, a signature of a heavy exciton. In the central band instead, the dispersion relation goes from parabolic to *M*-shaped, which means that the excitonic mass is negative around the Γ point. **b** Spectral function for $\bar{\boldsymbol{q}}_{1,2} = [\pm 0.033, 0.0]$ a.u., for both low and high frequency. In both cases, the curvature of the dispersion relation in the uppermost and lowermost bands is steep, a signature of a light exciton. Similarly to (**a**), the dispersion relation in the central band goes from parabolic to *M*-shaped, which means that the excitonic mass is negative around the Γ point.

UP in Fig. 3b, c has the same dispersion as in the uncoupled matter system (Fig. 3a), whereas the LP line is almost constant for all twist angles, in agreement with previous works[36]. This is shown in Fig. 3d, where we traced out the curves obtained by the UP and the LP of Fig. 3b, c together with the lowest branch of the bare excitonic system (Fig. 3a). A flat line in the spectrum means that the twist angle, which controls the size of the Moire Brillouin-Zone, has little influence on the excitonic states. This implies that the LP behaves as a low-energy unperturbed and unconfined exciton. Conversely, the dispersion of the UP is steeper and linear at small twist angles and then flattens out for larger angles, where it behaves similarly to the LP, i.e., as nearly free particles. Ref. 36 provides a complementary discussion on how bare photonic and excitonic states contribute to the UP and LP. In short, the effect of the twisting angle can be modified by the electromagnetic field of a cavity, which influences the excitonic response by causing Rabi splitting of the resonant transition. This results in a different localization for the upper and lower polariton, and may pave the way for new quantum phases[41].

We then consider a spatially structured cavity, where both creation of excitons and Moiré-like exciton-scattering are included, i.e., both $\mathcal{B}$ and $\mathcal{I}$ are finite in Eq. (3), while we let $\mathcal{M} = 0$ to isolate the effect of the periodic grating of the cavity. First, we analyze the results in Fig. 4, which shows the excitonic spectral function. In all panels, there are three different sets of bands. From the analysis of the polaritonic states, resulting from the diagonalization of Eq. (3), we identify the lowest energy sector to be mainly composed of an uncoupled excitonic state and the vacuum ($n = 0$) state of both photonic modes. The central one is mainly constituted by an uncoupled excitonic state and one photon excitation ($n = 1$) in either of the modes. Finally, the high-energy band corresponds to an uncoupled excitonic state and a single excitation in both photon modes. The separation between the three bands increases with the cavity energy Ω_c, with the diamagnetic term $\tilde{A}^2_{0,\bar{\boldsymbol{q}}}$ and with the interaction energy $\tilde{A}_{0,\bar{\boldsymbol{q}}}\mathcal{B}^{\nu,\lambda}_{ll',ij,\boldsymbol{Q}\bar{\boldsymbol{q}}}$. Inspecting the uppermost and bottommost energy bands of Fig. 4, the curvature of the dispersion relation increases with the transfer of cavity photon momentum. As the spectral function is related to the excitonic band structure, we can interpret this variation as the modification of the excitonic mass. Since a steeper curvature corresponds to a smaller mass, the exciton becomes lighter as the photon momentum increases. In the central band instead, the dispersion relation goes from parabolic to *M*-shaped (i.e., the Γ point is a local maximum instead of a global minimum). This implies that the excitonic mass is negative around this point, and might lead to the decay of the zero-momentum exciton towards one of the local minima, creating a new stable exciton-polariton state at finite momentum. It should be noted that for the central band to show such features, the condition $\tilde{A}_{0,\bar{\boldsymbol{q}}}\mathcal{B}^{\nu,\lambda}_{ll',ij,\boldsymbol{Q}\bar{\boldsymbol{q}}} \approx \tilde{A}_{0,-\bar{\boldsymbol{q}}}\mathcal{B}^{\nu,\lambda}_{ll',ij,\boldsymbol{Q},-\bar{\boldsymbol{q}}}$ should hold (i.e., both modes have the same interaction energy). Otherwise, the two exciton-polaritons would exist at different energy scales and could not scatter. To prove that this effect could be experimentally demonstrated, we show in Fig. 5 the linear susceptibility as a function of probe photon momentum. In this figure, going from left to right corresponds to going from Γ to *m* in Fig. 4b. As one can see, this observable is also able to capture the features discussed for the spectral function.

To better understand the physics, let us compare the effect of the bilinear coupling with that of the Moiré potential. In general, they both allow an exciton to scatter between different *k*-points. However, the different origin of the two terms plays a fundamental role in the effect on the excitonic system. The Moiré potential $\mathcal{M}$ acts as a periodic scattering potential, which allows momentum transfer between excitons. Conversely, the *optical* Moiré term $\mathcal{B}$, while also allowing the hopping of an exciton between *k*-points, does so at the expense of creating/annihilating a cavity photon. The underlying physics becomes even clearer when the excitons and the photons are off-resonant, so that photons can only be created/destroyed virtually. In this situation,

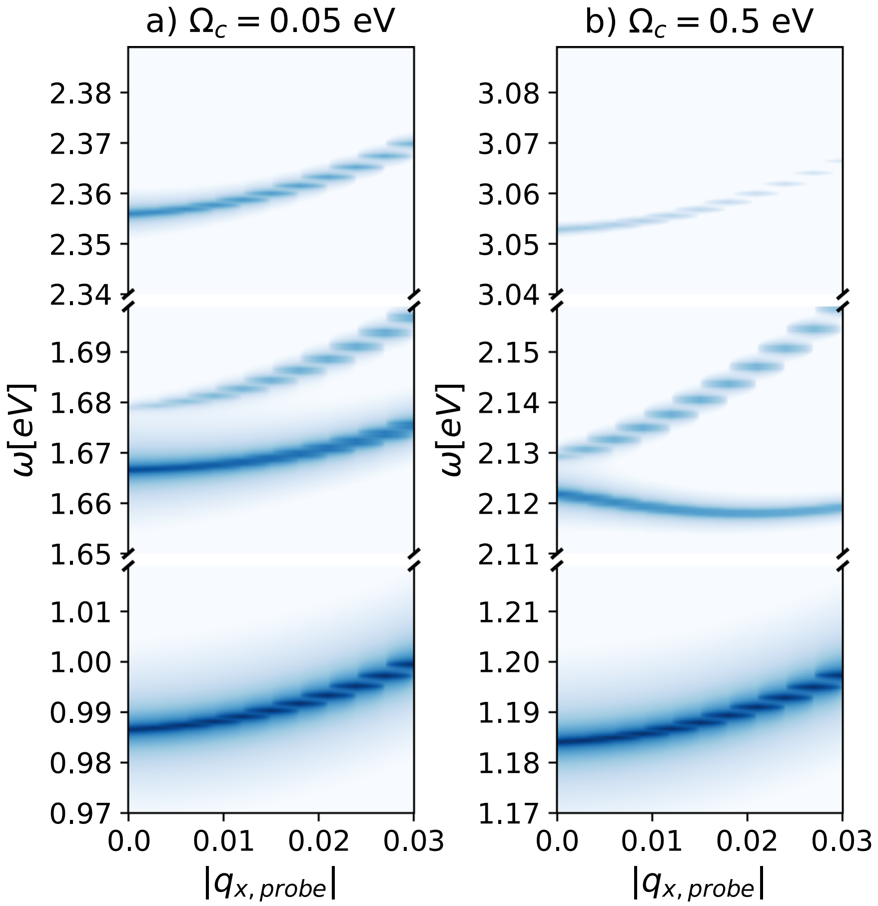

Fig. 5 | Imaginary part of the linear susceptibility at finite q for the untwisted heterostructure ($\mathcal{M} = 0$) in a dark spatially structured optical cavity with two photonic modes with $\bar{\boldsymbol{q}}_1 = [\mathbf{0.033}, \mathbf{0.0}]$ a.u.; $\bar{\boldsymbol{q}}_2 = [-\mathbf{0.033}, \mathbf{0.0}]$ a.u. We used $\tilde{A}_{0,\boldsymbol{q}} = 0.08$ a.u. for all panels. All panels use a normalized log scale for the intensity (see Fig. 2). On the x-axis, we report the absolute value of the momentum carried by the probe beam, while on the y-axis, its energy. $|\boldsymbol{q}_{x,\mathrm{probe}}| = 0.01$ a.u. means that the probe is composed of two modes, one with $\boldsymbol{q}_1 = [0.01, 0.0]$ a.u.; $\boldsymbol{q}_2 = [-0.01, 0.0]$ a.u. This figure should be compared with Fig. 4b. While the first and third bands maintain the parabolic dispersion regardless of the energy of the cavity, the central one visibly changes. **a** Low-frequency case. Here, the central band is parabolic. **b** High-frequency case. Here, the central band has a maximum at $|\boldsymbol{q}_{x,\mathrm{probe}}| = 0.0$ a.u., which can be interpreted as a negative excitonic mass (similarly to Fig. 4).

the *optical* Moiré term turns into a many-body, exciton-exciton interaction, whose momentum dependence is solely determined by the cavity design. To explicitly show this feature, we make use of the high-frequency limit of the QED Hamiltonian. Within this limit, we can write a photon-free QED Hamiltonian by downfolding the original one in a dressed excitonic space according to refs. 30,38,42,43:

$$\begin{aligned}\hat{H}_{\mathrm{QED}}^{\omega\to\infty} &\approx \left\langle 0_{\bar{\boldsymbol{q}}}, 0_{-\bar{\boldsymbol{q}}} | \hat{H} | 0_{\bar{\boldsymbol{q}}}, 0_{-\bar{\boldsymbol{q}}} \right\rangle \\ -\textstyle\sum_{\bar{\boldsymbol{q}}} \frac{1}{\omega_{\bar{\boldsymbol{q}}}} &\left[\left\langle 0_{\bar{\boldsymbol{q}}}, 0_{-\bar{\boldsymbol{q}}} | \hat{H} | 1_{\bar{\boldsymbol{q}}}, 0_{-\bar{\boldsymbol{q}}} \right\rangle \cdot \left\langle 1_{\bar{\boldsymbol{q}}}, 0_{-\bar{\boldsymbol{q}}} | \hat{H} | 0_{\bar{\boldsymbol{q}}}, 0_{-\bar{\boldsymbol{q}}} \right\rangle \right].\end{aligned} \tag{5}$$

Performing this expansion on the interaction Hamiltonian in Eq. (4) leads to (see Supplementary Information Section IV for the full derivation):

$$\begin{aligned}\hat{H}_{\mathrm{int}}^{\omega\to\infty} = &\sum_{ll',\nu} \sum_{i\in C, j\in V} \sum_{\boldsymbol{Q}} \mathcal{M}^{\nu,\lambda}_{ll',ij,\boldsymbol{Q}\boldsymbol{q}} \hat{X}^{\nu\dagger}_{ll',ij,\boldsymbol{Q}+\boldsymbol{q}} \hat{X}^{\nu}_{ll',ij,\boldsymbol{Q}} \\ &- \frac{2\tilde{A}_{0,\boldsymbol{q}}\tilde{A}_{0,-\boldsymbol{q}}}{\omega_{\boldsymbol{q}}} \sum_{ll'l_1l'} \sum_{iji_1j_1} \sum_{\boldsymbol{Q}\boldsymbol{Q}_1,\nu\nu_1} \Big(\mathcal{B}^{\nu,\lambda}_{ll',ij,\boldsymbol{Q},-\boldsymbol{q}} \mathcal{B}^{\nu_1,\lambda}_{l_1l',i_1j_1,\boldsymbol{Q}_1\boldsymbol{q}} \\ &\hat{X}^{\nu\dagger}_{ll',ij,\boldsymbol{Q}-\boldsymbol{q}} \hat{X}^{\nu_1\dagger}_{l_1l',i_1j_1,\boldsymbol{Q}_1+\boldsymbol{q}} \hat{X}^{\nu}_{ll',ij,\boldsymbol{Q}} \hat{X}^{\nu_1}_{l_1l',i_1j_1,\boldsymbol{Q}_1} \\ &- \sum_{\boldsymbol{q}} \mathcal{I}^{\nu,\lambda}_{ll',ij,\boldsymbol{Q}\boldsymbol{q}} \mathcal{I}^{\nu_1,\lambda,*}_{l_1l',i_1j_1,\boldsymbol{Q}_1\boldsymbol{q}} \hat{X}^{\nu\dagger}_{ll',ij,\boldsymbol{Q}} \hat{X}^{\nu_1}_{l_1l',i_1j_1,\boldsymbol{Q}_1} \Big)\end{aligned} \tag{6}$$

The striking result is the emergence of a four-excitonic operator term, i.e., a term that describes an interaction between two excitons, which is a fundamental difference with respect to the Moiré potential. This alters the excitonic dynamics as manifested by our calculated spectral functions and the non-trivial linear response features. These excitons-excitons interactions, absent in classical treatments, highlight the potential of quantum cavities to engineer correlated excitonic phases.

Discussion

In this work, we demonstrated that spatially structured optical cavities can precisely emulate Moiré-like excitonic confinement in Van der Waals heterostructures, circumventing the need for physical lattice twisting.

For classically light-driven cavities, momentum-carrying modes replicate the spatial modulation of a standard Moiré potential, leading to band folding and splitting, typical of a free particle in a periodic potential. Such effects are predicted to be in the meV energy scale (for the parameters we used).

Conversely, in dark cavities, the light-matter interaction is mediated solely by quantum vacuum fluctuations of the cavity modes, which induce long-range exciton-exciton interactions, fundamentally altering the excitonic dynamics. Note that we have recently observed that in Graphene cavity can induce long-range interaction for electrons[38]. These interactions, not present when the system interacts with classical light, highlight the potential of quantum cavities to engineer correlated excitonic phases. Most notably, we obtain a negative excitonic mass around the Γ point that could be an experimental fingerprint of the cavity-mediated excitonic interactions predicted in this work.

Our findings bridge the gap between twist engineering of two-dimensional heterostructures and cavity quantum electrodynamics, providing a versatile platform for optically programmable excitonic systems.

Methods

In this work, we distinguish between spatially unstructured cavities, of the Fabry–Perot kind, where the electromagnetic field is treated with a single effective mode description in the long-wavelength approximation[35] ($\bar{\boldsymbol{q}} = [q_x, q_y] = [0, 0]$), and spatially structured cavities, whose description requires two effective momentum-carrying modes ($\bar{\boldsymbol{q}}_1 = [q_x, 0]$, $\bar{\boldsymbol{q}}_2 = [-q_x, 0]$) corresponding to a cavity with a one-dimensional periodicity (like the one in Fig. 1d). Based on symmetry arguments, we assume that $\omega_{\bar{\boldsymbol{q}}_1} = \omega_{\bar{\boldsymbol{q}}_2}$ and $\tilde{A}_{0,\bar{\boldsymbol{q}}_1} = \tilde{A}_{0,\bar{\boldsymbol{q}}_2}$. Such photonic environments can be realized by means of dielectric metasurfaces[44,45], or in polaritonic and plasmonic cavities[46–48]. In order to illustrate the broad potential of cavity-structuring of excitons, we leave the cavity mode energy, volume, and grating wavelength as adjustable parameters.

In order to obtain the values of the modes' momentum used in the previous sections ($\bar{\boldsymbol{q}}_i = [\pm 0.009, 0.0], [\pm 0.021, 0.0], [\pm 0.033, 0.0]$ a.u.), one should design the grating of the cavity accordingly. We estimate that the periodicity of the corresponding grating should be $d = \frac{2\pi}{\bar{\boldsymbol{q}}_i} = 40$ nm, 16 nm, 10 nm. We expect these extreme grating sizes to be larger for the optical confinement of interlayer excitons.

In order to obtain the full exciton-polariton states, we start by solving the Mott–Wannier equation in the *k*-space (c.f. Supplementary Information Section V.A), which gives us access to the binding energy and the Mott–Wannier states. We considered only the 1*s* intralayer exciton in the $MoSe_2$ layer. The Mott–Wannier states are used to construct the excitonic creation and annihilation operators, as well as all the matrix elements appearing in Eq. (3). Refer to Supplementary Information Section I for the complete derivation. We represent the photonic modes using the Fock number states $\{|0\rangle, |1\rangle\}$. Finally, we obtain the full exciton-polariton states via the full diagonalization of Eq. (3). The physics of the coupled light-matter system is then investigated by computing excitonic quantities: the linear optical susceptibility (LS) function and the spectral function (SF). The former represents the optical response of the system, obtained from applying linear response theory to the polaritonic states[49]:

$$\chi(\omega, \Omega_c, \theta) = \sum_I \frac{|\mathcal{M}_{I,0}|^2}{\omega - (E_I(\Omega_c, \theta) - E_0(\Omega_c, \theta)) + i\eta} \tag{7}$$

where $\mathcal{M}_{I,0}$ is the transition matrix element between the polaritonic ground state Ψ_0 and an excited state Ψ_I. η is a small artificial broadening, Ω_c is the energy of the cavity modes, ω is the energy of the probe field, θ is the Moiré twist angle, and $E_I(\Omega_c, \theta)$ is the energy of the *I*th polaritonic state. Note that when we set $\mathcal{M} = 0$ (no standard Moiré potential), χ does not depend on θ. Furthermore, note that we only calculate the matter part of such a response by tracing out the photons. To investigate the excitonic dispersion, i.e., their band structure, we employ the spectral function defined as:

$$\mathcal{S}(\omega, \Omega_c, \theta, \boldsymbol{Q}) = \sum_I \frac{\langle \Psi_I | \hat{X}^\dagger_{\boldsymbol{Q}} | \Psi_0 \rangle \langle \Psi_0 | \hat{X}_{\boldsymbol{Q}} | \Psi_I \rangle}{\omega - (E_I(\Omega_c, \theta) - E_0(\Omega_c, \theta)) + i\eta} \tag{8}$$

This represents the probability of creating an exciton with an energy $E_I(\Omega_c, \theta)$ at a certain *k*-point. Note that when we set $\mathcal{M} = 0$ (no standard Moiré potential), $\mathcal{S}$ does not depend on θ. Refer to the Supplementary Information Section II for additional insights.

Data availability

The data that support the findings of this study are available from the corresponding authors upon request.

Code availability

The code that supports the findings of this study is available from the corresponding authors upon request.

References

1. Geim, A. K. & Grigorieva, I. V. Van der waals heterostructures. *Nature* **499**, 419–425 (2013).
2. Mak, K. F. & Shan, J. Photonics and optoelectronics of 2d semiconductor transition metal dichalcogenides. *Nat. Photonics* **10**, 216–226 (2016).
3. Novoselov, S., Mishchenko, A., Carvalho, A. & Castro Neto, A. H. 2d materials and van der Waals heterostructures. *Science* **353**, aac9439 (2016).
4. Shanmugam, V. et al. A review of the synthesis, properties, and applications of 2d materials. *Part. Part. Syst. Charact.* **39**, 2200031 (2022).
5. Kennes, D. M. et al. Moiré heterostructures as a condensed-matter quantum simulator. *Nat. Phys.* **17**, 155–163 (2021).
6. Mak, K. F., Lee, C., Hone, J., Shan, J. & Heinz, T. F. Atomically thin MoS_2: a new direct-gap semiconductor. *Phys. Rev. Lett.* **105**, 136805 (2010).
7. Latini, S., Olsen, T. & Thygesen, K. S. Excitons in van der Waals heterostructures: the important role of dielectric screening. *Phys. Rev. Lett.* **92**, 245123 (2015).
8. Gjerding, M. N. et al. Recent progress of the computational 2d materials database (c2db). *2D Mater.* **8**, 044002 (2021).
9. Wang, G. et al. Colloquium: excitons in atomically thin transition metal dichalcogenides. *Rev. Mod. Phys.* **90**, 021001 (2018).
10. Ren, W. et al. The 2d materials roadmap. *2D Mater.* in press https://doi.org/10.1088/2053-1583/ae2b82 (2025).
11. Bistritzer, R. & MacDonald, A. H. Moiré bands in twisted double-layer graphene. *Proc. Natl. Acad. Sci. USA* **108**, 12233–12237 (2011).
12. Cao, Y. et al. Unconventional superconductivity in magic-angle graphene superlattices. *Nature* **556**, 43–50 (2018).
13. Hennighausen, Z. & Kar, S. Twistronics: a turning point in 2d quantum materials. *Electron. Struct.* **3**, 014004 (2021).
14. Brem, S., Linderälv, C., Erhart, P. & Malic, E. Tunable phases of moiré excitons in van der Waals heterostructures. *Nano Lett.* **20**, 8534–8540 (2020).
15. Ovesen, S. et al. Interlayer exciton dynamics in van der Waals heterostructures. *Commun. Phys.* **2**, 23 (2019).
16. Xiong, R. et al. Correlated insulator of excitons in WSe_2/WS_2 moiré superlattices. *Science* **380**, 860–864 (2023).
17. Sharpe, A. L. et al. Emergent ferromagnetism near three-quarters filling in twisted bilayer graphene. *Science* **365**, 605–608 (2019).
18. Latini, S., Ronca, E., De Giovannini, U., Hübener, H. & Rubio, A. Cavity control of excitons in two-dimensional materials. *Nano Lett.* **19**, 3473–3479 (2019).
19. Flatten, L. C. et al. Room-temperature exciton-polaritons with two-dimensional WS_2. *Sci. Rep.* **6**, 33134 (2016).
20. Zhang, H. et al. Hybrid exciton-plasmon-polaritons in van der Waals semiconductor gratings. *Nat. Commun.* **11**, 3552 (2020).
21. Svendsen, M. K. et al. Combining density functional theory with macroscopic QED for quantum light-matter interactions in 2d materials. *Nat. Commun.* **12**, 2778 (2021).
22. Datta, B. et al. Highly nonlinear dipolar exciton-polaritons in bilayer MoS_2. *Nat. Commun.* **13**, 6341 (2022).
23. Latini, S. et al. Phonoritons as hybridized exciton-photon-phonon excitations in a monolayer h-bn optical cavity. *Phys. Rev. Lett.* **126**, 227401 (2021).

24. Deng, H., Weihs, G., Santori, C., Bloch, J. & Yamamoto, Y. Condensation of semiconductor microcavity exciton polaritons. *Science* **298**, 199–202 (2002).
25. Kasprzak, J. et al. Bose–Einstein condensation of exciton polaritons. *Nature* **443**, 409–414 (2006).
26. Appugliese, F. et al. Breakdown of topological protection by cavity vacuum fields in the integer quantum Hall effect. *Science* **375**, 1030–1034 (2022).
27. Sentef, M. A., Ruggenthaler, M. & Rubio, A. Cavity quantum-electrodynamical polaritonically enhanced electron-phonon coupling and its influence on superconductivity. *Sci. Adv.* **4**, eaau6969 (2018).
28. Mazza, G. & Georges, A. Superradiant quantum materials. *Phys. Rev. Lett.* **122**, 017401 (2019).
29. Hübener, H., Boström, E. V., Claassen, M., Latini, S. & Rubio, A. Quantum materials engineering by structured cavity vacuum fluctuations. *Mater. Quantum Technol.* **4**, 023002 (2024).
30. Latini, S. et al. The ferroelectric photo ground state of srtio$_3$: Cavity materials engineering. *Proc. Natl. Acad. Sci. USA* **118**, e2105618118 (2021).
31. Carusotto, I. & Ciuti, C. Quantum fluids of light. *Rev. Mod. Phys.* **85**, 299–366 (2013).
32. Viñas Boström, E., Sriram, A., Claassen, M. & Rubio, A. Controlling the magnetic state of the proximate quantum spin liquid α-rucl$_3$ with an optical cavity. *npj Comput. Mater.* **9**, 202 (2023).
33. Lu, I.-T. et al. Cavity engineering of solid-state materials without external driving. *Adv. Opt. Photonics* **17**, 441 (2025).
34. Sarkar, S. et al. Sub-wavelength optical lattice in 2d materials. *Sci. Adv.* **11**, eadv2023 (2025).
35. Svendsen, M.K. et al. Effective equilibrium theory of quantum light-matter interaction in cavities for extended systems and the long wavelength approximation. *Commun. Phys.* **8**, 425 (2025).
36. Fitzgerald, J. M., Thompson, J. J. P. & Malic, E. Twist angle tuning of moiré exciton polaritons in van der Waals heterostructures. *Nano Lett.* **22**, 4468–4474 (2022).
37. Rokaj, V., Ruggenthaler, M., Eich, F. G. & Rubio, A. Free electron gas in cavity quantum electrodynamics. *Phys. Rev. Res.* **4**, 013012 (2022).
38. Hang Liu et al. Cavity-mediated electron-electron interactions: Renormalizing Dirac states in graphene. *Sci. Adv.* **11**, eadz1855 (2025).
39. Oka, T. & Kitamura, S. Floquet engineering of quantum materials. *Annu. Rev. Condens. Matter Phys.* **10**, 387–408 (2019).
40. Hübener, H. et al. Engineering quantum materials with chiral optical cavities. *Nat. Mater.* **20**, 438–442 (2020).
41. Johnstone, D., Mishra, S., Zhu, Z., Yao, H. & Sanchez-Palencia, L. Weak superfluidity in twisted optical potentials. *Phys. Rev. Res.* **6**, L042066 (2024).
42. Li, J., Schamriß, L. & Eckstein, M. Effective theory of lattice electrons strongly coupled to quantum electromagnetic fields. *Phys. Rev. B* **105**, 165121 (2022).
43. Mikami, T. et al. Brillouin-Wigner theory for high-frequency expansion in periodically driven systems: Application to Floquet topological insulators. *Phys. Rev. B* **93**, 144307 (2016).
44. Barton, D. et al. High-q nanophotonics: sculpting wavefronts with slow light. *Nanophotonics* **10**, 83–88 (2020).
45. Danielsen, D. R. et al. Fourier-tailored light–matter coupling in van der Waals heterostructures. *ACS Nano* **19**, 20645–20654 (2025).
46. Herzig Sheinfux, H. et al. High-quality nanocavities through multimodal confinement of hyperbolic polaritons in hexagonal boron nitride. *Nat. Mater.* **23**, 499–505 (2024).
47. Galiffi, E. et al. Extreme light confinement and control in low-symmetry phonon-polaritonic crystals. *Nat. Rev. Mater.* **9**, 9–28 (2023).
48. Chen, Y. et al. Metasurface integrated monolayer exciton polariton. *Nano Lett.* **20**, 5292–5300 (2020).
49. Ruggenthaler, M., Tancogne-Dejean, N., Flick, J., Appel, H. & Rubio, A. From a quantum-electrodynamical light–matter description to novel spectroscopies. *Nat. Rev. Chem.* **2,** 0118 (2018).

Acknowledgements

We acknowledge support from the Villum foundation grant No. 72146 (S.L.), the Cluster of Excellence "CUI: Advanced Imaging of Matter" - EXC 2056 - project ID 390715994 (A.R.), European Research Council (ERC-2024-SyG-101167294; UnMySt) (A.R.) and Grupos Consolidados (IT1453-22) (A.R.), and the Max Planck-New York City Center for Non-Equilibrium Quantum Phenomena. We acknowledge support from the European Union Marie Sklodowska-Curie Doctoral Networks TIMES grant No. 101118915 (A.R.) and SPARKLE grant No. 101169225 (S.L.). The Flatiron Institute is a division of the Simons Foundation.

Author contributions

F.T. performed all calculations and implementations, analyzed the data, and wrote the first draft of the manuscript. H.H. and A.R. contributed to the discussion and interpretation of the data. S.L. contributed to the original idea of the paper, as well as to the discussion and interpretation of the data. All authors contributed to the final version of the manuscript.

Funding

Open Access funding enabled and organized by Projekt DEAL.

Competing interests

The authors declare no competing interests.

Additional information

Supplementary information The online version contains supplementary material available at https://doi.org/10.1038/s41467-025-67570-2.

Correspondence and requests for materials should be addressed to Francesco Troisi, Hannes Hübener, Angel Rubio or Simone Latini.

Peer review information *Nature Communications* thanks Giuseppe Meneghini and the other anonymous reviewer(s) for their contribution to the peer review of this work. A peer review file is available.

3.4 Publication III: Cavity-mediated electron-electron interactions: Renormalizing Dirac states in graphene

State of the art

Prior to this work, cavity materials engineering had established that vacuum fluctuations can modify the properties of materials, both theoretically [15, 16] and experimentally [55]. For gapped systems such as TMDs [15] or h-BN [16], these studies typically describe the material in a basis of electronic transitions on top of a fixed ground state, while the cavity mediates interactions between well-separated excitations. The low-energy properties of gapless materials like Graphene, which hosts inversion and time-reversal symmetry protected Dirac cones, are extremely sensitive to any modification of the ground-state electronic structure. In particular, the long-range nature of cavity-mediated interactions suggests that a consistent description should allow for a self-consistent reshaping of the ground state rather than only acting on a fixed set of transitions. Chiral optical cavities provide a route to break time-reversal symmetry and open topological gaps in model descriptions of Graphene [30, 82, 116]. Previous simulations indeed predicted an optical gap at the Dirac points using circularly polarized light [81]. Conversely, linearly polarized cavities, which do not break time-reversal symmetry, should not open any gap if the electronic states are fixed (i.e. they are not treated self-consistently). These observations motivate the development of a QED Hartree–Fock framework, where the ground state of Graphene is allowed to relax self-consistently, and cavity-induced electron-electron interactions are treated on equal footing with conventional Coulomb exchange.

Main findings

This contribution develops a photon-free, non-perturbative QED Hartree-Fock (QED-HF) framework via high-frequency downfolding of the Pauli-Fierz Hamiltonian, revealing cavity-induced nonlocal electron-electron interactions proportional to momentum operators $\frac{\hat{\boldsymbol{p}}_i \cdot \hat{\boldsymbol{p}}_j}{\omega}$ that arise from the vacuum fluctuations in the cavity. Applied to Graphene, QED-HF predicts different behavior for the Dirac states according to the polarization of the optical modes in the cavity. Chiral cavities (circular polarization) open a topological gap of $\Delta \sim 4$ meV, as the time-reversal symmetry protecting the Dirac cone is broken by the photons. Anisotropic linear polarized cavities, on the other hand, induce an gap of $\Delta \sim 2$ meV with wedge-shaped bands arising from long-range anisotropy. Note that this result is a pure quantum effect, which cannot be retried by classical methods and was very surprising to observe as linearly polarized light does not break time-reversal symmetry. Hence one would expect the Dirac cone to be preserved. Finally, the gapless Dirac cone is indeed preserved when isotropic dual modes are considered. However, in this case the Fermi velocity is renormalized, and it can be tuned via the modes amplitude and frequency.

Status and Publication details

This paper was published in *Science Advances* in October 2025 [51]. The supplementary information is available at https://www.science.org/doi/10.1126/sciadv.adz1855#supplementary-materials (not included in the present thesis).

Contribution

I had developed a code for simulating materials in optical cavities and used it to simulate Graphene [81], predicting the opening of a optical gap using circularly polarized light. Subsequently, the first author of Publication III developed the QED-HF framework (as well as its code) to explain such findings from the standpoint of the electronic states, as it is not obvious that aside from the optical gap there was also a gap in the electronic states. All authors have contributed to the analysis of the data and the revision of the manuscript.

SCIENCE ADVANCES | RESEARCH ARTICLE

CONDENSED MATTER PHYSICS

Cavity-mediated electron-electron interactions: Renormalizing Dirac states in graphene

Hang Liu[1]*, Francesco Troisi[1], Hannes Hübener[1], Simone Latini[1,2]*, Angel Rubio[1,3]*

Embedding materials in optical cavities has emerged as a strategy for tuning material properties. Here, we develop a nonperturbative quantum electrodynamical approach based on a photon-free self-consistent Hartree-Fock framework to model the coupling between cavity photons and electrons and crystals. We apply this approach to graphene coupled to cavity photons of different polarizations. Photons introduce nonlocal electron-electron interactions, solely due to the quantum nature of light, that lead to substantial renormalization of Dirac bands. The nonlocal interactions induced by anisotropic linearly polarized photons give rise to wedge-shaped bands and Dirac gap. When isotropic cavity photon modes are introduced, the Dirac cones remain gapless, but a Fermi velocity renormalization yet indicates the role of nonlocal interactions. This theoretical framework paves the way for revealing nonperturbative quantum effects in strongly coupled light-matter systems and allows for a more comprehensive discovery of cavity-induced phenomena.

INTRODUCTION

Engineering electromagnetic vacuum field fluctuations via optical cavities is emerging as a way to control the ground state of condensed matter systems (*1*–*8*). Cavity photon vacuum fluctuations have been experimentally demonstrated to control the reaction pathway of molecules by changing the potential energy landscape (*9*), affect the magneto-transport property of electron gas for tunable Landau levels and quantum Hall effects (*10*–*12*), and modify the electronic conductivity of organic and inorganic extended solids (*13*, *14*). These observations indicate that the vacuum fluctuations in optical cavities can be strong enough to mediate interactions and alter properties of quantum materials.

To understand and predict the impact of cavity vacuum fluctuations on materials, various theoretical approaches based on quantum electrodynamics (QED) have been used, with the main challenge being the modeling of cavity-mediated interactions, arising from the strong collective coupling of photons with electrons and nuclei. Photon-mediated interactions of a nonlocal type, beyond perturbation theory, are crucial for controlling atomic structures (*15*), charge transfer (*16*), chemical reactivity (*5*), and van der Waals forces (*17*) in molecules, as well as electron topology in atomic chains (*18*–*21*). These phenomena can only be grasped by approaches like Hartree-Fock (HF) approximation (*22*), coupled-cluster expansion (*16*), and exact diagonalization with partial or full configurations (*23*), which all share the capability of capturing photon-mediated nonlocal electron-electron interactions in a nonperturbative fashion. Moreover, quantum electrodynamical density functional theory (QEDFT) within the local-density approximation (*24*, *25*) provides another framework for exploring photon-mediated interactions and their consequent phenomena. It has been used for finite interacting systems, demonstrating cavity-induced donor-acceptor charge transfer (*26*) and spin glass behavior (*27*) in molecular clusters. The QEDFT is nonperturbative by construction; however, its functionals have not yet included nonlocal interactions. The present work can serve a guide to develop and improve QEDFT functionals in the future.

For extended crystalline systems, theoretical studies rely on a local approximation of cavity-induced interactions, and they are built on perturbative approximations (except for those using QEDFT) (*28*, *29*). Within perturbation theory, for example, the possibility of cavity-engineered topological phase transitions has been proposed in Su-Schrieffer-Heeger chains (*30*), graphene (*31*–*34*), and twisted layered materials (*35*, *36*). Also, modifications of superconducting properties in crystals have been explored using both perturbation theories (*37*–*40*) and nonperturbative QEDFT simulations (*41*). In the latter case, a local density approximation is used for the exchange-correlation functional, and therefore, if photon-mediated nonlocal interactions are to be included, then a different approach has to be devised.

Here, we develop a theoretical approach that addresses the coupling between optical cavities and extended crystals in a nonperturbative manner, enabling a precise description of photon-mediated nonlocal (long-range) electron interactions that arise from the quantum nature of cavity photons and have no counterparts for classical light fields. By making a high-frequency expansion of the exact QED Hamiltonian, we arrive at a photon-free Hamiltonian which features both local and nonlocal cavity-mediated electron interactions. It is important to stress that the nonlocal electron-electron interactions are not mediated by the Coulomb potential, but they result from the quantum vacuum fluctuations of the cavity photons. To solve the photon-free Hamiltonian, we perform the HF approximation on this photon-mediated interaction, arriving at what we call the photon-free QED-HF formulation, which is notably distinct from the HF method for Coulomb interactions. The direct and exchange interactions in the QED-HF formulation describe a kind of nonlocal electron-electron interaction, induced by fluctuating cavity photons, which should not be confused with that in the usual HF theory for the Coulomb electron-electron interactions. The photon-mediated nonlocal interactions arise even in a system of noninteracting electrons, where the coupling between electrons is mediated by the transverse part of the cavity vacuum field fluctuations.

With the photon-free QED-HF formulation, we investigate graphene coupled with various types of cavity electromagnetic fields

---

[1] Max Planck Institute for the Structure and Dynamics of Matter and Center for Free-Electron Laser Science, Luruper Chaussee 149, 22761, Hamburg, Germany. [2] Department of Physics, Technical University of Denmark, 2800 Kgs. Lyngby, Denmark. [3] Initiative for Computational Catalysis, The Flatiron Institute, 162 Fifth Avenue, New York, NY 10010, USA.
*Corresponding author. Email: hang.liu@mpsd.mpg.de (H.L.); simola@dtu.dk (S.L.); angel.rubio@mpsd.mpg.de (A.R.)

and find a substantial renormalization of Dirac electronic states. Our results show that the photon-mediated interactions induce a topologically nontrivial Dirac gap in graphene for a circularly polarized cavity photon mode and a trivial Dirac gap with a wedge-shaped band feature for a linearly polarized mode, as illustrated in Fig. 1, with the latter arising purely from the photon-induced nonlocal interactions. The gap opening from a circularly polarized mode, originating from time-reversal symmetry breaking, has a classical analog (*42*, *43*), while the gap opening from a linearly polarized mode is a result of the anisotropic long-range interactions and is a pure quantum effect induced by the cavity. This demonstrates a key difference in the phenomenology of cavity materials engineering versus Floquet engineering (*7*, *28*). When two cavity photon modes are present, all symmetries of intrinsic graphene can be restored, resulting in a gapless Dirac state with a modified Fermi velocity. Moreover, by tuning the mode polarization, amplitude, and frequency, the Dirac cones in graphene can be flexibly renormalized, establishing material symmetry engineering via optical cavities as a powerful tool for the manipulation of electronic band structure and its topology. The developed QED-HF theoretical framework is general and can be implemented as a first-principles method. Hence, it is applicable to a wide range of materials and cavity configurations and therefore opens the way to accurately model the electronic structure of materials strongly coupled to quantum vacuum field fluctuations without biasing the results through perturbative expansions.

RESULTS

Nonperturbative theory for interacting electrons and photons

Here, we present the theoretical framework for the nonperturbative modeling of an electronic system interacting with the fluctuating photons in a cavity. As discussed below, the framework is built using a HF approach and relies on a photon-free QED treatment of the light-matter coupled problem.

Photon-free QED Hamiltonian

For a system of N_e (nonrelativistic) electrons interacting with the electromagnetic field confined by a cavity, the minimal coupling prescription in Coulomb gauge together with an effective cavity photon mode description in the long-wavelength approximation (*44*) results in the following Pauli-Fierz QED Hamiltonian (*45*)

$$\widehat{H}=\sum_{i}^{N_e}\left[\frac{(\widehat{\mathbf{p}}_i-q\widehat{\mathbf{A}})^2}{2m}+\widehat{V}(\mathbf{r}_i)\right]+\hbar\omega\left(\frac{1}{2}+\widehat{a}^\dagger\widehat{a}\right) \tag{1}$$

where $\widehat{\mathbf{p}}_i=-i\hbar\nabla_{\mathbf{r}_i}$ is the momentum operator for the electrons (with electron charge $q=-|e|$ and mass m), and $\widehat{\mathbf{A}}=A_0(\widehat{a}^\dagger\mathbf{e}^*+\widehat{a}\mathbf{e})$ is the effective electromagnetic vector potential operator with mode amplitude A_0 and polarization vector $\mathbf{e}$, and ω is the cavity mode frequency. Physically, the Hamiltonian consists of three parts: the bare electron part $\widehat{H}_e=\sum_i^{N_e}\widehat{h}_e(\mathbf{r}_i)$ with $\widehat{h}_e(\mathbf{r}_i)=\frac{\widehat{\mathbf{p}}_i^2}{2m}+\widehat{V}(\mathbf{r}_i)$, the bare photon part $\widehat{H}_p=\hbar\omega\left(\frac{1}{2}+\widehat{a}^\dagger\widehat{a}\right)$, and the electron-photon interaction part $\widehat{H}_{int}=-\frac{q}{m}\sum_i^{N_e}\widehat{\mathbf{p}}_i\cdot\widehat{\mathbf{A}}+\frac{q^2N_e\widehat{\mathbf{A}}^2}{2m}$. The interaction part is in turn composed of a paramagnetic term with $\sum_i^{N_e}\widehat{\mathbf{p}}_i\cdot\widehat{\mathbf{A}}$ and a diamagnetic term with $\widehat{\mathbf{A}}^2$.

The diamagnetic term can be absorbed into the bare effective photon term using the Bogoliubov transformation in Supplementary Text A, reducing the Hamiltonian in Eq. 1 to

$$\widehat{H}=\widehat{H}_e+\hbar\tilde{\omega}\left(\frac{1}{2}\widehat{\tilde{a}}^\dagger\widehat{\tilde{a}}\right)-\frac{q}{m}\sum_{i}^{N_e}\widehat{\mathbf{p}}_i\cdot\widehat{\tilde{\mathbf{A}}} \tag{2}$$

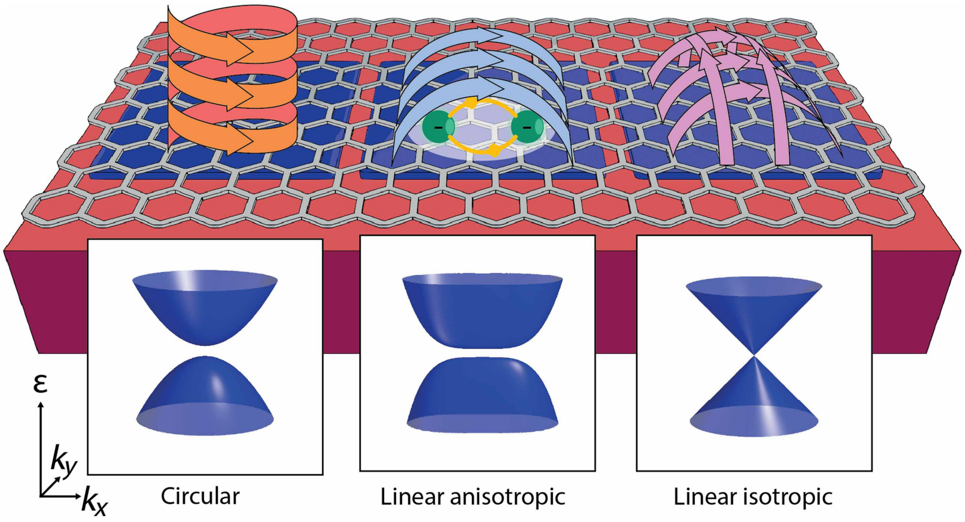

Fig. 1. Illustration of the renormalized Dirac cones of monolayer graphene coupled to cavity photon modes of different polarizations. Because of cavity-mediated electron interactions, a circularly polarized photon induces an isotropic Dirac gap with nontrivial band topology, while a linearly polarized photon induces a flat and anisotropic Dirac gap with trivial topology. In contrast, two isotropic linearly polarized photons, with the same frequency and amplitude and the perpendicular polarization directions, do not induce the Dirac gap but modify the Dirac Fermi velocity. In the setup, graphene is on the *xy* plane with $z = 0$, and *x* and *y* are along the zigzag and armchair directions of the graphene structure, respectively. k_x and k_y denote the coordinates in the two-dimensional reciprocal space of graphene, corresponding to the zigzag (*x*) and armchair (*y*) directions in real space, respectively. ε represents the energy of the QED-HF bands of graphene.

with the dressed mode frequency $\tilde{\omega}$ and vector potential operator $\hat{\tilde{\mathbf{A}}} = \tilde{A}_0(\hat{\tilde{a}}^{\dagger}\tilde{\mathbf{e}}^* + \hat{\tilde{a}}\tilde{\mathbf{e}})$. The polarization of the dressed mode remains the same as that of the undressed mode $\tilde{\mathbf{e}} = \mathbf{e}$. For a linearly polarized photon mode, diamagnetism renormalizes the mode frequency and amplitude to $\tilde{\omega} = \omega\sqrt{1 + \varsigma\frac{2N_e A_0^2}{\omega}}$ and $\tilde{A}_0 = A_0\frac{\sqrt{u+1} - \sqrt{u-1}}{\sqrt{2}}$ with $\varsigma = \frac{q^2}{m\hbar}$ (=1 in atomic unit) and $u = \frac{\varsigma N_e A_0^2 + \omega}{\sqrt{(2\varsigma N_e A_0^2 + \omega)\omega}}$, respectively. Differently, for a circularly polarized photon mode, diamagnetism renormalizes the mode frequency and amplitude to $\tilde{\omega} = \omega\left(1 + \varsigma\frac{N_e A_0^2}{\omega}\right)$ and $\tilde{A}_0 = A_0$, respectively.

The dressed Hamiltonian in Eq. 2 can be now represented in the dressed photon space $\{|\tilde{0}\rangle, \cdots, |\tilde{s}\rangle, \cdots\}$. Diagonal and subdiagonal matrix blocks have nonzero elements, and they satisfy $\langle\tilde{s}|\hat{H}|\tilde{s}\rangle = \langle\tilde{0}|\hat{H}|\tilde{0}\rangle + \tilde{s}\hbar\tilde{\omega}$ and $\langle\tilde{s}|\hat{H}|\tilde{s}+1\rangle = \sqrt{\tilde{s}+1}\langle\tilde{0}|\hat{H}|\tilde{1}\rangle$. This structure high-lights that when the dressed photon frequency is much higher than the typical electronic transition frequencies taken into account, the states in different photon sectors go off resonance. As a result, the Hamiltonian matrix can be conveniently downfolded into the zero photon sector and hence remove the photonic degrees of freedom (*46*, *47*). At the first order with respect to $\frac{\tilde{A}_0^2}{\tilde{\omega}}$, the downfolding is

$$\hat{H}_{\text{eff}} = \langle\tilde{0}|\hat{H}|\tilde{0}\rangle - \frac{\langle\tilde{0}|\hat{H}|\tilde{1}\rangle\,\langle\tilde{1}|\hat{H}|\tilde{0}\rangle}{\hbar\tilde{\omega}} \qquad (3)$$

where the integrals are calculated as $\langle\tilde{0}|\hat{H}|\tilde{0}\rangle = \hat{H}_e + \frac{\hbar\tilde{\omega}}{2}$, $\langle\tilde{0}|\hat{H}|\tilde{1}\rangle = -\frac{q\tilde{A}_0}{m}\sum_i^{N_e}\hat{\mathbf{p}}_i\cdot\mathbf{e}$, and $\langle\tilde{1}|\hat{H}|\tilde{0}\rangle = -\frac{q\tilde{A}_0}{m}\sum_i^{N_e}\hat{\mathbf{p}}_i\cdot\mathbf{e}^*$. This gives rise to the effective photon-free QED Hamiltonian

$$\hat{H}_{\text{eff}} = \hat{H}_e + \frac{\hbar\tilde{\omega}}{2} + \hat{H}_{\text{l}} + \hat{H}_{\text{nl}} \qquad (4)$$

where

$$\hat{H}_{\text{l}} = -\zeta\frac{\tilde{A}_0^2}{\tilde{\omega}}\sum_i^{N_e}(\hat{\mathbf{p}}_i\cdot\mathbf{e})(\hat{\mathbf{p}}_i\cdot\mathbf{e}^*) \qquad (5)$$

represents the photon-induced local single-electron interaction since it involves the momentum of the same particle i, and

$$\hat{H}_{\text{nl}} = -\zeta\frac{\tilde{A}_0^2}{\tilde{\omega}}\sum_i^{N_e}\sum_{j\neq i}^{N_e}(\hat{\mathbf{p}}_i\cdot\mathbf{e})(\hat{\mathbf{p}}_j\cdot\mathbf{e}^*) \qquad (6)$$

represents the photon-induced nonlocal electron-electron interaction involving two particles i and j, and $\zeta = \frac{\varsigma}{m}$ (= 1 in atomic unit). The induced electron-electron interaction is proportional to the electron momentum, which is different from the usual Coulomb electron-electron interaction that is proportional to $\frac{1}{|\mathbf{r}_i - \mathbf{r}_j|}$. It is important to note that the photon-induced nonlocal interaction depends on the amplitude, frequency, and polarization of a photon mode, highlighting its tunable nature for controlling matter properties. In addition, as the coupled embedded material size (i.e., N_e) increases, experimental setups should target a lower bare frequency or higher bare amplitude to achieve the desired interaction strength defined by $\frac{\tilde{A}_0^2}{\tilde{\omega}}$.

This cavity-mediated electron-electron interaction is a purely quantum phenomenon arising from the transverse component of the fluctuating photon fields. This is an effect that has no counterpart with classical light. To illustrate this explicitly, we use a coherent state of light, $|\tilde{\lambda}(t)\rangle = e^{-\frac{|\tilde{\lambda}|^2}{2}}\sum_{\tilde{s}=0}^{+\infty}\frac{\tilde{\lambda}^{\tilde{s}}}{\sqrt{\tilde{s}\,!}}e^{-i\tilde{\omega}(\tilde{s}+\frac{1}{2})t}|\tilde{s}\rangle$ satisfying $\hat{\tilde{a}}|\tilde{\lambda}(t)\rangle = \tilde{\lambda}e^{-i\tilde{\omega}t}|\tilde{\lambda}(t)\rangle$, as a proxy of classical light. We project the electron-photon Hamiltonian in Eq. 2 onto this state, yielding

$$\langle\tilde{\lambda}(t)|\hat{H}|\tilde{\lambda}(t)\rangle = \hat{H}_e + \hbar\tilde{\omega}\left(\frac{1}{2} + |\tilde{\lambda}|^2\right) - \frac{q}{m}\sum_i^{N_e}\hat{\mathbf{p}}_i\cdot\tilde{\mathbf{A}}(t) \qquad (7)$$

with $\tilde{\mathbf{A}}(t) = \tilde{A}_0(\tilde{\lambda}^* e^{i\tilde{\omega}t}\mathbf{e}^* + \tilde{\lambda}e^{-i\tilde{\omega}t}\mathbf{e})$. Through this projection, the vector potential operator $\hat{\tilde{\mathbf{A}}}$ acts as a classical vector potential $\tilde{\mathbf{A}}(t)$, leaving only light-mediated single electron corrections. The projected Eq. 7 is the Hamiltonian for classical time-periodic light driving in Floquet engineering (*7*).

Photon-free QED-HF formulation

To find the ground state of the many-particle Hamiltonian in Eq. 4, a HF approximation is applied to treat the photon-induced electron interactions in Eqs. 5 and 6. The electronic wave function is represented by a single Slater determinant that is constructed from the occupied single-particle orbitals $\{\varphi_i\}$ with energies $\{\varepsilon_i\}$. The orbitals can be obtained by solving the photon-free QED-HF equation (see Supplementary Text B for its derivation based on the minimization of the total energy)

$$\hat{\mathcal{F}}\,|\varphi_i\rangle = \varepsilon_i\,|\varphi_i\rangle \qquad (8)$$

with the Fock operator in first quantization

$$\mathcal{F}(\hat{\mathbf{r}}) = h(\hat{\mathbf{r}}) - \sum_j^{N_e}\mathcal{J}_j(\hat{\mathbf{r}}) - \mathcal{K}_j(\hat{\mathbf{r}}) \qquad (9)$$

The local part, consisting of the uncoupled electronic Hamiltonian and the operator from local interaction, is

$$h(\hat{\mathbf{r}}) = h_e(\hat{\mathbf{r}}) - \zeta\frac{\tilde{A}_0^2}{\tilde{\omega}}\hat{\Pi}_{\text{l}} \qquad (10)$$

with $\hat{\Pi}_{\text{l}} = (\hat{\mathbf{p}}_{\mathbf{r}}\cdot\mathbf{e})(\hat{\mathbf{p}}_{\mathbf{r}}\cdot\mathbf{e}^*)$. The direct operator from nonlocal interaction is

$$\mathcal{J}_j(\mathbf{r})f(\mathbf{r}) = \langle\varphi_j|\,\zeta\frac{\tilde{A}_0^2}{\tilde{\omega}}\hat{\Pi}_{\text{nl}}\,|\varphi_j\rangle f(\mathbf{r}) \qquad (11)$$

and the exchange operator from nonlocal interaction is

$$\mathcal{K}_j(\mathbf{r})f(\mathbf{r}) = \langle\varphi_j|\zeta\frac{\tilde{A}_0^2}{\tilde{\omega}}\hat{\Pi}_{\text{nl}}|f\rangle\varphi_j(\mathbf{r}) \qquad (12)$$

with $\hat{\Pi}_{\text{nl}} = (\hat{\mathbf{p}}_{\mathbf{r}}\cdot\mathbf{e})(\hat{\mathbf{p}}_{\mathbf{r}'}\cdot\mathbf{e}^*) + (\hat{\mathbf{p}}_{\mathbf{r}}\cdot\mathbf{e}^*)(\hat{\mathbf{p}}_{\mathbf{r}'}\cdot\mathbf{e})$ for any single-particle wave function $f(\mathbf{r})$. The integral in Eqs. 11 and 12 is for coordinate $\mathbf{r}'$. Because the Fock operator depends on its eigenstates, i.e., the occupied orbitals in Eq. 8, self-consistent calculations are required. While the self-consistent HF approach has been used for finite molecules in chemistry (*22*), only the nonself-consistent perturbative HF approach has been implemented for extended crystalline systems (*33*).

With spatial periodicity, the electrons in crystals outside a cavity are described by the Bloch states given by $h_e(\mathbf{r})\varphi_{n\mathbf{k}}^0(\mathbf{r}) = \varepsilon_{n\mathbf{k}}^0\varphi_{n\mathbf{k}}^0(\mathbf{r})$, where n and $\mathbf{k}$ define the bands and crystal momenta, respectively. To numerically solve Eq. 8, the Fock operator $\hat{\mathcal{F}}$ is expressed as a matrix, which we refer to as photon-free QED Fock matrix, in the basis set constructed from the electronic states $\{\varphi^0_{n\mathbf{k}}\}$ without interaction to cavity photons. The matrix elements $F_{n\mathbf{k}\,n'\mathbf{k}'} = \langle \varphi^0_{n\mathbf{k}} | \hat{\mathcal{F}} | \varphi^0_{n'\mathbf{k}'} \rangle = \delta_{\mathbf{k}\mathbf{k}'} \langle \varphi^0_{n\mathbf{k}} | \hat{\mathcal{F}} | \varphi^0_{n'\mathbf{k}} \rangle$ indicate that the matrix is diagonal in $\mathbf{k}$ space (see proof in Supplementary Text C). Thus, the QED Fock matrix can be constructed independently for each crystal momentum $\mathbf{k}$, i.e., $F_{nn'\mathbf{k}} = F_{\mathrm{l},nn'\mathbf{k}} + F_{\mathrm{nl},nn'\mathbf{k}}$. The contribution from the local operator is

$$F_{\mathrm{l},nn'\mathbf{k}} = \varepsilon^0_{n\mathbf{k}} \delta_{nn'} - \langle \varphi^0_{n\mathbf{k}} | \zeta \frac{\tilde{A}_0^2}{\tilde{\omega}} \hat{\Pi}_\mathrm{l} | \varphi^0_{n'\mathbf{k}} \rangle \tag{13}$$

and the contribution from the nonlocal operator is

$$F_{\mathrm{nl},nn'\mathbf{k}} = J_{nn'\mathbf{k}} + K_{nn'\mathbf{k}} \tag{14}$$

with the direct component

$$J_{nn'\mathbf{k}} = -\sum_{m\mathbf{k}'}^{\mathrm{occ}} \langle \varphi^0_{n\mathbf{k}} \varphi_{m\mathbf{k}'} | \zeta \frac{\tilde{A}_0^2}{\tilde{\omega}} \hat{\Pi}_\mathrm{nl} | \varphi^0_{n'\mathbf{k}} \varphi_{m\mathbf{k}'} \rangle \tag{15}$$

and the exchange component

$$K_{nn'\mathbf{k}} = \sum_{m}^{\mathrm{occ}} \langle \varphi^0_{n\mathbf{k}} \varphi_{m\mathbf{k}} | \zeta \frac{\tilde{A}_0^2}{\tilde{\omega}} \hat{\Pi}_\mathrm{nl} | \varphi_{m\mathbf{k}} \varphi^0_{n'\mathbf{k}} \rangle \tag{16}$$

where m indexes the occupied HF Bloch bands. The direct component $J_{nn'\mathbf{k}}$ accounts for the interaction of an electron with $\mathbf{k}$ to all the other electrons and itself, due to the sum of occupied orbitals for all crystal momenta $\mathbf{k}'$ in Eq. 15. In contrast, the exchange component $K_{nn'\mathbf{k}}$ accounts for the interaction of an electron with $\mathbf{k}$ to itself and the other electrons with the same crystal momentum $\mathbf{k}$, shown in Eq. 16. The self-direct and self-exchange interactions in direct and exchange components, respectively, exactly cancel with each other (see Supplementary Text B); as a result, the inclusion of both direct and exchange components guarantees the QED-HF approach to be self-interaction free.

The direct component $J_{nn'\mathbf{k}}$ is proportional to the total electron momentum $\mathbf{P} = \sum_{m\mathbf{k}'}^{\mathrm{occ}} \langle \varphi_{m\mathbf{k}'} | \hat{\mathbf{p}}_\mathbf{r} | \varphi_{m\mathbf{k}'} \rangle$ of the system. When $\mathbf{P} = 0$, the $J_{nn'\mathbf{k}}$ is zero, meaning that the Fock matrix is only contributed by the local and exchange components; thus, the Fock matrix for each crystal momentum $\mathbf{k}$ depends only on the states with the same crystal momentum $\mathbf{k}$, which allows the separate self-consistent iterations of wave functions for each $\mathbf{k}$. The resulting Fock matrix is solved and iteratively updated until convergence is reached.

In the local, direct and exchange components (Eqs. 13, 15, and 16] of the photon-free QED Fock matrix, the interaction prefactor $\frac{\tilde{A}_0^2}{\tilde{\omega}}$ scales with the number of electrons N_e, such as $\frac{\tilde{A}_0^2}{\tilde{\omega}} = \frac{A_0^2}{\omega}\left(1 + \zeta \frac{2N_e A_0^2}{\omega}\right)^{-1}$ and $\frac{\tilde{A}_0^2}{\tilde{\omega}} = \frac{A_0^2}{\omega}\left(1 + \zeta \frac{N_e A_0^2}{\omega}\right)^{-1}$ for a linearly and circularly polarized photon mode, respectively. This indicates that the modifications of electronic states by cavity fluctuating photons depend on the size of material systems.

As shown in (*44*), there is an intrinsic limit to the range over which electrons in a material are coupled to the effective cavity photon mode. Since the effective photon mode volume is finite, only the electrons within this volume should be counted in the light-matter interaction. This means that in the bulk limit (*44*), the light-matter coupling is maximized. Filling the mode volume with matter has an effect of the photon dressing from diamagnetism, which, in practice, implies that when fabricating and designing the cavity, the target frequency and amplitude of photon modes to be realized are the dressed ones. Last, compared with exact diagonalization, the photon-free QED-HF approximation is equivalent to an expansion of the electron-photon coupling problem on the ground and singly excited configuration states, as shown by the Brillouin's theorem for photon-induced electron interactions in Supplementary Text D.

The case of multiple cavity photon modes

A single effective photon mode inherently breaks the symmetry of matter by constraining the vacuum field to a single polarization. To include multiple polarizations, we allow for more cavity photon modes in the description of the light-matter interacting Hamiltonian. For a multimode cavity, the vector potential operator for $N_\mathrm{p} > 1$ photons is $\hat{\mathbf{A}} = \sum_\alpha^{N_\mathrm{p}} \hat{\mathbf{A}}_\alpha = \sum_\alpha^{N_\mathrm{p}} A_{0\alpha}(\hat{a}^\dagger_\alpha \mathbf{e}^*_\alpha + \hat{a}_\alpha \mathbf{e}_\alpha)$ with the mode index $\boldsymbol{\alpha}$. While the diamagnetic term resulting from this vector potential operator might mix different photons, a normal mode transformation $\hat{\mathbf{A}} = \sum_\alpha^{N_\mathrm{p}} \hat{\mathbf{A}}_\alpha \rightarrow \hat{\tilde{\mathbf{A}}} = \sum_\alpha^{N_\mathrm{p}} \hat{\tilde{\mathbf{A}}}_\alpha$ can be found (*45*), so that the multimode electron-photon Hamiltonian can be written as

$$\hat{H} = \hat{H}_\mathrm{e} + \sum_\alpha^{N_\mathrm{p}} \hbar\tilde{\omega}_\alpha \left(\frac{1}{2} + \hat{\tilde{a}}^\dagger_\alpha \hat{\tilde{a}}_\alpha\right) - \frac{q}{m} \sum_\alpha^{N_\mathrm{p}} \sum_i^{N_\mathrm{e}} \hat{\mathbf{p}}_i \cdot \hat{\tilde{\mathbf{A}}}_\alpha \tag{17}$$

with the dressed mode frequency $\tilde{\omega}_\alpha$, amplitude $\tilde{A}_{0\alpha}$, and polarization $\tilde{\mathbf{e}}_\alpha$.

A high-frequency downfolding procedure, equivalent to the one for single mode, can be applied to the multimode Hamiltonian in Eq. 17, which follows

$$\begin{aligned} \hat{H}_\mathrm{eff} = {} & \langle \tilde{0}_1, \cdots, \tilde{0}_{N_\mathrm{p}} | \hat{H} | \tilde{0}_1, \cdots, \tilde{0}_{N_\mathrm{p}} \rangle - \\ & \sum_\alpha^{N_\mathrm{p}} \Bigg[\frac{1}{\hbar\tilde{\omega}_\alpha} \langle \tilde{0}_1, \cdots, \tilde{0}_{N_\mathrm{p}} | \hat{H} | \tilde{0}_1, \cdots, \tilde{1}_\alpha, \cdots, \tilde{0}_{N_\mathrm{p}} \rangle \cdot \\ & \langle \tilde{0}_1, \cdots, \tilde{1}_\alpha, \cdots, \tilde{0}_{N_\mathrm{p}} | \hat{H} | \tilde{0}_1, \cdots, \tilde{0}_{N_\mathrm{p}} \rangle \Bigg] \end{aligned} \tag{18}$$

The multimode effective photon-free Hamiltonian is then given by

$$\hat{H}_\mathrm{eff} = \hat{H}_\mathrm{e} + \sum_\alpha^{N_\mathrm{p}} \left(\frac{\hbar\tilde{\omega}_\alpha}{2} + \hat{H}_{\mathrm{l},\alpha} + \hat{H}_{\mathrm{nl},\alpha} \right) \tag{19}$$

with $\hat{H}_{\mathrm{l},\alpha} = -\zeta \frac{\tilde{A}_{0\alpha}^2}{\tilde{\omega}_\alpha} \sum_i^{N_\mathrm{e}} (\hat{\mathbf{p}}_i \cdot \tilde{\mathbf{e}}_\alpha)(\hat{\mathbf{p}}_i \cdot \tilde{\mathbf{e}}^*_\alpha)$ and $\hat{H}_{\mathrm{nl},\alpha} = -\zeta \frac{\tilde{A}_{0\alpha}^2}{\tilde{\omega}_\alpha} \sum_i^{N_\mathrm{e}} \sum_{j \neq i}^{N_\mathrm{e}} (\hat{\mathbf{p}}_i \cdot \tilde{\mathbf{e}}_\alpha)(\hat{\mathbf{p}}_j \cdot \tilde{\mathbf{e}}^*_\alpha)$. This shows that the photon-free Hamiltonian in the case of multiple photons is a summation of the Hamiltonians corresponding to the demixed normal effective modes.

The photon-free QED-HF formulation can be directly extended to the cavities with multiple effective photon modes ($N_\mathrm{p} > 1$). The photon-free Hamiltonian in Eq. 19 features a summation of electron interactions from all the normal effective photon modes. Accordingly, the operator $\frac{\tilde{A}_0^2}{\tilde{\omega}} \hat{\Pi}_\mathrm{l}$ in Eq. 10 for a single mode should be replaced by $\sum_\alpha^{N_\mathrm{p}} \frac{\tilde{A}_{0\alpha}^2}{\tilde{\omega}_\alpha} \hat{\Pi}_{\mathrm{l},\alpha}$ with $\hat{\Pi}_{\mathrm{l},\alpha} = (\hat{\mathbf{p}}_\mathbf{r} \cdot \tilde{\mathbf{e}}_\alpha)(\hat{\mathbf{p}}_\mathbf{r} \cdot \tilde{\mathbf{e}}^*_\alpha)$, and the operator $\frac{\tilde{A}_0^2}{\tilde{\omega}} \hat{\Pi}_\mathrm{nl}$ in Eqs. 11 and 12 by $\sum_\alpha^{N_\mathrm{p}} \frac{\tilde{A}_{0\alpha}^2}{\tilde{\omega}_\alpha} \hat{\Pi}_{\mathrm{nl},\alpha}$ with $\hat{\Pi}_{\mathrm{nl},\alpha} = (\hat{\mathbf{p}}_\mathbf{r} \cdot \tilde{\mathbf{e}}_\alpha)(\hat{\mathbf{p}}_{\mathbf{r}'} \cdot \tilde{\mathbf{e}}^*_\alpha) + \hat{\Pi}_{\mathrm{nl},\alpha} = (\hat{\mathbf{p}}_\mathbf{r} \cdot \tilde{\mathbf{e}}_\alpha)(\hat{\mathbf{p}}_{\mathbf{r}'} \cdot \tilde{\mathbf{e}}^*_\alpha) + (\hat{\mathbf{p}}_\mathbf{r} \cdot \tilde{\mathbf{e}}^*_\alpha)(\hat{\mathbf{p}}_{\mathbf{r}'} \cdot \tilde{\mathbf{e}}_\alpha)$. Similar operator replacements should be applied to Eqs. 13, 15, and 16. Note that summing the interactions over multiple modes can effectively modify the interaction strength. In addition, the interaction term can vanish in certain cases. For example, this occurs when a two-dimensional material is coupled to out-of-plane polarized photon modes, as the material lacks an out-of-plane current response.

The QED-HF theoretical framework assumes cavity configurations where photon modes are dominated by the transverse component and exhibit negligible spatial variation on the scale of the matter system without resonance. However, it can be extended to include Coulomb-like direct and exchange interactions arising from the longitudinal photon component; it can also be adapted to on-resonant systems by incorporating higher-order downfolding expansions in the photon-free QED Hamiltonian. Moreover, the time-independent QED-HF framework can be adapted to model matter coupled to a driven cavity, where a dynamic Fock operator can be derived by approximating the wave function as a single time-dependent Slater determinant. When the system is time-periodic, Floquet theory can be used to eliminate the time dependence of the Fock operator and thereby get an effective QED-HF Floquet Hamiltonian, whose diagonalization yields the quasi-energy band structure of the driven system. Furthermore, the photon-free QED-HF method can be integrated into ab initio first-principles modeling packages to include the collective coupling between electrons, ions, and photons. Also, it can be extended to include correlations by combining it with QEDFT functional (*24*, *25*) while simultaneously improving the local approximation in QEDFT.

Effect of cavity-mediated nonlocal electron interactions on Dirac states in graphene

In this section, the photon-free QED-HF approach is used to study the modifications of Dirac states in graphene by cavity photons, with a specific focus on the modifications resulting from the cavity-mediated nonlocal electron-electron interaction.

The gapless Dirac states in graphene arise from the $2p_z$ orbitals of carbon atoms located at the A and B sites of a honeycomb lattice, satisfying, among others, time-reversal, spatial-inversion, and threefold rotational symmetries. Graphene is described by a tight-binding model with a nearest-neighbor (NN) hopping energy of $t_0 = -2.7$ eV (*48*), giving rise to Dirac cones with a Fermi velocity of $v_\mathrm{F} = 0.87 \times 10^6$ m/s at $\pm\mathbf{K}$ valleys. The main ingredient to calculate the cavity-mediated electron interactions in graphene is the momentum matrix element $\mathbf{p}_{mn\mathbf{k}} = -i\hbar\langle\varphi^0_{m\mathbf{k}}|\nabla_\mathbf{r}|\varphi^0_{n\mathbf{k}}\rangle$ with band indexes $m, n = \{v, c\}$ for lower valence (v) and upper conduction (c) Dirac bands with crystal momentum $\mathbf{k}$, whose evaluation from the contribution of $2p_z$ orbital (*49*, *50*) is described in Supplementary Text E.

In the ground state, the charge neutral graphene interacting with cavity photon modes has total momentum $\mathbf{P} = 0$. For each crystal momentum $\mathbf{k}$, the 2×2 QED Fock matrix in the basis set $\{\varphi^0_{v\mathbf{k}}, \varphi^0_{c\mathbf{k}}\}$ is iteratively constructed by following Eqs. 13 to 16 (see its explicit form for graphene in Supplementary Text F) and solved to find the cavity-renormalized HF orbitals. The photon-free QED-HF solutions are converged to an accuracy of 10^{-12} eV in the HF energy eigenvalue.

The following subsections present the cavity-renormalized Dirac states in graphene, interacting with linearly and circularly polarized cavity photon modes, as illustrated in Fig. 1. Graphene is on the xy plane with $z = 0$, and x and y are along the zigzag and armchair directions of the graphene structure, respectively. The corresponding directions in reciprocal space are denoted by k_x (zigzag) and k_y (armchair) with the unit of Å^{-1}. In this section, the frequency, amplitude, and polarization of dressed effective normal photon modes are denoted as ω, A_0, and $\mathbf{e}$, respectively, without a tilde symbol (~) in the notation for brevity.

Circularly polarized photon

To describe the interaction between the electrons in graphene and a circularly polarized cavity photon mode, we set the polarization vector to $\mathbf{e} = \mathbf{e}_x + i\mathbf{e}_y$ (parallel to the graphene plane), the photon energy to $\hbar\omega = 0.3$ eV, and the amplitude to $A_0 = 2 \times 10^{-8}\,\frac{\mathrm{kg \cdot m}}{\mathrm{C \cdot s}}$, which satisfies the high-frequency condition for the photon-free QED formulation for electrons close to the Dirac points and corresponds to an experimentally accessible mode volume $V = (320\text{Å})^3$ (*32*, *51*, *52*). We find that the photon-induced local interaction opens an energy gap at the Dirac points as previously reported in literature (*31*–*34*), while the nonlocal interaction further increases the size of the gap, a quantum effect which has thus far not been discussed. As shown in Fig. 2A, the local interaction breaks the degeneracy of the Dirac point at $+\mathbf{K}$ valley, resulting in the massive Dirac cone with a bandgap $\Delta \sim 2$ meV. With the inclusion of photon-induced nonlocal interaction, the Dirac gap is enlarged to $\Delta \sim 4$ meV (Fig. 2, A and B), and the valence and conduction electrons acquire a finite isotropic effective mass. This demonstrates that the photon-induced nonlocal electron-electron interaction in Eq. 6, originating from the quantum nature of cavity photons, plays an important role in the renormalization of Dirac states in graphene and can only be captured by a nonperturbative theoretical approach.

To analyze the formation of massive Dirac cones induced by a circularly polarized cavity photon, we evaluate the electronic wave function and the change of electron density in reciprocal and real space, respectively. In the basis set $\{\varphi^0_{v\mathbf{k}}, \varphi^0_{c\mathbf{k}}\}$, the wave function of the cavity-renormalized valence Dirac band in Fig. 2B is expressed as $\varphi_{v\mathbf{k}} = c_v\varphi^0_{v\mathbf{k}} + c_c\varphi^0_{c\mathbf{k}}$ for a given crystal momentum $\mathbf{k}$. Figure 2C shows $|c_c|^2$, i.e., the component of the original conduction Dirac state $\varphi^0_{c\mathbf{k}}$ without interaction to photon. This indicates that the original valence $\varphi^0_{v\mathbf{k}}$ and conduction $\varphi^0_{c\mathbf{k}}$ states are hybridized by the circularly polarized cavity photon mode, leading to the formation of a massive Dirac cone at $+\mathbf{K}$ valley (Fig. 2, A and B). The hybridization is isotropic in reciprocal space, as expected from the symmetry of the electron-photon coupling, and it is worth mentioning that the equivalent behavior is observed for the $-\mathbf{K}$ valley.

Figure 2D shows the cavity-induced modification of the electron density, $\Delta\rho(\mathbf{r}) = \sum_\mathbf{k} |\varphi_{v\mathbf{k}}|^2 - |\varphi^0_{v\mathbf{k}}|^2$, contributed from the reciprocal zone $\{k_x, k_y\} \in [-1, 1]\ 10^{-3}\text{Å}^{-1}$ with respect to crystal momenta $\pm\mathbf{K}$. The zone is large enough to contain all the modified Bloch states at $\pm\mathbf{K}$ valleys for obtaining the density variation (see Supplementary Text G for the calculation details of electron density). For the $+\mathbf{K}$ valley, the density increases at A sites and decreases at B sites. Oppositely, for the $-\mathbf{K}$ valley, the density decreases at A sites and increases at B sites. As a result, the electron density from $\pm\mathbf{K}$ valleys is different $|\varphi_{v,+\mathbf{K}}(\mathbf{r})|^2 \neq |\varphi_{v,-\mathbf{K}}(\mathbf{r})|^2$, indicating that time-reversal symmetry is broken by the circularly polarized photon.

The size of the cavity-induced Dirac gap can be tuned by adjusting the amplitude and frequency of the circularly polarized photon. As shown in Fig. 2E, for a fixed photon energy, the Dirac gap becomes larger with increasing mode amplitude, following the relation $\Delta \propto A_0^2$. For a fixed mode amplitude, instead, the Dirac gap becomes smaller with increasing mode frequency and evolves as $\Delta \propto \omega^{-1}$ (Fig. 2F). The overall evolution of the gap size follows $\Delta = \kappa\frac{A_0^2}{\omega}$. Although the evolution is similar to what is predicted for the Floquet Dirac gap in graphene induced by a time-periodic circularly polarized light field (*42*, *43*), the Floquet gap is only contributed from the

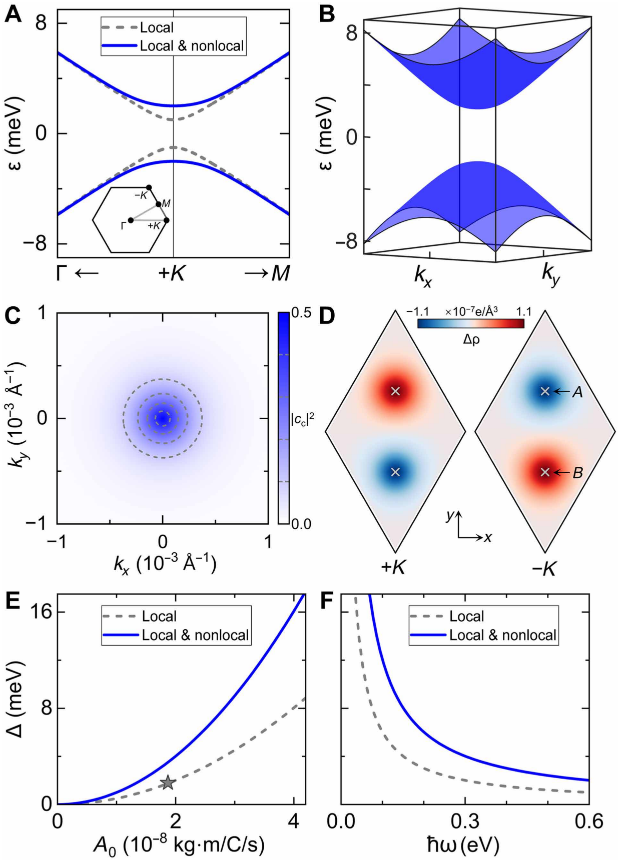

Fig. 2. Dirac states in graphene coupled with a circularly polarized photon mode. The mode has $\hbar\omega = 0.3\,\text{eV}$, $A_0 = 2\times10^{-8}\,\frac{\text{kg}\cdot\text{m}}{\text{C}\cdot\text{s}}$, and $\mathbf{e} = \mathbf{e}_x + i\mathbf{e}_y$. (**A**) HF bands of the +**K** valley (inset) along Γ ← +**K** → **M** path. (**B**) Representation of the blue band in (A) in the two-dimensional reciprocal zone $\{k_x, k_y\} \in [-1, 1]\ 10^{-3}\text{Å}^{-1}$ centered at the crystal momentum +**K**. (**C**) Component $|c_c|^2$ of the conduction basis state $\varphi^0_{c\mathbf{k}}$ for the lower valence band ($\varphi_{v\mathbf{k}} = c_v\varphi^0_{v\mathbf{k}} + c_c\varphi^0_{c\mathbf{k}}$) in (B). (**D**) Variation of the electron density, $\Delta\rho(\mathbf{r}) = \sum_{\mathbf{k}} |\varphi_{v\mathbf{k}}|^2 - |\varphi^0_{v\mathbf{k}}|^2$, at the specific $z = 0.33$ Å plane, where the $2p_z$ atomic orbital of carbon has its maximum. The left (right) shows the contribution to density from the +**K** (− **K**) valley. The cross signs mark the position of the *A* and *B* sites. (**E** and **F**) Evolution of the Dirac bandgap in (A) as a function of the A_0 (with fixed $\hbar\omega = 0.3$ eV) and photon energy $\hbar\omega$ (with fixed $A_0 = 2\times10^{-8}\,\frac{\text{kg}\cdot\text{m}}{\text{C}\cdot\text{s}}$), respectively. The star in (E) denotes the data from perturbation approach (*32*, *34*).

local electron interaction mediated by the classical light. The dependence on the mode amplitude and frequency originates from the interaction prefactor $\frac{A_0^2}{\omega}$ in Eqs. 5 and 6, and the coefficient κ is determined by the polarization-dependent momentum matrix elements of graphene. As a sanity check, we note that the gap size is on the order of 10 meV, while the cavity photon energy is on the order of 0.3 eV; hence, the high-frequency approximation for the photon-free QED Hamiltonian in Eq. 4 is justified.

A gap size of $\Delta = 1.8$ meV, induced by a circularly polarized cavity photon with $\hbar\omega = 0.3$ eV and $A_0 = 1.87\times10^{-8}\,\frac{\text{kg}\cdot\text{m}}{\text{C}\cdot\text{s}}$, has been previously reported on the basis of perturbation theory (*31*–*34*). This is quantitatively consistent with our results for the case with only the photon-mediated local electron interaction, which demonstrates that the photon-induced nonlocal electron-electron interaction is missed in the previous perturbation modeling. Thus, the nonperturbative self-consistent photon-free QED-HF approach is necessary for the predictions of the photon-induced nonlocal interaction on the renormalization of Dirac states in graphene, as a unique quantum effect arising from cavity photons (with no counterpart for classical light, as discussed in the "Photon-free QED Hamiltonian" section).

Linearly polarized photon

For a linearly polarized photon mode, we choose the polarization $\mathbf{e} = \mathbf{e}_x$ (i.e., along the zigzag direction of graphene) and keep the photon energy $\hbar\omega = 0.3$ eV and mode amplitude $A_0 = 2\times10^{-8}\,\frac{\text{kg}\cdot\text{m}}{\text{C}\cdot\text{s}}$ as before. As shown in Fig. 3A, the photon-mediated local interaction does not break the Dirac degeneracy. In contrast, with the induced nonlocal interaction, the Dirac degeneracy is destroyed, and a bandgap of $\Delta \sim 2$ meV is formed at both ±**K** valleys. As shown in Fig. 3B, the gapped Dirac cones are anisotropic in reciprocal space and so are the effective masses associated to the bands.

Different from the case of a circularly polarized photon where the renormalization is isotropic, the cavity-renormalized Dirac states by a linearly polarized photon are in an anisotropic superposition of valence and conduction basis states in reciprocal space. This can be quantified through the electron wave function $\varphi_{v\mathbf{k}} = c_v\varphi^0_{v\mathbf{k}} + c_c\varphi^0_{c\mathbf{k}}$ shown in Fig. 3C. Here, the conduction component $|c_c|^2$ has a butterfly shape elongated along the k_x direction in reciprocal space, indicating that threefold rotational symmetry is broken by the linearly polarized photon.

Figure 3D shows the modification of the electron density from the ±**K** valleys, where the density variation, which is the same for the two valleys, is mainly on the $A-B$ bonds between the NN sites. The density increases on the vertical bonds and decreases on the other bonds, showing that the threefold rotational symmetry, intrinsic to the bare graphene, is broken. At the same time, the renormalized Dirac electron wave functions satisfy $|\varphi_{v,+\mathbf{K}}(\mathbf{r})|^2 = |\varphi_{v,-\mathbf{K}}(\mathbf{r})|^2$, indicating that time-reversal symmetry is not broken. In other words, the Dirac gap opening in the case of a linearly polarized cavity photon is not a consequence of time-reversal symmetry breaking and instead connected to the long-range anisotropy (characterized by threefold rotational symmetry breaking) in the presence of the photon-induced nonlocal electron-electron interaction.

In Fig. 3 (A and B), approaching +**K** along the +**K** − Γ direction, the renormalized Dirac bands change abruptly to become perfectly flat in the direction of the cavity polarization vector. The bands are instead shaped like a wedge. As discussed below in the section related to the effective hopping integrals, these sharp kink features are a consequence of an unphysical infinitely long-range electron-electron interaction due to the long wavelength approximation and can be prevented by truncating the interaction range. By introducing a small sublattice potential difference $V_{AB} = \pm2\times10^{-5}t_0$ at *A* and *B* sites [or a weak spin-orbit coupling (SOC) strength, which would be there for realistic graphene], the bands smoothen, as shown in Fig. 3A. The long-range anisotropy from nonlocal interaction dominates the global band renormalization as in the case of $V_{AB} = 0$ (see Supplementary Text F and the section related to the effective hopping integrals).

To understand the flat-line band, we analyze the wave functions $\varphi_{v\mathbf{k}} = c_A\varphi^0_{A\mathbf{k}} + c_B\varphi^0_{B\mathbf{k}}$ for valence Dirac states in the sublattice basis set $\{\varphi^0_{A\mathbf{k}}, \varphi^0_{B\mathbf{k}}\}$ (see Supplementary Text E for the $\varphi^0_{A\mathbf{k}}$ and $\varphi^0_{B\mathbf{k}}$ functions). We specifically choose a path along k_y for $k_x = k_0 = -2\times$

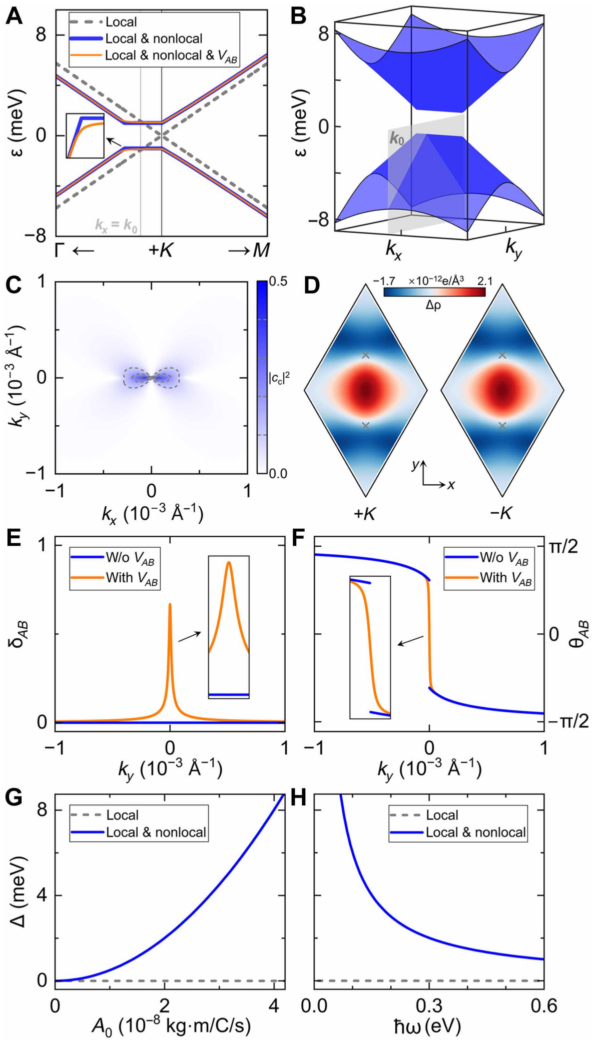

Fig. 3. Dirac states in graphene coupled with a linearly polarized photon mode. The mode has $\hbar\omega = 0.3$ eV, $A_0 = 2 \times 10^{-8} \frac{\text{kg}\cdot\text{m}}{\text{C}\cdot\text{s}}$, and $\mathbf{e} = \mathbf{e}_x$. (**A**) HF bands of the +**K** valley with and without nonlocal interaction. The former are also shown in the presence of a tiny sublattice potential value $V_{AB} = \pm 2 \times 10^{-5} t_0$. (**B**) Representation of the blue band in (A) in $\{k_x, k_y\} \in [-1, 1]\ 10^{-3}$ Å^{-1} centered at +**K**. (**C**) Component $|c_c|^2$ of the conduction basis state $\varphi^0_{c\mathbf{k}}$ for the lower valence band ($\varphi_{v\mathbf{k}} = c_v \varphi^0_{v\mathbf{k}} + c_c \varphi^0_{c\mathbf{k}}$) in (B). (**D**) Variation of electron density, $\Delta\rho(\mathbf{r}) = \sum_{\mathbf{k}} |\varphi_{v\mathbf{k}}|^2 - |\varphi^0_{v\mathbf{k}}|^2$, at $z = 0.33$ Å plane for $V_{AB} = 0$. The left (right) shows the contribution from the +**K** (− **K**) valley. (**E** and **F**) The difference of wave function amplitude δ_{AB} (phase θ_{AB}) between the A and B sites for the valence states across the plane $k_x = k_0 = -2 \times 10^{-4}$ Å^{-1} [the gray plane in (B)]. Blue (orange) lines are for graphene with $V_{AB} = 0$ ($\pm 2 \times 10^{-5} t_0$). (**G** and **H**) Evolution of the Dirac bandgap in (A) as a function of A_0 (with fixed $\hbar\omega = 0.3$ eV) and $\hbar\omega$ (with fixed $A_0 = 2 \times 10^{-8} \frac{\text{kg}\cdot\text{m}}{\text{C}\cdot\text{s}}$) for $V_{AB} = 0$, respectively.

10^{-4} Å^{-1} (indicated by the gray plane in Fig. 3B). We consider both the case of zero and finite sublattice potential V_{AB}. In Fig. 3E, we plot the quantity $\delta_{AB} = |c_{A\mathbf{k}}| - |c_{B\mathbf{k}}|$, which describes the difference in the magnitudes of the wave fuction coefficients for the two lattice sites. When $V_{AB} = 0$, both sites are equivalent, i.e., $\delta_{AB} = 0$, preserving spatial inversion symmetry. Looking at the phase difference $\theta_{AB} = \text{Arg}(c_{A\mathbf{k}}) - \text{Arg}(c_{B\mathbf{k}})$ in Fig. 3F, we observe a discontinuity crossing the flat line, where a QED-HF solution cannot be found exactly at the kink and flat line. This indicates the presence of an unphysical singularity. The singularity is removed by introducing a finite V_{AB}, as evidenced by the continuous and smooth behaviors of δ_{AB} and θ_{AB} in Fig. 3 (E and F).

Last, the size of the Dirac gap, induced by a linearly polarized photon, is also tunable through adjustments of the photon parameters. As shown in Fig. 3 (G and H), with only the local interaction, the Dirac cones remain gapless regardless of the choice of photon parameters. With the nonlocal electron-electron interaction included, the Dirac gap goes again as $\Delta = \xi \frac{A_0^2}{\omega}$, but the prefactor ξ is different from that for a circularly polarized mode. Also, the length of the flat line is affected by photon parameters and evolves as $L = \chi \frac{A_0^2}{\omega}$. The direction of the singular flat line in reciprocal space corresponds to the polarization direction of the photon mode in real space and hence can be rotated in the $k_x k_y$ plane at will by changing the mode polarization in the xy plane (see details in Supplementary Text H). The emergence of the singular flat-line band feature is analytically demonstrated using the two-dimensional low-energy effective Dirac model in Supplementary Text I, and also the prefactors ξ and χ for the bands evolution are analytically derived. The case of a linearly polarized cavity photon mode demonstrates that the nonperturbative QED-HF approach is essential to grasp the unique quantum effect, missed in perturbation theory, from the photon-induced nonlocal interaction in the collective electron-photon hybrid system.

Ellipticity and band topology

Here, we investigate the renormalization of Dirac states by a cavity photon as its polarization transitions from circular to linear. The elliptically polarized photon is implemented by setting the polarization vector to $\mathbf{e} = \mathbf{e}_x \cos\eta + i\mathbf{e}_y \sin\eta$ and keeping the mode frequency and amplitude as before. A circularly and linearly polarized photon mode has the ellipticity degree $\tan\eta = 1$ and 0 with the ellipticity angle $\eta = \frac{\pi}{4}$ and 0, respectively. As shown in Fig. 4A, for a single photon mode, the cavity-induced Dirac gap decreases with decreasing $\tan\eta$: With only the photon-mediated local interaction, the Dirac gap decreases to zero, whereas the gap stays finite with the nonlocal interaction included. We also note that decreasing the ellipticity degree, i.e., $\tan\eta = 1, 0.41, 0.02$ respectively with $\eta = \frac{\pi}{4}, \frac{\pi}{8}, \frac{\pi}{180}$, the Dirac dispersion becomes sharper around crystal momenta $\pm\mathbf{K}$ (Fig. 4B).

Since a circularly polarized light field can affect the band topology of Dirac states in graphene (*32*–*34*, *42*, *43*), we now discuss the evolution of the Berry curvature of cavity-renormalized Dirac bands as the ellipticity degree $\tan\eta$ goes from 1 to 0. The Berry curvature for the occupied valence Dirac band is computed, after the self-consistent QED-HF iterations, as

$$\Omega_{\mathbf{k}} = -\frac{2Im[\langle\varphi_{v\mathbf{k}}|\hat{v}_x|\varphi_{c\mathbf{k}}\rangle\langle\varphi_{c\mathbf{k}}|\hat{v}_y|\varphi_{v\mathbf{k}}\rangle]}{(\varepsilon_{c\mathbf{k}} - \varepsilon_{v\mathbf{k}})^2} \tag{20}$$

with velocity operators $\hat{v}_x = \frac{\partial\hat{\mathcal{F}}}{\partial k_x}$ and $\hat{v}_y = \frac{\partial\hat{\mathcal{F}}}{\partial k_y}$ and the photon-free QED Fock operator $\hat{\mathcal{F}}$. Figure 4C shows that, with circular polarization ($\tan\eta = 1$), the $\Omega_{\mathbf{k}}$ for the valence band is nonzero around the $\pm\mathbf{K}$ valleys. The integration of $\Omega_{\mathbf{k}}$ in the first Brillouin zone (BZ) gives rise to a finite Chern invariant $C = \frac{1}{2\pi}\int_{\text{BZ}} \Omega_{\mathbf{k}} d\mathbf{k} = 1$. This indicates that a circularly polarized photon induces a topologically nontrivial phase, which can support quantum anomalous Hall states, and is consistent with time-reversal symmetry breaking shown in the section related to circularly polarized photon modes.

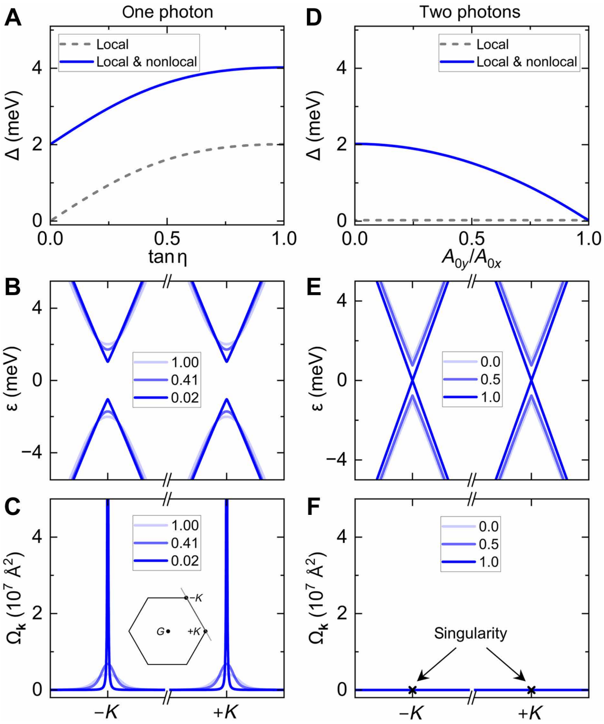

Fig. 4. Evolution of cavity-renormalized Dirac states and band topology. (**A**) Using a single photon mode with $\hbar\omega = 0.3$ eV, $A_0 = 2 \times 10^{-8}\,\frac{\text{kg}\cdot\text{m}}{\text{C}\cdot\text{s}}$, and $\mathbf{e} = \mathbf{e}_x\cos\eta + i\mathbf{e}_y\sin\eta$, the Dirac bandgap changes with mode ellipticity degree tanη. (**B**) HF bands of the ±**K** valleys, from local and nonlocal interactions, for ellipticity degrees tanη = 1,0.41, and 0.02, corresponding to ellipticity angles $\eta = \frac{\pi}{4}, \frac{\pi}{8}$, and $\frac{\pi}{180}$, respectively. (**C**) Berry curvature for the valence band in (B). (**D**) Change of the Dirac bandgap with mode amplitude ratio $\frac{A_{0y}}{A_{0x}}$ in the presence of two linearly polarized photon modes with $\mathbf{e} = \mathbf{e}_x$ and $\mathbf{e}_y$. The photon energy of the two modes is $\hbar\omega = 0.3$ eV, and the amplitude of x-polarized mode is fixed as $A_{0x} = 2 \times 10^{-8}\,\frac{\text{kg}\cdot\text{m}}{\text{C}\cdot\text{s}}$. (**E**) HF bands of ±**K** velleys, from local and nonlocal interactions, for the amplitude ratio $\frac{A_{0y}}{A_{0x}} = 0.0$,0.5, and 1.0. (**F**) Berry curvature for the valence band in (E), where the cross signs indicate that the Berry curvature is singular for the valence band at the crystal momenta ±**K**.

As the ellipticity degree tanη decreases, the Berry curvature gets sharper around the crystal momenta ±**K**, as shown in Fig. 4C. The Chern number is still $C = 1$, and hence the nontrivial topology is preserved for the elliptically polarized mode. The relation $\Omega_{-\mathbf{k}} = \Omega_{+\mathbf{k}} \neq 0$ indicates the preserved spatial-inversion symmetry and broken time-reversal symmetry. In addition, the $\boldsymbol{\Omega}_{\mathbf{k}}$ in two-dimensional BZ shows that the threefold rotational symmetry is broken, showing that the gap opening from the mode with $1 > \tan\eta > 0$ is also related to anisotropy in a long-range distance (accompanied with threefold rotational symmetry breaking).

For zero ellipticity degree $\tan\eta = 0$, i.e., a linearly polarized photon, the Berry curvature is zero everywhere in the BZ except on the flat-line band dispersion discussed in the section related to the linearly polarized photon, where its value cannot be calculated since the wave functions are singular. The zero Berry curvature for all the physical states indicates that the Dirac bandgap induced by a linearly polarized mode is topologically trivial.

Two linearly polarized photons: Isotropic case

Experimentally, it might be challenging to set up a cavity with a perfectly linearly polarized single photon mode, as it would require to fully suppress the mode with the other polarization direction. Hence, for a more general description, we discuss the case of two photon modes linearly polarized along the planar directions x and y. We start by considering an isotropic cavity with two degenerate linearly polarized photons with the same mode amplitude $A_0 = 2 \times 10^{-8}\,\frac{\text{kg}\cdot\text{m}}{\text{C}\cdot\text{s}}$ and the same photon energy $\hbar\omega = 0.3$ eV, as before. As shown in Fig. 5 (A and B), there is a very small difference (on the order of ~1 μeV) of energy eigenvlues in the renormalized Dirac bands when only local or both local and nonlocal interactions are included. Notably, the renormalized Dirac cones remain gapless, while the Fermi velocity is slightly modified. Along the +**K** → **M** paths, the Dirac Fermi velocity at the valley has the maximum variation of 0.5 per mil.

To show the effects of the two photons, we study again the wave functions and density of electrons for the renormalized Dirac cones. As shown in Fig. 5C, the original Dirac valence and conduction states hybridize with each other. Compared with that in the case of a circularly and linearly polarized photon, respectively, in Figs. 2C and 3C, the states hybridization at the +**K** valley is significantly weaker in the case of the two isotropic linearly polarized photons. Correspondingly, the renormalization of Dirac bands in Fig. 5 (A and B) is much weaker than that in the case of a circularly and linearly polarized photon, shown in Figs. 2 (A and B) and 3 (A and B), respectively.

The modification of the electron density is analyzed for the four valence states corresponding to the generic crystal momenta $-\mathbf{k}_0$, $+\mathbf{k}_0$, $+\mathbf{k}_0'$, and $+\mathbf{k}_0''$ at the ±**K** valleys (inset in Fig. 5D). The momenta $-\mathbf{k}_0$ and $+\mathbf{k}_0$ are related by inversion symmetry, and $+\mathbf{k}_0$, $+\mathbf{k}_0'$, and $+\mathbf{k}_0''$ are connected by threefold rotational symmetry. As shown in Fig. 5D, the density variation for each of the four crystal momenta satisfies $\Delta\rho(\mathbf{r}) = \Delta\rho(-\mathbf{r})$, showing that the interacting system has spatial-inversion symmetry. At the same time, $\Delta\rho_{-\mathbf{k}_0}(\mathbf{r}) = \Delta\rho_{+\mathbf{k}_0}(\mathbf{r})$ holds, indicating that time-reversal symmetry is preserved. Furthermore, the density variation for $+\mathbf{k}_0$, $+\mathbf{k}_0'$, and $+\mathbf{k}_0''$ satisfies $\Delta\rho_{+\mathbf{k}_0}(\mathbf{r}) = \Delta\rho_{+\mathbf{k}_0'}(\hat{C}_3\mathbf{r}) = \Delta\rho_{+\mathbf{k}_0''}(\hat{C}_3\hat{C}_3\mathbf{r})$, with $\hat{C}_3$ threefold rotational operator, showing that the interacting system is threefold rotation symmetric. Thus, the two isotropic linearly polarized photons do not break the symmetries of graphene, and consequently, the Dirac cones in the electron-photon interacting system remain gapless, while the Fermi velocity is modified. In Supplementary Text I, the analytical QED-HF solutions also suggest that the Dirac cones remain gapless for graphene interacting with two isotropic linearly polarized photons.

By changing the amplitude and frequency of the two linearly polarized photon modes, the renormalization of the Dirac Fermi velocity can be modified. As shown in Fig. 5 (E and F), for a fixed photon energy $\hbar\omega = 0.3$ eV, the Fermi velocity increases with the mode amplitude; with fixed mode amplitude $A_0 = 2 \times 10^{-8}\,\frac{\text{kg}\cdot\text{m}}{\text{C}\cdot\text{s}}$, instead, the Fermi velocity decreases with increasing frequency. This shows the variation of the Dirac Fermi velocity follows the relation $|\Delta v_{\text{F}}| = \tau\frac{A_0^2}{\omega}$, where τ is determined by the momentum elements of graphene. If only local interaction is included, then no changes in the Dirac Fermi velocity are observed.

Two linearly polarized photons: Anisotropic case

We now study the evolution of the Dirac states in graphene when changing the two linearly polarized photon modes from isotropic to anisotropic. For the two modes, the photon energy is fixed to be the same as before; the amplitude of the x mode is fixed as $A_{0x} = 2 \times 10^{-8}\,\frac{\text{kg}\cdot\text{m}}{\text{C}\cdot\text{s}}$, while the amplitude of the y mode is tuned

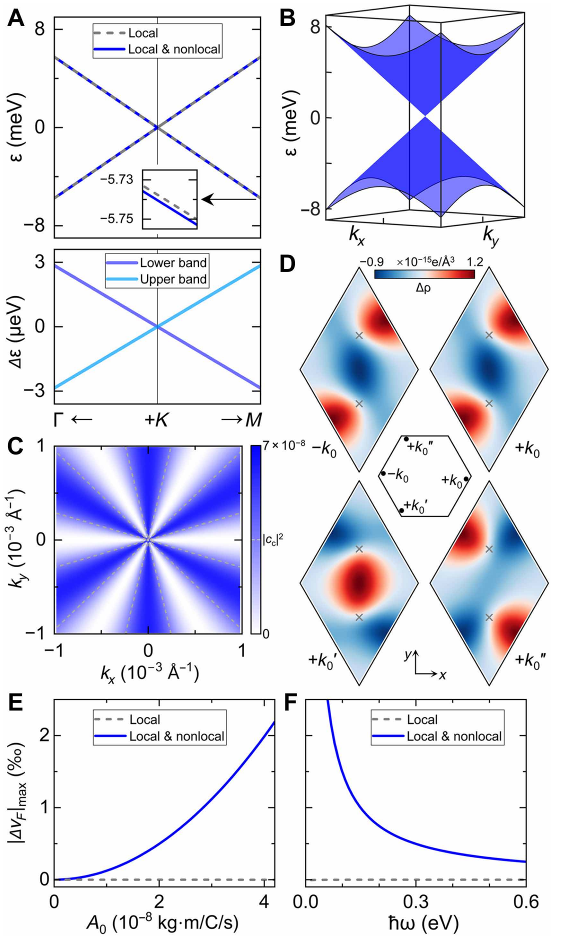

Fig. 5. Dirac states in graphene coupled with two isotropic linearly polarized photon modes. The two modes have the same $\hbar\omega = 0.3$ eV and $A_0 = 2 \times 10^{-8} \frac{\text{kg}\cdot\text{m}}{\text{C}\cdot\text{s}}$, but the perpendicular polarization vectors $\mathbf{e} = \mathbf{e}_x$ and $\mathbf{e}_y$. (**A**) HF bands for the +**K** valley. The bottom shows the variation of the bands due to addition of the nonlocal interaction. (**B**) Representation of the blue band in (A) in $\{k_x, k_y\} \in [-1, 1]\ 10^{-3}$Å^{-1} centered at +**K**. (**C**) Component $|c_c|^2$ of the conduction basis state $\varphi^0_{c\mathbf{k}}$ for the lower valence band ($\varphi_{v\mathbf{k}} = c_v\varphi^0_{v\mathbf{k}} + c_c\varphi^0_{c\mathbf{k}}$) in (B). (**D**) Variation of the electron density, $\Delta\rho(\mathbf{r}) = \sum_{\mathbf{k}} |\varphi_{v\mathbf{k}}|^2 - |\varphi^0_{v\mathbf{k}}|^2$, at $z = 0.33$ Å plane. The four panels show the contribution from the valence states with crystal momenta $-\mathbf{k}_0$, $+\mathbf{k}_0$, $+\mathbf{k}_0'$, and $+\mathbf{k}_0''$. $-\mathbf{k}_0$ is inversely symmetric to $+\mathbf{k}_0$, and the $+\mathbf{k}_0'$ and $+\mathbf{k}_0''$ are rotated by 120° and 240° with respect to $+\mathbf{k}_0$. (**E** and **F**) Evolution of the Fermi velocity along +**K** → **M** as a function of A_0 (with fixed $\hbar\omega = 0.3$ eV) and $\hbar\omega$ (with fixed $A_0 = 2 \times 10^{-8} \frac{\text{kg}\cdot\text{m}}{\text{C}\cdot\text{s}}$), respectively.

between $A_{0y} = 0$ and $A_{0y} = A_{0x}$. Such a cavity setup could be realized, for instance, in a cavity whose mirrors are made of a material with an anisotropic dielectric function. The most convenient way to represent the two cavity photon modes is by aligning them along the principal axes, which are assumed to be the perpendicular x and y directions here. Any other choice would be equivalent but would result in additional mode mixing terms in the Hamiltonian. As shown in Fig. 4D, we observe a smooth transition from the completely anisotropic case, with a Dirac bandgap $\Delta \sim 2$ meV induced by a single linearly polarized photon (Fig. 3), to the completely isotropic case, with no Dirac bandgap instead (Fig. 5). We stress once again that this behavior holds only if the photon-induced nonlocal interaction is included. In Fig. 4E, the bands along the $-\mathbf{K} \to +\mathbf{K}$ path are shown for different ratios $\frac{A_{0y}}{A_{0x}}$, evolving from the anisotropic to the isotropic case. Along with the reduction of gap size to zero, the length of the singular flat line of the Dirac bands (Fig. 3) gradually decreases to zero. The quantum effects on graphene of two anisotropic linearly polarized modes remain qualitatively the same as those in the single-mode case. Experimentally, such anisotropic photon mode configurations can be achieved using spatially anisotropic cavity designs, including Fabry-Pérot cavities with anisotropic mirror geometry or dielectric properties, split-ring resonator cavities with inherent structural anisotropy, and photonic crystal cavities (*29*, *53*–*55*).

As shown in Fig. 4F, the Berry curvature $\mathbf{\Omega}_{\mathbf{k}}$ of the valence Dirac band is zero, and it is undefined for the crystal momenta $\pm\mathbf{K}$, which shows that the Dirac gap induced by the two linearly polarized photon modes is topologically trivial regardless of the anisotropy. Note that, also for the graphene outside the cavity, the $\mathbf{\Omega}_{\mathbf{k}}$ is zero and undefined for the $\pm\mathbf{K}$. In addition, the relation $\mathbf{\Omega}_{-\mathbf{k}} = \mathbf{\Omega}_{+\mathbf{k}} = 0$ indicates that both time-reversal and spatial-inversion symmetries are preserved. The narrowing of Dirac gap is related to the recovery of isotropy (together with threefold rotational symmetry) when approaching the case of two isotropic photon modes, i.e., $\frac{A_{0y}}{A_{0x}} \to 1$.

Effective hopping integrals

In the section for the case of linearly polarized photons, we suggested that the presence of the singular flat line in the band structure of graphene coupled to a single linearly polarized photon is a symptom of the unphysical infinite-range description of the photon-induced interactions. To corroborate this claim, we here analyze the electron interactions in a real space tight-binding representation, where we map the interactions (both local and nonlocal) to hopping terms and show how a physical description of the interaction can be recovered. We compute the mediated effective electron hopping integrals by photon-induced interactions for arbitrary range as follows: The QED Fock matrix $F_{\{v,c\}\ \mathbf{k}}$ in the basis set $\{\varphi^0_{v\mathbf{k}}, \varphi^0_{c\mathbf{k}}\}$, directly obtained from the calculations in $\mathbf{k}$ space (as performed in all sections above), is transformed into $F_{\{A,B\}\ \mathbf{k}}$

$$F_{\{A,B\}\ \mathbf{k}} = \begin{bmatrix} F_{AA\ \mathbf{k}} & F_{AB\ \mathbf{k}} \\ F_{BA\ \mathbf{k}} & F_{BB\ \mathbf{k}} \end{bmatrix} \tag{21}$$

in the AB site representation with the basis set $\{\varphi^0_{A\mathbf{k}}, \varphi^0_{B\mathbf{k}}\}$, where $2p_z$ orbitals are used for the sites and the elements are constructed as $F_{IJ\ \mathbf{k}} = \sum_{\mathbf{R}} e^{i\mathbf{k}\cdot\mathbf{R}} t_{0I,\mathbf{R}J}$ with $I, J \in \{A, B\}$ and cell index $\mathbf{R}$ (see Supplementary Text E for the details of lattice structure). The effective electron hopping integrals in real space can be found from the Fourier transformation $t_{0I,\mathbf{R}J} = \frac{1}{N_{\mathbf{k}}} \sum_{\mathbf{k}} e^{-i\mathbf{k}\cdot\mathbf{R}} F_{IJ\ \mathbf{k}}$. Last, the range of the photon-induced interactions can be selected by truncating the effective hoppings in real space and performing an inverse Fourier transformation to get the QED Fock matrix in momentum space.

For the following results, we adopt the photon mode with energy of $\hbar\omega = 0.3$ eV and amplitude of $A_0 = 2 \times 10^{-7} \frac{\text{kg}\cdot\text{m}}{\text{C}\cdot\text{s}}$. The most interesting case is that of graphene coupled to a single linearly polarized photon. To aid numerical convergence, we introduced a nonsignificant sublattice potential difference $V_{AB} = \pm 0.004 t_0$ (which corresponds to a bandgap of 0.022 eV in the bare graphene); as shown later, the energy scales, affected by the range of the considered cavity-mediated interactions, are much larger than the one introduced by this sublattice potential. The schematic in Fig. 6A highlights the anisotropy at all orders of the

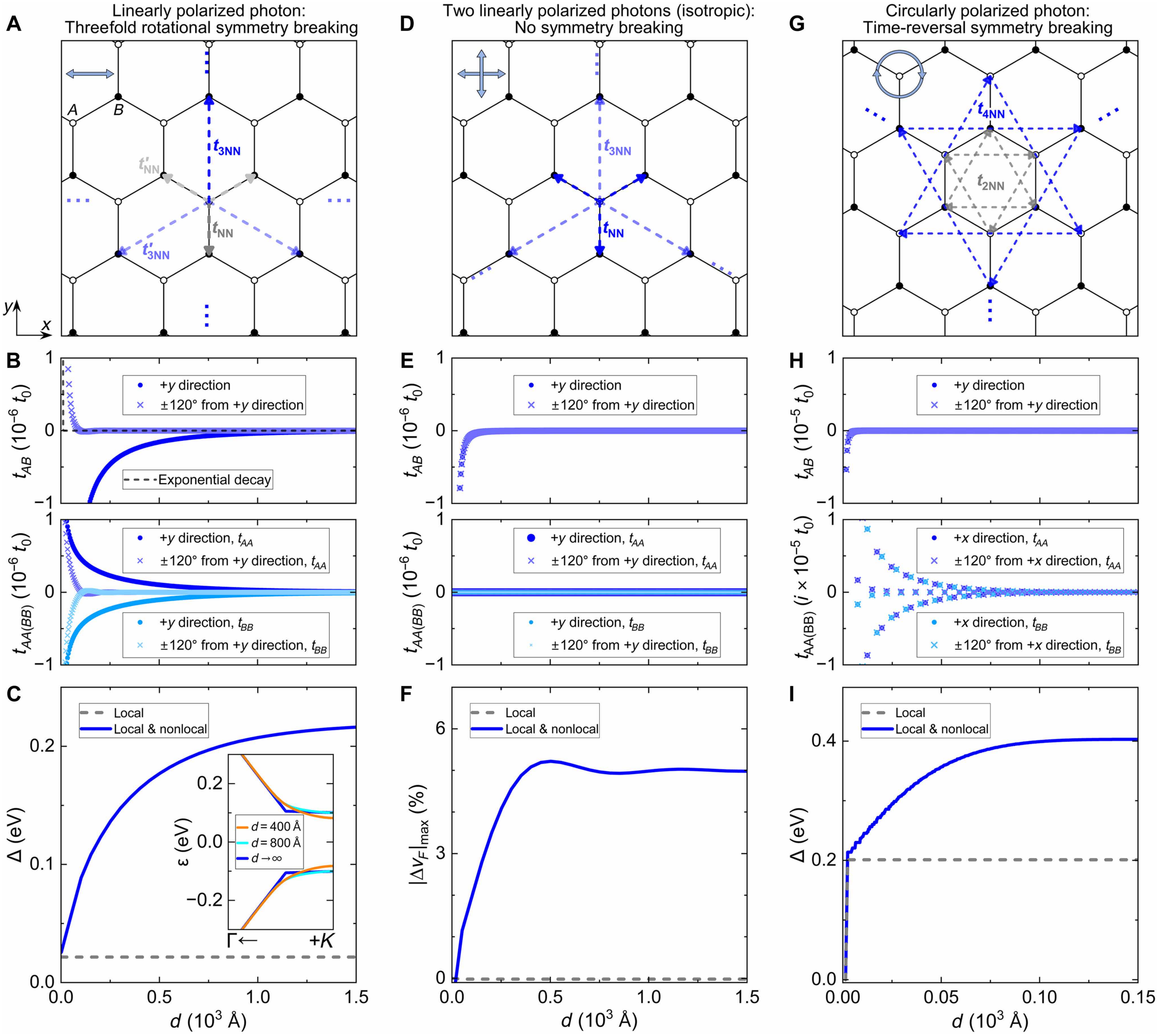

Fig. 6. Cavity-mediated effective hopping integrals in graphene. The photon energy is $\hbar\omega = 0.3$ eV, and the mode amplitude is $A_0 = 2 \times 10^{-7}\,\frac{\mathrm{kg \cdot m}}{\mathrm{C \cdot s}}$. (**A**) Schematic of hopping integrals from A to B sites, induced by a linearly polarized mode ($\mathbf{e} = \mathbf{e}_x$). Gray and light gray dashed lines show the NN integrals t_{NN} and t'_{NN}, while blue and light blue dashed lines show the third NN integrals $t_{3\mathrm{NN}}$ and $t'_{3\mathrm{NN}}$. (**B**) Hopping integrals, induced by a linearly polarized mode, change with distance between sites. (For numerical stability, we use a negligible $V_{AB} = \pm 0.004 t_0$). t_{AB}, t_{AA}, and t_{BB} along $+y$ and directions rotated by ±120° from $+y$ are shown. Hopping integrals with exponential decay in intrinsic graphene are shown. (**C**) The cavity-induced Dirac bandgap increases by including hopping integrals [in (B)] over a longer range. Inset shows the bands for truncated and infinite ranges. (**D**) Schematic of hopping integrals from A to B sites, induced by two isotropic linearly polarized modes. (**E**) Integrals t_{AB}, induced by two isotropic linearly polarized modes, change with distance between A and B sites. t_{AA} and t_{BB} remain unchanged at zero. (**F**) The cavity-renormalized Dirac Fermi velocity changes by including hopping integrals [in (E)] over a longer range. (**G**) Schematic of hopping integrals induced by a circularly polarized mode with $\mathbf{e} = \mathbf{e}_x + i\mathbf{e}_y$. Gray dashed lines show the second NN SOC-like integrals from local interaction, while blue dashed lines show long-range SOC integrals from nonlocal interaction. (**H**) Hopping integrals, induced by a circularly polarized mode, change with distance between sites. t_{AB} along $+y$ and directions rotated by ±120° from $+y$ are shown. SOC integrals between $A - A$ (and $B - B$) sites, along $+x$ and direction rotated by ±120° from $+x$, are shown. (**I**) The cavity-induced bandgap quickly plateaus with increasing hopping range.

hopping integrals by showing that the threefold rotational symmetry of the original graphene is lost. Figure 6B shows that the change in the electron hopping integrals, when including the cavity-induced nonlocal interaction, is finite and anisotropic over a long range of distance [over hundreds of nanometers, which is comparable to characteristic cavity confinement length (*44*)]. The hoppings decay much slower with distance than the exponentially decaying ones in pristine graphene. In Supplementary Text F and the section for the linearly polarized photon, we show that while t_{AB} provides an increase of the distance between conduction and valence bands across the BZ, the modified sublattice hoppings t_{AA} and t_{BB} provide a further modification to the bands close to the $\pm\mathbf{K}$ valleys.

Cutting the range of interaction (i.e., setting the effective hopping integrals to zero for a distance larger than a given threshold) has a direct effect on the size of the Dirac gap, as shown in Fig. 6C: Long-range hopping integrals up to at least ~150 nm are needed to reach convergence on the gap size of ~0.22 eV (note that this value is significantly larger than that from the artificial sublattice potential V_{AB} used for numerical stability). Crucially, the inset in Fig. 6C demonstrates that the kinks on the flat line in bands and the singular behavior of wave functions, discussed in the section for the linearly polarized photon, are removed when the interaction range is truncated. For instance, when the interaction is truncated to a finite range $d = 800$ or 400 Å, the band kinks are removed, but the flatness of the bands in the direction of the polarization remains (Fig. 6C). This confirms that the singularity is a consequence of the infinite range of the photon-induced interactions which no realistic cavities could support.

For comparison, we performed an equivalent analysis for the case of two isotropic linearly polarized photons and the case of a single circularly polarized photon. In the presence of two isotropic linearly polarized cavity photon modes (Fig. 6, D and E), we observe a range of interaction similar to the case for a single linearly polarized photon, but as discussed in the section related to the two linearly polarized isotropic photons, because no symmetry is broken, no electronic Dirac gap is opened. Nevertheless, the renormalization of the Fermi velocity at the $\pm\mathbf{K}$ valleys shows a dependence on the interaction range (Fig. 6F). Last, for a circularly polarized photon, Fig. 6G illustrates that SOC like effective electron hoppings are induced (already at the level of cavity-induced local interactions), indicating that time-reversal symmetry is broken. Effectively, the interacting electron-photon system can be mapped to an Haldane model. The cavity-induced nonlocal interaction introduces long-range effective SOC electron hoppings (Fig. 6, H and I), up to a distance of ~10 nm which is considerably smaller than that in Fig. 6 (B and C) for a single linearly polarized mode.

DISCUSSION

In conclusion, a nonperturbative QED-HF theoretical approach based on the photon-free self-consistent framework is formulated to address the photon-mediated local and nonlocal interactions of electrons in the extended materials collectively coupled with the fluctuating photons in optical cavities. The photon-induced nonlocal electron-electron interaction, originating from the quantum nature of light confined by a cavity, naturally arises in the formulation of our photon-free QED-HF approach. Such a nonlocal interaction, quite different from the Coulomb charge-charge repulsion interaction, is properly treated through the self-consistent iterations of electronic wave functions in the coupling systems of crystalline matter and optical cavities.

Using the QED-HF approach, we have shown that photon-induced nonlocal interaction plays a crucial role in the renormalization of the Dirac electronic properties in graphene. By accounting for only the photon-mediated local interaction, a circularly polarized photon opens a topologically nontrivial Dirac gap from time-reversal symmetry breaking, while a linearly polarized photon does not lift the band degeneracy at the Dirac points. In contrast, with the photon-induced nonlocal electron-electron interaction included, both the circularly and linearly polarized photon modes open a Dirac bandgap, with nontrivial and trivial electronic topology, respectively. The formation of topologically trivial gap with flat-band dispersion is related to the anisotropy in the presence of photon-induced interaction over a long range. With two isotropic linearly polarized photons, all the symmetries in intrinsic graphene are restored, and the Dirac cones remain gapless, while the Dirac Fermi velocity is slightly affected purely by the photon-induced nonlocal interaction. We repeatedly show that the nonperturbative nature of the QED-HF approach is crucial for describing the renormalization of the Dirac electronic structure by cavity photons, demonstrating that the nonperturbative treatment is a necessity to capture the key quantum features (missed in perturbative methods, even qualitatively) resulted from the collectivity of electron-photon coupling inherent to the quantum nature of cavity photons.

In contrast to our work, previous studies on graphene embedded in a cavity (*31–34*) rely on perturbation theory, which, by construction, only includes photon-induced local interactions. As a result, these works overlook the quantum phenomena arising from nonlocalities. Similarly, studies on crystals other than graphene, e.g., one-dimensional and twisted layered materials (*30*, *35*, *36*), suffer from the same perturbative considerations.

Along with the renormalization of electronic bands, the optical and transport properties of Dirac states in graphene are expected to be modified. The linearity of the massless Dirac bands in pristine graphene gives rise to a universal, frequency-independent, and spatially isotropic optical conductivity σ, namely, $\mathrm{Re}[\sigma] = \frac{e^2}{4\hbar}$ (*56*). When graphene is embedded inside a cavity, the opening of an electronic gap is expected to disrupt the universal behavior of the conductivity, inducing zero conductivity within the gap. When graphene is coupled to anisotropic cavity modes, the response of the material is expected to be altered differently in the x and y directions for frequencies above the gap, hence leading to an anisotropic optical conductivity. Furthermore, in the case of circular mode polarization, the emergent nontrivial topology of the effective graphene band structure is expected to give rise to a quantized Hall conductivity and related robust topological edge states for graphene when structured to a nanoribbon form. This suggests that graphene embedded in an optical cavity could serve as a platform for developing optoelectronic and topological devices.

The cavity-induced modifications of Dirac states in graphene differ from those achieved by other material engineering approaches. For instance, applying uniaxial strain to graphene introduces anisotropy, which shifts the Dirac points in reciprocal space without the opening of an electronic gap (*57*). An topologically trivial gap can be opened by placing graphene on a substrate, via inversion symmetry breaking (*58*), but this does not result in a flat dispersion with an infinite effective mass like that induced by a linearly polarized photon in a cavity. From a microscopic point of view, the difference stems from the fact that in both strain and substrate engineering, the modifications arise from changes to the local electronic potentials, whereas cavity coupling introduces fundamentally different nonlocal effects.

The modifications in graphene proposed in this work can be probed through various experimental techniques. As highlighted above, the Dirac gap manifests as zero optical conductivity within the gap frequency range, while anisotropy from linearly polarized modes appears as directional differences in optical conductivity. Circularly polarized modes reveal nontrivial topology via quantized Hall conductivity and ballistic transport in graphene nanoribbons. In addition, the QED-HF band structure and effective mass renormalization can be observed using angle-resolved photon emission spectroscopy.

As a general theoretical framework based on wave function iterations, our photon-free QED-HF approach can be used to study a wide range of electron-photon interacting material systems that inherently have the photon-mediated electron-electron interaction over large distances due to quantum cavity confinement effects. This opens the door to predicting cavity-induced quantum phenomena in extended crystalline matter and providing deeper insights into how quantum confinement effects mediate long-range interactions and fundamentally influence material properties. For example, it would be intriguing to investigate how cavity photons modify three-dimensional Dirac states, potentially revealing phenomena distinct from those observed in graphene as a two-dimensional Dirac system, such as the transition from Dirac to Weyl fermions in three dimensions. The manipulation of transition-metal dichalcogenides and their twisted Moiré superlattices by cavity photons also presents an exciting avenue for engineering the properties associated with valley electrons and charge-ordered states.

Supplementary Materials

This PDF file includes:
Supplementary Text
Figs. S1 to S4

REFERENCES AND NOTES

1. F. J. Garcia-Vidal, C. Ciuti, T. W. Ebbesen, Manipulating matter by strong coupling to vacuum fields. *Science* **373**, eabd0336 (2021).
2. J. Bloch, A. Cavalleri, V. Galitski, M. Hafezi, A. Rubio, Strongly correlated electron-photon systems. *Nature* **606**, 41–48 (2022).
3. A. Frisk Kockum, A. Miranowicz, S. De Liberato, S. Savasta, F. Nori, Ultrastrong coupling between light and matter. *Nat. Rev. Phys.* **1**, 19–40 (2019).
4. P. Forn-Díaz, L. Lamata, E. Rico, J. Kono, E. Solano, Ultrastrong coupling regimes of light-matter interaction. *Rev. Mod. Phys.* **91**, 025005 (2019).
5. M. Hertzog, M. Wang, J. Mony, K. Börjesson, Strong light-matter interactions: A new direction within chemistry. *Chem. Soc. Rev.* **48**, 937–961 (2019).
6. T. W. Ebbesen, Hybrid light-matter states in a molecular and material science perspective. *Acc. Chem. Res.* **49**, 2403–2412 (2016).
7. H. Hübener, U. De Giovannini, C. Schäfer, J. Andberger, M. Ruggenthaler, J. Faist, A. Rubio, Engineering quantum materials with chiral optical cavities. *Nat. Mater.* **20**, 438–442 (2021).
8. M. Ruggenthaler, N. Tancogne-Dejean, J. Flick, H. Appel, A. Rubio, From a quantum-electrodynamical light-matter description to novel spectroscopies. *Nat. Rev. Chem.* **2**, 0118 (2018).
9. A. Thomas, L. Lethuillier-Karl, K. Nagarajan, R. M. A. Vergauwe, J. George, T. Chervy, A. Shalabney, E. Devaux, C. Genet, J. Moran, T. W. Ebbesen, Tilting a ground-state reactivity landscape by vibrational strong coupling. *Science* **363**, 615–619 (2019).
10. X. Li, M. Bamba, Q. Zhang, S. Fallahi, G. C. Gardner, W. Gao, M. Lou, K. Yoshioka, M. J. Manfra, J. Kono, Vacuum Bloch-Siegert shift in Landau polaritons with ultra-high cooperativity. *Nat. Photon.* **12**, 324–329 (2018).
11. G. L. Paravicini-Bagliani, F. Appugliese, E. Richter, F. Valmorra, J. Keller, M. Beck, N. Bartolo, C. Rössler, T. Ihn, K. Ensslin, C. Ciuti, G. Scalari, J. Faist, Magneto-transport controlled by Landau polariton states. *Nat. Phys.* **15**, 186–190 (2019).
12. F. Appugliese, J. Enkner, G. L. Paravicini-Bagliani, M. Beck, C. Reichl, W. Wegscheider, G. Scalari, C. Ciuti, J. Faist, Breakdown of topological protection by cavity vacuum fields in the integer quantum Hall effect. *Science* **375**, 1030–1034 (2022).
13. E. Orgiu, J. George, J. A. Hutchison, E. Devaux, J. F. Dayen, B. Doudin, F. Stellacci, C. Genet, J. Schachenmayer, C. Genes, G. Pupillo, P. Samorì, T. W. Ebbesen, Conductivity in organic semiconductors hybridized with the vacuum field. *Nat. Mater.* **14**, 1123–1129 (2015).
14. G. Jarc, S. Y. Mathengattil, A. Montanaro, F. Giusti, E. M. Rigoni, R. Sergo, F. Fassioli, S. Winnerl, S. Dal Zilio, D. Mihailovic, P. Prelovšek, M. Eckstein, D. Fausti, Cavity-mediated thermal control of metal-to-insulator transition in 1T-TaS$_2$. *Nature* **622**, 487–492 (2023).
15. J. Galego, F. J. Garcia-Vidal, J. Feist, Cavity-induced modifications of molecular structure in the strong-coupling regime. *Phys. Rev. X* **5**, 041022 (2015).
16. T. S. Haugland, E. Ronca, E. F. Kjønstad, A. Rubio, H. Koch, Coupled cluster theory for molecular polaritons: Changing ground and excited states. *Phys. Rev. X* **10**, 041043 (2020).
17. J. P. Philbin, T. S. Haugland, T. K. Ghosh, E. Ronca, M. Chen, P. Narang, H. Koch, Molecular van der Waals Fluids in cavity quantum electrodynamics. *J. Phys. Chem. Lett.* **14**, 8988–8993 (2023).
18. C. J. Eckhardt, G. Passetti, M. Othman, C. Karrasch, F. Cavaliere, M. A. Sentef, D. M. Kennes, Quantum Floquet engineering with an exactly solvable tight-binding chain in a cavity. *Commun. Phys.* **5**, 122 (2022).
19. D.-P. Nguyen, G. Arwas, C. Ciuti, Electron conductance and many-body marker of a cavity-embedded topological one-dimensional chain. *Phys. Rev. B* **110**, 195416 (2024).
20. D. Shaffer, M. Claassen, A. Srivastava, L. H. Santos, Entanglement and topology in Su-Schrieffer-Heeger cavity quantum electrodynamics. *Phys. Rev. B* **109**, 155160 (2024).
21. J. Li, M. Eckstein, Manipulating intertwined orders in solids with quantum light. *Phys. Rev. Lett.* **125**, 217402 (2020).
22. T. Schnappinger, D. Sidler, M. Ruggenthaler, A. Rubio, M. Kowalewski, Cavity Born-Oppenheimer Hartree-Fock Ansatz: Light-matter properties of strongly coupled molecular ensembles. *J. Phys. Chem. Lett.* **14**, 8024–8033 (2023).
23. D. Sidler, M. Ruggenthaler, H. Appel, A. Rubio, Chemistry in quantum cavities: Exact results, the impact of thermal velocities, and modified dissociation. *J. Phys. Chem. Lett.* **11**, 7525–7530 (2020).
24. C. Schäfer, F. Buchholz, M. Penz, M. Ruggenthaler, A. Rubio, Making ab initio QED functional(s): Nonperturbative and photon-free effective frameworks for strong light-matter coupling. *Proc. Natl. Acad. Sci. U.S.A.* **118**, e2110464118 (2021).
25. D. Sidler, M. Ruggenthaler, C. Schäfer, E. Ronca, A. Rubio, A perspective on ab initio modeling of polaritonic chemistry: The role of non-equilibrium effects and quantum collectivity. *J. Chem. Phys.* **156**, 230901 (2022).
26. C. Schäfer, M. Ruggenthaler, H. Appel, A. Rubio, Modification of excitation and charge transfer in cavity quantum-electrodynamical chemistry. *Proc. Natl. Acad. Sci. U.S.A.* **116**, 4883–4892 (2019).
27. D. Sidler, T. Schnappinger, A. Obzhirov, M. Ruggenthaler, M. Kowalewski, A. Rubio, Unraveling a cavity-induced molecular polarization mechanism from collective vibrational strong coupling. *J. Phys. Chem. Lett.* **15**, 5208–5214 (2024).
28. H. Hübener, E. V. Boström, M. Claassen, S. Latini, A. Rubio, Quantum materials engineering by structured cavity vacuum fluctuations. *Mater. Quant. Technol.* **4**, 023002 (2024).
29. F. Schlawin, D. M. Kennes, M. A. Sentef, Cavity quantum materials. *Appl. Phys. Rev.* **9**, 011312 (2022).
30. O. Dmytruk, M. Schirò, Controlling topological phases of matter with quantum light. *Commun. Phys.* **5**, 271 (2022).
31. O. V. Kibis, O. Kyriienko, I. A. Shelykh, Band gap in graphene induced by vacuum fluctuations. *Phys. Rev. B* **84**, 195413 (2011).
32. X. Wang, E. Ronca, M. A. Sentef, Cavity quantum electrodynamical Chern insulator: Towards light-induced quantized anomalous Hall effect in graphene. *Phys. Rev. B* **99**, 235156 (2019).
33. C. B. Dag, V. Rokaj, Engineering topology in graphene with chiral cavities. *Phys. Rev. B* **110**, L121101 (2024).
34. K. Masuki, Y. Ashida, Berry phase and topology in ultrastrongly coupled quantum light-matter systems. *Phys. Rev. B* **107**, 195104 (2023).
35. C. Jiang, M. Baggioli, Q.-D. Jiang, Engineering flat bands in twisted-bilayer graphene away from the magic angle with chiral optical cavities. *Phys. Rev. Lett.* **132**, 166901 (2024).
36. D.-P. Nguyen, G. Arwas, Z. Lin, W. Yao, C. Ciuti, Electron-photon chern number in cavity-embedded 2D Moiré materials. *Phys. Rev. Lett.* **131**, 176602 (2023).
37. F. Schlawin, A. Cavalleri, D. Jaksch, Cavity-mediated electron-photon superconductivity. *Phys. Rev. Lett.* **122**, 133602 (2019).
38. J. B. Curtis, Z. M. Raines, A. A. Allocca, M. Hafezi, V. M. Galitski, Cavity quantum Eliashberg enhancement of superconductivity. *Phys. Rev. Lett.* **122**, 167002 (2019).
39. M. A. Sentef, M. Ruggenthaler, A. Rubio, Cavity quantum-electrodynamical polaritonically enhanced electron-phonon coupling and its influence on superconductivity. *Sci. Adv.* **4**, eaau6969 (2018).
40. A. Chakraborty, F. Piazza, Long-range photon fluctuations enhance photon-mediated electron pairing and superconductivity. *Phys. Rev. Lett.* **127**, 177002 (2021).
41. I.-T. Lu, D. Shin, M. K. Svendsen, H. Hübener, U. D. Giovannini, S. Latini, M. Ruggenthaler, A. Rubio, Cavity-enhanced superconductivity in MgB$_2$ from first-principles quantum electrodynamics (QEDFT). *Proc. Natl. Acad. Sci. U.S.A.* **121**, e2415061121 (2024).
42. T. Oka, H. Aoki, Photovoltaic Hall effect in graphene. *Phys. Rev. B* **79**, 081406 (2009).
43. T. Kitagawa, T. Oka, A. Brataas, L. Fu, E. Demler, Transport properties of nonequilibrium systems under the application of light: Photoinduced quantum Hall insulators without Landau levels. *Phys. Rev. B* **84**, 235108 (2011).
44. M. K. Svendsen, M. Ruggenthaler, H. Hübener, C. Schäfer, M. Eckstein, A. Rubio, S. Latini, Effective equilibrium theory of quantum light-matter interaction in cavities: Extended systems and the long wavelength approximation. arXiv:2312.17374 [cond-mat.mes-hall] (2023).
45. F. H. M. Faisal, *Theory of Multiphoton Processes* (Springer, 1987).
46. S. Latini, D. Shin, S. A. Sato, C. Schaefer, U. De Giovannini, H. Huebener, A. Rubio, The ferroelectric photo ground state of SrTiO$_3$: Cavity materials engineering. *Proc. Natl. Acad. Sci. U.S.A.* **118**, e2105618118 (2021).
47. Y. Ashida, A. İmamoğlu, E. Demler, Cavity quantum electrodynamics at arbitrary light-matter coupling strengths. *Phys. Rev. Lett.* **126**, 153603 (2021).

48. S. Reich, J. Maultzsch, C. Thomsen, P. Ordejón, Tight-binding description of graphene. *Phys. Rev. B* **66**, 035412 (2002).
49. E. Malic, A. Knorr, *Graphene and Carbon Nanotubes: Ultrafast Relaxation Dynamics and Optics* (John Wiley & Sons Ltd., 2013).
50. T. G. Pedersen, K. Pedersen, T. Brun Kriestensen, Optical matrix elements in tight-binding calculations. *Phys. Rev. B* **63**, 201101 (2001).
51. H. Herzig Sheinfux, L. Orsini, M. Jung, I. Torre, M. Ceccanti, S. Marconi, R. Maniyara, D. Barcons Ruiz, A. Hötger, R. Bertini, S. Castilla, N. C. H. Hesp, E. Janzen, A. Holleitner, V. Pruneri, J. H. Edgar, G. Shvets, F. H. L. Koppens, High-quality nanocavities through multimodal confinement of hyperbolic polaritons in hexagonal boron nitride. *Nat. Mater.* **23**, 499–505 (2024).
52. X. Jin, A. Cerea, G. C. Messina, A. Rovere, R. Piccoli, F. De Donato, F. Palazon, A. Perucchi, P. Di Pietro, R. Morandotti, S. Lupi, F. De Angelis, M. Prato, A. Toma, L. Razzari, Reshaping the phonon energy landscape of nanocrystals inside a terahertz plasmonic nanocavity. *Nat. Commun.* **9**, 763 (2018).
53. G. Jarc, S. Y. Mathengattil, F. Giusti, M. Barnaba, A. Singh, A. Montanaro, F. Glerean, E. M. Rigoni, S. D. Zilio, S. Winnerl, D. Fausti, Tunable cryogenic terahertz cavity for strong light–matter coupling in complex materials. *Rev. Sci. Instrum.* **93**, 033102 (2022).
54. G. Scalari, C. Maissen, D. Turčinková, D. Hagenmüller, S. D. Liberato, C. Ciuti, C. Reichl, D. Schuh, W. Wegscheider, M. Beck, J. Faist, Ultrastrong coupling of the cyclotron transition of a 2D electron gas to a THz metamaterial. *Science* **335**, 1323–1326 (2012).
55. P. Sivarajah, A. Steinbacher, B. Dastrup, J. Lu, M. Xiang, W. Ren, S. Kamba, S. Cao, K. A. Nelson, THz-frequency magnon-phonon-polaritons in the collective strong-coupling regime. *J. Appl. Phys.* **125**, 213103 (2019).
56. A. B. Kuzmenko, E. van Heumen, F. Carbone, D. van der Marel, Universal optical conductance of graphite. *Phys. Rev. Lett.* **100**, 117401 (2008).
57. C. Si, Z. Sun, F. Liu, Strain engineering of graphene: A review. *Nanoscale* **8**, 3207–3217 (2016).
58. K. Zollner, A. W. Cummings, S. Roche, J. Fabian, Graphene on two-dimensional hexagonal BN, AlN, and GaN: Electronic, spin-orbit, and spin relaxation properties. *Phys. Rev. B* **103**, 075129 (2021).

Acknowledgments: We thank M. Ruggenthaler and I.-T. Lu for the helpful discussions. **Funding:** This work was supported by the Cluster of Excellence "CUI: Advanced Imaging of Matter"–EXC 2056–project ID 390715994, SFB-925 "Light induced dynamics and control of correlated quantum systems"–project ID 170620586 of the Deutsche Forschungsgemeinschaft (DFG), the European Research Council (ERC-2024-SyG-UnMySt–101167294), the Villum Foundation (grant no. 72146), the European Union Marie Sklodowska-Curie Doctoral Networks (TIMES, grant no. 101118915; and SPARKLE, grant no. 101169225), the Alexander von Humboldt Foundation (Humboldt Research Fellowship), and the Max Planck-New York City Center for Non-Equilibrium Quantum Phenomena. The Flatiron Institute is a division of the Simons Foundation. **Author contributions:** Conceptualization: A.R., S.L., and H.H. Methodology: H.L., F.T., H.H., S.L., and A.R. Investigation: H.L. and F.T. Visualization: H.L. and S.L. Supervision: A.R., S.L., and H.H. Writing—original draft: H.L. and S.L. Writing—review and editing: H.L., F.T., H.H., S.L., and A.R. **Competing interests:** The authors declare that they have no competing interests. **Data and materials availability:** All data needed to evaluate the conclusions in the paper are present in the paper and/or the Supplementary Materials.

Submitted 22 May 2025
Accepted 24 September 2025
Published 24 October 2025
10.1126/sciadv.adz1855

4 Cavity-QED systems on Quantum Computing

Memento audere semper[1]
- G. D'Annunzio (1919)

Despite modern classical computers possess the computational resources for simulating cavity-QED Hamiltonians in the framework of the explicit many-body representation of the interaction between light and matter, the size of the system that one can describe remains limited by the hardware capabilities. In fact, the joint electron-photon Hilbert space grows exponentially with the number of Fock states and cavity modes that are used to represent the electromagnetic field, which rapidly makes the storage and handling of the matrix representation of the QED Hamiltonian unmanageable. To handle this complexity one typically has to reduce the dimension of the QED matrix, for example by considering a simple description of the cavity modes (e.g. by using a single effective mode) [15] or by using theories that allow to recast the photonic problem as an effective problem [16]. On the other hand, one can also improve the hardware or increase the allocated computational resources. However, the improvement of classical hardware is eventually limited by physical constraints. In fact, historically chip manufacturers have focused on reducing the dimension of the transistor, which is is the base building block of classical chips, so that more of them could be installed. Traditionally, this has evolved according to Moore's law [120], but as current state-of-the-art chips approach atomic scales [121] it becomes more and more challenging to reduce the dimension of transistor. Thus to increase the computational power of a classical hardware, one can either increase the number of cores, as it is done in graphical processing units (GPUs) or create custom chip architectures designed for specific applications, such as using tensor processing units (TPUs) for machine learning applications [122]. As each core focuses on solving only a small part of a complex numerical problem, this is an effective solution for handling big computations. However, it requires the development of complex parallel algorithms that distribute both the memory and the computational effort. Furthermore the improvement that one obtains in computational time by increasing the number of cores working on a problem does not always scale linearly, as typically there is an optimum number of cores and the allocation of more resources results in a reduced performance increase or even, if the algorithms are badly designed, in a degrade. Thus, while in general it remains possible to simulate cavity-QED system with classical computers, there is no clear path for future scalability.

---

[1] *Always remember to dare.* This famous quote from D'Annunzio, inspired from the latin expression *Audentes fortuna iuvat* (from *Aeneis, Vergilius*), refers to the fact that using quantum computing for studying QED system is novel and a daring act.

Quantum computing offers a complementary route to address this challenge. Quantum processing units (QPUs) are based on the qubit, which is the most basic building block of this technology. A qubit is essentially a quantum two-level system, and it is the quantum counterpart of the *bit*. The main difference between bits and qubits is that while the former can only be in either state 0 or 1, the latter is described by $|\Psi\rangle = \alpha\,|0\rangle + \beta\,|1\rangle$, where α, β are complex coefficients such that $|\alpha|^2 + |\beta|^2 = 1$, hence it can assume all possible combinations of the two fundamental states. An effective way of visualizing it is to consider $|\Psi\rangle$ as a vector moving along the Bloch sphere (cf. Fig. 4.1 and Section 4.1) [83]. Note that it is also possible to work with more than two states, for instance using a qutrit, described as $|\Psi\rangle = \alpha\,|0\rangle + \beta\,|1\rangle + \gamma\,|2\rangle$ [123, 124]. However, in this chapter I will only consider qubits. While a classical bit is almost universally implemented using a Silicon-based transistor, there are currently many technologies being researched to implement a qubit, most notably superconducting [125], trapped ions [126], neutral atoms [127] or photonic [128] hardware, each of them having upsides and downsides (cf. Section 4.2).

Quantum computers are particularly promising for the simulation of light-matter interacting systems because they can encode the same exponential structure of the joint electron-photon Hilbert space into a linearly scaling number of qubits [87, 129]. This feature is particularly attractive as it would allow for a more complete description of the electromagnetic field. After defining the number of qubits required to represent the system, as well as their initial state, one needs to encode the Hamiltonian as a unitary operation through quantum gates, which are organized in quantum circuits. Each quantum gate performs an operation on one or more qubits, essentially rotating the global state in the Bloch sphere. After all gates are applied, the final state is measured. Since the execution time of a single quantum circuit is in the order of a few seconds (including latency due to the job submission), quantum computers promise not only to provide a memory-efficient solution to QED systems, but also a time-efficient one.

However, operating a quantum computer is challenging due to quantum noise that deteriorates the quantum state encoded in the qubits, for example as a result of decoherence on the quantum gates. This is currently the main limitation of this technology, as it limits the number of gates, especially two-qubits gates, that can be executed. To match this constraint one has to design circuits having in mind the hardware constraints, which often implies that the same circuit could perform well on a specific QPU, while being inefficient on another.

Building on these ideas, the present chapter describes a first proposal for simulating a cavity-QED system with quantum computers based on superconducting architecture. It first provides a concise introduction to the elements of quantum computing that are most relevant to simulate a generic Hamiltonian. Subsequently, it provides an overview of different quantum technologies and their respective challenges. Then it explains how to encode fermions (electrons) and bosons (photons) on qubit registers, with emphasis on the Bravyi–Kitaev transform for fermions and a logarithmic encoding for bosons. Finally, it introduces Publication IV, which presents a hardware-efficient formulation of molecular cavity-QED Hamiltonians that adapts the photon sector to the connectivity constraints of near-term devices, enabling accurate quantum dynamics with error mitigation.

4.1 Quantum computing building blocks

This section provides the basic insights on the fundamental building blocks of a quantum computer.

The first and most basic one is the qubit, the quantum counterpart of the classical *bit.* A qubit is a controllable quantum two-level system, whose computational basis states are denoted as $|0\rangle$ (or $|{\uparrow}\rangle$) and $|1\rangle$ (or $|{\downarrow}\rangle$). In a QPU, a qubit can be realized using different technologies (e.g. superconducting circuits, ions, neutral atoms) which will be explored in more detail in Section 4.2. The general state of a qubit is given by $|\psi\rangle = \alpha\,|0\rangle + \beta\,|1\rangle$, where α, β are complex coefficients such that $|\alpha|^2 + |\beta|^2 = 1$, which ensures that $|\psi\rangle$ is normalized at all times (as it is a quantum state). Since the norm of $|\psi\rangle$ is fixed, $|\psi\rangle$ represents a point on a spherical surface, which is known as Bloch sphere (Fig. 4.1). $|\psi\rangle$ can then be expressed using polar coordinates as $|\psi\rangle = \cos\left(\frac{\theta}{2}\right)|0\rangle + e^{i\phi}\sin\left(\frac{\theta}{2}\right)|1\rangle$. As illustrated in Fig. 4.1, the angle θ represents a rotation from the z axis, while ϕ is a rotation from the x axis. In this picture, the computational basis state $|0\rangle$ lies on the positive side of the z axis, while the state $|1\rangle$ on its negative side. The main difference between a qubit and a classical bit is that while the latter can, at any given time, be either in the state $|0\rangle$ or in the state $|1\rangle$, a qubit can be in any linear combination of the two. Furthermore, it is important to distinguish between physical and logical qubits. The former is a physical device that behaves as a two-state quantum system, with state $|\psi\rangle$ [130]. A logical qubit is a more abstract concept, which represents a two-level quantum state on which it is possible to perform unitary transformation (error-corrected), as specified in a quantum algorithm or quantum circuit [131]. Typically, a logical qubit is composed by several physical qubits [130].

Collections of logical qubits are called quantum registers, the quantum counterpart of the classical register. Note that as current state-of-the-art quantum computers still operate with only physical qubits, for the present scope one may refer to quantum registers simply as a collection of qubits. Quantum registers constitute tensor-product spaces where each qubit has a state $|\psi\rangle$, while the overall state $|\Psi\rangle$ of the multi-qubit system being simulated is the result of entanglement of the individual qubit states contained in the register. In other words, the quantum state $|\Psi\rangle$ of a N-qubit register is defined in an Hilbert $\mathcal{H} = \mathcal{H}_{N-1} \otimes \mathcal{H}_{N-2} \otimes \cdots \otimes \mathcal{H}_1 \otimes \mathcal{H}_0$, where $\mathcal{H}_n$ is the 2 dimensional complex Hilbert space of the nth-qubit. Thus, a N-qubit register spans 2^N basis states. It is important to note that also a N-classical bits register has an associated size of 2^N, which is not surprising as the computational basis of bits and qubits is the same: $\{|0\rangle, |1\rangle\}$. However, the fundamental difference is that while a classical register can represent just one of these 2^N combinations, a quantum register can represent all of those at the same time, exploiting the quantum superposition and the entanglement

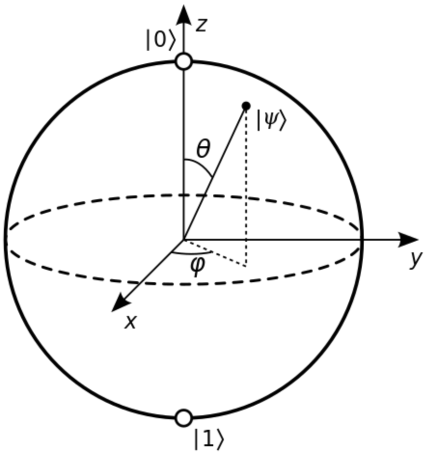

Figure 4.1: The Bloch sphere. The state $|0\rangle$ lies on the positive z axis thus will be denoted as $|\uparrow\rangle$. Conversely, $|1\rangle$ lies on the negative z axis.

between qubits. Note that classical registers also play a key role in quantum computing, as they collect the result of the measurement.

Once the initial state of a quantum register is defined, one has to encode the action of the Hamiltonian, which is done through the application of quantum gates. Quantum gates represent basic unitary operations performed on a set of qubits (typically one or two). Three (or more) qubits gates may be obtained by combining one- and two-qubits gates. Each of them is represented by a unitary matrix U such that $U\left|\psi_i\right\rangle = \left|\psi_f\right\rangle$. Since the action of U does not modify the norm $\left|\psi_i\right\rangle$, $\left|\psi_f\right\rangle$ is still a point of the Bloch sphere (where $\left|\psi_i\right\rangle$, $\left|\psi_f\right\rangle$ are single-qubit states). Hence, one-qubit gates represent a rotation of the state, while two-qubit gates are entangling operations in the joint space. Each QPU can perform only some quantum gates, called basis gates, while all others are expressed as a combination of the basis ones. The set of basis gates must constitute a universal basis set [83, 132], which mean that it shall be possible to approximate any unitary operation to an arbitrary precision starting from the chosen basis gates. For instance the superconducting hardware `ibm_brisbane`, developed by IBM, implements the following basis gates: ECR (2-qubit echoed cross-resonance gate, which allows to entangle two qubits), ID (the identity), $\mathrm{RZ}(\phi) = e^{-i\frac{\phi}{2}Z}$ (single-qubit rotation about the Z axis), $\mathrm{SX} = e^{i\frac{\pi}{4}}\mathrm{RX}(\frac{\pi}{2})$ (single-qubit 90 degrees rotation about the x axis with phase $e^{i\frac{\pi}{4}}$) and $\mathrm{X} = e^{-i\frac{\pi}{2}X}$ (single-qubit 180 degrees rotation about the x axis, which is the equivalent of a classical bit flip). Determining what gates shall be used and their sequence depends on the Hamiltonian to be encoded, which in turns is defined by the system and by the quantum algorithm of choice, and on the QPU that will perform the calculation. First, the mapping stage is performed, which typically depends only on the physical nature of the operators appearing the Hamiltonian (cf. Section 4.3) and generates Pauli operators. Subsequently, the transpilation stage is performed which adapts the required gates to the chosen QPU. The resulting collection of gates, together with the preparation of the qubits and the measurement, is called quantum circuit.

Before concluding, it is important to emphasize that although an N-qubit register can represent a superposition over 2^N computational basis states, a single measurement reveals only one outcome. According to the postulates of quantum mechanics, measuring a qubit collapses its state onto $|0\rangle$ or $|1\rangle$ with probabilities $|\alpha|^2$ and $|\beta|^2$, which are set by the gates applied. As a result, while the circuit state before measurement may be highly entangled and encodes the full quantum information of the system [83], the act of measurement returns only classical bits. o extract expectation values or reconstruct the underlying probability distribution, the circuit must therefore be executed and measured many times (shots) to build reliable statistics, reflecting the inherently probabilistic nature of quantum mechanics.

4.2 Different QPU technologies

When writing software, both for classical and quantum computing, it is essential to consider the characteristics of the hardware that will execute it. For instance, if one writes an image-processing kernel for both Intel and ARM classical chips, on Intel larger arrays and cache sizes allow to process more pixels per instruction (dividing the image in larger tiles), while on ARM the situation is reversed. However, ARM offers more cores, which compensate for the smaller tile size. Adapting to these hardware differences makes the same algorithm fast and efficient on each chip. On classical computer, in most cases the compiler handles this hidden complexity, and typically the worst-case scenario is a suboptimal execution time of the code. On the other hand, on present-day noisy intermediate-scale quantum (NISQ) computers efficiently formulate a quantum circuit makes all the difference between being able to retrieve the signal or reaching complete noise saturation.

Different technologies in the fabrication of qubits result in key differences in the connectivity scheme, which defines how each qubit interacts with the others (whether it is a direct interaction or it needs to be mediated), in the gate fidelity, which is a measure of how the accurate the operation performed is compared to a noiseless case, and in the execution time of gates. In this section I provide an overview of the current main QPUs architectures. Note that research in quantum computing is very dynamic, hence other technologies not mentioned here may become major in the future.

4.2.1 Superconducting hardware

Superconducting circuits-based devices [133] currently constitute the most widely used architecture for digital quantum computing, with major industry players such as IBM Quantum and Google Quantum as well as Rigetti and IQM [134]. Within this technology, qubits are defined between the ground and first excited state of a non-harmonic Josephson junction [135, 136], which consists of two superconducting electrodes separated by an insulating barrier. Superconducting circuits are lithographically fabricated by depositing aluminum or niobium on silicon or sapphire substrates and are operated at millikelvin temperatures. Their main advantages are fast gate times (which range from tens to a few hundred nanoseconds for single- and two-qubit gates), high gate fidelity and relative easiness in the fabrication process thanks to the maturity of lithographic deposition techniques. However, due to the pre-fabricated connections between two Josephson junctions, the qubits are typically arranged in quasi-planar grids with limited degree of connectivity (each qubit is typically coupled to two, three or four neighbors). To realize an interaction between two non-adjacent qubits one first has to bring the parts involved close, which is performed through a series of SWAP operations (each consisting of three noisy two-qubit gates). These features make superconducting QPUs well-suited to problems whose qubit interaction graph can be embedded in a linear chain or require minimal non-local interactions. Superconducting quantum computers are the technology of choice for the work presented in Publication IV [137] of the present thesis (cf. Section 4.4). In the context of QED simulations, star-like or all-to-all couplings arising from a single matter transition interacting with many photonic modes are challenging, and one needs to adapt the Hamiltonian the hardware topology. Publication IV addresses this by introducing a localized photonic basis that maps the photon sector to a 1D qubit chain, drastically reducing SWAP overhead while preserving the relevant light–matter physics.

4.2.2 Trapped-ions hardware

Trapped-ion devices [126, 138, 139], encode qubits in the internal states of ions confined in electromagnetic traps. The two states required for a qubit correspond to a specific transition in the fine, hyperfine or Zeeman structure of the ion and are characterized by long lifetimes, ranging from seconds (for electric quadrupole-allowed transitions in D-states) to hours (for octopole-allowed transition of F-states) in the case of optical qubits, and nearly metastable for Zeeman and hyperfine qubits [138]. Ion traps offer high-fidelity gates and, importantly for Hamiltonian simulation, near all-to-all connectivity within a string of ions which makes them naturally well-suited to implement dense interaction graphs. The main drawback is the gate speed, typically orders of magnitude slower than in superconducting circuits (up to microseconds for two-qubits gates [140]), which may become a bottleneck for algorithms requiring frequent mid-circuit control and extended statistics (measurements). Trapped-ion are rapidly gaining momentum in the industrial landscape of quantum computing companies, with important companies like IonQ, Quantinuum, AQT and eleQtron [134].

4.2.3 Neutral-atoms hardware

Neutral-atom devices [127, 141, 142] use arrays of individually laser-trapped atoms (cooled at microkelvin temperatures via Doppler cooling) with programmable geometries. The qubits are encoded in transitions between hyperfine states of each trapped atom (e.g. $5S_{1/2}$ in ^{87}Rb, between $|0\rangle = |F = 1, m_f = 0\rangle \leftrightarrow |1\rangle = |F = 2, m_f = 0\rangle$ [143]). Entanglement is created via excitation to high-lying Rydberg levels, which interact strongly over micrometer distances. Because the Rydberg interaction decays algebraically with distance, arrays arranged with $3 - 10$ μm spacing can realize flexible connectivities, meaning that any two atoms within this radius can be coupled directly. Thus, the effective interaction graph extends well beyond nearest neighbors and can approach quasi–all-to-all within local blocks. Similarly to trapped-ions, neutral-atoms are characterized by long lifetimes of the qubit states. However, an important issue in this technology is the trapped lifetime of each atom, that is the time that each atom remains in the laser trap. Such time is in the order of almost one hour [144], which makes frequent recalibration required. A further issue with this technology is the fidelity of the two-qubits gate, which is significantly lower compared to other technologies [142, 145]. Neutral-atom devices are also rapidly gaining momentum in the industrial landscape of quantum computing companies, with important companies like Infleqtion, Atom Computing, Pasqal, QuEra and planqc [134].

4.2.4 Photonic hardware

Photonic quantum computers [128, 146] use light to encode and process quantum information at room temperature, which is a significant advantage compared to the other technologies described, all operating a cryogenic temperatures. Information is encoded either in discrete single-photon qubits, in continuous variables (squeezed states), or in bosonic codes. More recently, hybrid schemes combining single-photon and coherent-state encoding were also developed, enabling near-deterministic Bell measurements and reduce resource overheads. Another major advantage of photonic-based quantum computing is the flexible connectivity scheme. In fact, the reconfigurable interferometer meshes and time-domain multiplexing yields all-to-all coupling within and across chips. The gate time is also quite low, as information is carried by light. The major issue for current devices is represented by the fidelity of gate operations, which is negatively affected by optical losses and single-photon detection efficiency. Companies involved in the development of this technology are PsiQuantum and Xanadu [134].

4.2.5 Summary

After this short overview of different QPUs, the key message should be that there is still no clear optimal solution for quantum computing. Each technology has strengths and drawbacks which, especially in the era of non-error corrected hardware, make a QPU optimal for a certain class of problems, but not for general purposes. When designing quantum algorithms or studying use-cases, one should design the circuit based on each QPU capability, as exceeding them will make simulation fail. The superconducting-focused strategy developed in Publication IV exemplifies this point, as it first shows that the connectivity required for simulating QED Hamiltonian exceeds the capabilities of superconducting hardware, but then shows that by unitarily transforming the photon sector enforcing nearest-neighbor couplings, the qubit interaction graph becomes compatible with the planar topology, enabling accurate dynamics with error mitigation on present-day QPUs.

4.3 Representing fermions and bosons in a quantum computer

In order to perform quantum simulations with a quantum computer one must be able to transform the Hamiltonian representing the system into a quantum circuit. This process consists of three main steps. The first one is called mapping, and transforms the Hamiltonian (typically written in terms of second quantized operators) into a sum of Pauli strings, which are a sequence of N Pauli operators $\hat{\sigma}_x$ (X), $\hat{\sigma}_y$ (Y), $\hat{\sigma}_z$ (Z) or the identity I, where N is the number of qubits in the qubit register. For example, if a quantum register is composed of four qubits, a Pauli string would look like $IIZZ$, meaning that the identity operation will be applied to two qubits, and the Z Pauli operator to the other two. Note that as discussed in Section 4.1 a qubit register is a tensor-product state, which implies that $IIZZ \to I \otimes I \otimes Z \otimes Z$. Mapping is required because all operations on qubits must be rotation on the Bloch sphere, and the set $\{I, X, Y, Z\}$ forms a complete basis set for all single-qubit operations [147]. Furthermore, it determines how many qubits are required to represent the system, which depends on physical parameters (e.g. on the number of states one wants to include) and on the nature of the second quantized operators to be mapped (which determines the mapping algorithm). The second step for obtaining a quantum circuit is choosing a quantum algorithm. For instance, one might be interested in computing the ground state of a system, which can be achieved using a Variational Quantum Eigensolver (VQE), or in studying the dynamics of the system, which can be achieved using the Trotter algorithm. Finally, the last step is adapting the circuit to the hardware (such as the the available connectivity scheme and to the quantum gates that a specific QPU can perform). This is called transpilation.

In this section I will only explore the mapping step, focusing on fermionic and bosonic operators, as in my thesis work I made contribution to it by implementing the mapping procedure for bosons and for the light-matter interaction terms. I will consider an example taken from the publication IV. In particular, here I report the Hamiltonian in Eq. 4 of publication IV, written explicitly for a two level system interacting with two effective cavity modes:

$$\hat{H} = \varepsilon_g \hat{c}_g^\dagger \hat{c}_g + \varepsilon_e \hat{c}_e^\dagger \hat{c}_e + \Omega_1 \hat{a}_1^\dagger \hat{a}_1 + \Omega_2 \hat{a}_2^\dagger \hat{a}_2 + \frac{\Omega_1 + \Omega_2}{2} - \hat{c}_e^\dagger \hat{c}_g \left(g_1^{eg} \hat{a}_1 + g_2^{eg} \hat{a}_2\right) - \hat{c}_g^\dagger \hat{c}_e \left(g_1^{eg} \hat{a}_1^\dagger + g_2^{eg} \hat{a}_2^\dagger\right) \tag{4.1}$$

where $\hat{c}^\dagger$ $(\hat{c})$ are electronic creation (annihilation) operators, ε_g (ε_e) is the energy of the electronic ground (excited) state, $\hat{a}^\dagger$ $(\hat{a})$ are photonic creation (annihilation) operators and Ω_i is the energy of the i-th mode and g_i^{eg} is the coupling strength. Refer to Section 2.1 of Publication IV for more details.

4.3.1 The fermionic Bravyi-Kitaev mapper

As in Eq. 4.1 both fermionic creation and annihilation operators appear, it is essential to be able to map them to Pauli operators. The first algorithm to map fermions to Pauli operators is the Jordan-Wigner transformation [148], first developed in 1928. It allows to exactly encode the fermionic operators, ensuring all commutation relations are preserved:

$$\hat{c}_p^\dagger = \frac{1}{2}\left(X_p - iY_p\right) \otimes_{q<p} Z_q, \quad \hat{c}_p = \frac{1}{2}\left(X_p + iY_p\right) \otimes_{q<p} Z_q \tag{4.2}$$

The resulting qubit operators are highly non-local. Fermions can be mapped more efficiently using the Bravyi-Kitaev (BK) mapper [149, 150, 151]. The BK transform redistributes the occupation and parity information of the fermionic states across the register so that the number of mapped operators grows only logarithmically with system size. Within this mapper, the fermionic operators are defined as follows [151]:

$$\hat{c}_p^\dagger = \frac{1}{2}\left(X_{U(p)} \otimes X_p - iX_{U(p)} \otimes Y_p\right) \otimes Z_{\rho(p)}, \quad \hat{c}_p = \frac{1}{2}\left(X_{U(p)} \otimes X_p + iX_{U(p)} \otimes Y_p\right) \otimes Z_{\rho(p)} \tag{4.3}$$

where $U(p)$ is the *update set* of qubit p, and $\rho(p)$ is the *parity set* of qubit p. Note that the BK mapper uses the same number of qubits of the JW mapper, but reduces the number of Pauli strings, typically lowering the number of two-qubit gates. Concretely for the Eq. 4.1, to represent a two level system the required number of qubits is 2. The diagonal terms $\hat{c}_p^\dagger \hat{c}_p$ are mapped to:

$$\hat{c}_g^\dagger \hat{c}_g + \hat{c}_e^\dagger \hat{c}_e \rightarrow h_1 II + h_2 IZ + h_3 ZZ$$

while the transition ones are:

$$\hat{c}_e^\dagger \hat{c}_g \rightarrow h_1 IY + h_2 IX + h_3 ZX + h_4 ZY$$

where the coefficients h_i can be computed by applying Eq. 4.3.

4.3.2 The bosonic logarithmic mapper

In Eq. 4.1 there are two types of bosonic operators, that are the particle number operators of each mode and the ones creating or destroying a photon in a mode. Mapping a bosonic mode has many similarities with representing an integer number on a classical computer. In fact, contrary to the case of fermions where a state can be either occupied or unoccupied, an infinite number of bosons can occupy the same quantum state (which is explained by the Bose-Einstein statistics). Therefore, representing a bosonic mode only requires the inclusion of enough Fock states so that the number of bosons occupying it becomes representable.

A first intuitive solution is to store the occupation in the position of the qubit, which is called linear mapper [85]. To represent $\{|0\rangle, |1\rangle, |2\rangle\}$ three qubits are needed: $|0\rangle \rightarrow |001\rangle, |1\rangle \rightarrow |010\rangle, |2\rangle \rightarrow |100\rangle$. The creation and annihilation operators for the mode k are linearly mapped to the qubit space, and they are defined as follows:

$$\hat{b}_k^\dagger = \sum_{n_k=0}^{n_k^{max}-1} \sqrt{n_k+1}\hat{\sigma}_{n_k}^+ \hat{\sigma}_{n_k+1}^-, \quad \hat{b}_k = \sum_{n_k=0}^{n_k^{max}-1} \sqrt{n_k+1}\hat{\sigma}_{n_k}^- \hat{\sigma}_{n_k+1}^+ \tag{4.4}$$

where n_k^{max} is the maximum occupation of the mode and k is the index of the mode. The operators $\hat{\sigma}_{n_k}^-$ and $\hat{\sigma}_{n_k}^+$ are a combination of Pauli matrices:

$$\hat{\sigma}_{n_k}^+ = \frac{1}{2}\left(\hat{\sigma}_{n_k}^x + i\hat{\sigma}_{n_k}^y\right) \equiv S_{n_k}^+ = \frac{1}{2}\left(X_{n_k} + iY_{n_k}\right) \tag{4.5}$$

$$\hat{\sigma}_{n_k}^- = \frac{1}{2}\left(\hat{\sigma}_{n_k}^x - i\hat{\sigma}_{n_k}^y\right) \equiv S_{n_k}^- = \frac{1}{2}\left(X_{n_k} - iY_{n_k}\right) \tag{4.6}$$

In order to represent a mode one needs $n_k^{max}+1$ qubits (in other words, for a single mode the length of the qubit register is $n_k^{max}+1$). In general, the memory complexity of this mapper (i.e. how many qubits it requires) is given by $\mathcal{O}\left(N_K n_k^{max}\right)$, where N_K is the number of bosonic modes. Hence, the scaling is linear with both the number of modes and the maximum allowed occupation per mode. One should note that since this mapper truncates the maximum occupation of a bosonic mode to represent it in the qubit register, the commutation relations of the mapped operator differ from the standard ones [129]. This essentially implies that one must also enforce that $\hat{b}^\dagger|n_k^{max}\rangle = 0$, which adds a further fundamental relation of the bosonic operator [152], preventing exceeding the maximum representable occupation.

However, the representation given by the linear mapper based on the position of the qubit is not optimal. As representing a boson is similar to counting integers, one can try to encode the qubit register in the same way the classical register is encoded (for unsigned integers):

$$0 = 00; |0\rangle = |0,0\rangle = |\uparrow,\uparrow\rangle$$

$$1 = 01; |1\rangle = |0,1\rangle = |\uparrow,\downarrow\rangle$$

$$2 = 10; |2\rangle = |1,0\rangle = |\downarrow,\uparrow\rangle$$

$$3 = 11; |3\rangle = |1,1\rangle = |\downarrow,\downarrow\rangle$$

On the left, the representation of the unsigned integers on two classical bits is reported, while on the right the representation of the Fock states on two qubits. In general, for N_q qubits one has [87]:

$$\begin{aligned}
|0\rangle &= |0_{N_q}, 0_{N_q-1}, ..., 0_1, 0_0\rangle \\
|1\rangle &= |0_{N_q}, 0_{N_q-1}, ..., 0_1, 1_0\rangle \\
|2\rangle &= |0_{N_q}, 0_{N_q-1}, ..., 1_1, 0_0\rangle \\
|3\rangle &= |0_{N_q}, 0_{N_q-1}, ..., 1_1, 1_0\rangle \\
&\dots \\
|2^{N_q}-1\rangle &= |1_{N_q}, 1_{N_q-1}, ..., 1_1, 1_0\rangle
\end{aligned} \tag{4.7}$$

Here the little-endian convention was used, meaning that the right-most entry is the least significant qubit. Using Eq. 4.7 and the well-known bosonic creation and annihilation relations, it is now possible to define what the action of the mapped operator should be [87, 152]:

$$\hat{b}_k^\dagger = \sum_{n=0}^{2^{N_q^k}-1} \sqrt{n+1}|n+1\rangle_k\langle n|_k, \quad \hat{b}_k = \sum_{n=1}^{2^{N_q^k}-1} \sqrt{n}|n-1\rangle_k\langle n|_k \tag{4.8}$$

where k is the mode index and $|n\rangle_k$ represents a generic Fock state of the mode k. In order to define the effect of the operator in terms of the Pauli matrices, here I report an example for a single mode using $N_q = 2$ qubits:

$$\hat{b}^\dagger = \sum_{n=0}^{2^2-2} \sqrt{n+1}|n+1\rangle\langle n| = |1\rangle\langle 0| + \sqrt{2}|2\rangle\langle 1| + \sqrt{3}|3\rangle\langle 2| = |0,1\rangle\langle 0,0| + \sqrt{2}|1,0\rangle\langle 0,1| + \sqrt{3}|1,1\rangle\langle 1,0| \tag{4.9}$$

where one can see that the outer operations are reduced to only four cases [87]:

$$|0\rangle\langle 0| = \frac{\mathcal{I}+\sigma^z}{2}, \quad |1\rangle\langle 1| = \frac{\mathcal{I}-\sigma^z}{2}, \quad |0\rangle\langle 1| = \sigma^+ = \frac{\sigma^x + i\sigma^y}{2}, \quad |1\rangle\langle 0| = \sigma^- = \frac{\sigma^x - i\sigma^y}{2} \tag{4.10}$$

Using the logarithmic mapper leads to a significant improvement respect to the linear one. Considering the operator $\hat{b}^\dagger$ (or $\hat{b}$) for a single mode, with maximum occupation $n_k^{max} = 3$, the the linear mapper requires $n_k^{max} + 1 = 4$ qubits and 12 Pauli terms, while the logarithmic mapper only needs $\log_2(n_k^{max} + 1) = 2$ qubits and 8 Pauli strings. This implies that the circuit will be shallower. However, one should note that while the logarithmic mapper always requires less qubits, in some cases it may require more Pauli strings. For instance, this is the case for a hopping bosonic term: $\hat{b}_1^\dagger \hat{b}_2$.

Finally, it is interesting considering what happens to the qubit registers when dealing with many bosonic modes. In the state $|m_K, m_{K-1}, ..., m_1, m_0\rangle = |m_K,\rangle \otimes |m_{K-1}\rangle \otimes ... \otimes |m_1\rangle \otimes |m_0\rangle$ each mode can be occupied with a different number of particles, as modes are independent. This implies each single-mode register should be independent. Thus, using a logarithmic mapper only implies that fewer qubits are needed to represent the generic mode k. Therefore, the memory complexity of the logarithmic mapper will scale linearly with respect to the number of modes, and logarithmically with respect to the number of Fock states per mode: $\mathcal{O}\left(N_K \log_2\left(n_k^{max}\right)\right)$. In the qubit register this translates to:

$$\begin{aligned} &|m_K, m_{K-1}, ..., m_0\rangle = \\ &|\underbrace{0_{\log_2(n^{max})}, 0_{\log_2(n^{max})-1}, ..., 0_0}_{\text{mode } K}, \underbrace{0_{\log_2(n^{max})}, 0_{\log_2(n^{max})-1}, ..., 0_0}_{\text{mode } K-1}, ..., \underbrace{0_{\log_2(n^{max})}, 0_{\log_2(n^{max})-1}, ..., 0_0}_{\text{mode } 0}\rangle \end{aligned} \tag{4.11}$$

Concretely for the Eq. 4.1, to represent two bosonic modes, each with maximum occupation $n^{max} = 1$ (i.e. using the Fock states $|0\rangle, |1\rangle$) the required number of qubits using the logarithmic mapper is 2. The diagonal terms $\hat{a}_p^\dagger \hat{a}_p$ are mapped to:

$$\hat{a}_1^\dagger \hat{a}_1 + \hat{a}_2^\dagger \hat{a}_2 \to h_1 II + h_2 IZ + h_3 ZI$$

while the creation ones are:

$$\hat{a}_1^\dagger \to h_1 IY + h_2 IX, \quad \hat{a}_2^\dagger \to h_1 YI + h_2 XI$$

4.3.3 The mixed mapper

The interaction terms in Eq. 4.1 contain products of fermionic and bosonic operators. Due to these terms, the QED Hamiltonian is defined in a joint fermionic and bosonic Hilbert space. In sections 4.3.1 and 4.3.2 the two systems were treated separately, defining a fermionic qubits register with $N_{q,f} = 2$ qubits and a bosonic one of $N_{q,b} = 2$ qubits. In quantum computing, a joint Hilbert space corresponds to a joint quantum register where the single registers of the single subsystems are concatenated in a well-defined order. The length of the total register is the sum of the ones of all sub-registers. Within each sub-register then, each operator is mapped with the specified mapper for that type for subsystem. In the case of Eq. 4.1, considering a two-level fermionic system mapped with the Bravyi-Kitaev mapper coupled to two photonic modes represented with $\{|0\rangle, |1\rangle\}$ and mapped with the bosonic logarithmic mapper, the total register would have 4 qubits organized as $|B_2 B_1 F_1 F_2\rangle$, where F_i is a qubit belonging to the fermionic system, and B_i is a qubit belonging to the bosonic one. Note that the Pauli string produced must have the same length of the joint register. This means that when mapping the uncoupled terms, one has to add an identity to the system that is not being mapper (e.g. $\hat{c}_i^\dagger \hat{c}_i \otimes_k \mathbb{I}_k$, where k is the photonic mode index). This construction preserves the chosen encoding within each sector, and guarantees a consistent qubit layout across Hamiltonian terms and observables.

Finally, the QED Hamiltonian in Eq. 4.1 can be mapped as follows:

$$\begin{aligned}\hat{H}^{QED}_{map} &= a_1 IIII + a_2 ZIII + a_3 IIIZ + a_4 IZII + a_5 IIZZ + \\ & a_6 IXIX + a_7 IXZX + a_8 IYIY + a_9 IYZY + a_{10} XIIX + a_{11} XIZX + a_{12} YIIY + a_{13} YIZY\end{aligned} \tag{4.12}$$

where the Pauli operators in blue correspond to the fermionic sub-register, and the one in black from the bosonic one.

4.4 Publication IV: Hardware-efficient formulation of molecular cavity-QED Hamiltonians

State of the art

Simulating cavity-QED systems faced fundamental limitations with both classical and quantum computing. Classical approaches struggled with the exponential scaling of the joint electron-photon Hilbert space, which leads to the introduction of heavy approximations such as using only a single effective cavity modes or using theories that allow to recast the photonic problem as an effective problem [16]. Quantum computing offers a promising alternative by encoding the photonic Hilbert space into linearly scaling qubit registers [129, 87]. Yet existing quantum implementations face critical bottlenecks. Earlier quantum simulations of light-matter systems typically employed spin representations for matter [85], limiting extensibility to complex molecular systems. Crucially, these works relied on hybrid quantum-classical algorithms (e.g., variational approaches) for time evolution rather than fully quantum solutions. Furthermore, the star-like connectivity characterizing multi-mode QED Hamiltonians, where matter qubits interact with all photonic modes, exceeds the limited qubit connectivity of superconducting devices, necessitating SWAP operations that amplify noise and restrict simulations to small systems.

Main findings

This work establishes a hardware-efficient mapping for cavity-QED simulations on near-term quantum hardware through three interconnected advances. First, we implemented this formalism via novel bosonic (`BosonicOp`) and mixed fermion-boson (`MixedOp`) operators in *Qiskit Nature*, including a logarithmic bosonic mapper that reduces qubit requirements from $\mathcal{O}(N_K n^{max})$ to $\mathcal{O}(N_K \log_2 n^{max})$ while preserving physical accuracy. Second, we developed a unitary transformation to map the cavity modes to a localized photonic basis that enforces nearest-neighbor couplings, allowing us to map the Hamiltonian to a 1D qubit chain compatible with superconducting device topology. This reformulation reduces CNOT gates compared to the standing-wave approach by eliminating all SWAPs gates. Finally, leveraging these tools, we performed a fully quantum Trotter evolution of a two-level system coupled to 24 and 36 photonic modes, computing Rabi oscillations. Despite hardware noise, zero-noise extrapolation recovered accurate dynamics, also maintaining robustness when relaxing strict 1D constraints. Collectively, these advances resolve prior connectivity barriers and establish a scalable pathway for cavity-QED quantum simulations.

Status and Publication details

This paper has been published as a preprint on *arXiv* in October 2025 [137]. It is currently under review in *Quantum - the open journal for quantum science*. The supplementary information is in the form of appendixes at the end of the article (which are included in the present thesis).

Contribution

I derived the theory, developed all the code (except for the `MixedOp` and `MixedMapper` classes, to which I contributed with technical design and code review), performed all simulations, analyzed the data, interpreted the results and wrote the first draft of the paper. All authors contributed to the revision of the manuscript. This work benefited from a few long visits to the IBM quantum group in Zurich (led by Ivano Tavernelli, co-supervisor of this Ph.D. work).

Hardware-efficient formulation of molecular cavity-QED Hamiltonians

Francesco Troisi[1], Simone Latini[2], Heiko Appel[1], Martin Lüders[1], Angel Rubio[1,3], and Ivano Tavernelli[4]

[1]Max Planck Institute for the Structure and Dynamics of Matter and Center for Free-Electron Laser Science, Luruper Chaussee 149, 22761, Hamburg, Germany

[2]Department of Physics, Technical University of Denmark, 2800 Kgs. Lyngby, Denmark

[3]Initiative for Computational Catalysis (ICC), The Flatiron Institute, 162 Fifth Avenue, New York, NY 10010, United States

[4]IBM Quantum, IBM Research Europe - Zurich, 8803 Rüschlikon, Switzerland

Light–matter coupled Hamiltonians are central to cavity materials engineering and polaritonic chemistry, but are challenging to simulate with classical hardware due to the scaling of the Hilbert space with the number of quantum photon modes and matter complexity. Leveraging the fact that quantum computers naturally represent photonic modes efficiently, we present a novel approach to simulate quantum-electrodynamical (QED) systems on near-term quantum hardware. After developing the bosonic and mixed operators in the *Qiskit Nature* framework, we employ them to simulate a first-order Trotterized Hamiltonian for a spontaneous-emission problem of a two-level system in an optical cavity. We find that using a standing-waves photonic basis approach leads to fidelity issues due to hardware connectivity constraints and two-qubits gates errors. Hence, we propose using a localized photonic basis approach that enforces nearest-neighbor couplings, thanks to which we can map the Hamiltonian as a 1D qubit chain. We significantly reduce the noise and, by applying the zero-noise extrapolation error mitigation technique, we recover the accurate quantum dynamics. Finally, we also show that this approach is resilient when relaxing the 1D qubit chain approximation.

Francesco Troisi: francesco.troisi@mpsd.mpg.de
Simone Latini: simola@dtu.dk
Angel Rubio: angel.rubio@mpsd.mpg.de
Ivano Tavernelli: ita@zurich.ibm.com

1 Introduction

Over the past decade quantum computers have evolved from proof-of-concept devices with only a few noisy qubits to programmable machines comprising hundreds of qubits. Current state-of-the-art processors, mostly based on superconducting circuits [1], but also ion-trap [2] and neutral-atom [3] arrays, have demonstrated problem-specific quantum advantage on carefully chosen problems, such as the Ising model [1] or sampling the output of a random quantum circuit [4]. Focusing only on superconducting hardware, technological advancements such as high-fidelity gates, native mid-circuit measurement and advanced error-mitigation protocols [5, 6], allowed the community to shift its focus from hardware demonstrations to physically relevant applications such as protein chain optimization [7] or hadron scattering observation [8]. However, since even state-of-the-art superconducting layouts are still quasi-planar, most previous works dealt with Hamiltonians that map naturally onto a linear chain of qubits, thereby avoiding or minimizing SWAP operations. Examples include Fermi-Hubbard models [9, 10], Ising [1] and molecular Hamiltonians [11]. Systems that mix particles of different nature, such as fermions and bosons, often feature star-like or all-to-all couplings which exceed the capabilities of current devices in terms of connectivity and efficiency.

Materials cavity quantum electrodynamics (QED) provides an example for such systems. Optical cavities confine the electromagnetic field in a small region, allowing to reach a strong light-matter coupling regime with embedded condensed matter systems [12, 13, 14]. Tuning the cavity frequencies can modify molecular polarizabilities [15, 16], modify inter-molecular properties [17], open gaps in Dirac materials [18] or reshape excitonic spectra [19, 20]. This emerging field is known as cavity materials engineering [14, 21]. Classical simulations of QED systems are costly due to the memory required to represent the full Hilbert space as well as to the time required to diagonalize the Hamiltonian, especially when dealing with many photonic modes. In fact, the photonic Hilbert space scales exponentially with the number of modes and the number of Fock states used to represent them. Hence, one typically describes a simple matter system coupled to many photonic modes [12] or relies on a single-effective (or few-effective) mode description of the electromagnetic field [20, 22]. On a quantum processor, by contrast, the same exponential structure can be encoded with a linearly scaling number of qubits. Combined with the short execution time of a quantum circuit, this promises to be a breakthrough in the simulation of QED systems.

As a first step towards a full quantum simulation where both light and matter retain their full complexity, in this work we study the quantum dynamics of a simple fermionic system (two-level system) coupled to a bath of photonic modes. First, we present the technical implementation of the Bosonic Operator and Mapper, required to represent the photonic modes on the quantum computer, and of the Mixed Operator and Mapper, which enable the representation of fermion–boson interactions, within the open-source Python package *Qiskit Nature* [23]. *Qiskit Nature* is part of *Qiskit*, IBM's open source quantum Software Development Kit (SDK) [24]. Subsequently, we study the time evolution of the aforementioned system, observing the Rabi oscillations. After representing the Hamiltonian on the quantum hardware and defining the initial state such that the matter systems starts in the excited state and all photonic modes in the vacuum, we simulate the quantum dynamics with the Trotter time evolution algorithm. In our approach, the matter system is described directly in terms of fermionic operators rather than spin particles. This represents a key novelty compared to previous works on the topic [25] and enables the extension of the method to more complex matter systems. Moreover, in this work we employ a Trotter approximation of the time evolution operator instead of a variational quantum approach, and we focus on demonstrating the system's scaling with an increasing number of modes rather than limiting the analysis to only a few modes. Furthermore, we also acknowledge a previous work on classical hardware [26] that studies the dynamics of a two-level fermionic system coupled to a bath of photonic modes, in particular comparing an exact quantum simulation to a multi-trajectory Ehrenfest dynamics approach. We present two formulations of the QED Hamiltonian, adapting it to the strong noise requirements of near-term quantum computers, and we show that, even with the presence of SWAP operations, we can extrapolate the noiseless dynamics for one of them, which paves the way for quantum simulations of cavity quantum electrodynamics.

The paper is organized as follows: Section 2 presents the theoretical model and the implementation details, Section 3 discusses the two formulations of the QED Hamiltonian as well as the noisy simulations. Finally Section 4 summarizes the results of the paper and provides directions for future work.

2 Methods

2.1 Model system and QED Hamiltonian

To study the behavior of a generic two-level system in an optical cavity, as the one in Fig. 1, we first model the two uncoupled systems (electrons and photons) and subsequently describe their interaction. All throughout this work we use atomic units.

The most efficient way to describe a two level system is using a spin representation [25]. However, since we want to keep our theory general and extendable to multi-level systems such as in atoms and molecules, we use Fermionic operators in the form of:

$$\hat{H}_m = \sum_i \varepsilon_i \hat{c}_i^\dagger \hat{c}_i \tag{1}$$

where $\hat{c}^\dagger, \hat{c}$ are electronic creation (annihilation) operators, and ε_i is the energy of the i-th state. We use $\{\varepsilon_1, \varepsilon_2\} = \{-0.6738, -0.2798\}$ Ha, which corresponds to a 1D Hydrogen atom described with the soft Coulomb potential [26]. The matter system is placed at the center of the cavity.

We describe the uncoupled light system with a set of effective harmonic oscillators:

$$\hat{H}_{ph} = \sum_{\alpha,\lambda} \Omega_\alpha \left(\hat{a}^\dagger_{\alpha,\lambda} \hat{a}_{\alpha,\lambda} + \frac{1}{2} \right) \tag{2}$$

where Ω_α represents the energy of the photonic mode α and λ is the polarization. We apply the long-wavelength approximation (LWA) [22] for the component of the momentum of the modes in the xy plane (in-plane), meaning that $\boldsymbol{q}_{\alpha,\parallel} = \mathbf{0}$. Conversely, we distinguish the momenta of the different modes in the direction of confinement, hence $q_{\alpha,z} = \frac{\pi\alpha}{L}$ where L is the length of the cavity. Consequently, $\Omega_\alpha = cq_{\alpha,z}$, where c is the speed of light [12]. We only consider one polarization ($\lambda = s$), hence we drop the index λ.

We couple light and matter by minimal coupling $\hat{\boldsymbol{p}} \rightarrow \hat{\boldsymbol{p}} + \hat{\boldsymbol{A}}$. Hence, the interaction Hamiltonian reads [12, 27]:

$$\hat{H}_{\text{int}} = -\sum_{ij,\alpha} d_{ij} \omega_{ij} \lambda_\alpha \hat{c}^\dagger_i \hat{c}_j \hat{q}_\alpha \tag{3}$$

where d_{ij} is the dipole matrix element, ω_{ij} is the energy of the ij transition, $\hat{q}_\alpha = \sqrt{\frac{1}{2\Omega_\alpha}} \left(\hat{a}^\dagger_\alpha + \hat{a}_\alpha \right)$ and $\lambda_\alpha = \sqrt{\frac{2}{L}} \sin(q_{\alpha,z} z)$ is the mode function. Note that since the matter system is placed at the center of the cavity ($z = \frac{L}{2}$), only the odd cavity modes will have a non-zero coupling. Despite the theory is written in general terms, in our implementation we enforce the rotating wave approximation (RWA), which simplifies the Hamiltonian by reducing the number terms, implying fewer Pauli strings h_j (c.f. Eq. 5) and fewer gates in the quantum circuit.

The full QED Hamiltonian is:

$$\hat{H}_{\text{QED}} = \hat{H}_{\text{m}} + \hat{H}_{\text{ph}} + \hat{H}_{\text{int}} \tag{4}$$

Note that we absorbed the diamagnetic term into the uncoupled photon Hamiltonian by performing a Bogoliubov transformation [18, 28].

2.2 Quantum dynamics

To study the quantum dynamics of the two-level system in an optical cavity, we prepare the initial state such that the matter is initially in the excited state, while all cavity modes are in the vacuum. Since this is not an eigenstate of the time-independent QED Hamiltonian in Eq. 4, the system will evolve according the time-dependent Schrödinger equation, hence: $|\psi(t)\rangle = e^{-i\hat{H}t} |\psi(0)\rangle$, where $|\psi(0)\rangle$ is the initial state of the system. One of the most common techniques for simulating time evolution in quantum computing is approximating the unitary time-evolution operator with a product formula. At first order, this corresponds to the Lie-Trotter formula. Given a Hamiltonian of the form $\hat{H} = \sum_{j=1}^{N_h} h_j$, that is to say that the Hamiltonian can be expressed as a sum of N_h Pauli strings h_j, the Lie-Trotter decomposition approximates the evolution operator as

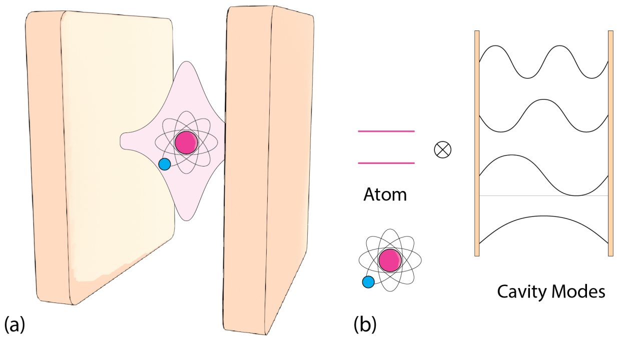

Figure 1: Schematics of a two-level fermionic system placed in the center of an optical cavity, coupled to a bath of cavity modes. a) Representation of a two-level atom placed in the center of an optical cavity. The direction of confinement is the z direction. b) Representation of the coupling of the atom with the cavity modes, visualized as standing waves. Note that only the odd modes (i.e. the ones that are non-zero in the center) couple to the matter.

$$\exp\left(-i\hat{H}t\right) \approx \left(\prod_{j=1}^{N_h} e^{-ih_j \frac{t}{d}} \right)^d, \tag{5}$$

where t is the simulation time and d is the number of time-steps. The associated error scales as $\mathcal{O}\left(\frac{N_h t^2}{d}\right)$, as the QED Hamiltonian can be split into even and odd parts [29]. The main limitation of this method lies in its circuit depth (the maximum number of layers of gates along the longest path), which tends to be large because the error scales quadratically with the total simulation time.

2.3 Bosonic operators in *Qiskit Nature*

In order to represent both Eq. 2 and Eq. 3 on a quantum computer, one needs to be able to represent bosonic operators. To do this, we developed the class `BosonicOp` in *Qiskit Nature*, representing a generic second-quantized bosonic operator. The documentation on how to use such class is released with *Qiskit Nature* (c.f. Appendix B.1 for the version details). In order to use such operator, one should translate it (map) to a Pauli operator. Hence, we implemented two mappers, the `BosonicLinearMapper` and `BosonicLogarithmicMapper`. Both mappers represent a boson as a set a of Fock states $\{|0\rangle, |1\rangle, ...\}$, up to a maximum occupation $n_\alpha^{\max}$. The two bosonic mappers differ in how the truncated Fock space is encoded on qubits and this leads to qualitatively different qubit operators, despite the similar ladder structure of the creation operator. In the `BosonicLinearMapper`, based on Ref. [25], a single mode α is represented by a register of $N_{\alpha,q} = n_\alpha^{\max} + 1$ qubits in a unary code, where the occupation n_α is stored as the position of a flag along the qubit register. For example, to represent $\{|0\rangle, |1\rangle, |2\rangle\}$ one would need three qubits, and would have $|0\rangle \to |001\rangle, |1\rangle \to |010\rangle, |2\rangle \to |100\rangle$. Therefore, the creation operator is represented by:

$$\hat{a}_\alpha^\dagger = \sum_{n_\alpha=0}^{n_\alpha^{\max}-1} \sqrt{n_\alpha + 1}\hat{\sigma}_{n_\alpha}^+ \hat{\sigma}_{n_\alpha+1}^- \tag{6}$$

and it shifts the flag from level n_α to $n_{\alpha+1}$ with the proper $\sqrt{n_\alpha + 1}$ amplitude. $\hat{\sigma}_{n_\alpha}^\pm$ follow the usual definition of combination of Pauli matrices. The qubit count scales as $\mathcal{O}\left(N_\alpha \left(n_\alpha^{max} + 1\right)\right)$. This construction yields operators that are strictly local on the mode register (only nearest neighbors along the rail interact), so bosonic hopping terms compile to shallow circuits at the price of a linear qubit overhead per mode.

By contrast, the `BosonicLogarithmicMapper`, based on Ref. [30, 31, 32], stores the occupation n in a binary representation over $N_{\alpha,q} = \lceil log_2(n_\alpha^{\max}+1) \rceil$ qubits. For example, to represent $\{|0\rangle, |1\rangle, |2\rangle\}$ one would need two qubits, and would have $|0\rangle \to |00\rangle, |1\rangle \to |01\rangle, |2\rangle \to |10\rangle$. In this encoding the creation (annihilation) operator has to increase (decrease) a binary-encoded number, and it is written as:

$$\hat{a}_\alpha^\dagger = \sum_{n=0}^{2^{N_{\alpha,q}}-2} \sqrt{n_\alpha + 1}\ |n+1\rangle_\alpha \langle n|_\alpha \tag{7}$$

The operator $|n+1\rangle_\alpha \langle n|_\alpha$ translates, for every qubit, to a combination of Pauli matrices (c.f. Appendix D.2). The consequence is a reduction of the qubit count, which scales as $\mathcal{O}\left(N_\alpha \log_2\left(n_\alpha^{\max}\right)\right)$, but at the cost of more Pauli strings and increased non-locality within the mode register, which generally leads to deeper circuits for bosonic hopping terms.

A detailed description of both mappers can be found in the Appendix D.

2.4 Mixed operators in *Qiskit Nature*

Light–matter Hamiltonians contain products of fermionic and bosonic operators (e.g. Eq. 3). To represent the corresponding joint Hilbert space in the qubit space, we developed the `MixedOp` (mixed operator) class in *Qiskit Nature*, together with its mapper `MixedMapper`. A `MixedOp` is a composite second-quantized operator which aggregates heterogeneous subsystems such as fermions (`FermionicOp`) and bosons (`BosonicOp`) into a single object representing their tensor product. In quantum-computing terms, this corresponds to forming a joint quantum register by concatenating the single registers of the single subsystems in a well-defined order. The `MixedMapper` then delegates the qubit encoding of each operator to the specified mapper for that type for subsystem. For instance, in this work we map the mixed operator $\hat{c}_i^\dagger \hat{c}_j \hat{a}_\alpha^\dagger$ by applying the Bravyi–Kitaev mapper to $\hat{c}_i^\dagger \hat{c}_j$ and the `BosonicLogarithmicMapper` to $\hat{a}_\alpha^\dagger$. The `MixedMapper` automatically computes the required register lengths, and assembles the mixed qubit operator by placing each mapped subsystem at the appropriate place in the joint quantum register. The result is a `SparsePauliOp` whose Pauli strings have length $N_j = N_{\text{reg},f} + N_{\text{reg},b}$ where $N_{\text{reg},f}$ ($N_{\text{reg},b}$) is the number of qubits in the original fermionic (bosonic) register. This construction preserves the chosen encoding within each sector, and guarantees a consistent qubit layout across Hamiltonian terms and observables. For instance, considering a two-level fermionic system mapped with the Bravyi-Kitaev mapper coupled to one mode represented with $\{|0\rangle, |1\rangle\}$ and mapped with the bosonic logarithmic mapper, one would have $N_{\text{reg},f} = 2$ and $N_{\text{reg},b} = 1$. Hence, the total register would have 3 qubits organized as $|B_1 F_1 F_2\rangle$, where F_i is a qubit encoding the fermionic system, and B_i is a qubit encoding the bosonic one.

2.5 Noise model and hardware

All numerical experiments are performed using *Qiskit* and *Qiskit Nature*. Noise is emulated with *Qiskit-Aer*, using real calibration data of the 156-qubit superconducting quantum computer `ibm_pittsburgh` (c.f. Appendix B.2 for the connectivity scheme). The noise model includes depolarization, thermal relaxation and readout assignment errors and it represents a *worst-case scenario*, as running on the quantum hardware gives access to state-of-the-art error mitigation techniques (such as dynamical decoupling and readout mitigation). Note that due to memory and time limitations of the classical HPC cluster running the simulations, we are not able to simulate more than 24 qubits.

3 Results

Here we present the results for the dynamics of the QED Hamiltonian in Eq. 4 for a two-level fermionic system. We represent such matter system using the `FermionicOp` class, and we map it using the Bravyi-Kitaev mapper. As a result, we use two qubits. We truncate the occupation of the cavity modes to $n^{\max} = 1$, meaning that the Fock space for each mode is $\{|0\rangle, |1\rangle\}$. Using the bosonic logarithmic mapper, each mode is mapped to a single qubit. The interaction terms are represented with the `MixedOp` and mapped using the `MixedMapper` (which wraps the Bravyi-Kitaev and the bosonic logarithmic mapper). Our initial state $|\psi(0)\rangle$ is made of the matter system being in its excited state, and all cavity modes in the vacuum. Then, we let the system evolve freely. Refer to Appendix B.4 for the numerical values. At every time-step, we measure the occupation of the matter excited state $\hat{n}_e = \hat{c}_e^\dagger \hat{c}_e$. To perform the measurement, we use the `Estimator` primitive as implemented in *QiskitAer*, which computes $\langle \psi(t)| \hat{n}_e |\psi(t)\rangle$. In terms of Pauli operators, this corresponds to $\langle \psi(t)| \frac{II+ZZ}{2} \otimes \mathbb{I}_{ph} |\psi(t)\rangle$, where I, Z are Pauli operators and $\mathbb{I}_{ph}$ represents the identity operator applied to all qubits representing a photonic mode.

3.1 Standing-waves photonic basis

We simulate the quantum dynamics by directly mapping the Hamiltonian in Eq. 4, without additional approximations, for a two-level system initially in the excited state and all photonic modes in the vacuum state. As we describe the electromagnetic field as a superposition of standing-waves, we refer to this section as the Standing-waves approach. Figure 2 shows the dynamics of the two-level system coupled to either $N_{\text{ph}} = 24$ or $N_{\text{ph}} = 36$ cavity modes. Note that since the two level system is placed in the center of the cavity, only the odd modes couple to it. Hence, the number of qubits in the photonic register is $N_q = 12$ or $N_q = 18$, respectively. In both cases, we report both the noiseless (statevector) simulation and the noisy one. While for the former we observe a full Rabi oscillation, the noisy curve quickly falls to the value of $\langle \hat{n}_e \rangle = 0.5$ and stays flat, meaning that the noise completely saturates the signal. Note that the plateau is at 0.5 instead of 0 due to the term $\frac{II}{2} \otimes \mathbb{I}_{ph}$ in the observable.

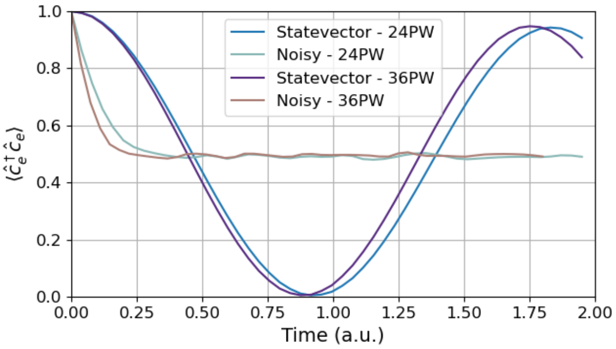

Figure 2: Quantum dynamics of a two-level system placed in the center of an optical cavity. The two-level system was initially in the excited state, while all photonic modes started in the vacuum state. For $N_{\text{ph}} = 24$ modes, the total number of qubits is 14 (2 for the matter, 12 for the photon modes). For $N_{\text{ph}} = 36$ modes, the total number of qubits is 20 (2 for the matter, 18 for the photon modes). For both cases, we report the exact statevector simulation (where we can observe a full Rabi oscillation) as well as the noisy curve (which reaches the saturation around $t \approx 0.25$ a.u.)

The reason for such an aggressive noise is twofold. Firstly, looking at the interaction Hamiltonian we notice that the electronic transition is coupled to all the cavity modes (through the terms $\sum_\alpha \hat{c}_i^\dagger \hat{c}_j (\hat{a}_\alpha^\dagger + \hat{a}_\alpha)$). This implies that one of the two qubits representing the matter system needs to interact with all the qubits of the photonic register, as depicted in Fig. 3(a). In the case of $N_{\text{ph}} = 24$ cavity modes, this means that one qubit has to communicate with 13 others (with 19 others for $N_{\text{ph}} = 36$). Since the maximum connectivity on the hardware `ibm_pittsburgh`

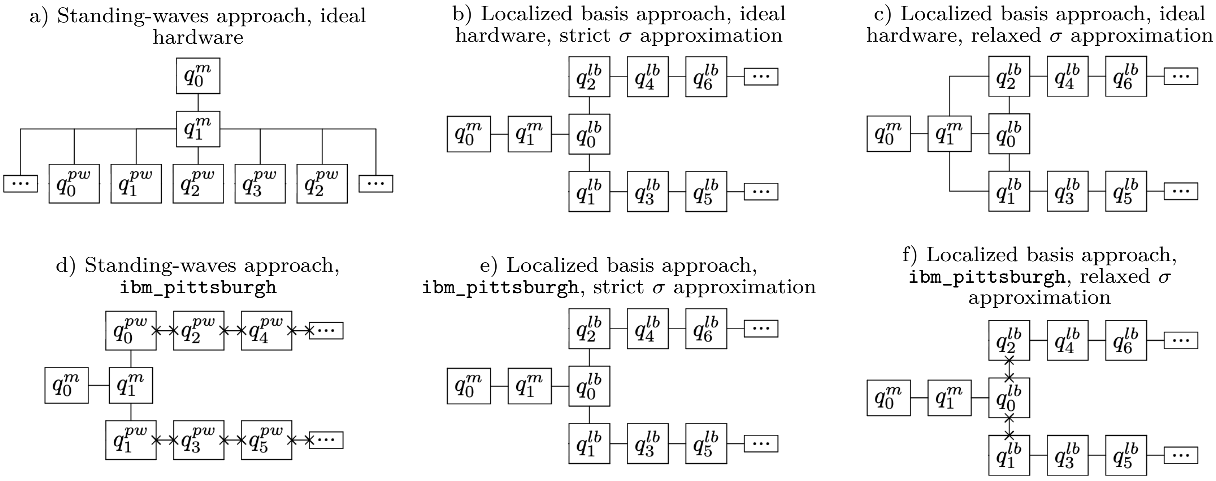

Figure 3: Schematics of the qubit connectivity for the standing-waves approach and the localized basis approach. Panels a), b) and c) represent the connectivity for an ideal hardware, while panels d), e) and f) show the connectivity after the circuit is transpiled to `ibm_pittsburgh`. a) Required connectivity for the standing-waves approach on an ideal hardware. All photonic qubits q^{pw} are connected to the *central* matter qubit q_1^m. b) Required connectivity for the localized basis approach on an ideal hardware, assuming that the tensor τ in Eq. 9 is tridiagonal and $\sigma \neq 0$ only between q_1^m and the central localized function q_0^{lb}. c) Required connectivity for the localized basis approach on an ideal hardware, assuming that the tensor τ in Eq. 9 is tridiagonal and $\sigma \neq 0$ between q_1^m and the three central localized function $q_0^{lb}, q_1^{lb}, q_2^{lb}$. d) Connectivity of the standing-waves approach mapped onto `ibm_pittsburgh`. All of the qubits representing a mode are divided into two branches, and SWAP operations (represents by the x in the connectors) are introduced to allow them to interact with q_1^m. e) Connectivity of the localized basis approach on the `ibm_pittsburgh`. Since we enforced τ and σ to match the hardware layout, no SWAP operations are required, which makes this panel identical to panel b). f) Connectivity of the localized basis approach on the `ibm_pittsburgh`, when $\sigma \neq 0$ for the three central localized functions. Since the required connectivity for the qubit q_1^m is 4, SWAP operations are required (in particular, 4 SWAPs per time-step between $q_0^{lb}, q_1^{lb}, q_2^{lb}$).

is 3 (and in general for superconducting quantum computers it is never larger than 4), in order to allow this interaction the transpiler introduces SWAP operations, as shown in Fig. 3(d). In particular, when q_1^m has to interact with q_2^{pw}, first the transpiler places a SWAP between q_0^{pw} and q_2^{pw}, then the interaction takes place and finally q_0^{pw} and q_2^{pw} are swapped back again. Note that each cavity mode is independent, hence the qubits in the photonic register do not interact with each other. The second reason is due to the high load on the central qubit. In fact, all of the CNOTs per time-step (except for the ones involved in the SWAP operations) involve the central qubit q_1^m, which in the case of $N_{\text{ph}} = 24$ cavity modes is 248 CNOTs (405 CNOTs for $N_{\text{ph}} = 36$).

3.2 Localized photonic basis

To address the connectivity bottlenecks, we perform a unitary transformation of the photonic modes with the aim of making the Hamiltonian representable as a 1D linear chain of qubits (so that no SWAP operation is needed). To achieve that, we consider a set of localized and orthogonal basis functions. By *localized* we mean that the function is peaked around a specific point inside the cavity and then quickly goes to zero (c.f. Appendix C.2). We project the photonic operators onto this new basis:

$$\hat{a}_\alpha = \sum_{l=0}^{\infty} P_{l\alpha}\, \hat{t}_l, \qquad \hat{a}_\alpha^\dagger = \sum_{l=0}^{\infty} P_{l\alpha}^*\, \hat{t}_l^\dagger, \tag{8}$$

where $P_{l\alpha} = \int L_l(z)\, e^{iq_{\alpha,z}z}\mathrm{d}z$ is the projection of the α-th mode onto the $L_l(z)$-th basis function. The operators $\hat{t}^\dagger, \hat{t}$ create (annihilate) an excitation in the specified localized basis function and, importantly, we treat them as bosons. In this work, we use a set of triangular basis functions (c.f. Appendix C.2 for the exact definition), but others may be employed as well (i.e. rectangular). Expanding the Hamiltonian in Eq. 4 with the operators in Eq. 8, we obtain (c.f. Appendix C.1 for

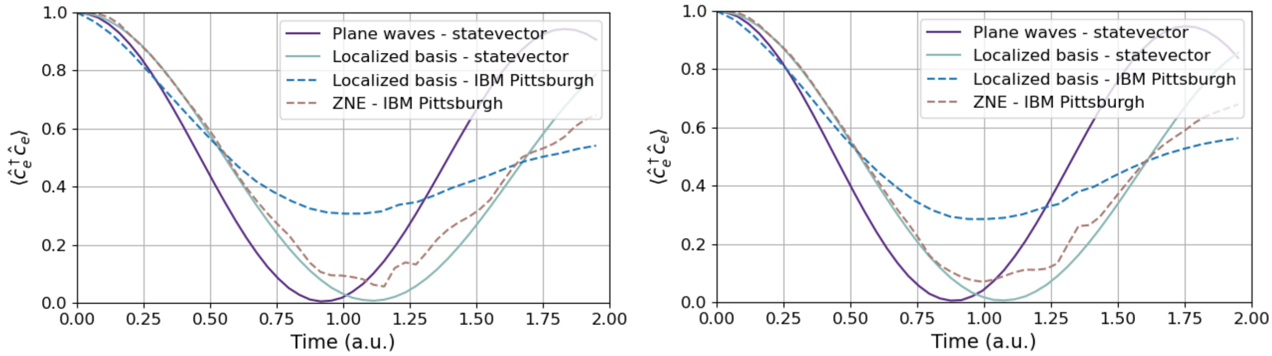

a) 24 modes, 13 localized functions, $\sigma_7 \neq 0$

b) 36 modes, 19 localized functions, $\sigma_{10} \neq 0$

c) 24 modes, 13 localized functions, $\sigma_6, \sigma_7, \sigma_8 \neq 0$

d) 36 modes, 19 localized functions, $\sigma_9, \sigma_{10}, \sigma_{11} \neq 0$

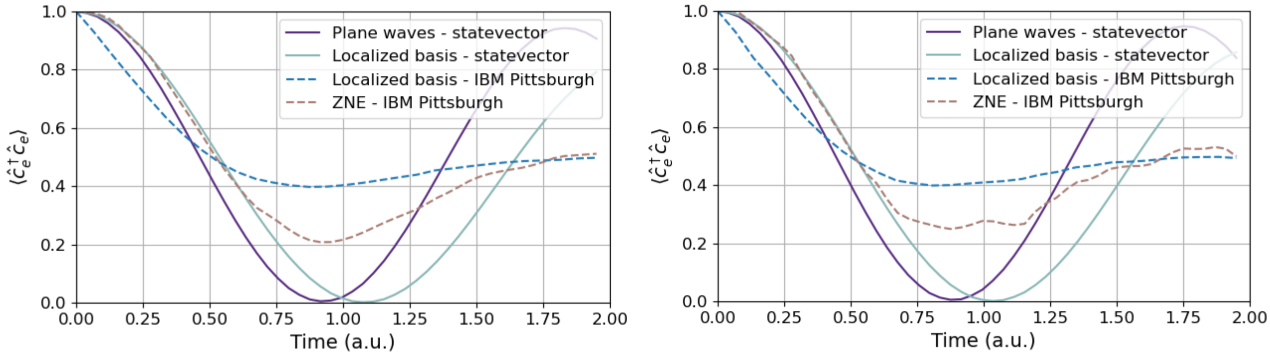

Figure 4: Quantum dynamics of a two-level system placed in the center of an optical cavity when the modes are described with the localized basis approach (c.f. Section 3.2), assuming that the tensor τ in Eq. 9 is tridiagonal and $\sigma \neq 0$ only for a few central localized functions (1 in panels a and b, 3 in panels c and d). The two-level system was initially in the excited state, while all cavity modes started in the vacuum state. Due to the constraints on τ and σ, the statevector simulation for the localized basis does not reproduce the standing-waves reference, but still represents a good approximation. Note that relaxing the constraint on σ leads to a better approximation for the statevector simulation, as it can be seen by comparing panel a with c, or b with d. The zero-noise extrapolation (ZNE) dynamics is obtained using a linear fit. a) $N_{\text{ph}} = 24$ cavity modes, approximated with $N_{\text{loc}} = 13$ localized functions, using $N_q = 15$ qubits. $\sigma \neq 0$ only for the central localized function (σ_7). b) $N_{\text{ph}} = 36$ cavity modes, approximated with $N_{\text{loc}} = 19$ localized functions, using $N_q = 21$ qubits. $\sigma \neq 0$ only for the central localized function (σ_{10}). c) $N_{\text{ph}} = 24$ cavity modes, approximated with $N_{\text{loc}} = 13$ localized functions, using $N_q = 15$ qubits. $\sigma \neq 0$ for the three central localized functions ($\sigma_6, \sigma_7, \sigma_8$). d) $N_{\text{ph}} = 36$ cavity modes, approximated with $N_{\text{loc}} = 19$ localized functions, using $N_q = 21$ qubits. $\sigma \neq 0$ for three central localized functions ($\sigma_9, \sigma_{10}, \sigma_{11}$).

the complete derivation):

$$\hat{H}_{\text{QED}}^{\text{loc}} = \hat{H}_m + \sum_{\alpha}^{N_{ph}} \frac{\Omega_\alpha}{2} + \sum_{ll'}^{N_{loc}} \tau_{ll'} \hat{t}_l^\dagger \hat{t}_{l'} - \sum_{ij} d_{ij}\omega_{ij} \sum_{l}^{N_{loc}} \left(\sigma_l^* \hat{t}_l^\dagger + \sigma_l \hat{t}_l \right) \hat{c}_i^\dagger \hat{c}_j \tag{9}$$

where $\hat{H}_m$ is the matter Hamiltonian defined in Eq. 1, i, j are indexes that span over the matter states and ω_{ij} is the energy of the matter transition. N_{loc} is the number of localized functions used in the expansion. The tensor $\tau_{ll'} = \sum_\alpha \Omega_\alpha P_{l\alpha}^* P_{l'\alpha}$ represents the hopping between the localized functions l and l', while $\sigma_l = \sum_\alpha \lambda_\alpha \sqrt{\frac{1}{2\Omega_\alpha}} P_{l,\alpha}$ represents (together with $d_{ij}\omega_{ij}$) the probability amplitude of having a transition between the state i and j through the destruction of a localized excitation at l. As the operators $\hat{t}^\dagger, \hat{t}$ have bosonic nature, we represent them using the `BosonicOp` class and, limiting their occupation to the state $|1\rangle$, they require only one qubit to be encoded on the quantum computer. The localized Hamiltonian in Eq. 9 requires, in general, a much worse connectivity than the Hamiltonian in Eq. 4 due to the fact that the interaction term behaves in the same way (coupling each matter transition to all the localized functions), and in addition the hopping tensor τ requires an all-to-all connectivity between the qubits representing the localized functions. In order for the Hamiltonian to be representable as a linear chain, the tensor τ should be tridiagonal (meaning that an excitation can only hop to the neighboring basis function) and σ should be non-zero only for one localized function. If these two conditions are met, the required qubit connectivity becomes the one shown in Fig. 3(b, e), where a qubit has to interact at most with three neighboring qubits (which is supported by the honeycomb layout of `ibm_pittsburgh`). In Appendix C.3 we discuss the limitations of such approximations.

Fig. 4 shows the quantum dynamics of the two-level system coupled to the cavity modes described using the localized basis approach. We focus on panels (a, b), where τ and σ are truncated to meet the aforementioned conditions. First, we note that the ideal (statevector) simulation of the localized basis approach, while still qualitatively capturing the physics of the Rabi oscillations, does not quantitatively reproduce the statevector simulations of the standing-waves approach (which is our reference). This is expected as we use a finite set of localized functions and we truncate both τ and σ to meet the connectivity requirements. Such a result represents a good trade-off between algorithmic fidelity (i.e. how well we can reproduce the reference result) and noise resilience. In fact, thanks to the improved connectivity, the noisy curve reaches the noise saturation value of $\langle \hat{n}_e \rangle \approx 0.5$ for $t > 2$ a.u., compared to the standing-waves approach where it was reached at $t \approx 0.25$ a.u. Furthermore, the noisy curve in Fig. 4(b) shows that even when expanding the localized basis set (hence, when using more qubits) the noise remains almost constant. In fact, Fig. 4(b) uses six qubits more than Fig. 4(a), but the noisy curve follows that same dynamics. This resilience is a major improvement as it allows to apply the zero-noise extrapolation (ZNE) technique [33, 34] to mitigate the quantum error. In the ZNE one deliberately amplifies the error from the quantum gates and then extrapolates the zero-noise curve. We only amplify the two-qubits gates as they are responsible for the majority of the noise. We do that by substituting a single two-qubit gate with three two-qubits gates, which in a noiseless environment does not modify the simulation as the application of two consecutive two-qubits gates is equal to the identity (c.f. Appendix B.3 for more details). By applying such a technique, we can quantitatively reconstruct the noiseless dynamics up to half of the Rabi oscillation, and only qualitatively in the second part of the oscillation. This is a striking result because it shows that algorithms based on product formulas (such as Trotter), which are usually considered a bad choice for near-term quantum dynamical application due to their circuit depth, can be successfully used to simulate cavity-QED systems.

3.3 Beyond the linear chain approximation

In the previous section we enforced a strictly 1D connectivity by truncating the hopping tensor τ to a tridiagonal form and allowing the coupling vector σ to be non-zero only for the central localized function. While this choice maximizes hardware compatibility, it reduces algorithmic fidelity with respect to the standing-waves reference. We now relax the linear-chain constraint.

In the following, we keep τ tridiagonal but allow σ to be non-zero for the three central localized functions. Then, the connectivity scheme becomes the one shown in Fig. 3(c). In this scenario, the matter qubit q_1^m requires connections with 4 other qubits, which exceeds the maximum connectivity on `ibm_pittsburgh`. Hence, the transpiler introduces SWAP operations, as shown in Fig. 3(f). In particular, the circuit will have two SWAPs per time-steps between q_0^{lb} and q_1^{lb}, and other two between q_0^{lb} and q_2^{lb}.

Fig. 4(c,d) shows the quantum dynamics for $N_{\text{ph}} = 24$ and $N_{\text{ph}} = 36$ modes, approximated with $N_{\text{loc}} = 13$ and $N_{\text{loc}} = 19$ localized functions, respectively. Comparing the statevector simulations for the localized basis approach between Fig. 4(a) and Fig. 4(c) (or between Fig. 4(b) and Fig. 4(d)), we notice that relaxing the constraint on σ leads to a better agreement with the reference standing-waves curve. In general, the amount of the improvement will depend on the ratio between the coupling of the central function σ_{central} and the coupling of the neighboring localized functions σ_{neighbor}. In all panels of Fig. 4 we have $\frac{\sigma_{\text{neighbor}}}{\sigma_{\text{central}}} < 20\%$, hence the improvement is small. On the contrary, comparing the noisy curve between Fig. 4(a) and Fig. 4(c) (or between Fig. 4(b) and Fig. 4(d)) we notice that the overhead of SWAP operation has a significant impact, as the noisy curve reaches the noise saturation value of $\langle \hat{n}_e \rangle \approx 0.5$ at $t \approx 1.5$ a.u., compared to the Fig. 4(a, b) where saturation happened after $t = 2$ a.u. Despite this expected worsening, the noisy simulations remain substantially more robust than in the standing-waves approach (where the noise saturation was reached at $t \approx 0.25$ a.u.), and, more importantly, still allows the application of the ZNE technique. We apply it following the procedure described in Sec. 3.2, and we recover the short-time dynamics with high accuracy up to $t \approx 0.7$ a.u. (about 10 time-steps). Beyond this time, the extrapolated curve starts to deviate more noticeably as errors compound across the deeper circuit. Yet, it still tracks the qualitative behavior of the reference localized basis statevector simulation. Moreover, given the fast development of quantum hardware, one can expect it will soon be possible to retrieve the quantitative behavior as well (c.f. Appendix A).

4 Conclusions and outlook

In this work we have introduced a novel approach for simulating cavity-QED Hamiltonians on near-term quantum processors. First, we presented the implementation of the `BosonicOp` and `MixedOp` classes, together with their respective mappers, in *Qiskit Nature*. These allow to represent a QED Hamiltonian, which comprises of both pure fermionic and bosonic operators and mixed operators, on a quantum computer. Subsequently, we used them to study the quantum dynamics of a two-level system in an optical cavity, using two approaches (both based on a Trotterized Hamiltonian).

We find that directly encoding the QED Hamiltonian (which we call standing-waves approach) fails on noisy hardware due to its star-like connectivity. In fact, due to the nature of the interaction Hamiltonian, one of the qubits representing the matter system has to interact with all the qubits that represent a cavity mode. To overcome this, we propose a novel approach where we perform a unitary transformation on the QED Hamiltonian and represent the modes with a localized photonic basis, such that the matter only interacts with one basis function and each site only interacts with its nearest neighbor. This allows to represent the Hamiltonian as a 1D chain of qubits, hence matching the hardware topology and avoiding SWAP operations. This enables error mitigation via zero-noise extrapolation to recover the quantum dynamics up to half the Rabi oscillation. Furthermore, we showed that the noise scaling on this localized approach is robust enough that we can still recover a significant portion of the quantum dynamics when we relax the 1D constraints on the qubit connectivity, even in the presence of SWAP operations. Despite not being able to exactly reproduce the standing-waves reference, these findings show that product-formula time evolution, when combined with hardware-aware mappings, are effective for QED simulations even on near-term devices. Considering the fast development of the quantum hardware, one can assume that in the next few years, with the advent of fault-tolerant devices, it will be possible to retrieve the full Rabi oscillation even when the Hamiltonian is not representable as a linear chain (c.f. Appendix A).

Future work should point to different directions. Firstly, we focused on a two level system, which only allows a description of simple models. One should consider a multi-level molecule. On the algorithmic side, one should try to improve the definition of the localized functions, such that the conditions on the hopping tensor τ and on the interaction coefficient σ are met with a softer truncation. Alternatively, one could further relax the requirements on those quantities, especially on σ, to improve the algorithmic fidelity. This will be especially interesting once fault-tolerant superconducting quantum computers will be released in the next few years or on other architectures (i.e. ion-trap, neutral atoms ...) which naturally have an all-to-all qubit connectivity.

Data availability

The data that support the findings of this study is available from the corresponding authors upon reasonable request.

Code availability

The code that support the findings of this study is available from the corresponding authors upon reasonable request.

Acknowledgements

The authors sincerely thank Anthony Gandon for his precious work in the implementation of the `MixedOp` and `MixedMapper` classes in *Qiskit Nature*. We also thank Max Rossmannek for his contribution in the design of the classes implemented in *Qiskit Nature*. This research was supported by NCCR MARVEL, a National Center of Competence in Research, funded by the Swiss National Science Foundation (grant number 205602) and by RESQUE funded by the Swiss National Science Foundation (grant number 225229). We acknowledge support from the Villum foundation grant No. 72146, the Cluster of Excellence "CUI: Advanced Imaging of Matter" - EXC 2056 - project ID 390715994, European Research Council (ERC-2024-SyG-101167294; UnMySt) and Grupos Consolidados (IT1453-22), and the Max Planck-New York City Center for Non-Equilibrium Quantum Phenomena. We acknowledge support from the European Union Marie Sklodowska-Curie Doctoral Networks TIMES grant No. 101118915 and SPARKLE grant No. 101169225. The Flatiron Institute is a division of the Simons Foundation.

Author contribution

F.T. derived the theory, developed all the code (except for the `MixedOp` and `MixedMapper` classes, to which he contributed with technical design and code review), performed all simulations, analyzed the data, interpreted the results and wrote the paper. S.L. contributed to the derivation of the theory, to the interpretation of the results and partly to the writing of the paper. M.L. and H.A. contributed to the derivation of the theory and to the interpretation of the results. I.T. contributed to the derivation of the theory, to the analysis of the data and to the interpretation of the results. A.R. contributed to the interpretation of results. A.R. and I.T. conceived the project. All authors contributed to the revision of the manuscript.

Competing Interests

All authors declare no financial or non-financial competing interests.

References

[1] Youngseok Kim, Andrew Eddins, Sajant Anand, Ken Xuan Wei, Ewout van den Berg, Sami Rosenblatt, Hasan Nayfeh, Yantao Wu, Michael Zaletel, Kristan Temme, and Abhinav Kandala. "Evidence for the utility of quantum computing before fault tolerance". Nature **618**, 500–505 (2023).

[2] K. Wright, K. M. Beck, S. Debnath, J. M. Amini, Y. Nam, N. Grzesiak, J.-S. Chen, N. C. Pisenti, M. Chmielewski, C. Collins, K. M. Hudek, J. Mizrahi, J. D. Wong-Campos, S. Allen, J. Apisdorf, P. Solomon, M. Williams, A. M. Ducore, A. Blinov, S. M. Kreikemeier, V. Chaplin, M. Keesan, C. Monroe, and J. Kim. "Benchmarking an 11-qubit quantum computer". Nature Communications**10** (2019).

[3] T. M. Graham, Y. Song, J. Scott, C. Poole, L. Phuttitarn, K. Jooya, P. Eichler, X. Jiang, A. Marra, B. Grinkemeyer, M. Kwon, M. Ebert, J. Cherek, M. T. Lichtman, M. Gillette, J. Gilbert, D. Bowman, T. Ballance, C. Campbell, E. D. Dahl, O. Crawford, N. S. Blunt, B. Rogers, T. Noel, and M. Saffman. "Multi-qubit entanglement and algorithms on a neutral-atom quantum computer". Nature **604**, 457–462 (2022).

[4] Frank Arute, Kunal Arya, Ryan Babbush, Dave Bacon, Joseph C. Bardin, Rami Barends, Rupak Biswas, Sergio Boixo, Fernando G. S. L. Brandao, David A. Buell, Brian Burkett, Yu Chen, Zijun Chen, Ben Chiaro, Roberto Collins, William Courtney, Andrew Dunsworth, Edward Farhi, Brooks Foxen, Austin Fowler, Craig Gidney, Marissa Giustina, Rob Graff, Keith Guerin, Steve Habegger, Matthew P. Harrigan, Michael J. Hartmann, Alan Ho, Markus Hoffmann, Trent Huang, Travis S. Humble, Sergei V. Isakov, Evan Jeffrey, Zhang Jiang, Dvir Kafri, Kostyantyn Kechedzhi, Julian Kelly, Paul V. Klimov, Sergey Knysh, Alexander Korotkov, Fedor Kostritsa, David Landhuis, Mike Lindmark, Erik Lucero, Dmitry Lyakh, Salvatore Mandrà, Jarrod R. McClean, Matthew McEwen, Anthony Megrant, Xiao Mi, Kristel Michielsen, Masoud Mohseni, Josh Mutus, Ofer Naaman, Matthew Neeley, Charles Neill, Murphy Yuezhen Niu, Eric Ostby, Andre Petukhov, John C. Platt, Chris Quintana, Eleanor G. Rieffel, Pedram Roushan, Nicholas C. Rubin, Daniel Sank, Kevin J. Satzinger, Vadim Smelyanskiy, Kevin J. Sung, Matthew D. Trevithick, Amit Vainsencher, Benjamin Villalonga, Theodore White, Z. Jamie Yao, Ping Yeh, Adam Zal-

cman, Hartmut Neven, and John M. Martinis. “Quantum supremacy using a programmable superconducting processor”. Nature **574**, 505–510 (2019).

[5] Kristan Temme, Sergey Bravyi, and Jay M. Gambetta. “Error mitigation for short-depth quantum circuits”. Physical Review Letters**119** (2017).

[6] Suguru Endo, Zhenyu Cai, Simon C. Benjamin, and Xiao Yuan. “Hybrid quantum-classical algorithms and quantum error mitigation”. Journal of the Physical Society of Japan **90**, 032001 (2021).

[7] Anastasia Agathangelou, Dilhan Manawadu, and Ivano Tavernelli. “Quantum algorithm for protein side-chain optimisation: Comparing quantum to classical methods” (2025). arXiv:2507.19383.

[8] Julian Schuhmacher, Guo-Xian Su, Jesse J. Osborne, Anthony Gandon, Jad C. Halimeh, and Ivano Tavernelli. “Observation of hadron scattering in a lattice gauge theory on a quantum computer” (2025). arXiv:2505.20387.

[9] C. Kokail, C. Maier, R. van Bijnen, T. Brydges, M. K. Joshi, P. Jurcevic, C. A. Muschik, P. Silvi, R. Blatt, C. F. Roos, and P. Zoller. “Self-verifying variational quantum simulation of lattice models”. Nature **569**, 355–360 (2019).

[10] Uliana E. Khodaeva, Dmitry L. Kovrizhin, and Johannes Knolle. “Quantum simulation of the one-dimensional fermi-hubbard model as a z_2 lattice-gauge theory”. Physical Review Research**6** (2024).

[11] Max Rossmannek, Fabijan Pavošević, Angel Rubio, and Ivano Tavernelli. “Quantum embedding method for the simulation of strongly correlated systems on quantum computers”. The Journal of Physical Chemistry Letters **14**, 3491–3497 (2023).

[12] Johannes Flick, Michael Ruggenthaler, Heiko Appel, and Angel Rubio. “Atoms and molecules in cavities, from weak to strong coupling in quantum-electrodynamics (qed) chemistry”. Proceedings of the National Academy of Sciences **114**, 3026–3034 (2017).

[13] Michael Ruggenthaler, Dominik Sidler, and Angel Rubio. “Understanding polaritonic chemistry from ab initio quantum electrodynamics”. Chemical Reviews **123**, 11191–11229 (2023).

[14] I-Te Lu, Dongbin Shin, Mark Kamper Svendsen, Simone Latini, Hannes Hübener, Michael Ruggenthaler, and Angel Rubio. “Cavity engineering of solid-state materials without external driving”. Advances in Optics and Photonics **17**, 441 (2025).

[15] Dominik Sidler, Thomas Schnappinger, Anatoly Obzhirov, Michael Ruggenthaler, Markus Kowalewski, and Angel Rubio. “Unraveling a cavity-induced molecular polarization mechanism from collective vibrational strong coupling”. The Journal of Physical Chemistry Letters **15**, 5208–5214 (2024).

[16] Jacob Horak, Dominik Sidler, Thomas Schnappinger, Wei-Ming Huang, Michael Ruggenthaler, and Angel Rubio. “Analytic model reveals local molecular polarizability changes induced by collective strong coupling in optical cavities”. Physical Review Research**7** (2025).

[17] Dominik Sidler, Michael Ruggenthaler, and Angel Rubio. “Collectively-modified intermolecular electron correlations: The connection of polaritonic chemistry and spin glass physics” (2024). arXiv:2409.08986.

[18] Hang Liu, Francesco Troisi, Hannes Huebener, Simone Latini, and Angel Rubio. “Cavity-mediated electron-electron interactions: Renormalizing dirac states in graphene” (2025). arXiv:2505.10166.

[19] Simone Latini, Enrico Ronca, Umberto De Giovannini, Hannes Hübener, and Angel Rubio. “Cavity control of excitons in two-dimensional materials”. Nano Letters **19**, 3473–3479 (2019).

[20] Francesco Troisi, Hannes Hübener, Angel Rubio, and Simone Latini. “Cavity-qed-controlled two-dimensional moiré excitons without twisting” (2025). arXiv:2508.02388.

[21] Hannes Hübener, Emil Viñas Boström, Martin Claassen, Simone Latini, and Angel Rubio. “Quantum materials engineering by structured cavity vacuum fluctuations”. Materials for Quantum Technology **4**, 023002 (2024).

[22] Mark Kamper Svendsen, Michael Ruggenthaler, Hannes Hübener, Christian Schäfer, Martin Eckstein, Angel Rubio, and Simone Latini. "Theory of quantum light-matter interaction in cavities: Extended systems and the long wavelength approximation" (2023). arXiv:2312.17374.

[23] The Qiskit Nature Developers and Contributors. "Qiskit nature 0.6.0" (2023).

[24] Ali Javadi-Abhari, Matthew Treinish, Kevin Krsulich, Christopher J. Wood, Jake Lishman, Julien Gacon, Simon Martiel, Paul D. Nation, Lev S. Bishop, Andrew W. Cross, Blake R. Johnson, and Jay M. Gambetta. "Quantum computing with qiskit" (2024).

[25] Alexander Miessen, Pauline J. Ollitrault, and Ivano Tavernelli. "Quantum algorithms for quantum dynamics: A performance study on the spin-boson model". Physical Review Research**3** (2021).

[26] Norah M. Hoffmann, Christian Schäfer, Angel Rubio, Aaron Kelly, and Heiko Appel. "Capturing vacuum fluctuations and photon correlations in cavity quantum electrodynamics with multitrajectory ehrenfest dynamics". Physical Review A**99** (2019).

[27] V. Bužek, G. Drobný, Min Gyu Kim, M. Havukainen, and P. L. Knight. "Numerical simulations of atomic decay in cavities and material media". Physical Review A **60**, 582–592 (1999).

[28] Vasil Rokaj, Michael Ruggenthaler, Florian G. Eich, and Angel Rubio. "Free electron gas in cavity quantum electrodynamics". Physical Review Research**4** (2022).

[29] A. Chiesa, F. Tacchino, M. Grossi, P. Santini, I. Tavernelli, D. Gerace, and S. Carretta. "Quantum hardware simulating four-dimensional inelastic neutron scattering". Nature Physics **15**, 455–459 (2019).

[30] Xin-Yu Huang, Lang Yu, Xu Lu, Yin Yang, De-Sheng Li, Chun-Wang Wu, Wei Wu, and PingXing Chen. "Qubitization of bosons". Progress in High Energy Physics PHEP**2025** (2025).

[31] Rolando D. Somma, Gerardo Ortiz, Emanuel H. Knill, and James Gubernatis. "Quantum simulations of physics problems". In Eric Donkor, Andrew R. Pirich, and Howard E. Brandt, editors, Quantum Information and Computation. SPIE (2003).

[32] Bo Peng, Yuan Su, Daniel Claudino, Karol Kowalski, Guang Hao Low, and Martin Roetteler. "Quantum simulation of boson-related hamiltonians: techniques, effective hamiltonian construction, and error analysis". Quantum Science and Technology **10**, 023002 (2025).

[33] Ying Li and Simon C. Benjamin. "Efficient variational quantum simulator incorporating active error minimization". Physical Review X**7** (2017).

[34] Suguru Endo, Simon C. Benjamin, and Ying Li. "Practical quantum error mitigation for near-future applications". Physical Review X**8** (2018).

[35] Libor Veis, Jakub Višňák, Hiroaki Nishizawa, Hiromi Nakai, and Jiří Pittner. "Quantum chemistry beyond born–oppenheimer approximation on a quantum computer: A simulated phase estimation study". International Journal of Quantum Chemistry **116**, 1328–1336 (2016).

A Outlook for future hardware

In this appendix we repeat the simulations for the quantum dynamics of a two-level system when the cavity modes are approximated with the localized basis approach (c.f. Fig. 4 of the main text), comparing different generations of quantum hardware. Since in Sec. 3.2 and Sec. 3.3 we showed that this approach is resilient to noise when increasing the number of localized function, here we reproduce only Fig. 4(a,c), corresponding to 24 modes approximated with 13 localized functions. We compare the performance of the following hardware: `ibm_brisbane` (127 superconducting qubits, with QPU *Eagle r3*), `ibm_pittsburgh` (156 superconducting qubits, with QPU *Heron r3*) and a custom

Table 1: QPU Specifications and Performance Metrics as of *September 10th, 2025*

Name	Qubits	QPU Type	Gates	2Q Layer	CLOPS	Read Err	2Q Err	SX Err	T1 (μs)	T2 (μs)
Brisbane	127	Eagle r3	ecr, id, rz, sx, x	1.72×10^{-2}	180K	2.05×10^{-2}	6.76×10^{-3}	2.49×10^{-4}	222.44	133.23
Pittsburgh	156	Heron r3	cz, id, rx, rz, rzz, sx, x	4.14×10^{-3}	250K	4.33×10^{-3}	1.52×10^{-3}	1.80×10^{-4}	296.33	357.45
Custom	156	N/A	cz, id, rx, rz, rzz, sx, x	4.14×10^{-4}	250K	4.33×10^{-4}	1.52×10^{-4}	1.80×10^{-5}	2960.33	3570.45

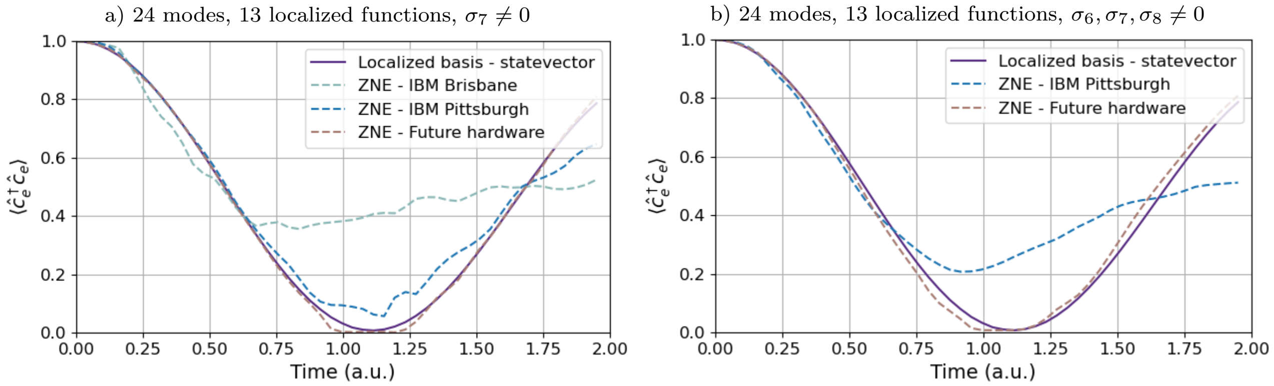
a) 24 modes, 13 localized functions, $\sigma_7 \neq 0$

b) 24 modes, 13 localized functions, $\sigma_6, \sigma_7, \sigma_8 \neq 0$

Figure 5: Quantum dynamics of a two-level system placed in the center of an optical cavity when the modes are described with the localized basis approach, assuming that the tensor τ in Eq. 9 is tridiagonal and $\sigma \neq 0$ only for a few central localized functions (1 in panel a , 3 in panel b). The two-level system was initially in the excited state, while all cavity modes started in the vacuum state. The ZNE dynamics is obtained using a linear fit. $N_{\text{ph}} = 24$ cavity modes, approximated with $N_{\text{loc}} = 13$ localized functions, using $N_q = 15$ qubits. $\sigma \neq 0$ only for the central localized function (σ_7). b) $N_{\text{ph}} = 24$ cavity modes, approximated with $N_{\text{loc}} = 13$ localized functions, using $N_q = 15$ qubits. $\sigma \neq 0$ for the three central localized functions ($\sigma_6, \sigma_7, \sigma_8$).

superconducting hardware, representing a future development of IBM's QPUs. This latter was modeled such that it has the same layout of `ibm_pittsburgh` (c.f. Fig. 6), but with a significantly better noise. Particularly, we accessed the real-time calibration data of `ibm_pittsburgh` and we decreased the average one- and two-qubit gate errors, e_1^{pitts} and e_2^{pitts}, respectively, as well as readout errors of the device, $e_{\text{read}}^{\text{pitts}}$, while simultaneously increasing average relaxation time T_1 and dephasing time T_2, by a factor η [25]:

$$e_1^{\text{custom}} = \frac{e_1^{\text{pitts}}}{\eta}, \quad e_2^{\text{custom}} = \frac{e_2^{\text{pitts}}}{\eta}, \quad e_{\text{read}}^{\text{custom}} = \frac{e_{\text{read}}^{\text{pitts}}}{\eta}, \quad T_1^{\text{custom}} = \eta T_1^{\text{pitts}}, \quad T_2^{\text{custom}} = \eta T_2^{\text{pitts}} \tag{10}$$

We used $\eta = 10$. The resulting data (for all hardware) are summarized in Table 1.

The results are presented in Fig. 5. Panel (a) compares the performances of `ibm_brisbane`, `ibm_pittsburgh` and the custom hardware when σ is non-zero only for one localized function, and the Hamiltonian is represented as a linear chain of qubits (c.f. Fig. 3(b,e)). `ibm_brisbane` is able to reproduce the noiseless curve only up to $t \approx 0.7$ a.u., while the other QPUs make it possible to reconstruct the full Rabi oscillation (i.e. they do not reach the noise saturation within the plotted interval). In the case of the custom QPU, the noiseless curve and its noisy equivalent are almost indistinguishable (except when $\langle \hat{n}_e \rangle \to 0$). Panel (b) compares the performances when σ is non-zero only for three central localized function, hence the "beyond the linear chain approximation" case discussed in Sec. 3.3 (c.f. Fig. 3(c,f) for the required connectivity). We did not include `ibm_brisbane` because of its poor performance in panel (a) (the noise in this case is much bigger). While `ibm_pittsburgh` is able to reproduce the noiseless curve only up to $t \approx 0.75$ a.u., the custom hardware retrieves the full Rabi oscillation (despite the presence of deviations).

This result confirms what we stated in the main text, showing that product-formula time evolution, when combined with hardware-aware mappings, are effective for QED simulations, especially when considering the hardware that will be available in the next few years.

B Numerical methods

B.1 Qiskit SDK

To perform the simulations we used the following versions of Qiskit SDK Python packages: `qiskit`: v1.4.4, `qiskit-aer`: v0.17.1, `qiskit-ibm-runtime`: v0.41.1, `qiskit-nature`: cloned from *main* branch of the repository (commit SHA: 4cc927ce539219505defac61cd70ded081507361).

B.2 Hardware layout

We emulated the hardware `ibm_pittsburgh` on a classical HPC cluster. At the time of writing, this is IBM's flagship's hardware. Its QPU (of type *Heron r3*) has 156 superconducting qubits, organized in a 2D honeycomb lattice (c.f. Fig. 6). The majority of the qubits is connected to 2 other qubits, while the highest connectivity is 3. Refer to Table 1 for more details.

B.3 Noise simulation & mitigation

The noise model was simulated by accessing the real-time calibration data of the QPU through the Python package `qiskit-ibm-runtime`, and built using the `NoiseModel` class implemented in the Python package `qiskit-aer`. In order to obtain the noisy simulations (in Fig. 2 and Fig. 4), we ran each circuit 10 times, and then averaged. The required precision of the Estimator job was set to 10^{-4}.

In order to mitigate the error, we used the zero-noise extrapolation (ZNE) technique. To perform it, we first simulated the circuit as it was transpiled (for a total of 10 simulations). Averaging these 10 simulations, we obtained the unamplified noisy curve (which is reported in Fig. 4, as the dashed blue curve). Subsequently, we executed a circuit where 10% of the two-qubits gates was amplified (again, we performed a total of 10 simulations and then averaged). This way, we obtained the 10% amplified noise curve. The gate amplification was performed by substituting the desired two-qubits gate with 3 two-qubits gates. Since the application of two consecutive two-qubits gates is equivalent to an identity gate, on a noiseless hardware this operation does not change the outcome. However, on a noisy QPU it amplifies the error probability. We then repeated same amplification procedure, increasing the percentage to $20\%, 30\%, 40\%, 50\%, 60\%$ of the total two-qubits gates. To extract the ZNE curve, we then interpolated the averaged curves with a linear interpolation, obtaining the dashed brown line in Fig. 4.

B.4 Time evolution & other parameters

We simulate the time evolution by Trotterizing the QED Hamiltonian. To contain the number of two-qubits gates we use the Lie-Trotter formula, which is a first order approximation. The chosen time-step is $\Delta t = 0.075$ a.u. and the total duration is $t_f = 2.0$ a.u., for a total of 26 time steps.

We set the dipole matrix element in Eq. 3 to $d_{eg} = 60$ a.u., which is an arbitrary value that allows us to observe a full Rabi oscillation in total simulated time. The energy of the electronic transition of the two-level system is $\omega_{eg} = 0.394$ Ha. When we simulate $N_{\text{ph}} = 24$ modes we set the cavity length to $L = 13000$ a.u., while when we simulate $N_{\text{ph}} = 36$ modes we set it to $L = 19500$ a.u.. This ensures that half of the effective modes are below ω_{eg}, and the other half are above that value (ensuring a symmetrical cavity).

C Localized basis

In this appendix we provide more information on the localized basis approach described in Section 3.2 of the main text.

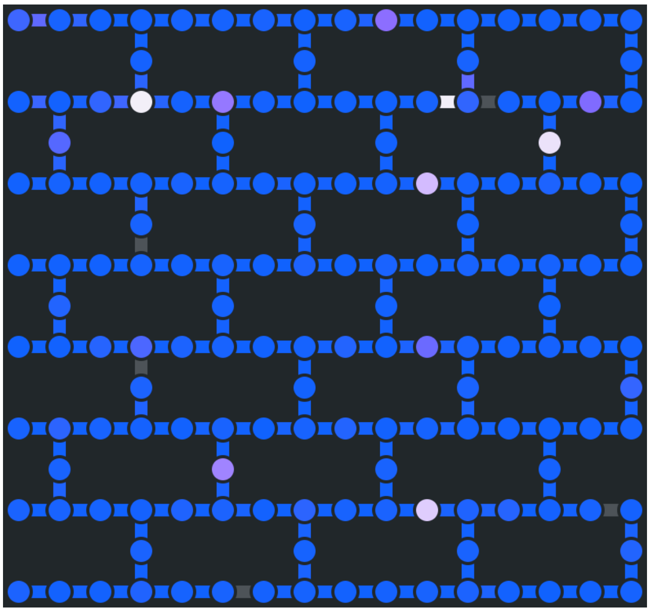

Figure 6: QPU layout of *IBM Pittsburgh*. The color of each qubit gives information about its readout error, while the color of each connection represents the error of a *cz* operation between the connected qubits. In both cases, the color blue represents a small error probability, the color white a large error.

C.1 Derivation

First, we show how to obtain the localized QED Hamiltonian (Eq. 9 of the main text). Note that this derivation will only assume the new basis to be orthogonal, but not localized. Hence, it is general to a larger class of basis functions. Let us define the expansion of the photonic creation and annihilation operators onto the new basis as:

$$\hat{a}_\alpha = \sum_{l=0}^{\infty} P_{l\alpha}\, \hat{t}_l, \qquad \hat{a}_\alpha^\dagger = \sum_{l=0}^{\infty} P_{l\alpha}^*\, \hat{t}_l^\dagger,$$

where $P_{l\alpha} = \int L_l(\boldsymbol{r})\, e^{i\boldsymbol{q}_\alpha \cdot \boldsymbol{r}} \mathrm{d}\boldsymbol{r}$ is the projection of the α-th mode onto the l-th basis function. If the cavity is planar, such as in this work, then the integral $P_{l\alpha}$ is only along the confinement direction (in our case z). Note that such transformation is unitary in the infinite limit (i.e. $\alpha \to \infty, l \to \infty$). Substituting the projections of the photonic creation and annihilation operators into the QED Hamiltonian in Eq. 4 leads to:

$$\hat{H}_{\text{QED}} = \hat{H}_m + \sum_\alpha \Omega_\alpha \left(\frac{1}{2} + \sum_{ll'} P_{l\alpha}^* P_{l'\alpha} \hat{t}_l^\dagger \hat{t}_{l'} \right) - \sum_{ij} d_{ij}\omega_{ij} \hat{c}_i^\dagger \hat{c}_j \sum_\alpha \lambda_\alpha \sqrt{\frac{1}{2\Omega_\alpha}} \sum_l \left(P_{l\alpha}^* \hat{t}_l^\dagger + P_{l\alpha} \hat{t}_l \right) \tag{11}$$

where $\hat{H}_m = \sum_i \varepsilon_i \hat{c}_i^\dagger \hat{c}_i$ is the matter Hamiltonian defined in Eq. 1, i, j are indexes that span over the matter states, ω_{ij} is the energy of the matter transition ij and d_{ij} is its dipole matrix element. Finally, reordering the previous expression and introducing the quantities:

$$\tau_{ll'} = \sum_\alpha \Omega_\alpha P_{l\alpha}^* P_{l'\alpha}, \quad \sigma_l = \sum_\alpha \lambda_\alpha \sqrt{\frac{1}{2\Omega_\alpha}} P_{l\alpha} \tag{12}$$

leads to:

$$\hat{H}_{\text{QED}}^{\text{loc}} = \hat{H}_m + \sum_\alpha \frac{\Omega_\alpha}{2} + \sum_{ll'} \tau_{ll'} \hat{t}_l^\dagger \hat{t}_{l'} - \sum_{ij,l} d_{ij}\omega_{ij} \hat{c}_i^\dagger \hat{c}_j \left(\sigma_l^* \hat{t}_l^\dagger + \sigma_l \hat{t}_l \right) \tag{13}$$

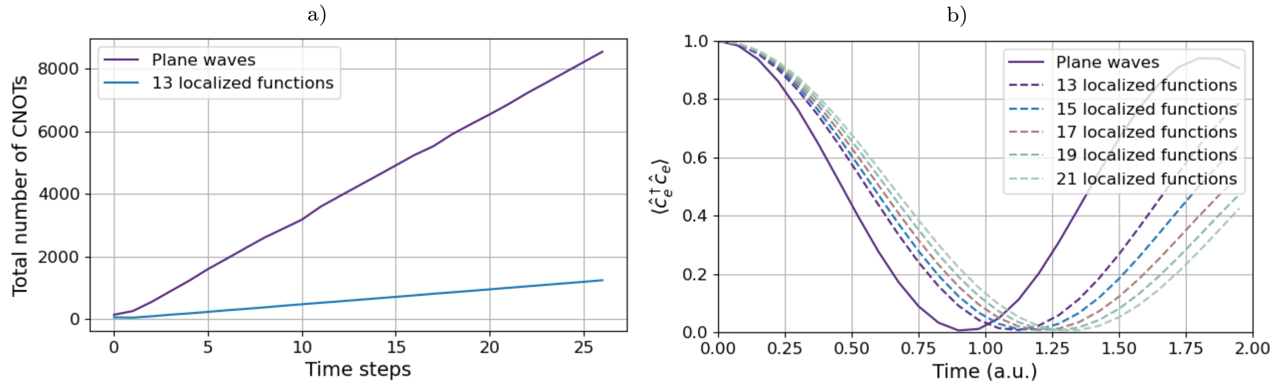

Figure 7: The two panels were obtained for the two-level system in the main text coupled to 24 cavity modes. a) Evolution of the total number of CNOTs for the standing-waves approach and for the localized basis approach when τ is tridiagonal and σ is non-zero only for the central function. b) Noiseless quantum dynamics of the two-level system.

C.2 Basis functions of choice

We choose a set of localized basis functions $L_l(z)$ defined as:

$$L_l(z) = \begin{cases} 1 - m_l|z - z_{0,l}|, & z \in \left[-\frac{1}{m_l} + z_{0,l}, \frac{1}{m,l} + z_{0,l}\right] \\ 0, & \text{otherwise} \end{cases} \tag{14}$$

which represents a triangle centered at $z_{0,l}$ with steepness m_l. We define such functions such that they cover all points in the planar cavity (which goes from $z = 0$ to $z = L$). To achieve that, we define $m_l = \frac{2N_{\text{loc}}}{L}$, where N_{loc} is the number of localized basis functions and $z_{0,l} = \frac{1}{m_l}\left(1 + l\frac{L}{N_{\text{loc}}}\right)$. This definition ensures the orthogonality of the basis functions. We then normalize each function such that $\langle L_l(z)|L_{l'}(z)\rangle = \delta_{ll'}$, hence obtaining an orthonormal set. Such definition is ideal because if N_{loc} is odd, then one function will peak at the center of the cavity ($z = \frac{L}{2}$), which is where the two-level system is located.

C.3 Limitations

The limitations of the localized standing-waves approach are mainly to the hardware constraints. In the following we only consider a two level system, hence we drop the indexes i, j in the localized QED Hamiltonian. Each basis function (i.e. each operator $\hat{t}$) requires one qubit to be represented on the quantum computer, and the connectivity is determined by the shape of the hopping tensor τ and by σ. As we discuss in the main text, if τ is tridiagonal (i.e. an excitation can only hop to nearest neighbor localized function) and σ is non-zero only for the central localized function, then the connectivity scheme is the one pictured in Fig. 3(c). Then, $\hat{H}^{\text{loc}}_{\text{QED}}$ can be mapped to the hardware without any need for SWAP operations and the number of total CNOTs improved significantly compared to the standing-waves approach, as shown in Fig. 7. Relaxing such conditions would result in the need of SWAP operations. For instance, if one allows σ to be non zero for the central three localized function , then the qubit q_1^m would need to interact with $q_0^{lb}, q_1^{lb}, q_2^{lb}$. To achieve this, the transpiler would need to first make q_1^m and q_0^{lb} interact. Subsequently, swap q_1^{lb} and q_0^{lb}, make q_1^m and q_0^{lb} and re-swap q_1^{lb} and q_0^{lb} (and then follow the same procedure for q_0^{lb}). Aside from introducing many noisy two-qubits gates, they would all be localized on a few physical qubits, strongly increasing the error probability. Hence, the two conditions on σ and τ shall be met.

However, given the localized functions described in Appendix C.2, the two conditions are never met. Thus, one has to manually truncate τ and σ. First, one should always choose an odd number of basis functions, as with an even number of them there would be two σ with the same values. This would make the manual truncation ineffective and force to introduce SWAP operations. Secondly, due to the need to enforce the conditions on τ and σ, one has an optimal number of localized function for which the approximation is best. Fig. 7(b) shows that using more localized functions results in a worse approximation of the standing-waves reference, even in a noiseless simulation.

D Bosonic operator mappers

This appendix details how the bosonic mappers implemented in *Qiskit Nature* work.

D.1 The linear mapper

The `BosonicLinearMapper` is based on Section II.C of Ref. [25]. As the name suggests, the creation and annihilation operators for the mode k are linearly mapped to the qubit space, and they are defined as follows:

$$\hat{b}_k^\dagger = \sum_{n_k=0}^{n_k^{max}-1} \sqrt{n_k+1}\hat{\sigma}_{n_k}^{+}\hat{\sigma}_{n_k+1}^{-} \tag{15}$$

$$\hat{b}_k = \sum_{n_k=0}^{n_k^{max}-1} \sqrt{n_k+1}\hat{\sigma}_{n_k}^{-}\hat{\sigma}_{n_k+1}^{+} \tag{16}$$

where n_k^{max} is the maximum occupation of the mode and k is the index of the mode. The operators $\hat{\sigma}_{n_k}^{-}$ and $\hat{\sigma}_{n_k}^{+}$ are a combination of Pauli matrices:

$$\hat{\sigma}_{n_k}^{+} = \frac{1}{2}\left(\hat{\sigma}_{n_k}^{x} + i\hat{\sigma}_{n_k}^{y}\right) \equiv S_{n_k}^{+} = \frac{1}{2}\left(X_{n_k} + iY_{n_k}\right) \tag{17}$$

$$\hat{\sigma}_{n_k}^{-} = \frac{1}{2}\left(\hat{\sigma}_{n_k}^{x} - i\hat{\sigma}_{n_k}^{y}\right) \equiv S_{n_k}^{-} = \frac{1}{2}\left(X_{n_k} - iY_{n_k}\right) \tag{18}$$

In order to represent a mode we need $n_k^{max}+1$ qubits (in other words, for a single mode the length of the qubit register is $n_k^{max}+1$). In general, the memory complexity of this mapper (i.e. how many qubits it requires) is given by $\mathcal{O}\left(N_K n_k^{max}\right)$, where N_K is the number of bosonic modes. Hence, the scaling is linear with both the number of modes and the maximum allowed occupation per mode. One should note that since this mapper truncates the maximum occupation of a bosonic mode to represent it in the qubit register, the commutation relations of the mapped operator differ from the standard ones. Please refer to Section 4, equation 22 of Ref. [31] for more details. This essentially implies that we have a further fundamental relation of the bosonic operator [35]:

$$\hat{b}^\dagger |n_k^{max}\rangle = 0 \tag{19}$$

which prevents exceeding the maximum representable occupation.

Let us look at a generic occupation number vector, which gives a representation of the physical qubits in the register. Every entry can be either $0(\uparrow)$ or $1(\downarrow)$. For a generic system, with K modes and n^{max} Fock states per mode (all modes have the same maximum occupation), this would look like:

$$\begin{aligned}&|m_K, m_{K-1}, ..., m_1, m_0\rangle = \\ &|\underbrace{0_{n^{max}}, 0_{n^{max}-1}, ..., 0_1, 0_0}_{\text{mode } K}, \underbrace{0_{n^{max}}, 0_{n^{max}-1}, ..., 0_1, 0_0}_{\text{mode } K-1}, ..., \underbrace{0_{n^{max}}, 0_{n^{max}-1}, ..., 0_1, 0_0}_{\text{mode } 1}, \underbrace{0_{n^{max}}, 0_{n^{max}-1}, ..., 0_1, 0_0}_{\text{mode } 0}\rangle\end{aligned} \tag{20}$$

In *Qiskit*, the right-most entry represents the least significant qubit (little-endian convention). Note that when an operator is mapped, it has to perform an action (which could be an identity operation) on every qubit in the register.

D.2 The logarithmic mapper

Mapping a bosonic mode has many similarities with representing an integer number on a classical computer. In fact, contrary to the case of Fermions where a state can be either occupied or unoccupied, an infinite number of Bosons can occupy the same quantum state (which is explained by the Bose-Einstein statistics). Therefore, representing a bosonic mode only requires the inclusion of enough Fock states so that the number of bosons occupying it becomes representable. Since the computational basis of bits and qubits is the same, this problem is not different than representing integers on classical bits. Thus, it is natural to try to encode the qubit register in the same way the classical register is encoded. To do this, we shall consider the representation of unsigned integers:

$$0 = 00; |0\rangle = |0,0\rangle = |\uparrow,\uparrow\rangle$$

$$1 = 01; |1\rangle = |0,1\rangle = |\uparrow,\downarrow\rangle$$

$$2 = 10; |2\rangle = |1,0\rangle = |\downarrow,\uparrow\rangle$$

$$3 = 11; |3\rangle = |1,1\rangle = |\downarrow,\downarrow\rangle$$

On the left, the representation of the unsigned integers on two classical bits is reported, while on the right the representation of the Fock states on two qubits. In general, for N_q qubits one has [32]:

$$\begin{gathered} |0\rangle = |0_{N_q}, 0_{N_q-1}, ..., 0_1, 0_0\rangle \\ |1\rangle = |0_{N_q}, 0_{N_q-1}, ..., 0_1, 1_0\rangle \\ |2\rangle = |0_{N_q}, 0_{N_q-1}, ..., 1_1, 0_0\rangle \\ |3\rangle = |0_{N_q}, 0_{N_q-1}, ..., 1_1, 1_0\rangle \\ ... \\ |2^{N_q}-1\rangle = |1_{N_q}, 1_{N_q-1}, ..., 1_1, 1_0\rangle \end{gathered} \tag{21}$$

Again, we use the little-endian convention so the right-most entry is the least significant qubit. Using Eq. 21 and the well-known bosonic creation and annihilation relations, it is now possible to define what the action of the mapped operator should be [32, 35]:

$$\hat{b}^\dagger = \sum_{n=0}^{2^{N_q}-2} \sqrt{n+1}|n+1\rangle\langle n| \tag{22}$$

$$\hat{b} = \sum_{n=1}^{2^{N_q}-1} \sqrt{n}|n-1\rangle\langle n| \tag{23}$$

where $|n\rangle$ represents a generic Fock state. In order to define the effect of the operator in terms of the Pauli matrices, let us consider an example with $N_q = 2$ qubits. Then, using Eq. 21 to expand Eq. 22 we get:

$$\hat{b}^\dagger = \sum_{n=0}^{2^2-2} \sqrt{n+1}|n+1\rangle\langle n| = |1\rangle\langle 0| + \sqrt{2}|2\rangle\langle 1| + \sqrt{3}|3\rangle\langle 2| = |0,1\rangle\langle 0,0| + \sqrt{2}|1,0\rangle\langle 0,1| + \sqrt{3}|1,1\rangle\langle 1,0| \tag{24}$$

As one can see, after using the state vector to expand the Eq. 22 and Eq. 23, the outer operations are reduced to only four cases. These correspond to all possible combinations of the states where the physical qubit can exist [32]:

$$|0\rangle\langle 0| = \frac{\mathcal{I}+\sigma^z}{2}, \quad |1\rangle\langle 1| = \frac{\mathcal{I}-\sigma^z}{2}, \quad |0\rangle\langle 1| = \sigma^+ = \frac{\sigma^x + i\sigma^y}{2}, \quad |1\rangle\langle 0| = \sigma^- = \frac{\sigma^x - i\sigma^y}{2} \tag{25}$$

Let us now compare mapping the operator $\hat{b}^\dagger$ (or $\hat{b}$) for a system composed of a single mode with the logarithmic and with the linear mapper, assuming that the maximum occupation of the mode is

$n_k^{max} = 3$. For the linear mapper, one needs $n_k^{max} + 1 = 4$ qubits and 12 Pauli terms in the mapped Hamiltonian. For the logarithmic mapper, on the other hand, one only needs $\log_2 \left(n_k^{max} + 1\right) = 2$ qubits. Also, the number of terms in the mapped operator is reduced to 8. This implies that the circuit will be shallower.

Finally, let us explore what happens to the logarithmic mapper for a generic case of N_K boson modes. In Eq. 20 we discussed the generic state vector for N_K modes and n^{max} Fock states per mode for the linear mapper. In the state $|m_K, m_{K-1}, ..., m_1, m_0\rangle = |m_K,\rangle \otimes |m_{K-1}\rangle \otimes ... \otimes |m_1\rangle \otimes |m_0\rangle$ each mode can be occupied with a different number of particles due to the tensor product between the modes. This implies each single-mode register should be independent. Since the physical object is the same (i.e. the bosonic creation or annihilation operator), the behavior of the logarithmic mapper should be analogous, so the global register still requires N_K single-mode registers. Thus, using a logarithmic mapper instead of the linear mapper only affects the fact that fewer qubits are needed to represent the generic mode k. Therefore, the complexity of the logarithmic mapper will scale linearly with respect to the number of modes, and logarithmically to the number of Fock states per mode: $\mathcal{O}\left(N_K \log_2 \left(n_k^{max}\right)\right)$.

As a consequence, we can extend Eq. 22 and Eq. 23 to the multi-mode case by adding a mode index:

$$\hat{b}_k^\dagger = \sum_{n=0}^{2^{N_q^k}-1} \sqrt{n+1}|n+1\rangle_k\langle n|_k \tag{26}$$

$$\hat{b}_k = \sum_{n=1}^{2^{N_q^k}-1} \sqrt{n}|n-1\rangle_k\langle n|_k \tag{27}$$

where N_q^k is the number of qubits used to represent the mode k. Finally, one should note that using the logarithmic mapper instead of the linear one, while always ensuring the usage of less qubits, may require more Pauli strings. For instance, this is the case for a hopping bosonic term: $\hat{b}_1^\dagger \hat{b}_2$.

5 Summary, Conclusions, and Perspectives

Questa conclusione, benché trovata da povera gente, c'è parsa così giusta, che abbiam pensato di metterla qui, come il sugo di tutta la storia.
La quale, se non v'è dispiaciuta affatto, vogliatene bene a chi l'ha scritta, e anche un pochino a chi l'ha raccomodata. Ma se in vece fossimo riusciti ad annoiarvi, credete che non s'è fatto apposta.[1]
- I Promessi Sposi, A. Manzoni (1842)

This thesis explored light–matter interaction simulations across three complementary fronts, specifically enhanced semiclassical descriptions beyond the dipole approximation, fully quantized cavity QED for materials engineering and quantum computing. This was achieved by presenting four contributions [50, 51, 72, 137], all of which constitute significant advances in their respective fields, addressing problems in molecular and condensed-matter physics. Together they aim at building a coherent toolbox for predicting and controlling quantum material properties in electromagnetic environments.

In the first part, I discussed the central role that semiclassical methods still have for the description of light-matter interacting systems, particularly in spectroscopy and high-intensity application, but also for their potential in modeling QED systems. In Publication I, I presented a tool which is able to couple a matter system described within TDDFT with the Maxwell equations through the full minimal coupling prescription in Coulomb gauge. In particular, it was showed that by self-consistently propagating the coupled electron–photon dynamics it is possible to coherently describe multiple phenomena such as the formation and evolution of the Cherenkov radiation from a single-electron wavepacket in a medium, as well as studying the soft XUV spectroscopy of benzene, where non-chiral light induces magneto-optical signatures through higher-order couplings. The authors also highlighted the need to go beyond the multipolar expansion for treating the dipole approximation by studying the Lamb-like radiative shift due to the self-induced transverse field on a sodium dimer. To achieve this, the authors developed a tool that propagates the electronic dynamics under the effect of the electromagnetic field (forward interaction), and but also includes the effect of the electronic dynamics on the electromagnetic field (backward interaction). A crucial part for realizing the forward interaction was implementing

---

[1] *This conclusion, though arrived at by such plain people, has seemed so true that we have decided to set it down here as the moral of our whole story. For the which, gentle reader, if it has not displeased you entirely, feel thankful to the scribe who wrote it, and a little also to the one who has revised it. But if, on the contrary, we have succeeded only in boring you, be assured that we have not done so on purpose.* This is the conclusion of the classic Italian novel *I promessi sposi* (The Betrothed). I hope not to have bored you with my work!

a reliable and robust Helmholtz decomposition, which enabled origin-independent coupling via a numerically stable reconstruction of the transverse vector potential from the Riemann–Silberstein field. These results establish a general *ab initio* semiclassical framework that recovers key QED phenomena via radiation reaction and captures non-dipolar physics. Looking ahead, this tool will be used in several applications such as twisted light, where the electromagnetic field carries a finite orbital angular momentum, strong field phenomena and high-energy spectroscopy. Furthermore, the application explored in Publication I focused on molecular physics. Hence, a natural direction for future development is to address condensed matter systems. While the general theoretical formalism is expected to be trivially extendable (as TDDFT can be used for solids), the numerical treatment is expected to be complicated. For instance, looking at the Helmholtz decomposition, one has to deal with non-zero fields at the border of the Brillouin zone of the material (which is where the properties of the material are studied). As discussed in Section 2.2, this may lead to spikes and instabilities.

In the second part of the thesis I discussed the emerging field of cavity materials engineering, presenting two contributions. The aim of this area of study is to exploit the strong coupling between light and matter, reachable using an optical cavity, to modify the properties of the embedded materials. Starting from the Pauli-Fierz Hamiltonian, which gives a low-energy description of QED using both quantized matter and photons, I introduced the long-wavelength approximation and the effective mode formalism for studying condensed matter systems. This was applied to study both dark cavities, where the interaction is mediated by the quantum vacuum fluctuations, and classically driven cavities, where classical light is shined on the material. In both cases, I showed that the technique of Hamiltonian downfolding is an effective analytical tool as it allows to understand the effect of the interaction by deriving a photon-free, non-perturbative effective Hamiltonian. Using these concepts, in Publication II I showed that spatially structured cavities provide an all-optical route to Moiré-like exciton confinement in TMD heterostructures, without the need of twisting the layer. In fact, the classical driving at finite in-plane momentum emulates a superlattice potential, folding bands and opening miniband gaps. In dark structured cavities, the bilinear light–matter coupling generates nonlocal exciton–exciton interactions mediated by virtual photons, renormalizing masses and inducing negative curvature of the excitonic states. This momentum-selective mechanism is set by cavity design and cannot be captured in classical treatments, underscoring the unique materials control afforded by quantum light. In the specific case of excitonic heterostructures in TMDs, being able to replicate the Moiré physics in an all-optical way, opens many interesting possibilities as experimentally it is enough to generate a monolayer, which can be realized with much more precision than a bilayer. Looking ahead, the fabrication of structured cavities is challenging as sub-wavelength patterning must be achieved while preserving high-Q factor of the cavity, as nanofabrication tolerances and surface roughness can degrade the finesse, introduce scattering, and limit scalability and reproducibility. In Publication III I showed how optical cavities are effective in modifying topological properties, specifically through the selective opening of an optical and electronic gap in Graphene. To model this we developed a photon-free, self-consistent QED Hartree–Fock theory that incorporates cavity-mediated local and nonlocal electron–electron interactions proportional to momentum operators. This theory predict predicts that the polarization of the cavity mode can be used to engineer the shape of the optical gap. Specifically, a circularly polarized mode breaks time-reversal and open isotropic topological gaps, an anisotropic single linearly polarized mode induces a gap and wedge-shaped bands through a cavity-mediate long-range potential, and two isotropic linear modes preserve gapless cones but renormalize the Fermi velocity. Note that the case of a wedge-shaped band is particularly relevant as it cannot be explained with classical arguments, hence constituting an example of pure quantum effect. Together, these studies demonstrate that cavity material engineering can mediate long-range, symmetry-tunable electron and exciton interactions that fundamentally alter band topology and transport properties. Looking forward, cavity material engineering may have a significant impact on the field of semiconductors based on the 2D materials. In fact, as traditional Silicon-based chips are being pushed to their physical limits [121], quantum materials, especially light-modified, may provide novel solutions in the optoelectronics industry [153, 154]. Surely, one interesting future direction will be the development of QEDFT, which will allow for a much cheaper theoretical modeling a condensed matter cavity QED system thanks to the development of exchange-correlation functional that account for the action of the quantized electromagnetic field.

Finally, in the third part of the thesis I addressed the computational bottleneck of simulating large electron–photon Hilbert spaces with classical computers, and proposed using quantum computing as a possible solution. In fact, quantum computers are efficient in representing photonic modes, as they require as little as one qubit, and combined with the short execution time of quantum circuits, it promises to be a viable solution for simulating QED systems. Quantum computers are currently transitioning from the NISQ era to the error correction era, where the number of available qubits, combined with a high fidelity of gate operations, will allow to correct quantum errors, hence to simulate more complicated systems. In the wait for such a breakthrough, circuit design must take into deep consideration the hardware constraints. Publication IV exemplifies this as I show that simulating QED systems is indeed possible on current state-of-the-art quantum computers, provided that the Pauli-Fierz Hamiltonian is formulated in a hardware-aware manner. More specifically, I introduced a localized photonic basis via unitary transformation of standing-wave modes (typically used to describe the cavity modes). By enforcing nearest-neighbor hopping and coupling the matter primarily to central localized functions, the interaction graph maps to a 1D qubit chain compatible with planar superconducting connectivity, strongly reducing SWAP overhead compared to star-like standing-wave mappings. Using first-order Trotter evolution and zero-noise extrapolation, I recovered accurate Rabi dynamics for a two-level system coupled to dozens of modes. Furthermore, I showed that even when relaxing strict 1D constraints of the interaction graph it is still possible to recover the quantum dynamics (using error mitigation techniques). This work shows that product-formula time evolution, when paired with hardware-aware encodings of bosons and photons, is a viable method on noisy devices and scales to many cavity modes. This work was made possible by the efficient implementation of efficient mapping of the fermionic and bosonic operators, as well as of the complicated interaction terms. Specifically, the logarithmic bosonic encoding reduced qubit counts from linear to logarithmic. Looking ahead, the quantum error correction era will allow to address the main issue of the approach, which is the accumulation of the quantum error as the quantum circuit becomes longer. This will not only allow to use the Trotter algorithm for more timesteps, but also to increase the complexity of the matter system and of the bosonic system. Specifically, it will be crucial in the future to include more Fock states, as it will allow to capture multi-photon effects clearly demonstrating quantum advantage.

In a nutshell, this thesis presented three numerical techniques to study light-matter interacting systems, each of them having advantages and drawbacks. Then, a key message of this thesis is that one should always carefully consider the characteristics of the system, and choose the most suitable method.

I believe the work presented in this thesis lays the groundwork for tackling one of the central challenges in modern QED, which is the simulation of large light-matter coupled systems, especially in the multi-mode case. By developing and employing effective photon-free techniques, such as Hamiltonian downfolding and self-consistent QED Hartree–Fock theory, we have shown that it is possible to capture non-perturbative cavity effects without explicitly propagating the full photonic Hilbert space. This opens the door to studying realistic cavities with many modes, where explicit many-body representation approaches quickly become intractable. In the short term, it will be possible to systematically apply these techniques to new classes of materials to unravel new phenomena, while ultimately waiting for the full development of QEDFT. At the same time, quantum computing offers a complementary path forward. The hardware-aware encodings and localized photonic bases introduced in this thesis demonstrate that even current noisy devices can meaningfully simulate QED dynamics. As error correction matures, I expect these methods to scale toward genuinely complex multi-mode scenarios, where even photon-free approaches reach their limits.

Bibliography

[1] Ramakrishna Janaswamy. “Geometrical optics and Fermat’s principle”. In: *Engineering Electrodynamics (Second Edition)*. 2053-2563. IOP Publishing, 2025, 9-1 to 9–28. DOI: `10.1088/978-0-7503-5884-2ch9`. URL: `https://dx.doi.org/10.1088/978-0-7503-5884-2ch9`.

[2] N. W. Ashcroft and N. D. Mermin. *Solid State Physics*. Holt-Saunders, 1976.

[3] Stefan A. Maier. *Plasmonics: Fundamentals and Applications*. Springer US, 2007. ISBN: 9780387378251. DOI: `10.1007/0-387-37825-1`. URL: `http://dx.doi.org/10.1007/0-387-37825-1`.

[4] Esra Ilke Albar et al. “Time-resolved plasmon-assisted generation of optical-vortex pulses”. In: *Scientific Reports* 13 (Sept. 2023), p. 14748. DOI: `10.1038/s41598-023-41606-3`. URL: `https://doi.org/10.1038/s41598-023-41606-3`.

[5] Lasse Kragh Sørensen et al. “Implementation of a semiclassical light-matter interaction using the Gauss-Hermite quadrature: A simple alternative to the multipole expansion”. In: *Physical Review A* 99.1 (Jan. 2019). ISSN: 2469-9934. DOI: `10.1103/physreva.99.013419`. URL: `http://dx.doi.org/10.1103/PhysRevA.99.013419`.

[6] Alba de las Heras et al. “Extreme-ultraviolet vector-vortex beams from high harmonic generation”. In: *Optica* 9.1 (Jan. 2022), p. 71. ISSN: 2334-2536. DOI: `10.1364/optica.442304`. URL: `http://dx.doi.org/10.1364/OPTICA.442304`.

[7] Esra Ilke Albar et al. “High-order harmonic generation with orbital angular momentum beams: Beyond-dipole corrections”. In: *Phys. Rev. A* (Nov. 2025), p. 063109. DOI: `10.1103/c1yg-2svv`. URL: `https://link.aps.org/doi/10.1103/c1yg-2svv`.

[8] Ferenc Krausz and Misha Ivanov. “Attosecond physics”. In: *Reviews of Modern Physics* 81.1 (Feb. 2009), pp. 163–234. ISSN: 1539-0756. DOI: `10.1103/revmodphys.81.163`. URL: `http://dx.doi.org/10.1103/RevModPhys.81.163`.

[9] Mauro Nisoli et al. “Attosecond Electron Dynamics in Molecules”. In: *Chemical Reviews* 117.16 (May 2017), pp. 10760–10825. ISSN: 1520-6890. DOI: `10.1021/acs.chemrev.6b00453`. URL: `http://dx.doi.org/10.1021/acs.chemrev.6b00453`.

[10] Michael Ruggenthaler et al. “From a quantum-electrodynamical light–matter description to novel spectroscopies”. In: *Nature Reviews Chemistry* 2.3 (Mar. 2018). ISSN: 2397-3358. DOI: `10.1038/s41570-018-0118`. URL: `http://dx.doi.org/10.1038/s41570-018-0118`.

[11] Tao E. Li, Hsing-Ta Chen, and Joseph E. Subotnik. “Comparison of Different Classical, Semiclassical, and Quantum Treatments of Light–Matter Interactions: Understanding Energy Conservation”. In: *Journal of Chemical Theory and Computation* 15.3 (Feb. 2019), pp. 1957–1973. ISSN: 1549-9626. DOI: `10.1021/acs.jctc.8b01232`. URL: `http://dx.doi.org/10.1021/acs.jctc.8b01232`.

[12] Rodney Loudon. *The Quantum Theory of Light.* 3rd ed. Oxford University Press, 2000. ISBN: 9780198501763.

[13] Anton Frisk Kockum et al. “Ultrastrong coupling between light and matter”. In: *Nature Reviews Physics* 1.1 (Jan. 2019), pp. 19–40. ISSN: 2522-5820. DOI: `10.1038/s42254-018-0006-2`. URL: `http://dx.doi.org/10.1038/s42254-018-0006-2`.

[14] Yuto Ashida, Ataç İmamoğlu, and Eugene Demler. “Cavity Quantum Electrodynamics at Arbitrary Light-Matter Coupling Strengths”. In: *Physical Review Letters* 126.15 (Apr. 2021). ISSN: 1079-7114. DOI: `10.1103/physrevlett.126.153603`. URL: `http://dx.doi.org/10.1103/PhysRevLett.126.153603`.

[15] Simone Latini et al. “Cavity Control of Excitons in Two-Dimensional Materials”. In: *Nano Letters* 19.6 (May 2019), pp. 3473–3479. ISSN: 1530-6992. DOI: `10.1021/acs.nanolett.9b00183`. URL: `http://dx.doi.org/10.1021/acs.nanolett.9b00183`.

[16] Simone Latini et al. “The ferroelectric photo ground state of $SrTiO_3$: Cavity materials engineering”. In: *Proceedings of the National Academy of Sciences* 118.31 (July 2021). ISSN: 1091-6490. DOI: `10.1073/pnas.2105618118`. URL: `http://dx.doi.org/10.1073/pnas.2105618118`.

[17] Max Planck. “Entropie und Temperatur strahlender Wärme”. In: *Annalen der Physik* 306.4 (Jan. 1900), pp. 719–737. ISSN: 1521-3889. DOI: `10.1002/andp.19003060410`. URL: `http://dx.doi.org/10.1002/andp.19003060410`.

[18] A. Einstein. “Über einen die Erzeugung und Verwandlung des Lichtes betreffenden heuristischen Gesichtspunkt”. In: *Annalen der Physik* 322.6 (Jan. 1905), pp. 132–148. ISSN: 1521-3889. DOI: `10.1002/andp.19053220607`. URL: `http://dx.doi.org/10.1002/andp.19053220607`.

[19] Paul A. M. Dirac. “The quantum theory of the emission and absorption of radiation”. In: *Proceedings of the Royal Society of London. Series A, Containing Papers of a Mathematical and Physical Character* 114.767 (Mar. 1927), pp. 243–265. ISSN: 2053-9150. DOI: `10.1098/rspa.1927.0039`. URL: `http://dx.doi.org/10.1098/rspa.1927.0039`.

[20] Albert Einstein. “Zur Quantentheorie der Strahlung”. In: *Physikalische Zeitschrift* 18 (1917). English title: On the Quantum Theory of Radiation, pp. 121–128.

[21] Willis E. Lamb and Robert C. Retherford. “Fine Structure of the Hydrogen Atom by a Microwave Method”. In: *Phys. Rev.* 72 (3 Aug. 1947), pp. 241–243. DOI: `10.1103/PhysRev.72.241`. URL: `https://link.aps.org/doi/10.1103/PhysRev.72.241`.

[22] Peter W. Milonni and Wallace Arden Smith. “Radiation reaction and vacuum fluctuations in spontaneous emission”. In: *Phys. Rev. A* 11 (3 Mar. 1975), pp. 814–824. DOI: `10.1103/PhysRevA.11.814`. URL: `https://link.aps.org/doi/10.1103/PhysRevA.11.814`.

[23] H. B. G. Casimir and D. Polder. “The Influence of Retardation on the London-van der Waals Forces”. In: *Phys. Rev.* 73 (4 Feb. 1948), pp. 360–372. DOI: `10.1103/PhysRev.73.360`. URL: `https://link.aps.org/doi/10.1103/PhysRev.73.360`.

[24] X. Fan et al. “Measurement of the Electron Magnetic Moment”. In: *Physical Review Letters* 130.7 (Feb. 2023). ISSN: 1079-7114. DOI: `10.1103/physrevlett.130.071801`. URL: `http://dx.doi.org/10.1103/PhysRevLett.130.071801`.

[25] K. Hagiwara et al. "Improved predictions for g2 of the muon and $\alpha_{QED}(M_Z^2)$". In: *Physics Letters B* 649.2–3 (May 2007), pp. 173–179. ISSN: 0370-2693. DOI: `10.1016/j.physletb.2007.04.012`. URL: `http://dx.doi.org/10.1016/j.physletb.2007.04.012`.

[26] Pierre Cladé et al. "Determination of the Fine Structure Constant Based on Bloch Oscillations of Ultracold Atoms in a Vertical Optical Lattice". In: *Physical Review Letters* 96.3 (Jan. 2006). ISSN: 1079-7114. DOI: `10.1103/physrevlett.96.033001`. URL: `http://dx.doi.org/10.1103/PhysRevLett.96.033001`.

[27] Michael Ruggenthaler et al. "Quantum-electrodynamical density-functional theory: Bridging quantum optics and electronic-structure theory". In: *Physical Review A* 90.1 (July 2014). ISSN: 1094-1622. DOI: `10.1103/physreva.90.012508`. URL: `http://dx.doi.org/10.1103/PhysRevA.90.012508`.

[28] Johannes Flick et al. "Atoms and molecules in cavities, from weak to strong coupling in quantum-electrodynamics (QED) chemistry". In: *Proceedings of the National Academy of Sciences* 114.12 (Mar. 2017), pp. 3026–3034. ISSN: 1091-6490. DOI: `10.1073/pnas.1615509114`. URL: `http://dx.doi.org/10.1073/pnas.1615509114`.

[29] M. A. Sentef, M. Ruggenthaler, and A. Rubio. "Cavity quantum-electrodynamical polaritonically enhanced electron-phonon coupling and its influence on superconductivity". In: *Science Advances* 4.11 (Nov. 2018). ISSN: 2375-2548. DOI: `10.1126/sciadv.aau6969`. URL: `http://dx.doi.org/10.1126/sciadv.aau6969`.

[30] Hannes Hübener et al. "Engineering quantum materials with chiral optical cavities". In: *Nature Materials* 20.4 (Nov. 2020), pp. 438–442. ISSN: 1476-4660. DOI: `10.1038/s41563-020-00801-7`. URL: `http://dx.doi.org/10.1038/s41563-020-00801-7`.

[31] Emil Viñas Boström et al. "Controlling the magnetic state of the proximate quantum spin liquid α-RuCl$_3$ with an optical cavity". In: *npj Computational Materials* 9.1 (Oct. 2023). ISSN: 2057-3960. DOI: `10.1038/s41524-023-01158-6`. URL: `http://dx.doi.org/10.1038/s41524-023-01158-6`.

[32] I-Te Lu et al. "Cavity-enhanced superconductivity in MgB$_2$ from first-principles quantum electrodynamics (QEDFT)". In: *Proceedings of the National Academy of Sciences* 121.50 (Dec. 2024). ISSN: 1091-6490. DOI: `10.1073/pnas.2415061121`. URL: `http://dx.doi.org/10.1073/pnas.2415061121`.

[33] Hannes Hübener et al. "Quantum materials engineering by structured cavity vacuum fluctuations". In: *Materials for Quantum Technology* 4.2 (June 2024), p. 023002. ISSN: 2633-4356. DOI: `10.1088/2633-4356/ad4e8b`. URL: `http://dx.doi.org/10.1088/2633-4356/ad4e8b`.

[34] D. N. Basov et al. "Polariton panorama". In: *Nanophotonics* 10.1 (Nov. 2020), pp. 549–577. ISSN: 2192-8606. DOI: `10.1515/nanoph-2020-0449`. URL: `http://dx.doi.org/10.1515/nanoph-2020-0449`.

[35] Mark Kamper Svendsen et al. "Effective equilibrium theory of quantum light-matter interaction in cavities for extended systems and the long wavelength approximation". In: *Communications Physics* 8.1 (Nov. 2025). ISSN: 2399-3650. DOI: `10.1038/s42005-025-02365-x`. URL: `http://dx.doi.org/10.1038/s42005-025-02365-x`.

[36] P. Forn-Díaz et al. “Ultrastrong coupling regimes of light-matter interaction”. In: *Reviews of Modern Physics* 91.2 (June 2019). ISSN: 1539-0756. DOI: `10.1103/revmodphys.91.025005`. URL: `http://dx.doi.org/10.1103/RevModPhys.91.025005`.

[37] Itai Keren et al. *Cavity-altered superconductivity.* 2025. DOI: `10.48550/ARXIV.2505.17378`. URL: `https://arxiv.org/abs/2505.17378`.

[38] Giacomo Jarc et al. “Cavity-mediated thermal control of metal-to-insulator transition in 1T-TaS2”. In: *Nature* 622.7983 (Oct. 2023), pp. 487–492. ISSN: 1476-4687. DOI: `10.1038/s41586-023-06596-2`. URL: `http://dx.doi.org/10.1038/s41586-023-06596-2`.

[39] Hongjing Xu et al. *Vacuum-dressed superconductivity in NbN observed in a high-Q terahertz cavity.* 2026. DOI: `10.48550/ARXIV.2601.08191`. URL: `https://arxiv.org/abs/2601.08191`.

[40] Dominik Sidler et al. “Unraveling a Cavity-Induced Molecular Polarization Mechanism from Collective Vibrational Strong Coupling”. In: *The Journal of Physical Chemistry Letters* 15.19 (May 2024), pp. 5208–5214. ISSN: 1948-7185. DOI: `10.1021/acs.jpclett.4c00913`. URL: `http://dx.doi.org/10.1021/acs.jpclett.4c00913`.

[41] Jacob Horak et al. “Analytic model reveals local molecular polarizability changes induced by collective strong coupling in optical cavities”. In: *Physical Review Research* 7.1 (Mar. 2025). ISSN: 2643-1564. DOI: `10.1103/physrevresearch.7.013242`. URL: `http://dx.doi.org/10.1103/PhysRevResearch.7.013242`.

[42] Dominik Sidler, Michael Ruggenthaler, and Angel Rubio. “Collectively-modified inter-molecular electron correlations: The connection of polaritonic chemistry and spin glass physics”. In: *arXiv* (2024). DOI: `10.48550/ARXIV.2409.08986`. arXiv: `2409.08986`. URL: `https://arxiv.org/abs/2409.08986`.

[43] Christian Schäfer et al. “Shining light on the microscopic resonant mechanism responsible for cavity-mediated chemical reactivity”. In: *Nature Communications* 13.1 (Dec. 2022). ISSN: 2041-1723. DOI: `10.1038/s41467-022-35363-6`. URL: `http://dx.doi.org/10.1038/s41467-022-35363-6`.

[44] Giacomo Mazza and Antoine Georges. “Superradiant Quantum Materials”. In: *Physical Review Letters* 122.1 (Jan. 2019). ISSN: 1079-7114. DOI: `10.1103/physrevlett.122.017401`. URL: `http://dx.doi.org/10.1103/PhysRevLett.122.017401`.

[45] Yuto Ashida et al. “Quantum Electrodynamic Control of Matter: Cavity-Enhanced Ferroelectric Phase Transition”. In: *Physical Review X* 10.4 (Nov. 2020). ISSN: 2160-3308. DOI: `10.1103/physrevx.10.041027`. URL: `http://dx.doi.org/10.1103/PhysRevX.10.041027`.

[46] I-Te Lu et al. “Cavity engineering of solid-state materials without external driving”. In: *Advances in Optics and Photonics* 17.2 (May 2025), p. 441. ISSN: 1943-8206. DOI: `10.1364/aop.544138`. URL: `http://dx.doi.org/10.1364/AOP.544138`.

[47] W. Pauli and M. Fierz. “Zur Theorie der Emission langwelliger Lichtquanten”. In: *Il Nuovo Cimento* 15.3 (Mar. 1938), pp. 167–188. ISSN: 1827-6121. DOI: `10.1007/bf02958939`. URL: `http://dx.doi.org/10.1007/BF02958939`.

[48] H. A. Bethe. “The Electromagnetic Shift of Energy Levels”. In: *Physical Review* 72.4 (Aug. 1947), pp. 339–341. ISSN: 0031-899X. DOI: `10.1103/physrev.72.339`. URL: `http://dx.doi.org/10.1103/PhysRev.72.339`.

[49] Michael Ruggenthaler, Dominik Sidler, and Angel Rubio. “Understanding Polaritonic Chemistry from Ab Initio Quantum Electrodynamics”. In: *Chemical Reviews* 123.19 (Sept. 2023), pp. 11191–11229. ISSN: 1520-6890. DOI: `10.1021/acs.chemrev.2c00788`. URL: `http://dx.doi.org/10.1021/acs.chemrev.2c00788`.

[50] Francesco Troisi et al. “Cavity-QED-controlled two-dimensional Moiré excitons without twisting”. In: *Nature Communications* 17.1 (Dec. 2025). ISSN: 2041-1723. DOI: `10.1038/s41467-025-67570-2`. URL: `http://dx.doi.org/10.1038/s41467-025-67570-2`.

[51] Hang Liu et al. “Cavity-mediated electron-electron interactions: Renormalizing Dirac states in graphene”. In: *Science Advances* 11.43 (Oct. 2025). ISSN: 2375-2548. DOI: `10.1126/sciadv.adz1855`. URL: `http://dx.doi.org/10.1126/sciadv.adz1855`.

[52] Hanan Herzig Sheinfux et al. “High-quality nanocavities through multimodal confinement of hyperbolic polaritons in hexagonal boron nitride”. In: *Nature Materials* 23.4 (Feb. 2024), pp. 499–505. ISSN: 1476-4660. DOI: `10.1038/s41563-023-01785-w`. URL: `http://dx.doi.org/10.1038/s41563-023-01785-w`.

[53] Itai Keren et al. *Cavity-altered superconductivity.* 2025. DOI: `10.48550/ARXIV.2505.17378`. URL: `https://arxiv.org/abs/2505.17378`.

[54] Gian Marcello Andolina et al. “Amperean superconductivity cannot be induced by deep subwavelength cavities in a two-dimensional material”. In: *Physical Review B* 109.10 (Mar. 2024). ISSN: 2469-9969. DOI: `10.1103/physrevb.109.104513`. URL: `http://dx.doi.org/10.1103/PhysRevB.109.104513`.

[55] Gunda Kipp et al. “Cavity electrodynamics of van der Waals heterostructures”. In: *Nature Physics* (Oct. 2025). ISSN: 1745-2481. DOI: `10.1038/s41567-025-03064-8`. URL: `http://dx.doi.org/10.1038/s41567-025-03064-8`.

[56] Feliciano Giustino. *Materials Modelling using Density Functional Theory.* Oxford University Press, 2014.

[57] D. R. Hartree. “The Wave Mechanics of an Atom with a Non-Coulomb Central Field. Part II. Some Results and Discussion”. In: *Mathematical Proceedings of the Cambridge Philosophical Society* 24.1 (Jan. 1928), pp. 111–132. ISSN: 1469-8064. DOI: `10.1017/s0305004100011920`. URL: `http://dx.doi.org/10.1017/S0305004100011920`.

[58] V. Fock. “Selfconsistent field mit Austausch für Natrium”. In: *Zeitschrift für Physik* 62.11–12 (Nov. 1930), pp. 795–805. ISSN: 1434-601X. DOI: `10.1007/bf01330439`. URL: `http://dx.doi.org/10.1007/BF01330439`.

[59] P. Hohenberg and W. Kohn. “Inhomogeneous Electron Gas”. In: *Physical Review* 136.3B (Nov. 1964), B864–B871. ISSN: 0031-899X. DOI: `10.1103/physrev.136.b864`. URL: `http://dx.doi.org/10.1103/PhysRev.136.B864`.

[60] W. Kohn and L. J. Sham. “Self-Consistent Equations Including Exchange and Correlation Effects”. In: *Physical Review* 140.4A (Nov. 1965), A1133–A1138. ISSN: 0031-899X. DOI: `10.1103/physrev.140.a1133`. URL: `http://dx.doi.org/10.1103/PhysRev.140.A1133`.

[61] Camilla Pellegrini et al. “Optimized Effective Potential for Quantum Electrodynamical Time-Dependent Density Functional Theory”. In: *Physical Review Letters* 115.9 (Aug. 2015). ISSN: 1079-7114. DOI: `10.1103/physrevlett.115.093001`. URL: `http://dx.doi.org/10.1103/PhysRevLett.115.093001`.

[62] Johannes Flick et al. “Ab Initio Optimized Effective Potentials for Real Molecules in Optical Cavities: Photon Contributions to the Molecular Ground State”. In: *ACS Photonics* 5.3 (Jan. 2018), pp. 992–1005. ISSN: 2330-4022. DOI: `10.1021/acsphotonics.7b01279`. URL: `http://dx.doi.org/10.1021/acsphotonics.7b01279`.

[63] Johannes Flick et al. “Light–Matter Response in Nonrelativistic Quantum Electrodynamics”. In: *ACS Photonics* 6.11 (Oct. 2019), pp. 2757–2778. ISSN: 2330-4022. DOI: `10.1021/acsphotonics.9b00768`. URL: `http://dx.doi.org/10.1021/acsphotonics.9b00768`.

[64] Christian Schäfer et al. “Making ab initio QED functional(s): Nonperturbative and photon-free effective frameworks for strong light–matter coupling”. In: *Proceedings of the National Academy of Sciences* 118.41 (Oct. 2021). ISSN: 1091-6490. DOI: `10.1073/pnas.2110464118`. URL: `http://dx.doi.org/10.1073/pnas.2110464118`.

[65] Mark Kamper Svendsen et al. “Ab Initio Calculations of Quantum Light–Matter Interactions in General Electromagnetic Environments”. In: *Journal of Chemical Theory and Computation* 20.2 (Jan. 2024), pp. 926–936. ISSN: 1549-9626. DOI: `10.1021/acs.jctc.3c00967`. URL: `http://dx.doi.org/10.1021/acs.jctc.3c00967`.

[66] I-Te Lu et al. “Electron-photon exchange-correlation approximation for quantum-electrodynamical density-functional theory”. In: *Physical Review A* 109.5 (May 2024). ISSN: 2469-9934. DOI: `10.1103/physreva.109.052823`. URL: `http://dx.doi.org/10.1103/PhysRevA.109.052823`.

[67] Hang Liu et al. “Modifying electronic and structural properties of 2D van der Waals materials via cavity quantum vacuum fluctuations: a first-principles QEDFT study [Invited]”. In: *Optical Materials Express* 15.9 (Aug. 2025), p. 2105. ISSN: 2159-3930. DOI: `10.1364/ome.568454`. URL: `http://dx.doi.org/10.1364/OME.568454`.

[68] Mark Kamper Svendsen et al. “Combining density functional theory with macroscopic QED for quantum light-matter interactions in 2D materials”. In: *Nature Communications* 12.1 (May 2021). ISSN: 2041-1723. DOI: `10.1038/s41467-021-23012-3`. URL: `http://dx.doi.org/10.1038/s41467-021-23012-3`.

[69] Norah M. Hoffmann et al. “Benchmarking semiclassical and perturbative methods for real-time simulations of cavity-bound emission and interference”. In: *The Journal of Chemical Physics* 151.24 (Dec. 2019). ISSN: 1089-7690. DOI: `10.1063/1.5128076`. URL: `http://dx.doi.org/10.1063/1.5128076`.

[70] Norah M. Hoffmann et al. “Capturing vacuum fluctuations and photon correlations in cavity quantum electrodynamics with multitrajectory Ehrenfest dynamics”. In: *Physical Review A* 99.6 (June 2019). ISSN: 2469-9934. DOI: `10.1103/physreva.99.063819`. URL: `http://dx.doi.org/10.1103/PhysRevA.99.063819`.

[71] René Jestädt et al. “Light-matter interactions within the Ehrenfest–Maxwell–Pauli–Kohn–Sham framework: fundamentals, implementation, and nano-optical applications”. In: *Advances in Physics* 68.4 (Oct. 2019), pp. 225–333. ISSN: 1460-6976. DOI: `10.1080/00018732.2019.1695875`. URL: `http://dx.doi.org/10.1080/00018732.2019.1695875`.

[72] Franco P. Bonafé et al. “Full minimal coupling Maxwell-TDDFT: An ab initio framework for light-matter interaction beyond the dipole approximation”. In: *Phys. Rev. B* 111 (8 Feb. 2025), p. 085114. DOI: `10.1103/PhysRevB.111.085114`. URL: `https://link.aps.org/doi/10.1103/PhysRevB.111.085114`.

[73] Carlos M. Bustamante et al. “Dissipative Equation of Motion for Electromagnetic Radiation in Quantum Dynamics”. In: *Physical Review Letters* 126.8 (Feb. 2021). ISSN: 1079-7114. DOI: `10.1103/physrevlett.126.087401`. URL: `http://dx.doi.org/10.1103/PhysRevLett.126.087401`.

[74] Arto Sakko et al. “Time-dependent density functional approach for the calculation of inelastic x-ray scattering spectra of molecules”. In: *The Journal of Chemical Physics* 133.17 (Nov. 2010). ISSN: 1089-7690. DOI: `10.1063/1.3503594`. URL: `http://dx.doi.org/10.1063/1.3503594`.

[75] Nicolás O. Foglia, Dimitrios Maganas, and Frank Neese. “Going beyond the electric-dipole approximation in the calculation of absorption and (magnetic) circular dichroism spectra including scalar relativistic and spin–orbit coupling effects”. In: *The Journal of Chemical Physics* 157.8 (Aug. 2022). ISSN: 1089-7690. DOI: `10.1063/5.0094709`. URL: `http://dx.doi.org/10.1063/5.0094709`.

[76] Rosario R. Riso et al. “Strong Coupling in Chiral Cavities: Nonperturbative Framework for Enantiomer Discrimination”. In: *Physical Review X* 13.3 (July 2023). ISSN: 2160-3308. DOI: `10.1103/physrevx.13.031002`. URL: `http://dx.doi.org/10.1103/PhysRevX.13.031002`.

[77] Christian Schäfer and Denis G. Baranov. “Chiral Polaritonics: Analytical Solutions, Intuition, and Use”. In: *The Journal of Physical Chemistry Letters* 14.15 (Apr. 2023), pp. 3777–3784. ISSN: 1948-7185. DOI: `10.1021/acs.jpclett.3c00286`. URL: `http://dx.doi.org/10.1021/acs.jpclett.3c00286`.

[78] Yair Litman et al. “First-Principles Simulations of Tip Enhanced Raman Scattering Reveal Active Role of Substrate on High-Resolution Images”. In: *The Journal of Physical Chemistry Letters* 14.30 (July 2023), pp. 6850–6859. ISSN: 1948-7185. DOI: `10.1021/acs.jpclett.3c01216`. URL: `http://dx.doi.org/10.1021/acs.jpclett.3c01216`.

[79] Nicolas Tancogne-Dejean et al. “Octopus, a computational framework for exploring light-driven phenomena and quantum dynamics in extended and finite systems”. In: *The Journal of Chemical Physics* 152.12 (Mar. 2020). ISSN: 1089-7690. DOI: `10.1063/1.5142502`. URL: `http://dx.doi.org/10.1063/1.5142502`.

[80] Adrià Delhom. "Minimal coupling in presence of non-metricity and torsion". In: *The European Physical Journal C* 80.8 (Aug. 2020). ISSN: 1434-6052. DOI: `10.1140/epjc/s10052-020-8330-y`. URL: `http://dx.doi.org/10.1140/epjc/s10052-020-8330-y`.

[81] Francesco Troisi. "QED solver for ab-initio cavity materials engineering". Master's thesis. Politecnico di Milano, 2022. URL: `https://hdl.handle.net/10589/195033`.

[82] Xiao Wang, Enrico Ronca, and Michael A. Sentef. "Cavity quantum electrodynamical Chern insulator: Towards light-induced quantized anomalous Hall effect in graphene". In: *Physical Review B* 99.23 (June 2019). ISSN: 2469-9969. DOI: `10.1103/physrevb.99.235156`. URL: `http://dx.doi.org/10.1103/PhysRevB.99.235156`.

[83] Michael A. Nielsen and Isaac L. Chuang. *Quantum Computation and Quantum Information: 10th Anniversary Edition*. Cambridge University Press, June 2012. ISBN: 9780511976667. DOI: `10.1017/cbo9780511976667`. URL: `http://dx.doi.org/10.1017/CBO9780511976667`.

[84] Muhammad AbuGhanem. "IBM quantum computers: evolution, performance, and future directions". In: *The Journal of Supercomputing* 81.5 (Apr. 2025). ISSN: 1573-0484. DOI: `10.1007/s11227-025-07047-7`. URL: `http://dx.doi.org/10.1007/s11227-025-07047-7`.

[85] Alexander Miessen, Pauline J. Ollitrault, and Ivano Tavernelli. "Quantum algorithms for quantum dynamics: A performance study on the spin-boson model". In: *Physical Review Research* 3.4 (Dec. 2021). ISSN: 2643-1564. DOI: `10.1103/physrevresearch.3.043212`. URL: `http://dx.doi.org/10.1103/PhysRevResearch.3.043212`.

[86] Xin-Yu Huang et al. "Qubitization of Bosons". In: *Progress in High Energy Physics PHEP* 2025.2 (May 2025). DOI: `10.31526/PHEP.2025.03`. URL: `https://phep.andromedapublisher.org/index.php/PHEP/article/view/3`.

[87] Bo Peng et al. "Quantum simulation of boson-related Hamiltonians: techniques, effective Hamiltonian construction, and error analysis". In: *Quantum Science and Technology* 10.2 (Mar. 2025), p. 023002. ISSN: 2058-9565. DOI: `10.1088/2058-9565/adbf42`. URL: `http://dx.doi.org/10.1088/2058-9565/adbf42`.

[88] P. Ehrenfest. "Bemerkung über die angenäherte Gültigkeit der klassischen Mechanik innerhalb der Quantenmechanik". In: *Zeitschrift für Physik* 45.7–8 (July 1927), pp. 455–457. ISSN: 1434-601X. DOI: `10.1007/bf01329203`. URL: `http://dx.doi.org/10.1007/BF01329203`.

[89] Hsing-Ta Chen et al. "Ehrenfest+R dynamics. II. A semiclassical QED framework for Raman scattering". In: *The Journal of Chemical Physics* 150.4 (Jan. 2019). ISSN: 1089-7690. DOI: `10.1063/1.5057366`. URL: `http://dx.doi.org/10.1063/1.5057366`.

[90] M.A.L. Marques and E.K.U. Gross. "TIME-DEPENDENT DENSITY FUNCTIONAL THEORY". In: *Annual Review of Physical Chemistry* 55.1 (June 2004), pp. 427–455. ISSN: 1545-1593. DOI: `10.1146/annurev.physchem.55.091602.094449`. URL: `http://dx.doi.org/10.1146/annurev.physchem.55.091602.094449`.

[91] Carsten A. Ullrich. *Time-Dependent Density-Functional Theory: Concepts and Applications*. Illustrated, Reprint. Oxford Graduate Texts. OUP Oxford, 2011, p. 526. ISBN: 9780199563029.

[92] Erich Runge and E. K. U. Gross. “Density-Functional Theory for Time-Dependent Systems”. In: *Physical Review Letters* 52.12 (Mar. 1984), pp. 997–1000. ISSN: 0031-9007. DOI: `10.1103/physrevlett.52.997`. URL: `http://dx.doi.org/10.1103/PhysRevLett.52.997`.

[93] Lionel Lacombe and Neepa T. Maitra. “Developing new and understanding old approximations in TDDFT”. In: *Faraday Discussions* 224 (2020), pp. 382–401. ISSN: 1364-5498. DOI: `10.1039/d0fd00049c`. URL: `http://dx.doi.org/10.1039/D0FD00049C`.

[94] A. Castro and M.A.L. Marques. “Propagators for the Time-Dependent Kohn-Sham Equations”. In: *Time-Dependent Density Functional Theory*. Springer Berlin Heidelberg, 2006, pp. 197–210. ISBN: 9783540354260. DOI: `10.1007/3-540-35426-3_12`. URL: `http://dx.doi.org/10.1007/3-540-35426-3_12`.

[95] René Jestädt. “Fully coupled Maxwell-Kohn-Sham systems”. en. PhD thesis. TU Berlin, 2020. DOI: `10.14279/DEPOSITONCE-9825`. URL: `https://depositonce.tu-berlin.de/handle/11303/10932`.

[96] V. B. Berestetskii, E. M. Lifshitz, and L. P. Pitaevskii. *Relativistic Quantum Theory, Part 1.* Vol. 4. Course of Theoretical Physics. Oxford: Pergamon Press, 1971.

[97] Iwo Bialynicki-Birula. “Progress in Optics”. In: Elsevier, 1996, pp. 245–294. ISBN: 9780444825308. DOI: `10.1016/s0079-6638(08)70316-0`. URL: `http://dx.doi.org/10.1016/S0079-6638(08)70316-0`.

[98] Hermann von Helmholtz. “Über Integrale der hydrodynamischen Gleichungen, welche den Wirbelbewegungen entsprechen”. In: *Journal für die reine und angewandte Mathematik* 1858.55 (1858), pp. 25–55. DOI: `10.1515/crll.1858.55.25`. URL: `https://doi.org/10.1515/crll.1858.55.25`.

[99] J. Willard Gibbs and Edwin Bidwell Wilson. *Vector Analysis: A Text-Book for the Use of Students of Mathematics and Physics*. New York: C. Scribner’s Sons, 1901. URL: `https://archive.org/details/vectoranalysiste00gibbiala`.

[100] Sheldon Axler, Paul Bourdon, and Wade Ramey. “Bounded Harmonic Functions”. In: *Harmonic Function Theory*. Springer New York, 1992, pp. 31–44. ISBN: 9780387215273. DOI: `10.1007/0-387-21527-1_2`. URL: `http://dx.doi.org/10.1007/0-387-21527-1_2`.

[101] A. J. Chorin and J. E. Marsden. *A Mathematical Introduction to Fluid Mechanics*. Springer US, 1990. ISBN: 9781468403640. DOI: `10.1007/978-1-4684-0364-0`. URL: `http://dx.doi.org/10.1007/978-1-4684-0364-0`.

[102] Edward N. Lorenz. “Deterministic Nonperiodic Flow”. In: *Journal of the Atmospheric Sciences* 20.2 (Mar. 1963), pp. 130–141. ISSN: 1520-0469. DOI: `10.1175/1520-0469(1963)020<0130:dnf>2.0.co;2`. URL: `http://dx.doi.org/10.1175/1520-0469(1963)020%3C0130:DNF%3E2.0.CO;2`.

[103] A M Stewart. “Vector potential of the Coulomb gauge”. In: *European Journal of Physics* 24.5 (July 2003), pp. 519–524. ISSN: 1361-6404. DOI: `10.1088/0143-0807/24/5/308`. URL: `http://dx.doi.org/10.1088/0143-0807/24/5/308`.

[104] Andrew Chubykalo, Augusto Espinoza, and Rolando Alvarado Flores. “Helmholtz Theorems, Gauge Transformations, General Covariance and the Empirical Meaning of Gauge Conditions”. In: *Journal of Modern Physics* 07.09 (2016), pp. 1021–1044. ISSN: 2153-120X. DOI: `10.4236/jmp.2016.79092`. URL: `http://dx.doi.org/10.4236/jmp.2016.79092`.

[105] Dennis W. Lindle and Oliver Hemmers. “Breakdown of the dipole approximation in soft-X-ray photoemission”. In: *Journal of Electron Spectroscopy and Related Phenomena* 100.1–3 (Oct. 1999), pp. 297–311. ISSN: 0368-2048. DOI: `10.1016/s0368-2048(99)00052-3`. URL: `http://dx.doi.org/10.1016/S0368-2048(99)00052-3`.

[106] Nicholas Rivera et al. “Shrinking light to allow forbidden transitions on the atomic scale”. In: *Science* 353.6296 (July 2016), pp. 263–269. ISSN: 1095-9203. DOI: `10.1126/science.aaf6308`. URL: `http://dx.doi.org/10.1126/science.aaf6308`.

[107] Patrick J. Lestrange, Franco Egidi, and Xiaosong Li. “The consequences of improperly describing oscillator strengths beyond the electric dipole approximation”. In: *The Journal of Chemical Physics* 143.23 (Dec. 2015). ISSN: 1089-7690. DOI: `10.1063/1.4937410`. URL: `http://dx.doi.org/10.1063/1.4937410`.

[108] Simon Vendelbo Bylling Jensen, Mads Middelhede Lund, and Lars Bojer Madsen. “Nondipole strong-field-approximation Hamiltonian”. In: *Physical Review A* 101.4 (Apr. 2020). ISSN: 2469-9934. DOI: `10.1103/physreva.101.043408`. URL: `http://dx.doi.org/10.1103/PhysRevA.101.043408`.

[109] J F McGilp. “Epioptics: linear and non-linear optical spectroscopy of surfaces and interfaces”. In: *Journal of Physics: Condensed Matter* 2.40 (Oct. 1990), pp. 7985–8006. ISSN: 1361-648X. DOI: `10.1088/0953-8984/2/40/001`. URL: `http://dx.doi.org/10.1088/0953-8984/2/40/001`.

[110] Jonathan H. Fetherolf and Timothy C. Berkelbach. “Linear and nonlinear spectroscopy from quantum master equations”. In: *The Journal of Chemical Physics* 147.24 (Dec. 2017). ISSN: 1089-7690. DOI: `10.1063/1.5006824`. URL: `http://dx.doi.org/10.1063/1.5006824`.

[111] Herbert Spohn. *Dynamics of Charged Particles and their Radiation Field.* Cambridge University Press, Aug. 2004. ISBN: 9780511535178. DOI: `10.1017/cbo9780511535178`. URL: `http://dx.doi.org/10.1017/CBO9780511535178`.

[112] Walter Greiner and Joachim Reinhardt. *Field Quantization.* Springer Berlin Heidelberg, 1996. ISBN: 9783642614859. DOI: `10.1007/978-3-642-61485-9`. URL: `http://dx.doi.org/10.1007/978-3-642-61485-9`.

[113] Dorte Rubæk Danielsen et al. “Fourier-Tailored Light–Matter Coupling in van der Waals Heterostructures”. In: *ACS Nano* 19.22 (May 2025), pp. 20645–20654. ISSN: 1936-086X. DOI: `10.1021/acsnano.5c02025`. URL: `http://dx.doi.org/10.1021/acsnano.5c02025`.

[114] Simone Latini et al. “Phonoritons as Hybridized Exciton-Photon-Phonon Excitations in a Monolayer h-BN Optical Cavity”. In: *Physical Review Letters* 126.22 (June 2021). ISSN: 1079-7114. DOI: `10.1103/physrevlett.126.227401`. URL: `http://dx.doi.org/10.1103/PhysRevLett.126.227401`.

[115] Takashi Oka and Sota Kitamura. “Floquet Engineering of Quantum Materials”. In: *Annual Review of Condensed Matter Physics* 10.1 (Mar. 2019), pp. 387–408. ISSN: 1947-5462. DOI: `10.1146/annurev-conmatphys-031218-013423`. URL: `http://dx.doi.org/10.1146/annurev-conmatphys-031218-013423`.

[116] Hannes Hübener et al. “Creating stable Floquet–Weyl semimetals by laser-driving of 3D Dirac materials”. In: *Nature Communications* 8.1 (Jan. 2017). ISSN: 2041-1723. DOI: `10.1038/ncomms13940`. URL: `http://dx.doi.org/10.1038/ncomms13940`.

[117] Rafi Bistritzer and Allan H. MacDonald. “Moiré bands in twisted double-layer graphene”. In: *Proceedings of the National Academy of Sciences* 108.30 (July 2011), pp. 12233–12237. ISSN: 1091-6490. DOI: `10.1073/pnas.1108174108`. URL: `http://dx.doi.org/10.1073/pnas.1108174108`.

[118] Zachariah Hennighausen and Swastik Kar. “Twistronics: a turning point in 2D quantum materials”. In: *Electronic Structure* 3.1 (Mar. 2021), p. 014004. ISSN: 2516-1075. DOI: `10.1088/2516-1075/abd957`. URL: `http://dx.doi.org/10.1088/2516-1075/abd957`.

[119] Samuel Brem et al. “Tunable Phases of Moiré Excitons in van der Waals Heterostructures”. In: *Nano Letters* 20.12 (Sept. 2020), pp. 8534–8540. ISSN: 1530-6992. DOI: `10.1021/acs.nanolett.0c03019`. URL: `http://dx.doi.org/10.1021/acs.nanolett.0c03019`.

[120] Gordon E. Moore. “Cramming more components onto integrated circuits, Reprinted from Electronics, volume 38, number 8, April 19, 1965, pp.114 ff.” In: *IEEE Solid-State Circuits Society Newsletter* 11.3 (2006), pp. 33–35. DOI: `10.1109/N-SSC.2006.4785860`.

[121] Dexter Johnson. *IBM Introduces the World’s First 2-nm Node Chip*. 2021. URL: `https://spectrum.ieee.org/ibm-introduces-the-worlds-first-2nm-node-chip`.

[122] Norman P. Jouppi et al. “In-Datacenter Performance Analysis of a Tensor Processing Unit”. In: *SIGARCH Comput. Archit. News* 45.2 (June 2017), pp. 1–12. ISSN: 0163-5964. DOI: `10.1145/3140659.3080246`. URL: `https://doi.org/10.1145/3140659.3080246`.

[123] Peter B R Nisbet-Jones et al. “Photonic qubits, qutrits and ququads accurately prepared and delivered on demand”. In: *New Journal of Physics* 15.5 (May 2013), p. 053007. ISSN: 1367-2630. DOI: `10.1088/1367-2630/15/5/053007`. URL: `http://dx.doi.org/10.1088/1367-2630/15/5/053007`.

[124] M. A. Yurtalan et al. “Implementation of a Walsh-Hadamard Gate in a Superconducting Qutrit”. In: *Physical Review Letters* 125.18 (Oct. 2020). ISSN: 1079-7114. DOI: `10.1103/physrevlett.125.180504`. URL: `http://dx.doi.org/10.1103/PhysRevLett.125.180504`.

[125] Youngseok Kim et al. “Evidence for the utility of quantum computing before fault tolerance”. In: *Nature* 618.7965 (June 2023), pp. 500–505. ISSN: 1476-4687. DOI: `10.1038/s41586-023-06096-3`. URL: `http://dx.doi.org/10.1038/s41586-023-06096-3`.

[126] K. Wright et al. “Benchmarking an 11-qubit quantum computer”. In: *Nature Communications* 10.1 (Nov. 2019). ISSN: 2041-1723. DOI: `10.1038/s41467-019-13534-2`. URL: `http://dx.doi.org/10.1038/s41467-019-13534-2`.

[127] T. M. Graham et al. “Multi-qubit entanglement and algorithms on a neutral-atom quantum computer”. In: *Nature* 604.7906 (Apr. 2022), pp. 457–462. ISSN: 1476-4687. DOI: `10.1038/s41586-022-04603-6`. URL: `http://dx.doi.org/10.1038/s41586-022-04603-6`.

[128] H. Aghaee Rad et al. “Scaling and networking a modular photonic quantum computer”. In: *Nature* 638.8052 (Jan. 2025), pp. 912–919. ISSN: 1476-4687. DOI: `10.1038/s41586-024-08406-9`. URL: `http://dx.doi.org/10.1038/s41586-024-08406-9`.

[129] Rolando D. Somma et al. “Quantum simulations of physics problems”. In: *Quantum Information and Computation*. Ed. by Eric Donkor, Andrew R. Pirich, and Howard E. Brandt. SPIE, Aug. 2003. DOI: `10.1117/12.487249`. URL: `http://dx.doi.org/10.1117/12.487249`.

[130] Bilal Shaw et al. “Encoding one logical qubit into six physical qubits”. In: *Physical Review A* 78.1 (July 2008). ISSN: 1094-1622. DOI: `10.1103/physreva.78.012337`. URL: `http://dx.doi.org/10.1103/PhysRevA.78.012337`.

[131] Reinier W. Heeres et al. “Implementing a universal gate set on a logical qubit encoded in an oscillator”. In: *Nature Communications* 8.1 (July 2017). ISSN: 2041-1723. DOI: `10.1038/s41467-017-00045-1`. URL: `http://dx.doi.org/10.1038/s41467-017-00045-1`.

[132] Adriano Barenco et al. “Elementary gates for quantum computation”. In: *Physical Review A* 52.5 (Nov. 1995), pp. 3457–3467. ISSN: 1094-1622. DOI: `10.1103/physreva.52.3457`. URL: `http://dx.doi.org/10.1103/PhysRevA.52.3457`.

[133] Morten Kjaergaard et al. “Superconducting Qubits: Current State of Play”. In: *Annual Review of Condensed Matter Physics* 11.1 (Mar. 2020), pp. 369–395. ISSN: 1947-5462. DOI: `10.1146/annurev-conmatphys-031119-050605`. URL: `http://dx.doi.org/10.1146/annurev-conmatphys-031119-050605`.

[134] McKinsey & Company. *The Year of Quantum: From concept to reality in 2025*. `https://www.mckinsey.com/capabilities/tech-and-ai/our-insights/the-year-of-quantum-from-concept-to-reality-in-2025`. June 2025.

[135] B.D. Josephson. “Possible new effects in superconductive tunnelling”. In: *Physics Letters* 1.7 (July 1962), pp. 251–253. ISSN: 0031-9163. DOI: `10.1016/0031-9163(62)91369-0`. URL: `http://dx.doi.org/10.1016/0031-9163(62)91369-0`.

[136] V. V. Ryazanov et al. “Coupling of Two Superconductors through a Ferromagnet: Evidence for a π-Junction”. In: *Physical Review Letters* 86.11 (Mar. 2001), pp. 2427–2430. ISSN: 1079-7114. DOI: `10.1103/physrevlett.86.2427`. URL: `http://dx.doi.org/10.1103/PhysRevLett.86.2427`.

[137] Francesco Troisi et al. “Hardware-efficient formulation of molecular cavity-QED Hamiltonians”. In: *arXiv* (2025). DOI: `10.48550/ARXIV.2510.17461`. URL: `https://arxiv.org/abs/2510.17461`.

[138] Colin D. Bruzewicz et al. “Trapped-ion quantum computing: Progress and challenges”. In: *Applied Physics Reviews* 6.2 (May 2019). ISSN: 1931-9401. DOI: `10.1063/1.5088164`. URL: `http://dx.doi.org/10.1063/1.5088164`.

[139] J. I. Cirac and P. Zoller. “Quantum Computations with Cold Trapped Ions”. In: *Physical Review Letters* 74.20 (May 1995), pp. 4091–4094. ISSN: 1079-7114. DOI: `10.1103/physrevlett.74.4091`. URL: `http://dx.doi.org/10.1103/PhysRevLett.74.4091`.

[140] V. M. Schäfer et al. “Fast quantum logic gates with trapped-ion qubits”. In: *Nature* 555.7694 (Mar. 2018), pp. 75–78. ISSN: 1476-4687. DOI: `10.1038/nature25737`. URL: `http://dx.doi.org/10.1038/nature25737`.

[141] M Saffman. “Quantum computing with atomic qubits and Rydberg interactions: progress and challenges”. In: *Journal of Physics B: Atomic, Molecular and Optical Physics* 49.20 (Oct. 2016), p. 202001. ISSN: 1361-6455. DOI: `10.1088/0953-4075/49/20/202001`. URL: `http://dx.doi.org/10.1088/0953-4075/49/20/202001`.

[142] Karen Wintersperger et al. “Neutral atom quantum computing hardware: performance and end-user perspective”. In: *EPJ Quantum Technology* 10.1 (Aug. 2023). ISSN: 2196-0763. DOI: `10.1140/epjqt/s40507-023-00190-1`. URL: `http://dx.doi.org/10.1140/epjqt/s40507-023-00190-1`.

[143] Dolev Bluvstein et al. “A quantum processor based on coherent transport of entangled atom arrays”. In: *Nature* 604.7906 (Apr. 2022), pp. 451–456. ISSN: 1476-4687. DOI: `10.1038/s41586-022-04592-6`. URL: `http://dx.doi.org/10.1038/s41586-022-04592-6`.

[144] Zhenpu Zhang et al. “High Optical Access Cryogenic System for Rydberg Atom Arrays with a 3000-Second Trap Lifetime”. In: *PRX Quantum* 6.2 (May 2025). ISSN: 2691-3399. DOI: `10.1103/prxquantum.6.020337`. URL: `http://dx.doi.org/10.1103/PRXQuantum.6.020337`.

[145] Simon J. Evered et al. “High-fidelity parallel entangling gates on a neutral-atom quantum computer”. In: *Nature* 622.7982 (Oct. 2023), pp. 268–272. ISSN: 1476-4687. DOI: `10.1038/s41586-023-06481-y`. URL: `http://dx.doi.org/10.1038/s41586-023-06481-y`.

[146] Jaehak Lee et al. *Photonic Hybrid Quantum Computing.* 2025. DOI: `10.48550/ARXIV.2510.00534`. URL: `https://arxiv.org/abs/2510.00534`.

[147] Maxime Dion, Tania Belabbas, and Nolan Bastien. *Efficiently manipulating Pauli strings with PauliArray.* 2024. DOI: `10.48550/ARXIV.2405.19287`. URL: `https://arxiv.org/abs/2405.19287`.

[148] P. Jordan and E. Wigner. “Über das Paulische Äquivalenzverbot”. In: *Zeitschrift für Physik* 47.9–10 (Sept. 1928), pp. 631–651. ISSN: 1434-601X. DOI: `10.1007/bf01331938`. URL: `http://dx.doi.org/10.1007/BF01331938`.

[149] Sergey B. Bravyi and Alexei Yu. Kitaev. “Fermionic Quantum Computation”. In: *Annals of Physics* 298.1 (May 2002), pp. 210–226. ISSN: 0003-4916. DOI: `10.1006/aphy.2002.6254`. URL: `http://dx.doi.org/10.1006/aphy.2002.6254`.

[150] Andrew Tranter et al. “A Comparison of the Bravyi–Kitaev and Jordan–Wigner Transformations for the Quantum Simulation of Quantum Chemistry”. In: *Journal of Chemical Theory and Computation* 14.11 (Sept. 2018), pp. 5617–5630. ISSN: 1549-9626. DOI: `10.1021/acs.jctc.8b00450`. URL: `http://dx.doi.org/10.1021/acs.jctc.8b00450`.

[151] Jacob T. Seeley, Martin J. Richard, and Peter J. Love. "The Bravyi-Kitaev transformation for quantum computation of electronic structure". In: *The Journal of Chemical Physics* 137.22 (Dec. 2012). ISSN: 1089-7690. DOI: `10.1063/1.4768229`. URL: `http://dx.doi.org/10.1063/1.4768229`.

[152] Libor Veis et al. "Quantum chemistry beyond Born–Oppenheimer approximation on a quantum computer: A simulated phase estimation study". In: *International Journal of Quantum Chemistry* 116.18 (June 2016), pp. 1328–1336. ISSN: 1097-461X. DOI: `10.1002/qua.25176`. URL: `http://dx.doi.org/10.1002/qua.25176`.

[153] Ravi P Srivastava et al. "2D materials in functional optoelectronics: recent advances and future prospects". In: *Nanotechnology* 36.39 (Sept. 2025), p. 392001. ISSN: 1361-6528. DOI: `10.1088/1361-6528/ae074a`. URL: `http://dx.doi.org/10.1088/1361-6528/ae074a`.

[154] Ali Azimi et al. "Photonics in Flatland: challenges and opportunities for nanophotonics with 2D semiconductors". In: *npj Nanophotonics* 2.1 (Dec. 2025). ISSN: 2948-216X. DOI: `10.1038/s44310-025-00092-3`. URL: `http://dx.doi.org/10.1038/s44310-025-00092-3`.

Acknowledgments

My doctorate in theoretical physics was carried out between November 2022 and January 2026 in the Theory Department of the Max Planck Institute for the Structure and Dynamics of Matter in Hamburg, Germany.

This thesis is dedicated to my grandfather Vaifro, who sadly passed away a few months before its completion. I know you would have been proud to see me reach this milestone, and I am sure you will be watching over my defense and the rest of my life from wherever you are. I will always carry you in my heart.

My deep gratitude goes to those who made this Ph.D. possible, my supervisor Angel Rubio and my co-supervisors Simone Latini and Ivano Tavernelli. There have been many ups and downs along the way, but I am proud of what we achieved together and of the valuable contributions we made to advancing the understanding of light–matter interactions. An even deeper gratitude goes to Simone, with whom I worked most closely and who very patiently guided me throughout these years, especially during the difficult moments. In the acknowledgments of my Master's thesis I wrote, "*I am sure you will be a great professor in your new tenure position at DTU and will inspire many students*". While I cannot speak for the others, you have certainly been an inspiration to me!

A big thank you also goes to my friends in Hamburg, with whom I shared countless moments and who became among my closest friends. Without your support, it would have been impossible to complete this journey. Among you, special thanks go to Paolo Lazzaroni, Elia Stocco, Franco Bonafé and George Trenins. Thank you for always being by my side, I will never forget the memories we made together. And lastly, but certainly not least given all we went through, a huge thank you goes to Ilke Albar.

I would also like to thank everyone else I met in Hamburg and around the world over these past three and a half years. I am proud of all these connections and look forward to visiting you in your respective cities!

Finally, I would like to thank my friends and family back in Italy. Even from afar, and despite all the times I failed to call, I have always felt your love and support. I know I can always count on you, both to celebrate our successes and to support each other in difficult moments.